Demystifying the powering mechanism of Low-Luminosity Active Galactic Nuclei

YAHERLYN DIAZ

Instituto de Física y Astronomía
Facultad de Ciencias

Universidad de Valparaíso
Doctorado en Astrofísica

Profesoras guía:
Patricia Arévalo
Lorena Hernández-García

August 2022
Valparaíso. Chile.

To my family, for their love and support during all these years.
To the memory of my grandparents.

A mi familia, por el amor y apoyo durante todo estos años.
En memoria a mis abuelos.

This thesis is solely my own composition,

except where specifically indicated in the text.

Yaherlyn Diaz
August 2022.
Valparaíso. Chile.

Acknowledgements

Many good people have helped me in this part of my life. I consider myself extremely lucky to have had Dra. Patricia Arévalo and Dra. Lorena Hernández-García as my supervisors, with their infectious enthusiasm for extragalactic astronomy, they have provided me with excellent guidance over the last four and a half years and have opened up a number of fantastic opportunities for me to progress as a researcher. Words cannot express how grateful I am for their enthusiasm, support, and guidance.

I would like to express my sincere appreciation to Dr. Claudio Ricci, who has been a great mentor to me with his professional experience and knowledge. His important suggestions have been invaluable, and without his persistent help, the goal of this project would not have been achieved. Thank you for having your door always open and for all our extremely interesting scientific discussions during my doctoral work.

I would also like to thank the members of the evaluation committee of this thesis, Prof. Paulina Lira and Prof. Veronica Motta, for taking the valuable time to review my work and providing me their invaluable insights and suggestions.

I am very grateful to the group LNA-AGN, especially Dr. Alberto Rodríguez-Ardila, for sharing his broad knowledge about AGN with me. He has certainly contributed to my scientific enrichment and has become a very dear friend. I would like to thank Denimara, Fernando, Marcos, Murilo, Raquel, Daniel and Panda for their enthusiasm and for the extremely interesting scientific discussions we have had over the years.

This project would not have been possible without my whole family. I will never find enough words to express my gratitude to my parents and sister who have supported me throughout my life, regardless of distance. Finally, I feel truly blessed to have Santiago as my partner. He has shown an incredible amount of care, support, and patience during my time as a graduate student.

Finally, I would like to thank the Max Planck Society by a Max Planck partner group, FIB-UV scholarship and the Millenium Nucleus NCN19-058 (TITANs) for the financial support provided during the PhD.

Abstract

Despite the long history of studies of active galactic nuclei (AGN), details on the structure of the accretion mechanism are far from clear. The work presented in this thesis is directed at unveiling properties of the structures in AGN through broad-band X-ray spectroscopy, with particular emphasis on broad X-ray band using *XMM-Newton+NuSTAR+Swift* (0.5–110.0 keV) data. With its unprecedented spectral sensitivity in this energy band, the combination of these telescopes provides the key observational diagnostics of the properties of the AGN X-ray source, the corona, and the surrounding gas in the accretion disk and the torus.

In this thesis we focused on the study of of Low-luminosity AGN (LLAGN), aiming at disentangle their inner structure, with emphasis on the reflection and the accretion mechanism. The first part of the document is centered on the development of the methodology and its application to one particular LLAGN, NGC 3718 ($L/L_{\rm Edd} \sim 10^{-5}$). Developing a methodology to study properties of potential reflectors and explore the improvement in the spectral index estimation considering high energy data and torus or disk like reflection models. We found that the inclusion of these models and high energy data allows to place strong constraints on the geometry and physical features of the surroundings as well to obtain more restricted values of a torus and a disk reflector.

Then we applied this methodology to a sample of 17 LLAGN from BASS/DR2 combining observations from *XMM-Newton*, *NuSTAR* and *Swift* and applying the same methodology that was previously developed in the first work in NGC 3718. From the analysis of the X-ray data of the AGN sample, we found a relation which is indicative of a change in the column density of the torus like reflector at lower accretion rates. Also, we confirm an anti-correlation between Γ-Eddington ratio with smaller scatter than previously reported, thanks to the inclusion of high energy data and the reflection models. The change in the correlation Γ-λ_{Edd} at $\sim 10^{-3}$ that we found is in agreement with a different accretion mechanism compared with higher accretion AGN as was previously reported in the literature.

Contents

CHAPTER 1

Introduction

Just over a century has passed since the first observations of active galactic nuclei (AGN) were recorded. As AGN continued to be discovered over the following years it became clear that they were among the most powerful energy of persistent objects in the Universe and we now know that they are extremely luminous over the whole electromagnetic spectrum. For many decades these energetic phenomena, residing at the centre of galaxies, were largely considered rare, yet fascinating, objects to study.

It is supposed that AGN are powered by matter falling into supermassive black holes (SMBH) with masses that can be of $10^8 M_\odot$ or more (Rees, 1984). These powerful engines undergo one of the most efficient processes to convert matter into energy. The study of their emitted radiation can be used to probe general relativistic effects and to study black hole (BH) growth. Especially at X-ray wavelengths, thought to be emitted in the direct proximity of the central SMBH, we can learn about the behavior of matter and radiation in extreme gravitational fields. Despite the fact that these exotic objects have been known for more than a century, many mysteries connected to AGN accretion and evolution remain unsolved, making this one of the most active research fields in Astrophysics.

In addition, in order to explain the variety of AGN observed in the universe, a Unified Model (UM) for AGN was proposed (Antonucci, 1993), where the idea is that AGN can be unified through an orientation based scheme where a toroidal structure (usually known as the torus) plays a key role. According to this model, AGN can be

classified as type I or II depending of the inclination relative to the obscuring torus. If we observe the AGN through the torus, the emission of the inner source will be attenuated and several emission features may be missing, then they are classified as type II. In the opposite case, if we get a direct view of the inner AGN source and the torus contributes to the observed spectrum only through its emission, and they can be classified as type I. However, this simplistic model cannot explain certain characteristics observed in the variety of the AGN family. For instance the decrease of the fraction of absorbed objects with the luminosity (and the accretion rate) of AGN (Ricci et al., 2017a), and consistent with the scenario in the infrared, (González-Martín et al., 2017), who found a relation between the luminosity of the AGN and the covering factor of this toroidal distribution. In fact, these authors found that there is a decrease in the torus emission in the low luminosity regime, pointing to a possible disappearance of the torus in low luminosity sources. However, it is not clear how change the properties of the torus in the X-rays in this luminosity regime. We can use the X-ray spectra also to study the properties of the gas geometry and to put constrains in properties of this structure analysing the reflection. In this thesis we are going to study changes on the gas in the torus with the accretion rate, using the reflection to infer properties as the column density or the covering factor and study their evolution with the luminosity in a sample of AGN.

In this chapter, I provide an overview of AGN as a phenomenon. In the first section I will give a brief summary of the steps in astronomy history that lead us to the knowledge on AGN we have today (see Sec. 1.1). In the sections afterward I will address the physics behind AGN and SMBH (see Sec. from 1.3 to 1.5). I end the chapter with a discussion of the X-ray observed in AGN (sect. 1.6) and an overview of astronomical X-ray instruments, discussing the observatories most relevant in this thesis, in particular *XMM-Newton*, *NuSTAR* and *Swift* (see Sec. 1.7).

1.1 Active Galactic Nuclei

The term AGN is used to define the center of galaxies containing a SMBH (M_{BH} $\sim 10^6$-10^9 $M_\odot$, where $M_\odot$ is the solar mass) that is efficiently fed by material through an accretion disk (e.g., Kormendy & Richstone 1995; Kormendy & Ho 2013). As the name implies, AGN are stronger emitters ($\sim 10^{36}$ - 10^{48} erg s^{-1}, Peterson 1997) than the nuclei of "normal" galaxies, as for example the Milky Way, which releases $\sim 10^{34}$ erg s^{-1} (van den Bergh, 1999) and it is assumed, that accretion onto a supermassive black hole

(SMBH) is the mechanism responsible for such a high energy release (Rees, 1984).

AGN have many interesting properties, including: (1) they emit across the whole electromagnetic spectrum, from γ rays to sub-mm, and can be detected up to high redshifts (currently z = 7.1: Mortlock et al. 2011); (2) rapid variability of their nuclei at different frequencies from radio to gamma rays (e.g., Hernández-García et al. (2014)); (3) Its spectrum contains strong emission lines, mainly found in the infra-red and optical/UV part of the spectrum, with line ratios that are typical of excitation by no stellar radiation field; and (4) an unresolved nucleus with small angular size.

The most notably distinct observational characteristic of AGN is the presence of emission lines with widths upwards of thousands of km s^{-1}. Also, the presence of narrow, non variable forbidden emission lines is a distinguishing observational feature of some AGN. Another observational aspect of AGN is that the continuum spectral distribution is very distinct from an integrated stellar continuum characteristic of normal galaxies. From the Observational point of view, AGN are very blue.

As you can see, AGN are very complex and interesting objects. Then, in the following I introduce how AGN look at different wavelengths (Sect. 1.2), then their classification (Sect. 1.4), the different components that constitute an AGN (Sect. 1.4), then the unified model (Sect. 1.5), the X-ray properties of AGN (Sections 1.6 and 1.7), and the context and focus of this thesis (Section 1.8).

1.2 A panchromatic view of an AGN

The emission of AGN cover the entire electromagnetic spectrum ranging from radio emission right up to γ-rays. The spectral energy distribution (SED) of AGN is complex because their spectra are due to a combination of various physical processes that take place in different regions around the SMBH. Then, different wavelength regimes provide different windows of AGN physics. In the the optical/ultraviolet (UV) band, the thermal emission from the accretion disk is observed, the infrared (IR) band is mostly sensitive to thermal emission from the dust heated by the primary UV radiation, while the X-ray band traces the reprocessed emission of the primary optical/UV emission from hot gas; the radio emission, due to synchrotron radiation, which can be relatively strong (radio-loud AGN) or weak (radio-quiet AGN). The sum of the different components emitting at these wavelengths give place to the typical SED of AGN, which is shown in Fig. 1.1 as a schematic representation from radio frequencies to hard X-rays. In the following I will describe some of the most prominent characteristics of AGN in

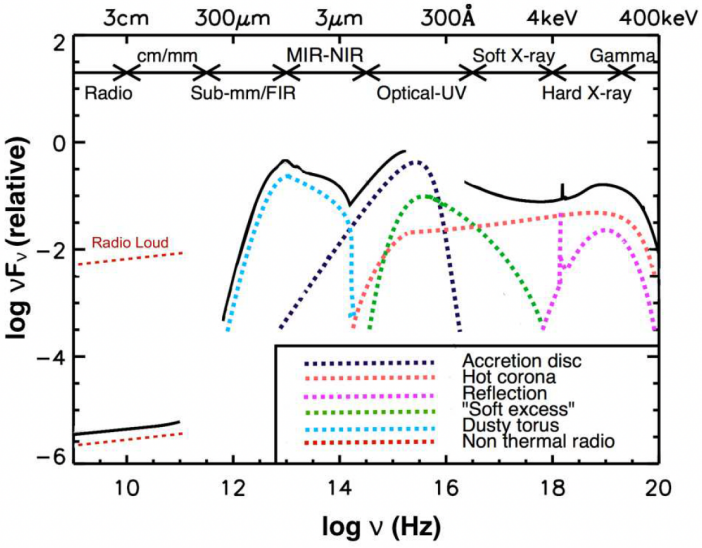

Figure 1.1: Schematic representation of the AGN SED (black curve), based on the observed SEDs of radio-quiet quasars (e.g., Elvis et al. 1994). The different colored curves (with an arbitrary offset) represent the physical components (see Section 1.2). Note that the primary emission from the AGN accretion disk peaks in the UV region. Radio loud AGN have radio emission that can be several orders of magnitude higher than radio-quiet AGN (shown with the labeled red).

different wavebands.

1.2.1 Radio emission

The dominant emission process in the radio band is synchrotron emission, i.e. radiation by charged particles gyrating at relativistic velocities through magnetic fields. Being of non-thermal origin, this emission is parameterized by a power law of the form $S_\nu \propto \nu^{-\alpha}$ where S_ν is the flux density [expressed in Jy] at frequency ν, and α is the spectral index.

It is found that ∼10% AGN are strong radio sources (radio loud - RL) while other have much weaker emission at radio wavelengths (radios quiet - RQ) (Padovani et al., 2011). Historically, the distinction between radio-loud and radio-quiet objects is based on the radio loudness parameter Kellermann et al. (1989), $R = F_R/F_o$, which is defined as the ratio of monochromatic luminosities at the radio (5 GHz) and optical (B band at 4400 $\AA$), where RQ objects are characterised by relatively low radio-to-optical flux density ratios ($R \leq 10$) .

1.2.2 Infrared emission

The emission in the infrared (IR) has a thermal origin and is due to dust grains that re-radiate the absorbed optical and ultraviolet photons emitted by the AGN as well as by stars in their host galaxies. (Perez Garcia et al., 1998) using *Infrared Space Observatory (ISO)* observations showed that the integrated mid-infrared (MIR) and far-infrared (FIR) thermal emission of some AGN, can be modeled with a combination of three different components: warm (T$\sim$150 K), due to dust heated by the AGN. The cold component (T$\sim$ 40-50 K) comes from dust heated by star-forming regions and the very cool component (T$\sim$ 10-20 K) arises from dust heated by the general interstellar radiation field of the galaxy. The IR spectrum is consistent with thermal emission from dust forming a torus around the SMBH, where the dust is heated by the ionizing radiation from the accretion disk. Also, superimposed to this continuum, the polycyclic aromatic hydrocarbons (PAH) features are observed and which can be considered to be originated in very small amorphous carbon dust grains or very large carbon-rich ring molecules (e.g. Draine & Li 2001). The most prominent, well-known PAH emissions, are the 6.2μm, 7.7μm, 8.6μm, 11.2μm and 12.7μm bands (e.g. Weedman et al. 2005).

In addition, The IR continuum seems to vary in the same manner as the optical/UV emission, but with a time delay corresponding to the light travel-time between the central, compact optical/UV-emitting region and the much more distant dust grains (e.g., Clavel et al. 1989). Then, from the observed delays, we can infer the position of the emitting dust from the nucleus (See for example, Arévalo et al. 2009; McHardy et al. 2014; Lira et al. 2015).

Furthermore, observations at the end of the far-infrared band show a sub-millimeter break, which is normally attributed to the rapid loss of efficiency of dust grains at longer wavelengths.

1.2.3 Optical-UV emission

The most notable feature observed in the optical/UV spectra in AGN is the so-called *big blue bump (BBB)*. Its origin is attributed to the thermal emission, very likely from the accretion disk surrounding the black hole (e.g., Shields 1978; Malkan & Sargent 1982), and it is modeled as a multi-color blackbody spectrum, as can be seen in the dot-dot-dashed dark blue line in Fig. 1.1.

A detailed analytical description of the disk structure has not been possible so

far. The main reason for that is the lack of a proper understanding of the viscous processes that lead to the transport of angular momentum. Nevertheless, Shakura & Sunyaev (1973) proposed a useful approximate solution to the problem of the angular momentum transport, applicable to geometrically thin but optically thick accretion disks, with a constant rate of accretion. In this model, the rotation is assumed to be Keplerian and the disk is in a steady state and the viscosity (called alpha viscosity) can be approximated as $v = \alpha c_s H$, where c_s is the speed of sound, H the disk thickness and α is a parameter between zero (no accretion) and approximately one (maximum rate of accretion). This parametrisation has been useful in algebraically expressing the disk properties.

According with Pringle (1981), in a geometrically thin, optically thick disk, and assuming the conservation of mass and angular momentum, the energy dissipated per unit surface per time in the disk can be expressed as:

$$D(R) = \frac{3GM_{BH}\dot{m}}{8\pi R^3}\left[1 - \left(\frac{R_{ISCO}}{R}\right)^{1/2}\right] \tag{1.1}$$

Where G is the gravitational constant, $\dot{m}$ denotes the rate of matter being accreted, M_{BH} is the black hole mass and R_{ISCO} is the radius of the innermost stable circular orbit.

According with this equation, the dissipated energy does not depend explicitly on viscosity. This allows us to study the emission of AGN and derive results without the need to understand in detail the exact energy dissipation mechanism. Assuming, in addition, that the liberated energy can be dissipated locally, meaning that the disk is optically thick at every radius, and as a result, each disk annulus at radius R emits a black body radiation, the disk temperature can be estimated using the Stefan-Boltzmann law. Combining this with equation 1.1, the disk temperature profile is, hence, given by:

$$T(R) = \left\{\frac{3GM_{BH}\dot{m}}{8\pi R^3\sigma}\left[1 - \left(\frac{R_{ISCO}}{R}\right)^{1/2}\right]\right\}^{1/4} \tag{1.2}$$

where σ is the Stefan-Boltzmann constant[1]. For large radii, $R \gg R_{ISCO}$, the above equation is simplified to:

$$T(R) = \left\{\frac{3GM_{BH}\dot{m}}{8\pi R^3\sigma}\right\}^{1/4} \tag{1.3}$$

[1] $\sigma = 5.67\times10^5$ erg cm^2 s^1 K^4

which shows that the disk temperature increases closer to the black hole, having the radial dependence of T$\propto$ R$^{3/4}$. This is an important prediction which can be tested by observations. Expressing the various parameters in terms of typical AGN values, the equation above can be further reduced to:

$$T(R) \simeq 2.8 \times 10^5 \left(\frac{\dot{m}}{\dot{m_{Edd}}}\right)^{1/4} \left(\frac{M_{BH}}{10^8 M_\odot}\right)^{-1/4} \left(\frac{R}{6R_g}\right)^{-3/4} [K] \tag{1.4}$$

Thus, for a a given accretion rate, the disk temperature is larger for less massive black holes, while for a given black hole mass, the disk temperature increases with the accretion rate. For typical values of the accretion rate and the black hole mass, the disk temperature reaches values of the order of 10^5 K. Such large temperatures can explain the BBB in the optical spectra of AGN.

Finally, we will see the predicted spectrum of the accretion disk emission. Following the assumptions made above, one may conceptualise the disk radiation as the sum of black body emissions, each originating from a disk annulus with radius R and width ΔR. Subsequently, the total disk emission is given by:

$$F_\nu \propto \int_{R_{out}}^{R_{ISCO}} B_\nu(T(R)) 2\pi R dR \tag{1.5}$$

where B$_\nu$ is the Planck function describing the black body emission and T(R) is the temperature at each radius as given by equation 1.2. For frequencies h$\nu \gg kT_{max}$, where k is the Boltzmann constant, h denotes the Planck constant, and T$_{max}$ is the maximum temperature of the disk, the disk emission follows a Wien-like exponential drop, which corresponds to the high-energy spectral emission of the hottest annuli. h$\nu \ll kT_{out}$, where T$_{out}$ is the temperature at the outer disk, the disk emission follows the Rayleigh-Jeans tail of the coolest annuli. Finally, in the intermediate range k T$_{out}$ $\gg$h$\nu \gg kT_{max}$ one, starting from equation 1.5, may show that the disk emission follows a power-law distribution of F$\propto \nu^{1/3}$.

A typical disk spectrum is shown in Fig. 1.2. The spectrum increases with energy, exhibiting a hump feature in the ultraviolet before dropping exponentially. The accretion disk emission has been found to reproduce well the observed spectrum of high luminosity AGN as quasars (Malkan & Sargent, 1982).

To sum up, the black hole/accretion disk assumption has been quite successfully in explaining several observational characteristics of AGN, among which the emission of large luminosities from a small region and the BBB.

Also, The optical/UV emission of obscured AGN, is affected by contamination

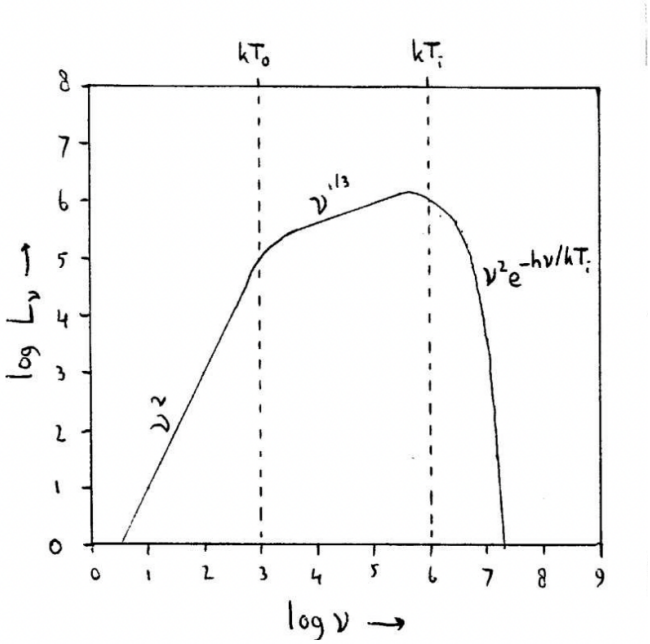

Figure 1.2: The spectrum of an accretion disk that emits locally a black body. The units along both axes are arbitrary. T_0 represents T_{out} and T_i is T_{max}. Taken from: https://personal.sron.nl/

from the host galaxy and intrinsic reddening caused by dust. In the most obscured galaxies the main component of the optical continuum is the starlight from the host galaxy, although a featureless emission is also found to contribute significantly to the spectrum. In addition, the optical spectrum shows strong broad permitted emission lines in some types of AGN as well as narrow forbidden and permitted emission lines superposed on the continuum.

1.2.4 X-rays and γ-ray observations

Active galactic nuclei are generous emitters of X-rays and up to γ-rays, with some of them being luminous X-ray Sources (Elvis et al., 1978). The X-ray emission come from the central engine: the inner region of the accretion disk or from the corona (see section 1.6, for more details). On the other hand, γ-rays are linked to the presence of relativistic jets, they are thought to be produced by inverse Compton effect on synchrotron photons within the jet (Zhang & Cheng, 1997). Both X-ray and γ-ray emission can be modelled with a power-law ($F_\nu \propto \nu^{-\alpha}$, where α is the energy index), being described with an spectral index (Γ, where $\Gamma=\alpha+1$).

1.2.5 Indicators of bolometric luminosity

The luminosity over the full electromagnetic spectrum by the AGN is defined as the bolometric luminosity L_{Bol}. The characterization of L_{Bol} is a challenging task for several reasons. For example, we need to take into account the contamination from the host galaxy to the nuclear emission. The main limitation is that much of the rest-frame UV SED is hidden, either due to galactic absorption in low redshift objects, or intergalactic absorption in high redshift objects, then, this is a source of uncertainty and specially relevant for low luminosity AGN (LLAGN). Additionally, due to the nature of the multi-wavelength feature of the AGN emission, observations from a variety of telescopes are necessary in order to build up complete and detailed SED.

Unless a wealth of multi-photometric data are available, it is necessary to use the so-called bolometric correction to derive the AGN bolometric luminosity. This parameter is defined as the ratio between the bolometric luminosity and the luminosity in a given spectral band, b, i.e. $K_b = L_{Bol}/L_b$. One of the first attempts to derive the bolometric correction was carried out by Elvis et al. (1994), who estimated the bolometric correction in different bands using a mean energy distribution from a sample of 47 AGN. Later, Shankar et al. (2004) gave a preliminary estimate of the hard X-ray bolometric correction, while Marconi et al. (2004) derived an estimate of the bolometric corrections in the optical B, soft and hard X-ray and IR bands, similarly to Hopkins et al. (2007). However Vasudevan & Fabian (2007) studied a sample of 54 X-ray bright ($L_X > 10^{43}$ erg s^{-1}) AGN, pointing out that particular classes of sources (as radio-loud or X-ray weak sources) might have different bolometric correction relations than the rest of the AGN population. Lusso et al. (2012) analyzed a sample of about 900 X-ray selected AGN deriving the bolometric corrections in the same bands as Marconi et al. (2004), separately for type 1 and type 2 sources, and valid for approximately three orders of magnitude in luminosity. Netzer (2019) provided simple power-law approximations of the bolometric corrections in the optical and hard X-ray bands, obtained by combining theoretical calculations of optically thick, geometrically thin accretion disks, and observational X-ray properties of AGN. Very recently, Duras et al. (2020) analysed a sample of $\sim$1000 type 1 and type 2 AGN, obtaining two bolometric corrections in agreement in the overlapping luminosity range. They found a $K_{2-10} = L_{Bol}/L_{2-10}$ constant at $\log(L_{Bol}/L_\odot) <$11, while it increases up to about one order of magnitude at $\log(L_{Bol}/L_\odot) \sim$14.5.

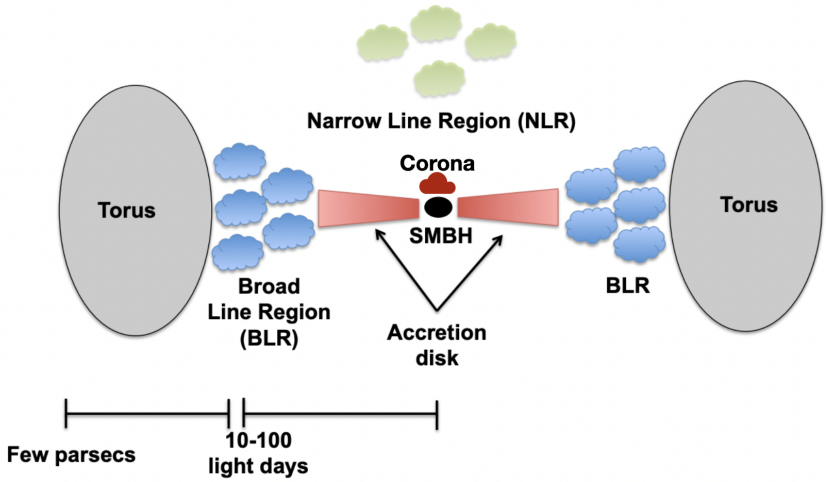

Figure 1.3: Typical structure (not on scale) of an AGN. Adapted from: https://www.isdc.unige.ch

1.3 Anatomy of an AGN

In the following we specify the main components of AGN, from the smallest scales outward and illustrated in Fig. 1.3:

The Supermassive Black Hole:

It is now widely accepted that most massive galaxies contain a SMBH at their center and this is the source of gravity powering the nuclear activity. From the short time scales variations observed in AGN it is possible to obtain an upper limit on the size of the central source, which together with mass estimates point towards very high densities, in a relatively tiny place. In fact, some AGN are near and massive enough which make possible to measure the angular size. For instance, the Event Horizon Telescope used interferometry at sub-mm wavelengths to image the black hole shadow in M87 (Goddi et al., 2019) and, recently Sgr A* (Event Horizon Telescope Collaboration et al., 2022).

The estimation of the black hole mass is a very complex process as the SMBH is invisible. In the following we summarize some approaches used to estimate this parameter:

1. Reverberation mapping: it is based on the time delay (or lag) between flux variations in the ionizing continuum of the AGN and flux variations from the surrounding region being irradiated (the broad line region - BLR) (Blandford & Mc-

Kee, 1982; Kaspi et al., 2000; Peterson & Horne, 2004). Changes in the radiative flux lead to changes in the reprocessed emission, so the light curves of the two regions should be strongly correlated. However, since the light from the reprocessed emission has to travel an additional distance to get to us, the variations in the reprocessed emission will arrive later than the variations in the ionizing flux. The supermassive black hole mass, M_{SMBH}, can be estimated using the following equation:

$$M_{\rm SMBH} = \frac{R_{\rm BLR} v^2}{G} \propto \frac{c\tau v^2}{G}$$

Where $R_{\rm BLR}$ is the distance from the central source to the BLR, c the speed of light, v the cloud velocity and G is the gravitational constant.

2. The BLR size-luminosity relationship: measure the BLR size with the reverberation mapping technique requires long-term monitoring of the continuum and emission line fluxes, then it was proposed by Kaspi et al. (2000) using observational data from 34 nearby AGN, an empirical relation between the BLR size ($R_{\rm BLR}$) and the optical continuum luminosity at 5100 $\mathring{A}$ ($L_{5100\mathring{A}}$). This relation has often been used to estimate the BLR size and then M_{SMBH}. The connection between the black hole mass and $L_{5100\mathring{A}}$ is given by:

$$M_{\rm SMBH} = 4.817 \times \left(\frac{\lambda L_{5100\mathring{A}}}{10^{44} [erg s^{-1}]} \right)^{0.7} FWHM(H_\beta)^2$$

where FWHM refers to the full width at half maximum of the broad component in the Hβ emission line. Due to observational limitations, this relation can only be used for objects at low redshift. At high redshift, the line is present in the near-infrared band, so other emission lines such as MgII and CIV are used (see, e.g., Netzer et al. 2007 for more details).

3. The M_{SMBH}-σ relation: M_{SMBH}, has been found to correlate with several global properties of their host galaxies (see, e.g., Kormendy & Ho 2013; Ferrarese & Ford 2005; Shankar 2009; for reviews), including bulge mass and stellar velocity dispersion, suggesting a link between galaxy growth and the SMBH. All studies point to a connection between these quantities as $M_{SMBH} \propto \sigma^4$.

Corona

It is widely accepted that the primary X-ray emission from the AGN arises from optical/UV photon inverse Compton scattered by a corona of hot and relativistic electrons situated above the SMBH. This Comptonized emission has the shape of a power-law, of the form:

$$N_{ph}[photonss^1] = AE^{\Gamma}$$

where N_{ph} is the number of photons emitted per unit time and energy, with a photon index of typically Γ $\sim$1.8 - 2 (Nandra et al., 1997). A is a constant and E represents the energy. The power-law continuum shows in most cases a high energy roll-over located at a few hundred keV and is mainly related to the temperature of the electron plasma in the corona (Liu et al., 2003).

There are several possible scenarios to describe the nature and morphology of the corona (see Figure 1.4). One possible scenario is the lamp-post model, in which the corona is a point-like source above the SMBH and along its spin axis (see Niedźwiecki et al. 2016 and references therein). This configuration could arise at the base of a jet, for example (Vincent et al., 2016). If the corona is formed instead in the atmosphere of the accretion disk, we would observe a sandwich corona configuration. Another possibility is a spherical or toroidal corona, which could be formed by the accretion flow from the disk to the black hole (Bambi et al., 2017).

The Accretion Disk:

The most accepted theory is that accretion onto the SMBH is the mechanism responsible of the high energy in AGN (Rees, 1984), where in an optically thick and geometrically thin rotating disk formed from in-falling material and looses its angular momentum through friction within the disk. It radiates thermally (with the innermost regions being hottest) and is the primary source of electromagnetic radiation due to accretion.

The accretion is limited by the radiation pressure. At high accretion rates the luminosity increases and so does the outward force exerted by the radiation (F_{rad}). On a free electron this force is:

$$F_{rad} = \frac{L\sigma_T}{4\pi r^2 c}$$

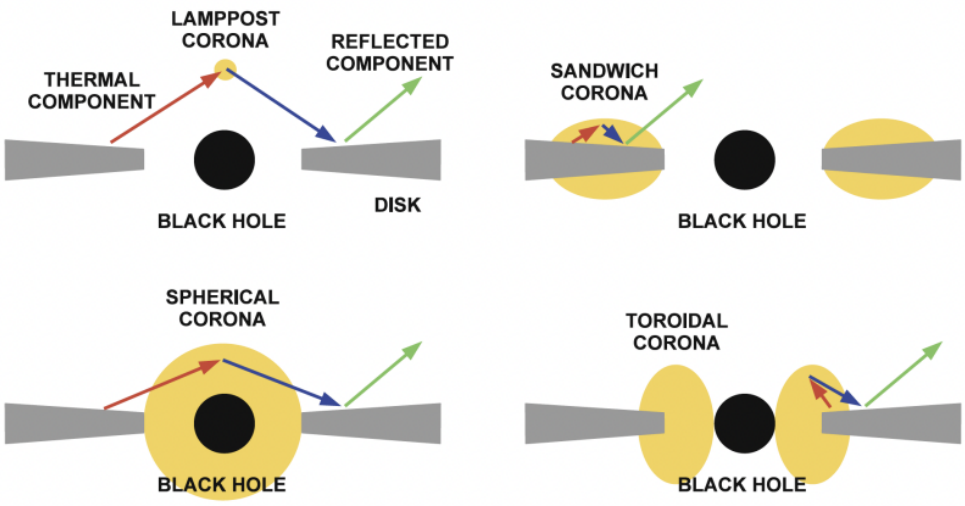

Figure 1.4: Examples of possible corona geometries: lamp post geometry (top left), sandwich (top right), toroidal (bottom left) and spherical (bottom right) (Bambi et al., 2021).

where L is the luminosity, r is the radii, c is the speed of light and $\sigma_T = 6.65 \times 10^{25}$ cm^2 is the Thomson cross-section. The radiation pressure balances the gravitational force ($F_G = G\,M\,m_p/r^2$, where m_p is the mass of the proton) at the so called Eddington luminosity. For a fully ionized medium in a spherically symmetric geometry such a luminosity is

$$L_{edd} = \frac{4\pi M m_p c}{\sigma_T} \simeq 1.5 \times 10^{38} (M/M_\odot)[erg \quad s^{-1}]$$

The Eddington luminosity can be written, in terms of accretion rate as $L_{Edd} = \eta \dot{M}_{Edd} c^2$. Thus, the accretion rate of a disk radiating at the Eddington luminosity is

$$\dot{M}_{Edd} = \frac{L_{edd}}{\eta c^2} = \frac{4\pi M m_p}{\eta c \sigma_T} \approx 1.5 \times 10^{38} (M/M_\odot)[M_\odot \quad yr^{-1}]$$

The ratio between the bolometric luminosity of an object, L_{Bol}, and its Eddington limit is called the Eddington ratio:

$$\lambda_{Edd} = \frac{L_{Bol}}{L_{Edd}}$$

Objects with $\lambda_{Edd} < 1$ are accreting in the sub-Eddington regime, while those with $\lambda_{Edd} > 1$ in the super-Eddington one. Although this derivation of the Eddington luminosity is limited by the spherical symmetry approximation, which clearly does not

represent the physical situation of an accreting disk, it still provides an useful approximation of the limit of the luminosity for an accreting system.

According with the formula given by Eracleous et al. (2010):

$$\lambda_{Edd} = \frac{L_{Bol}}{L_{Edd}} = 7.7 \times 10^{-7} \left(\frac{L_{Bol}[ergs^{-1}]/10^{40}}{M_{BH}[M_{\odot}]/10^{8}} \right)$$

In the following, we describe different kinds of energy emission from the different accretion disks, which are classified according to their shape into thin, slim, and thick disks:

1. Shakura-Sunyaev accretion disks: Matter falling onto a compact object from infinity acquires kinetic energy as its gravitational potential energy decreases. In order to conserve the angular momentum the matter cannot fall directly into the compact object, but it is commonly believed to form an accretion disk. The simplest case of accretion disks are the disk described by Shakura & Sunyaev (1973). In this picture, the matter is supposed to form a geometrically thin and optically thick disk, and follows Keplerian orbits at any radius ($v \sim (M_{SMBH}/R)^{1/2}$). The fundamental parameters governing their properties are λ_{Edd}, M_{SMBH}, and the spin, determine the geometry of the disk, the gas temperature, the overall luminosity and the spectrum (Netzer, 2013). This kind of disks are considered cooling dominated flows, where the cooling is very efficient because there is a balance between losing angular momentum and increasing kinetic energy due to local viscosity. The most accepted theory is that it may be emitting mostly UV because their temperatures are around 10^5 K for $M_{SMBH} = 10^8 M_{\odot}$, where $M_{\odot}$ is the solar mass .

2. Inefficient accretion flows: Advection-dominated accretion flows (ADAFs; for reviews see Narayan et al. (1994); Yuan et al. (2007)) are very hot, geometrically thick, optically thin flows which are typically at low radiative efficiencies ($L \ll 0.1\dot{M}c^2$) and occur at low accretion rates ($\dot{M} \leq 0.01\dot{M}_{Edd}$). The optically thick advection-dominated accretion flow (or optically thick ADAF, also called, Radiatively Invefficient accretion flow, RIAF) solution was found for objects accreting at super-Eddington accretion rates (Abramowicz et al., 1988). In this scenario, the large optical depth of the inflowing gas traps most of the radiation, advecting it into the central SMBH.

   In many LLAGN, another component in the accretion flow besides the ADAF is required in order to account for a number of observations, including a promi-

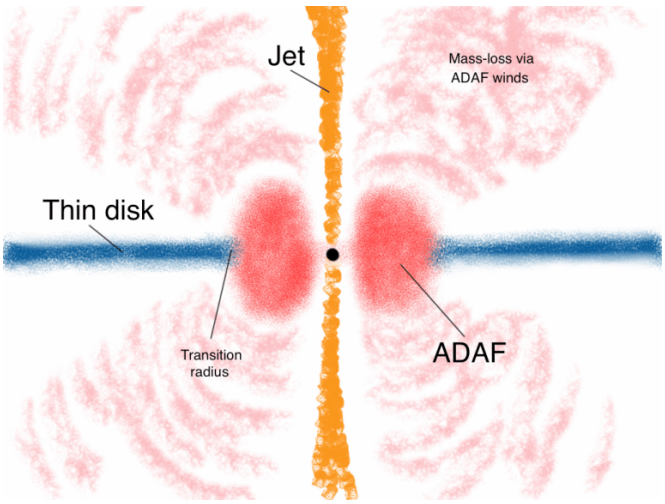

Figure 1.5: Cartoon illustrating the model for the central engines of LLAGNs. It consists of three components: an inner ADAF, an outer truncated thin disk and a relativistic jet. Taken from: Nemmen et al. (2013)

nence in the mid or near-IR and steep fall-off of the spectrum in the optical/UV region – a "red bump" (Nemmen et al., 2006; Ho, 2008a) – as well as the presence of double peaked Balmer emission lines (e.g., Storchi-Bergmann et al. 2003; Eracleous et al. 2009): the emission from a thin accretion disk whose inner radius is truncated at the outer radius of the ADAF (two-temperature ADAF). In this scenario, the accreting gas has a very low density, and is unable to cool efficiently within an accretion time. The viscous energy is therefore stored in the gas as thermal energy instead of being radiated, and is advected into the central object, then, the gas is optically thin, and has a two-temperature configuration. The accretion flow may begin as a standard thin disk but somehow at a certain transition radius it gradually switches from a cold to a hot ADAF mode. The details on how this transition might happen are still not well understood (Manmoto et al., 2000; Yuan & Zdziarski, 2004; Narayan & McClintock, 2008), but it seems to be analogous to the transition between the different spectral states in black hole binary systems (Done et al., 2007).

The Broad Line Region:

Broad emission lines are one of the dominant characteristics of AGN spectra. These lines are assumed to be Doppler-broadened, and are thought to be produced in a region close to the black hole, normally referred as BLR. The bulk motions in the BLR are

regulated by gravity (due to the black hole) and radiation pressure (from the accretion disk), although the influence of outflows should probably also be taken into account. The widths of AGN broad lines span over two orders of magnitude and range from a minimum of FWHM $\sim$ 500 km s^{-1} to FWHM $\sim 10^4$ km s^{-1}. The strongest lines observed in the typical spectrum of an AGN are the hydrogen Balmer-series lines (Hα, Hβ and Hγ), the hydrogen Lyα, and lines from abundant ions (Mg II, C III, and C IV).

The line emission from the BLR arises in photoionised gas, illuminated by the far/extreme UV and X-ray continuum radiation, originating in and above the accretion disk (e.g. Davidson & Netzer (1979)). However, the nature and structure of the BLR is still not fully understood. There is some suggestion that the BLR is related to the accretion disk. Theoretical models based on accretion disk outflow scenarios suggest that the broad line emission originates in a wind emerging from the accretion disk (e.g. Murray et al. 1995; Proga et al. 2000; Kollatschny 2003; Elvis 2017), or that the accretion disk, BLR and obscuring medium (also known as the equatorial, dusty torus) are individual parts of a dynamical structure that changes as a function of AGN luminosity (Elitzur & Shlosman, 2006). Other theoretical models propose that the BLR is part of a large continuous obscuring structure with the broad emission lines originating from within the dust sublimation radius (Netzer & Laor, 1993).

Narrow Line Region:

The narrow-line region (NLR) is the most extensive component of AGN, and the only one which can be resolved by optical observations. Unlike the BLR, in the NLR the electron density is low enough that many forbidden transitions are not collisionally suppressed. Also, this region consists on gas and dust with smaller column densities than the BLR ($\sim 10^{20-21}$ cm^{-2}) and low densities ($\sim 10^4$ cm^{-3}) located at about 100-1000 pc from the nucleus. Typical velocities of the clouds are about 500 km s^{-1}. Due to the low densities, the observed spectrum of the NLR includes intense forbidden lines (Netzer, 2013).

The NLR is normally found to be axisymmetric rather than spherically symmetric. One of the most interesting features of AGN are the "ionization cones" (e.g., Pogge 1988) which are clearly detected in maps of high-excitation lines as [O III]λ5007 $\AA$ These cones have a [OIII]λ5007/Hα flux ratio higher than one, which is characteristic of low-density gas ionized by the AGN continuum. Outside the cone the ratio is instead lower than unity,implying that the gas is mostly ionized by starlight.

Relativistic jets:

After the first observations of radio lobes in galaxies in the early 50's (Jennison & Das Gupta, 1953), it was thought that these structures were ejected and completely detached from the host galaxy. It was not until the late 1960's that it was realized (Rees & Sciama, 1966) that they could actually be powered through jets emitted from the center of galaxies. In the last few decades, in particular thanks to the development of radio interferometry techniques, it has been possible to detect jets in many sources and to resolve even their inner parts (e.g., Chang et al. (2010)). This is a high-velocity stream of particles launched in opposite directions perpendicularly to the accretion disk and radiating non-thermally via synchrotron and inverse-Compton processes. In about 10% of AGN, the relativistic jet is so strong and so well collimated that it propagates out to distances of $\sim$100 kpc.

Jets are now known to extend on scales from parsec to Mpc, are highly collimated and can have continuous appearance or can present knots. The production, acceleration and collimation of jets is still poorly understood. Some of the most popular models are based on magnetohydrodynamics, and involve the presence of strong electromagnetic fields that convert the rotational kinetic energy of a rotating black hole into an outflow through coupling with differential rotation.

The torus:

The dusty molecular torus surrounding the central engine of AGN is expected to consist of molecular gas as well as of warm and hot (T$\sim$ 100-1500 K) dust. The simplest torus is made of a smooth matter distribution. More elaborated structures, made of clumps and inter-clump material, are preferred by observations. The gas at the inner radius of the torus is ionized by the central source. Deeper in, the torus contains dusty molecular gas. Its inner radius is set by the dust sublimation temperature (see e.g. Netzer & Laor 1993; Netzer 2015), and its geometry is subject to extensive research. The torus has been proposed to be clumpy (Nenkova et al., 2008; Hönig & Kishimoto, 2010; Marinucci et al., 2016). The origin of the torus could, for example, involve matter coming off the relatively cold, outer regions, of the accretion disk. That matter could form a clumped wind structure about the disk perimeter. Alternatively, the matter could accrete from ambient matter from within the host galaxy. Also, scenarios involving outflowing clouds from the disk embedded in a hydromagnetically driven disk wind have been proposed.

1.4 AGN classification

The complex structure of AGN is reflected in their spectra/images, with many different emission/absorption processes acting at the same time. In addition, according to the properties of their optical spectra, AGN are classified into Seyfert galaxies, quasars, blazars, Low-ionization nuclear emission-line region (LINER) and radiogalaxies. Here we report a simple taxonomy of the main types of AGN:

1.4.1 Seyfert

Originally classified by Carl Seyfert (Seyfert, 1943). They are the most common AGN in the local universe, and they have high central surface brightness, although the host galaxy is still clearly detectable; they tend to be spirals, with massive galactic bulges and the presence of an interstellar medium. Since their original discovery, the classification has evolved such that they show in their optical spectra high-ionisation emission lines. Seyfert galaxies are, divided into two groups: Seyfert 1 and Seyfert 2 (Sy1 and Sy2, respectively), as was first realized by Khachikian & Weedman (1974). The spectral differences between Seyfert 1 and Seyfert 2 can be seen in Fig. 1.6. Many Seyfert galaxies exhibit permitted line profiles with both very broad and relatively narrow components (Osterbrock & Koski, 1976; Osterbrock, 1981). These objects have been classified as type 1.2, 1.5, 1.8 or 1.9 Seyfert galaxies, depending on the relative contributions of the two components to the total permitted line profiles.

- Type 1 Seyfert galaxies: are those with highly ionized, broad permitted lines, together with narrow forbidden lines. The narrow lines come from the NLR (see Section 1.3 for more details), and have a full width at half maximum (FWHM) of a few hundred km s^{-1}. On the other hand, the broad lines have widths Doppler-broadened up to 10^4 km s^{-1} and are related with the BLR. There are certain objects, known as Narrow-Line Seyfert 1 galaxies (NLS1), which do show the broad lines (Type-2 galaxies; see below), but they are narrower than in the typical broad-line Seyfert 1. NLS1 are thought to have high accretion rates and, very probably, small black hole masses; see, e.g., Bian & Zhao (2003).

- Type 2 Seyfert galaxies: show only the narrow lines. They have an [OIII]λ5007 $\AA$ to Hβ ratio < 3 (Shuder & Osterbrock, 1981); Seyfert 2 also tend to show weaker [Fe II] (or higher ionisation iron) emission lines than their Seyfert 1 counterparts.

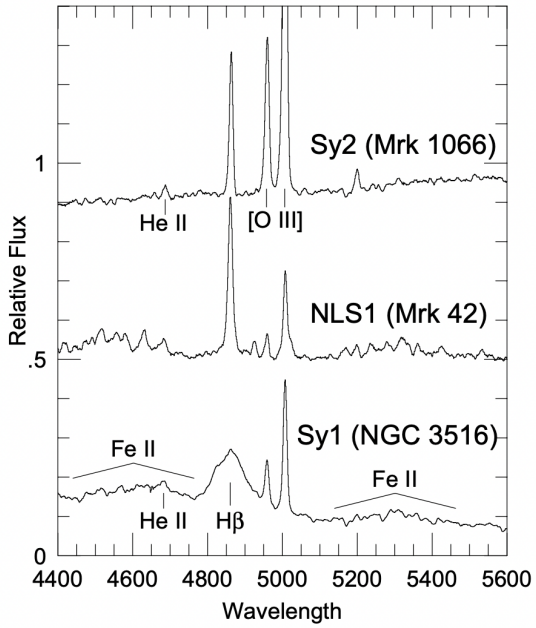

Figure 1.6: Typical optical spectra (in the region of Hβ) of Sy2 Mrk 1066 (above), NLS1 Mrk 42 (center) and Sy1 NGC 3516 (below) (adapted from Pogge et al. 2000).

1.4.2 Quasars

Or QSOs Schmidt (1963) are the most luminous of the AGN family with a bolometric luminosity $L_{bol} \sim 10^{44}$-10^{47} erg s^{-1}. Their spectra are similar to those of Seyferts. However they are usually found at higher redshift ($z > 0.1$) and the host galaxy is hardly, if not at all, resolved.

1.4.3 Radio galaxies

Radio galaxies are moderate or bright AGN and their peculiarity is their powerful emission in the radio-mm band. The radio lobes in these galaxies are powered by a jet of particles and emit non-thermal, synchrotron radiation (e.g., Blandford & Rees 1974). They can be classified as Broad Line radio Galaxies (BLRGs) or Narrow Line radio Galaxies (NLRGs) depending on the presence of broad or narrow emission lines in their optical-UV spectra.

1.4.4 Blazars

A blazar is an active galactic nucleus (AGN) with a relativistic jet (a jet composed of ionized matter traveling at nearly the speed of light) directed very nearly towards an observer and emitting Doppler-boosted radiation via synchrotron emission. The blazar class includes BL Lac objects (Schmidt, 1963) and Optically Violent Variable (OVV) quasars. They are characterized by a non-thermal, highly variable, beamed continuum emission. BL Lac objects are characterized by a strong continuum and absent both emission and absorption lines. These are radio-loud objects, with strong, mostly non-thermal, highly polarized radiation, varying rapidly with large amplitudes. OVVs are similar to BL Lac objects, with the difference that their spectra are showing strong broad emission lines (Antonucci, 2012).

Radio quasars are divided, according to the value of their radio spectral index, in flat-spectrum radio quasars (FSRQ) and steep-spectrum radio quasars (SSRQ). This classification reflects the different extension of the radio emitting region in the two classes: a flat spectrum indicates a self-absorbed synchrotron emission from a compact region, whereas a steeper spectrum reflects the dominance of the emission from the radio lobes over the nuclear emission.

1.4.5 LINER

Low Ionisation Nuclear Emission-Line Region galaxies are the least luminous of the classifications. They were first identified by Heckman (1980) and are, in fact, very common. LINERS show only weak nuclear activity and its optical emission is largely dominated by the host galaxy. The emission line spectra indicate the existence of a non-stellar continuum (Netzer, 1990). The observational difference, in the optical region, between LINERS and Seyfert 2-type galaxies lies in the relative strength of certain emission lines, where high ionization lines ([O II]$\lambda\lambda$ 3727, 3729) are stronger than low-ionisation emission lines ([O III]λ5007 line, O Iλ 6300/[O III]λ5007$<$0.33 and [N II]λ 6584/Hα $>$ 0.6).

AGN can be distinguished from normal non-active galaxies in different ways. One of the most commonly used diagnostics are the so called BPT diagrams (Baldwin et al., 1981), that show the ratios of several lines (e.g., [O III]/Hβ vs [NII]/Hα, [OIII]/Hβ vs [S II]/Hα, and [OIII]/Hβ vs [O I]/Hα). Comparing these ratios to theoretical values, one can easily spot the objects that cannot be photo-ionized by pure stellar emission,

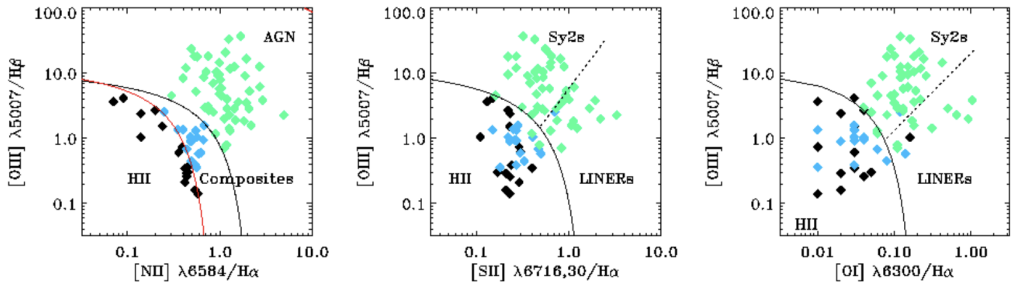

Figure 1.7: BPT diagram for a large number of IR-selected objects. taken from (Brightman & Nandra, 2011b). HII galaxies are in black, Seyfert 2 in blue, and LINER green.

but need other mechanisms, such as AGN or shocks, as can be seen in Fig. 1.7.

1.5 Unified model

Not all the features described in Sect. 1.3 are observed in all AGN. Besides all the observational diversity, it is now largely accepted that all the radio-quiet AGN classes share the same intrinsic structure and the different observed characteristics are due to the different inclination relative to the obscuring torus. One of the most important observational evidence of this obscuring structure was in 1985, when Antonucci & Miller 1985 observed the Seyfert 2 galaxy NGC 1068 in polarized light. The scattered light in the nuclear region revealed broad lines, like those seen ubiquitously in Seyfert 1 galaxies. This suggests that Type 1 and Type 2 Seyfert galaxies are intrinsically the same. In Seyfert 1 galaxies, the observer can look at both the BLR and the NLR at the same time, whereas Seyfert 2 are observed edge on, so that the BLR is obscured and one can see only the NLR. This led to the idea which is known as AGN unification model (UM, see Antonucci (1993); Urry & Padovani (1995); Bianchi et al. (2012) for a review).

According to this model, and as can be seen in Figure 1.8, the inner part of the AGN, up to the BLR, is supposed to be enshrouded in a torus-like structure, composed of dust and gas, that opaque to most of the electromagnetic radiation. Therefore, an observer looking at AGN edge-on (i. e. on the torus plane) can not see the innermost region of the AGN, because the view is obstructed by the intercepting material. In this case, only the narrow emission lines are directly visible. vice-versa, an observer looking face-on (i.e. along the axis) has a direct view of the BLR, the NLR and the accretion disk emission. The UM explains the major differences between type-1 and

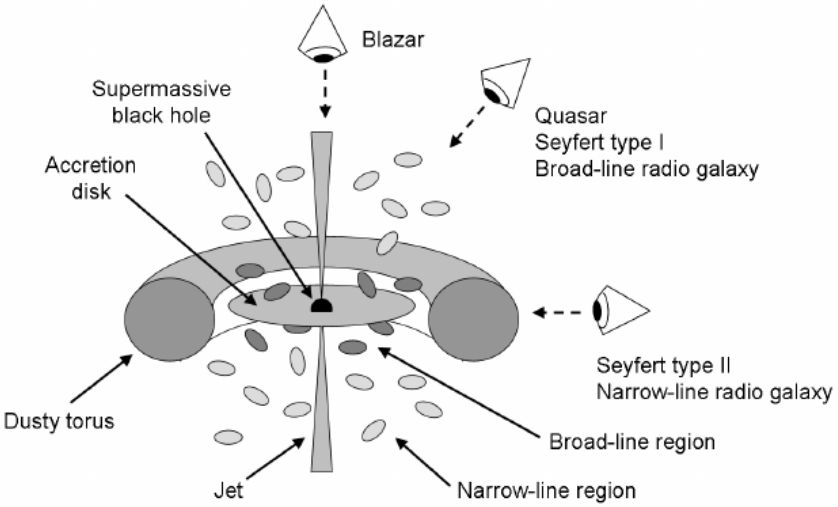

Figure 1.8: The geometry of the AGN assumed in unified models where the classification of the central light source mainly depends on the viewing angle. The approximate viewing angles of certain types of AGN have been indicated, although many subgroups have been omitted. The individual components of the central engine are not plotted to scale. Taken from: Zackrisson (2005)

type-2 AGN with a surprisingly small number of assumptions.

Observational evidence supporting the UM came from spectropolarimetric data, where objects classified as Seyfert 2s showed broad polarized Balmer lines, indicating a hidden BLR (Miller & Goodrich, 1990; Tran, 2003). Evidence at other wavelengths are also in agreement with the UM. At X-rays, in general, Seyfert 1s have column densities $N_H < 10^{22} cm^{-2}$ (i.e., unobscured view of the SMBH), while it is higher in type 2s (i.e., obscured view of the SMBH) (e.g., Risaliti et al. 2002; Guainazzi et al. 2005a; Koss et al. 2017, indicating that the column density is related with the obscuring material along our line of sight.

1.5.1 limitations

Although the UM allow us to explain much of the complex AGN phenomenology, an increasing set of observations appear to be in conflict with some of the key predictions of the UM (Bianchi et al., 2012), e.g. that each Seyfert 2 has an obscured Seyfert 1 nucleus (a hidden broad-line region).

Furthermore, some sub-classes of objects were not taken into account in this simple

version of the UM and in fact are not well accommodated under this scheme, such as NLSy1s or LINERs. For this reason, and based on recent observations of large AGN samples that provide detailed information, several efforts have been made to modify the UM. The modifications in which the scientific community are involved right now mainly concern the nature of the torus, the dependence on the luminosity, and black hole and galaxy evolution (Netzer, 2015).

In the case of LLAGN as LINERs, it has been suggested that the torus and even the BLR may disappear at low luminosities (Elitzur & Shlosman, 2006; Elitzur & Ho, 2009; González-Martín, 2018). Elitzur & Shlosman (2006) proposed that at low luminosities (i.e. $L_{Bol} < 10^{42}$ erg s^{-1}) the obscuring torus might disappear, with the assumption that the obscuring clouds in the torus are created in a disk-wind outflow rather than being due to accretion of material from the galaxy. Recently, there are many works pointing out to a relation between the luminosity (or the accretion rate) and the torus. For example, in González-Martín et al. (2017) used *Spitzer* data and reported a lower contribution from the torus in the low luminosity regime, in agreement with the disappearance or a lower covering factor of the torus. On the other hand, Ricci et al. (2017b) using *Swift*/BAT observations found a relation between the fraction of obscured sources and the accretion rate. They found that AGN with $\lambda_{Edd} \sim$ 0.02-0.05 exhibit a decline of the Compton-thin circumnuclear material (dropping from covering factor of 80% to 30%), because AGN at these accretion rates is expected that the central engine expel their circumnuclear material through radiation pressure. On the other hand, sources at $\lambda_{Edd} \leq 10^{-4}$ show a decrease of covering factor, with only $\sim$40% of the sources being obscured by Compton-thin material. It has been proposed that in sources at low accretion rates only a limited amount of obscuring material is puffed up, leading to a smaller covering factor. Later, Esparza-Arredondo et al. (2021), combining *NuSTAR* and *Spitzer* observations found that the distribution of the gas and dust in AGN is complex. They find three gas-dust distribution combinations possible in their sample of AGN: clumpy-clumpy, smooth-smooth, and smooth-clumpy, where most of them are in agreement with the notion that gas could also be located in the dust-free region. Therefore, this may indicate that evolutionary processes or different properties between these types of objects (or its luminosities) should be taken into account in the new version of the UM.

1.6 The X-ray emission of AGN

X-rays are not able to penetrate the Earth's atmosphere, and it is thus necessary to fly instrumentation at high altitudes. The X-ray domain has seen an enormous evolution over recent decades, and it is currently one of the key energy ranges to study AGN.

X-ray emission has been found to be an universal characteristic of AGN (Elvis et al., 1978). Besides being one of the hallmarks of AGN, the X-ray emission also allows to probe the physical conditions very close to the central black hole and the accretion disk. The X-ray radiation has a different origin than the UV/optical one. For typical values of black hole mass and accretion rate, the inner disk reaches temperatures of the order of 10^5 K or, equivalently, kT$\sim$10 eV. Therefore, it cannot account for the observed X-ray emission. Instead, the X-rays are believed to be produced by Comptonisation of soft photons in an optically thin region of high temperature. In addition, they are relatively unaffected by obscuration and they are less contamination from non-AGN sources, allowing a census of accretion events over a wide obscuration interval.

The X-ray continuum is ubiquitous in AGN and can be explained by thermal Comptonization of the soft UV radiation (Haardt & Maraschi, 1993). This continuum is reprocessed by cold neutral circumnuclear medium (e.g. the accretion disk or the molecular torus) and gives rise to a reflection hump at around 30 keV and a broad iron, Kα line emission at around 6.4 keV (Matt et al., 1991). In addition to the main power-law, observations can show a rise of the spectrum below 1-2 keV (Arnaud et al., 1985; Bianchi et al., 2009). This feature is called soft excess and its origin is still under debate (Done et al., 2007). The main features of AGN X-ray spectra are discussed below and are shown in Figure 1.9.

The primary emission

The spectral shape of the X-ray emission from AGN is a power-law, with a photon index ranging between 1.7 and 2.2 (Nandra & Pounds, 1994a; Bianchi et al., 2009). The power-law continuum shows a high-energy cut-off, presumably due to the cut-off of the energy distribution of the electrons responsible for the X-ray emission and usually located around a few hundreds keV (see (Perola et al., 2002; Malizia et al., 2014; Marinucci et al., 2016; Fabian et al., 2015, 2017) and references therein). These features are directly related to the temperature and optical depth of the plasma of hot electrons responsible for the power-law emission.

This primary continuum in AGN is produced by a Comptonization mechanism;

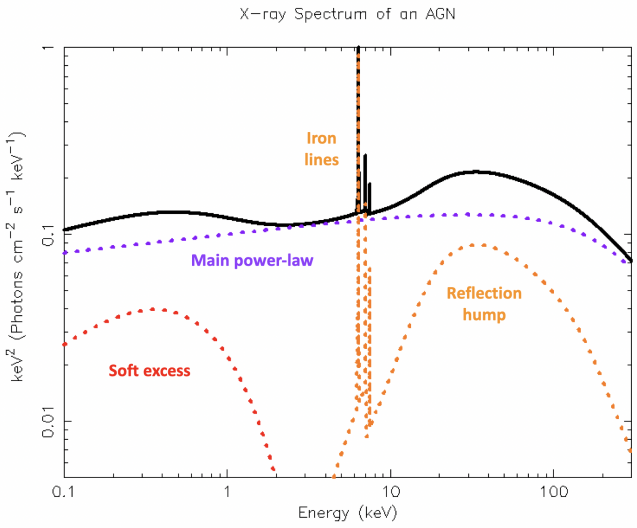

Figure 1.9: Theoretical X-ray spectrum of an AGN, including the direct emission (main power-law), reflected emission and soft excess. The power-law has a cut off at 300 keV. Taken from: https://science.clemson.edu/ctagn/project/

this process is believed to arise from the inner regions of AGN, close to the central super-massive black hole, in the corona, similarly to what is observed in the solar corona. In this region electrons inverse-Compton scatter some of the low-energy UV and optical photons from the disk to X-ray energies (Fabian et al., 1989). The analysis of the primary X-ray continuum can give information about the parameters of this plasma of electrons, like temperature and optical depth.

Reflection

The reflection component is produced by Compton scattering of the primary emission in materials surrounding the central SMBH (like the accretion disk and the torus). The main features of the reflection component are a continuum, due to electron scattering which peaks at around 30-40 keV (reflection hump) and the FeKα emission line. However, the shape of the reflection component changes depending on the ionization state of the reprocessing material. In Fig. 1.10 we show the reflected emission from an ionized and a neutral material. In the following sections, I will introduce separately the two situations.

- Neutral reflection: Reprocessed emission from neutral material is commonly observed in AGN through the iron Kα emission line and the reflection hump. However, if the reflecting material is Compton-thin, but still has a significant column

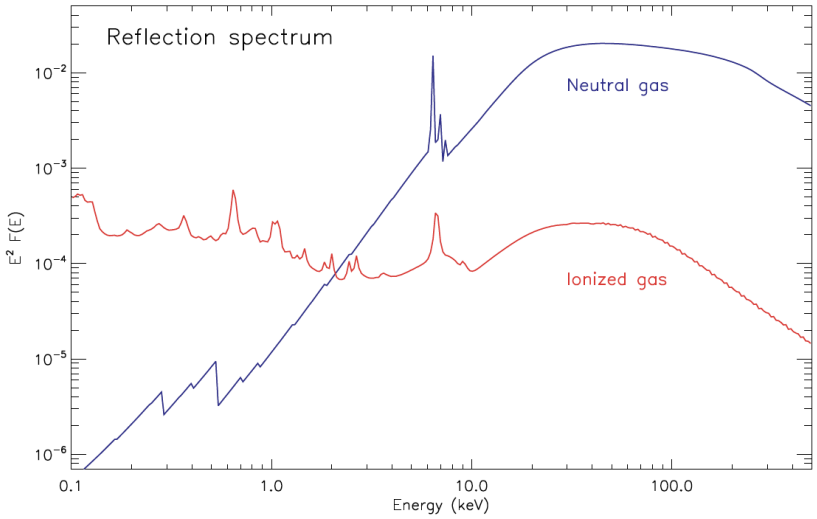

Figure 1.10: Reflection spectrum from ionized and neutral Compton thick matter. The power-law primary continuum in both cases has a photon index of $\Gamma = 1.8$, the ionization parameter is $\xi = 300$ for the ionized gas. The normalization used are arbitrary. Taken from: (Ricci, 2011)

density ($N_H \sim 10^{23}$ cm^2), no Compton hump is produced, and one would observe only the iron Kα line (Matt et al., 2003).

The spectrum of the reflection component is determined by the competition between photoelectric absorption and Compton scattering. For neutral matter, photoelectric absorption dominates below 10 keV, while Compton scattering has a stronger influence above this energy.

- Ionized reflection: If the material responsible for the reprocessed emission is ionized, photoelectric absorption has a lower influence on the re-emitted photons, and the albedo below 10 keV increases. The first calculations of the influence of the ionization state of the reflection component were done by Ross & Fabian (1993). Further works on this subject were done by Zycki & Czerny (1994); Ross et al. (1999) or (Ballantyne et al., 2001).

  The ionization parameter ξ is often used to describe the degree to which gas (assumed to have constant density) is ionized. This parameter is defined as

$$\xi = \frac{4\pi F_x}{n_{\rm H}}$$

where F_x is the illuminating X-ray flux, normally taken in the 0.01 - 100 keV energy band, and $n_{\rm H}$ is the hydrogen number density of the reflecting material. When the

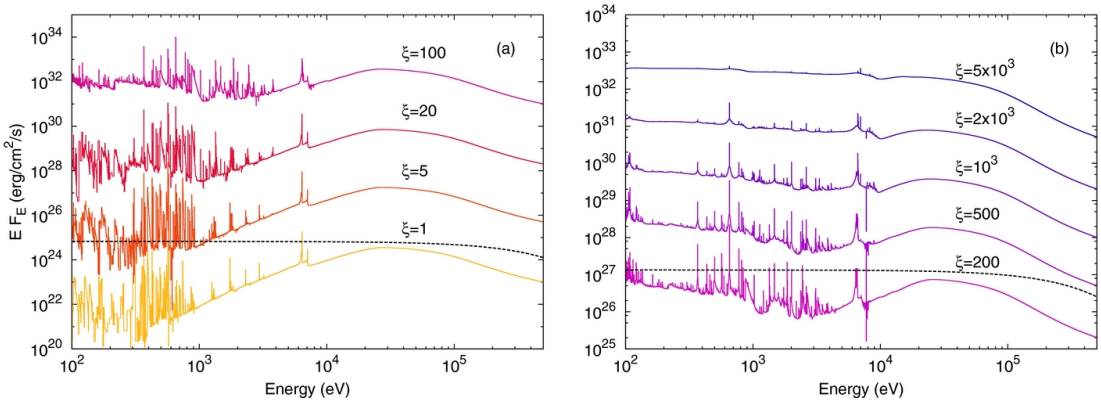

Figure 1.11: Reflection model assuming a disk-like ionized reflector. In panel (a), solid lines show the models for ξ = 1, 5, 20, and 100, multiplied by factors of 1, 10^2, 10^4, and 10^6, respectively, to improve clarity. The dashed line represents the incident power law for the model with ξ = 1. In panel (b), solid lines are the reflected spectra for ξ = 200, 500, 1000, 2000, and 5000, multiplied by factors of 1, 10, 10^2, 10^3, and 10^4, respectively. The dashed line is the incident power-law for the ξ = 200 case. In all cases, Γ = 2 and AFe = 1. Taken from: García et al. (2013)

value of ξ increases, due to either an increase of the flux F_x or a decrease of the density $n_{\rm H}$, the gas becomes more ionized. As can be seen in Fig. 1.11, the value of ξ greatly affects the shape of the spectrum of the reprocessed emission. In the following I will report some of the processes that concur for different values of ξ to modify the emitted spectrum.

- ξ <100 erg cm s^{-1}: For low values of the ionization parameter the gas is very weakly ionized, and most of the X-ray emission is absorbed below ∼10 keV. Although quantitatively the spectrum is similar to that obtained for a neutral slab, below 1 keV one can see recombination lines from ionized oxygen and carbon, where the strongest spectral feature is the FeKα line at 6.4 keV.

- 100< ξ <700 erg cm s^{-1}: As the gas starts to become more ionized, the metals are able to absorb a smaller fraction of the incident X-ray photons, and the albedo of the reflector increases. This produces an apparent deepening of the iron absorption edge and a very weak FeKα line. This happens because the photons of the fluorescent iron line are trapped and destroyed before escaping the disk. For this values of ξ, FeXVII-XXIII are the most abundant ions of iron.

- 700< ξ <7000 erg cm s^{-1}: For these values of the ionization parameter the gas is so ionized that all the metals apart from iron are fully ionized. Thus the soft X-

ray spectrum has only weak spectral features, which are significantly broadened by Compton scattering. On the other hand, the iron emission line is very strong, and its centroid is at ∼6.7 keV. The iron absorption edge is shifted to ∼9 keV. As ξ increases, the gas becomes so hot that Compton scattering starts to significantly blur the iron Kα line and the edge.

- ξ >7000 erg cm s^{-1}: For very large value of ξ the last electrons leave the iron nucleus. The iron line at 6.97 keV is suppressed, which results in a very weak and Compton broadened iron line.

Iron Kα line

The FeKα line is now known to be often constituted by two components, a narrow and a broad one. The widths of the narrow line component are normally of the order of a few thousands km s^{-1}, values that could be consistent with the line originating in the torus (e.g., Reeves et al. 2007). However, the lack of a correlation between the width of the narrow Fe Kα line and the Hβ width or the black hole mass (Nandra, 2006) suggests that a significant fraction of the narrow Fe Kα line should be produced in some other region. A possible explanation is that the line is created in the outer part of the accretion disk. This would explain the rapid (tens of ks) variability observed in some objects (e.g., Petrucci et al. 2002). Part of the line is also thought to be produced by more distant matter (e.g., Reeves et al. 2007), likely in the obscuring torus (e.g., Bianchi et al. 2004). Some objects have shown evidence of Doppler-shifted iron Kα lines, called transient iron lines, originated in the disk or in an outflow (e.g. , Yaqoob et al. (2003)).

On the other hand, broad iron Kα emission lines are observed. The line is very likely produced in an accretion disk rotating around a black hole. The broad red tail of the line profile is mainly produced in the innermost region of the accretion disk, between 0.62-3 rg (rg is the gravitational radius), in a region where even the blue wing of the emitted line profile is redshifted due to the enormous gravitational potential. The narrow line component is mostly produced in a region farther outward, typically at 3-5 rg. In Fig.1.12 an observation of the broad iron Kα line of MCG-6-30-15 is shown (from Bian & Zhao 2003). Observations have shown the presence of broad iron lines in several more objects (e.g., Piconcelli et al. 2006). However, studies of large samples of Seyfert galaxies found that broadened iron Kα lines are not ubiquitous, but they are found in only $\sim$ 30 - 40% of the objects (Guainazzi et al., 2006; Nandra et al.,

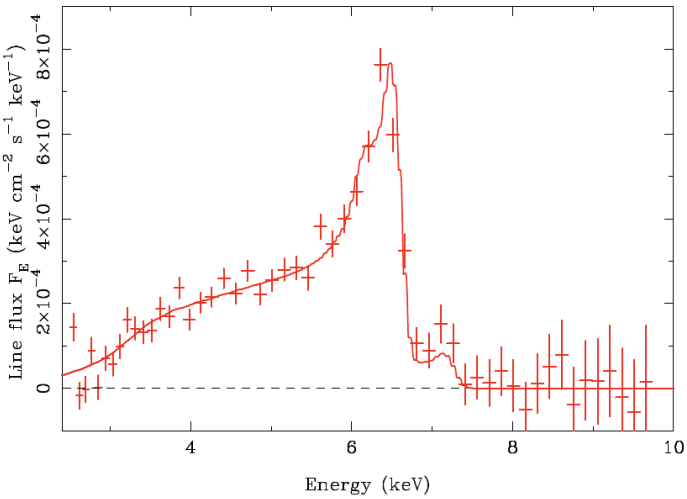

Figure 1.12: The broad iron Kα line of MCG-6-30-15 as observed by the long (325 ks) look of XMM-Newton (Vaughan et al., 2003). The skewed line profile is thought to be the key signature of the innermost region of the accretion disk in the presence of strong gravity.

2007). By stacking the spectra of several sources, after dividing them in luminosity bins, Guainazzi et al. (2006) found that a broad red wing is clearly present only in the lower luminosity bin ($L_{2-10keV} < 10^{43}$ erg s^{-1}). They also found that the relativistic lines appear to be more intense in Sy1 than in Sy2, that could be explained by different orientation angles, assuming that the torus and the disk lie in the same plane.

The reason why broad iron Kα lines are not present in all AGN is still debated, and several hypothesis have been put forward.

- Ionized disk: A certain degree of ionization is expected in accretion disks, above all for high accretion rates (Ross et al., 1999). A strong reduction of the line flux is expected for moderate (due to resonant trapping) and very large (due to full ionization) degrees of ionization (Matt et al., 1996).

- Truncated disk: The disk might be truncated before the last stable orbit, thus producing less intense broad iron Kα lines. Accretion disks are believed to be truncated in Galactic black holes, of which AGN are thought to be a scaled-up version. Possible evidence of truncated disk in AGN has been found (e.g., Matt & Guainazzi 2005; Lobban et al. 2010; Lubiński et al. 2010).

- Line so broad to be hardly recognizable. This might happen if the line emission is confined to the inner part of the accretion disk rotating around the Kerr black

hole.

Fabian et al. (2009) have claimed the first detection of a strong, blurred iron line in the spectrum of the NLS1 1H 0707-495. However, several works have shown that the broad iron Kα lines might also be created by outflows (e.g., Turner et al. 2009).

The soft excess

Many AGN show an extra emission below $\sim$ 2 keV, away from the extrapolated 2-10 keV power-law emission. It is known as soft-excess and was first seen by Arnaud et al. (1985) in the Seyfert galaxy Mrk 841. It is a common feature in AGN spectra but the precise origin of this soft excess is still unknown and under debate (Bianchi et al., 2009).

Three models have been proposed to explain it: 1) an additional Comptonization component (Dewangan et al., 2007), 2) ionised reflection (Crummy et al., 2006), or 3) complex or ionised absorption (Done et al., 2007). At soft energies a thermal emission can also be observed, with kT ranging from 0.1 to a few keV (Risaliti et al., 2002; Guainazzi et al., 2005a; González-Martín et al., 2009).

Absorption in the X-rays

Absorption manifests itself through two processes in the X-rays: photoelectric absorption (bound-bound and bound-free transitions), and Compton scattering (free-free transitions), and it can play an important role in the X-ray spectrum of AGN. To model the effect of absorption on the X-ray spectra of AGN, one has to take into account both effects.

At X-ray energies around 10 keV, absorption by material associated to the interstellar medium become noticeable. Due to this material, the primary continuum of the AGN is suppressed by photoelectric absorption, which is energy-dependent and starts being effective at column densities N_H $\sim 10^{21}$ cm^{-2}. Fig. 1.13 shows the effect when there is no absorption ($N_H < 10^{18}$ cm^{-2}), and when absorption becomes important (N_H $\sim 10^{21.5}$ cm^{-2}). When the absorbing column density reaches $N_H = 1.5\times10^{24}$ cm^{-2},the source is dominated by Compton scattering and the continuum is completely suppressed below 10 keV. The sources with such a high absorption are known as Compton-thick objects (Maiolino et al., 1998).

Large number of Seyfert 2 present large column densities in the line of sight ($N_H > 10^{23}$ cm^{-2}) that can be due to the presence of the torus in the line of sight (consistent

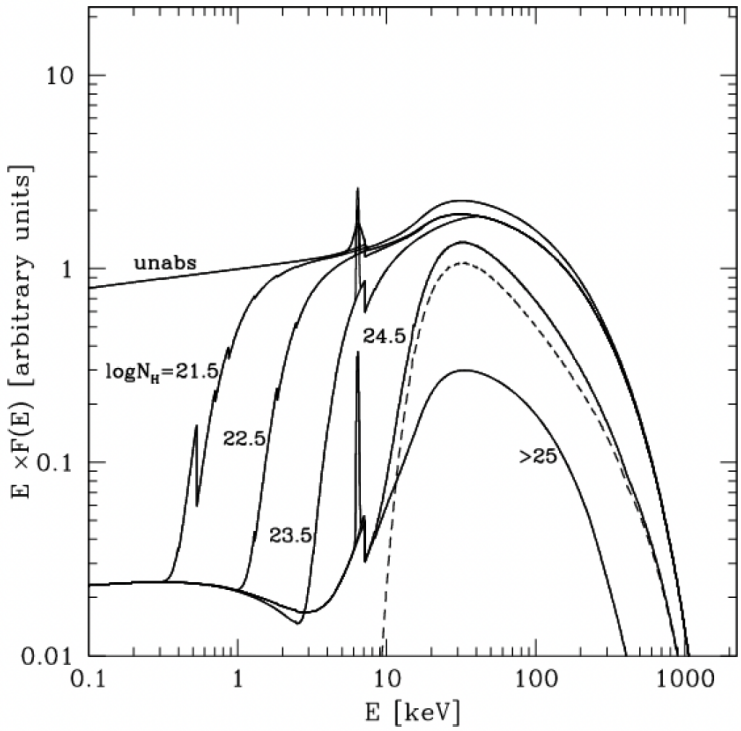

Figure 1.13: Effect of X-ray absorption in the spectra of AGN. Taken from Gilli et al. (2007).

with the UM), however, many Seyfert 1 (and Seyfert 2) show Compton-thin absorption ($N_H \sim 10^{22}$ cm^{-2}). This absorption component is thought to have a different origin than the molecular torus, and several hypothesis have been put forward to explain it. Matt et al. (2003) proposed that the dust lanes in the host galaxies of AGN found by the Hubble Space Telescope survey (Malkan et al., 1998) might have an important role. Other possible culprits might be the BLR, the host galaxy disk (Maiolino et al., 1995), or starburst regions (e.g., Weaver et al. 2002).

1.7 X-ray missions

The Earth's atmosphere is opaque to X-rays, thus X-ray instruments have to be mounted on high altitude rockets, balloons or satellites. Even if the technology to send detectors via rockets was already devised in 1929 by Edward Hulburt and used in 1949 by Herbert Friedman to detect solar X-rays, the true birth of X-ray astrophysics can be a dated to 1962, when Riccardo Giacconi imaged with a rocket-born detector the first extra-solar X-ray source Scorpius (Sco) X-1. Sco X-1 was later identified with a neutron star in a binary system with a low mass star.

X-ray astronomy and the technology required for it are complicated further by the difficulties in focusing X-ray photons. X-ray photons are approximately 1000 times more energetic than optical photons. In fact, if X-ray instruments would have the same structure as optical ones, the X-ray photons will penetrate the mirrors like a bullet penetrates a wall. Thus, X-ray photons have to hit the mirror at a grazing angle to be focused, similarly to the way bullets ricochet when they hit a wall at a grazing angle. The grazing angle is about a degree for energies up to 10 keV but it decreases for higher energies. For this reason, the point spread function (PSF) of X-ray telescopes is energy-dependent. In this work, we mainly concentrate on the three observatories *XMM-Newton*, *NuSTAR* and *Swift*.

XMM-Newton

XMM-Newton is an X-ray observatory satellite named in honor of Sir Isaac Newton. It is a mission developed by the European Space Agency (ESA), dedicated to explore the Universe in the soft-X-ray part of the electromagnetic spectrum, between 0.2 and 12 keV (XMM-Newton Handbook, 2010)[2]. *XMM-Newton* was launched in December 10, 1999. This observatory carries two distinct types of telescopes, an X-ray telescope, and an optical/UV telescope, and three types of instruments are on board the satellite:

- The European Photon Imaging Camera (EPIC), for X-ray imaging, X-ray spectroscopy, and photometry (Strüder et al., 2001)).
- The Reflection Grating Spectrometer (RGS), for high-resolution X-ray spectroscopy and spectro-photometry (den Herder et al., 2001).
- The Optical Monitor (OM), for optical/UV imaging and spectroscopy (Turner et al., 2001).

The basic characteristics of *XMM-Newton* are: simultaneous operation of all science instruments; spatial resolution of 6" FWHM, sspectral resolution (E/dE)$\sim$ 20-50 and field of view (FOV) 27.5'x27.5' and simultaneous optical/UV observations. A detailed description of the *XMM-Newton* mission can be found in XMM Users Handbook (2010).

The *XMM-Newton* observatory has three telescopes for collecting X-ray photons. The optics of each telescope consist of 58 nested mirror modules. They are designed to

[2]https://xmm-tools.cosmos.esa.int/

Figure 1.14: Artist's impression of the XMM-Newton spacecraft. Taken from https://www.esa.int/.

operate in the X-ray energy range of 0.1 keV to 12.0 keV, with a focal length of 7.5 m, and X-ray point-spread function values for FWHM of about 6". Each mirror module consists on two parts. The front part has a paraboloid surface and the rear part a hyperboloid surface. This configuration allows for double reflection of the grazing X-rays, and therefore, focusing of X-rays. Behind each of the X-ray telescopes, an EPIC camera is installed, providing extremely sensitive imaging observations.

EPIC cameras

The *XMM-Newton* telescope carries three EPIC cameras of two different types:

- Two MOS (Metal Oxide Semi-conductor) CCD arrays type;
- Fully depleted pn CCDs

Each camera has a field of view (FOV) of 30'. The cameras allow several modes of data acquisition, and different cameras may operate in different modes. The MOS and pn cameras are fundamentally different. They have different geometries and differ in others properties as well, such as their readout time.

All EPIC CCDs operate in a photon counting mode, producing so-called "event lists". An event is an X-ray hitting the detector. An event list includes information about the event's attributes, such as position, time and energy, among others. EPIC cameras are not only sensitive to X-ray photons but also to infrared, visible and ultra-violet light. The cameras include blocking filters to reduce the contamination of the X-ray signal by those photons.

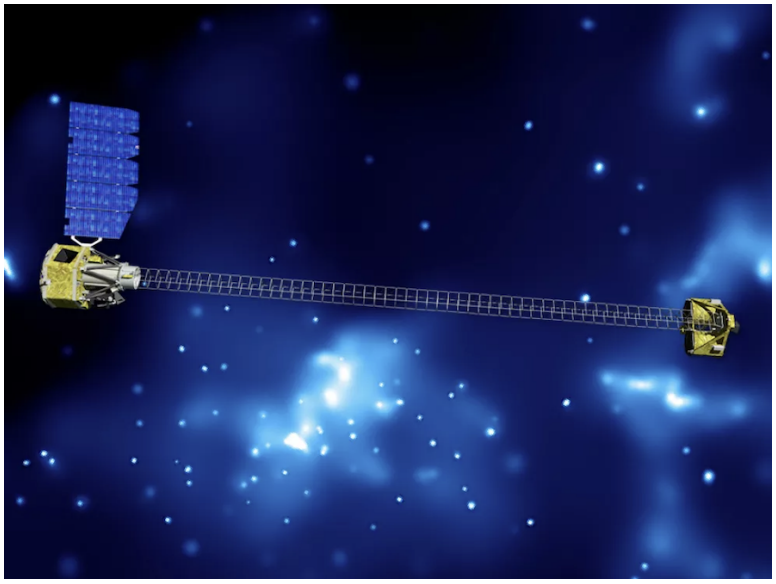

Figure 1.15: Artist's concept of NuSTAR on orbit. NuSTAR has two identical optics modules in order to increase sensitivity. The background is an image of the galactic center obtained with the Chandra X-ray Observatory. Taken from: NASA.

NuSTAR: The Nuclear Spectroscopic Telescope Array

The Nuclear Spectroscopic Telescope Array (*NuSTAR*) is a NASA Small Explorer mission carrying the first focusing hard X-ray telescope (3-80 keV) to orbit. *NuSTAR* was launched on June 13, 2012. This observatory has an order of magnitude better angular resolution, and it is two orders of magnitude more sensitive than any existing hard X-ray instrument operating in the same energy band.

NuSTAR consists of two co-aligned hard X-ray telescopes which are pointed at targets by a three-axis-stabilized spacecraft. The *NuSTAR* telescope consists of three main parts:

- the optics, or mirrors, which focus the light;
- the detectors, which record the image;
- an extendible mast, which holds the optics and detectors at the required 10 meters separation distance once in orbit.

Optics

NuSTAR has two optics units aligned to look at the same location in the sky (Harrison et al., 2013). The two sets of images are added together on the ground to see

fainter objects. The optics have an angular resolution of $\sim$ 12″ (FWHM), and a field of view of $\sim$10′.

Detectors

To register the image focused by the optics, *NuSTAR* requires high-energy X-ray detectors capable of measuring the position and energy of the incoming X-rays. in this case, the detectors are called focal plane detectors because they reside where light from the telescope is focused. Each telescope has a corresponding Focal Plane Module (FPM) consisting of four 32x32 pixel Cadmium Zinc Telluride (CdZnTe) detectors surrounded by a Cesium Iodide (CsI) anti-coincidence shield.

The Mast

Bridging the mirrors and the detectors is a mast, a little over 10 meters long. Because hard X-rays graze off the mirrors at nearly parallel angles, hard X-ray telescopes require long focal lengths (the distance between the optics and the detectors, or focal plane). The mast is of low weight, compact and provides a stiff and stable structure connecting the precisely aligned benches.

Swift

Swift is a NASA Midex (medium-class Explorer) mission. It was launched on November 20, 2004. The Swift Gamma Ray Burst Explorer is a three-telescope space observatory for studying gamma-ray bursts (GRBs) and monitoring the afterglow in X-ray, and UV/Visible light at the location of a burst. To maximise its scientific potential it has rapid response capabilities and is equipped with three telescopes that cover the γ-ray, X-ray and UV/optical energy range:

- Burst Alert Telescope (BAT, Barthelmy et al. 2005).
- X-ray Telescope (XRT, Burrows et al. 2005).
- Ultraviolet/Optical Telescope (UVOT, Roming et al. 2005).

Swift is engineered to rapidly slew to a burst as soon as a GRB is detected by the BAT, and can place the GRB in the field of view (FOV) of the XRT and UVOT within 100 s.

Swift/BAT

The BAT is designed to cover the prompt emission from GRBs over the whole sky. With a large field of view (1.4 sr) and a quick slew time, it can detect the position of GRBs in the sky with an accuracy of 1-4′ in 15 seconds. The BAT works in the energy

band from 15 keV to 150 keV and it uses a coded-aperture mask composed of $\sim$ 54000 lead tiles, of dimensions 5x5x1 mm, which is mounted on a 5 cm thick composite honeycomb panel and placed 1 meter above the detector plane. The 12x0.6 m sensitive area of the BAT detector plane is formed by 32768 pieces of 4x4x2 mm CdZnTe (CZT). Groups of 128 detector elements are collected into 8x16 arrays, each one of which is connected to 128-channel readout Application Specific Integrated Circuits (ASICs). The detector modules, which contain each two such arrays, are further grouped in blocks of eight. The hierarchical structure, together with the coded-aperture technique, allows the possibility of losing individual pixels, individual detector modules and even whole blocks without losing the ability to detect GRBs and determine positions.

Swift/XRT

The *Swift*/XRT is composed of a grazing incidence Wolter Type I X-ray telescope with 12 nested mirrors, which are made to focus on single MOS charge-coupled device (CCD), similar to those on the XMM-Newton EPIC MOS cameras. It has an effective area of 110 cm^2, 23.6′×23.6′ field of view, 18″ resolution and a covers the 0.2-10 keV energy range. The X-ray telescope can acquire fluxes, perform spectral analysis and produce light curves of GRBs and their afterglow, covering a dynamic range that spans over seven orders of magnitude.

Swift/UVOT

The UVOT is a 30 cm modified Ritchey-Chrétien reflector with two micro channel plate intensified CCD detectors that are modelled on the OM on-board *XMM-Newton*. They are photon counting devices that are capable of detecting very low signal levels, unaffected by CCD read-out noise and cosmic ray events. The UVOT contains three optical and three ultra-violet (UV) lenticular filters that cover the wavelength range 1600-6000 $\mathring{A}$, a white band filter that has a good response ranging from 1600-8000 $\mathring{A}$, and a blocked filter. The instrument also has a visible grism and an UV grism, which provides low-resolution spectra ($\lambda/\mathrm{d}\lambda \sim 75$) in the 28005200 $\mathring{A}$ and 16002900 $\mathring{A}$ energy range, respectively, for sources that are brighter than 17 mag for the optical and 15mag for the UV.

1.8 Motivation of this thesis

The overall aim of this thesis is to shed light on the inner structure of LLAGN. Note that we refers as LLAGN in this thesis to galaxies with accretion rates below 10^{-2}.

Previous studies (see for example González-Martín et al. 2017) using *Spitzer* observation, found a possible disappearance of the torus in the low luminosity regime. On the other hand, Ricci et al. (2017b) using X-ray data from *Swift* found that the probability of an AGN to be obscured is mostly driven by the Eddington ratio, where LLAGN are not able to inflate a torus (e.g., Elitzur 2008) or small amounts of circumnuclear gas. Then, the luminosity (or the accretion rate) has influence in the torus properties, showing that in fact, in the low luminosity regime this structure could disappear. Our aim is to analyse if there is a disappearance, or there is a change in properties of this structure compare with their high luminosity counterparts. An analysis of the scattered X-ray spectrum can reveal the presence and properties of the obscuring torus even in unobscured AGN. Therefore, the X-ray spectrum is an useful tool to study the properties of obscuration in AGN because it gives information on the circumnuclear material even if it does not lie in the line of sight to the observer. Then, we will study the torus/disk by the reflection with a high-quality X-ray spectra (combination of three satellites: *NuSTAR*, *XMM-Newton* and *Swift*).

In addition, a careful analysis of the reflection component is also crucial to study the accretion mechanism. Given the partial degeneracy between the curvature of the scattered spectral component and the curvature of the coronal emission, without a good constraint on reflection it is difficult to estimate the real shape of the coronal spectrum. The study of the accretion mechanism in AGN has been approached by relating the spectral index of the power law continuum, Γ, and the Eddington ratio, λ_{Edd}. This relation shows a positive trend for high luminosity sources above a threshold value of λ_{Edd} and negative trend below this threshold (see Gu & Cao 2009; She et al. 2018; Younes et al. 2011 and references therein). However, in the case of LLAGN, which fall in the anti-correlation of this relation, shows a high dispersion that is still not understood — it could be due to the sensitivity of the measurements or to intrinsic diversity of the nuclei. Then, estimating Γ using high-quality X-ray data and studying how sensitive is this parameter to the reflection model used in the fit is an important step to constrain the origin of the scatter in this relation.

The first part of this thesis is focused on the development of the technique to put constrains in properties of the torus or the disk like reflector in LLAGN (Chapter 2, see also Diaz et al. 2020). Then, in Chapter 3 we applied the previous technique to a sample of LLAGN, and explore a possible improvement in the scatter in the relation between Γ - λ_{Edd}. In Chapter 4 an overall summary of the work presented here and some ideas for future work are provided.

Additionally, in Appendix A we show the effect of the inclusion of the *NuSTAR+XMM-Newton* data and reflection models in the spectral index estimation. In Appendix B notes and comparisons with previous results for individual objects in the sample presented in Chapter 2. In appendix C and D we present the Tables and all the individual spectral models in the sample of galaxies. Finally, Appendix D provides a list of other scientific work where I have been involved.

CHAPTER 2

Pilot project

The work in this chapter has been published in Monthly Notices of the Royal Astronomical Society (see Diaz et al. 2020 for more details).

In this chapter, we develop a methodology to study the reflection and its influence in the estimation in the coronal parameters. To perform this analysis we focus on NGC 3718 ($\lambda_{\rm Edd} \sim 10^{-5}$) combining observations from *XMM–Newton* and the deepest to date *NuSTAR* (0.5–79 keV) spectrum of a LLAGN, to constrain potential reflectors, and analyze how the fitted coronal parameters depend on the reflection model. In this low luminosity object the reflection is indeed absent or undetectable due to its intrinsically weak features together with the low statistics inherent to LLAGN. We test models representing both an accretion disk (Relxill) and a torus-like (MYTorus and Borus) neutral reflector.

2.1 Introduction

As we said in previous Chapter (see Sect. 1.5), orientation is not the sole explanation for the different types of AGN. Differences in accretion rate are also important, with NLSy1s at one extreme of this parameter and at least some LINERs galaxies at the other. It has become apparent that the physical extent of the obscuring material (i.e.,

the torus) is itself a function of the accretion rate (e.g., Ricci et al., 2017b). These authors found that the fraction of obscured sources, or covering factor of the Compton-thin circumnuclear material, grows with the accretion rate and then exhibits a sharp decline at an Eddington ratio ($\lambda_{\rm Edd}$=$L_{\rm Bol}/L_{\rm Edd}$, where $L_{\rm Bol}$ is the bolometric luminosity and $L_{\rm Edd}$ is the Eddington-limit luminosity) of $\sim$$10^{-2}$. This value of $\lambda_{\rm Edd}$ corresponds to the Eddington limit for dust. According to this result, the probability of an AGN to be obscured is mostly driven by the Eddington ratio, resulting in a radiation-regulated unification model. The decline of covering fractions at high accretion rates can be explained by the AGN being powerful enough to radiatively blow away the circumnuclear material, while the decline at low accretion rates points either to a lower ability to inflate a torus (e.g., Elitzur 2008) or to smaller amounts of circumnuclear gas leading to lower accretion rates. Current open questions include the nature of the torus, and its dependence on luminosity, black hole mass and galaxy evolution (e.g., Netzer, 2015).

The primary X-ray emission originates in a corona close to the accretion disk (e.g., Haardt & Maraschi, 1993) and is well represented by a power-law model (e.g., Nandra & Pounds, 1994b; Nandra et al., 1997; Risaliti, 2002; Cappi et al., 2006; González-Martín et al., 2009). When this X-ray continuum is scattered by the surrounding gas, new features are imprinted in the spectrum, producing fluorescent emission lines, most notably Fe Kα 6.4 keV, and a broad hump-like continuum peaking around 10–30 keV (e.g., Piro et al., 1990). The relative strength of these two features is related to the column density of the scattering gas, while their overall flux is proportional to the gas covering fraction as seen from the central engine. Therefore, a careful analysis of the scattered X-ray spectrum can reveal the presence and properties of the obscuring torus even in unobscured AGN. Therefore, the X-ray spectrum is an useful tool to study the properties of obscuration in AGN because it gives information on the circumnuclear material even if it does not lie in the line of sight to the corona.

Studying the properties of the reflector spectrum is a difficult task because it is affected by additional absorption, the uncertain spectral slope of the power-law and a possible high energy cut-off ($E_{\rm cut}$), which mimics the curvature of the scattered light, and by the additional contribution of ionized reflection (e.g., from the accretion disk). For this reason, hard X-ray observations of AGN, above 10 keV, are of paramount importance to constrain the complete reflection spectrum. A careful analysis of the reflection component is also crucial to study the accretion mechanism. Given the partial degeneracy between the curvature of the scattered spectral component and the

curvature of the coronal emission, without a good constraint on reflection it is difficult to estimate the real shape of the coronal spectrum. In particular, LLAGN are thought to have a different accretion mechanism compared to more powerful AGN (Yamaoka et al., 2005a; Yuan et al., 2007; Gu & Cao, 2009; Younes et al., 2011; Xu, 2011; Hernández-García et al., 2016; She et al., 2018). The standard accretion disk model (Shakura & Sunyaev, 1973; Koratkar & Blaes, 1999) can successfully explain the AGN power in the regime of high accretion rates ($\lambda_{\rm Edd} > 10^{-3}$). The standard disk is geometrically thin and optically thick, with viscous dissipation balancing radiative cooling locally. On the other hand, in the low-accretion regime ($\lambda_{\rm Edd} \leq 10^{-3}$), the standard cool disk model is no longer able to fit the observations. These low-luminosity AGN are found to be radiatively inefficient (Ho, 2008b). In this regime advection-dominated accretion flows (ADAFs; e.g, Narayan et al. 1994) are expected.

One of the distinctive features of LLAGN is the low level of reflection features that they display in their X-ray spectra (e.g., Younes et al., 2019; Osorio-Clavijo et al., 2019), together with the small contribution from torus emission in the mid-IR band (e.g., González-Martín et al., 2017). This small amplitude complicates the study of reflection in LLAGN, requiring high quality, high energy data. These observations can be explained in the context of a disappearing torus with decreasing accretion rates (Elitzur, 2008). Some material, however, must surround the X-ray emitting region, e.g., the rest of the accretion flow itself and possibly a flattened-out or thinned remnant of the torus and the reflection off these structures should be visible in a sufficiently precise X-ray spectrum. The goal of our work is to constrain the properties of these remnant structures to establish whether the observed low reflection implies a completely clear sky as viewed from the corona, or if a large torus or untruncated disk are still compatible with the observations.

In this chapter, we use simultaneous observations by *XMM-Newton* and *NuSTAR* to study in detail the LLAGN NGC 3718, a nearby galaxy at redshift[1] z=0.003. This galaxy is classified as a type 1.9 LINER (optical classification, e.g., Ho et al. 1997; Cazzoli et al. 2018), with a black-hole mass $\log(M_{BH}) = 7.85 \pm 1.42$ given by Hernández-García et al. 2014 and determined using the correlation between stellar velocity dispersion and black-hole mass of Tremaine et al. (2002), where the stellar velocity dispersion used was $\sigma = 169.9$ km s^{-1} (Ho et al., 2009). It has a low accretion rate $\lambda_{\rm Edd} \sim 4 \times 10^{-5}$, estimated from its mass, its 2–10 keV X-ray luminosity ($\log [L_X/({\rm erg\ s^{-1}})]$=40.4, Satyapal et al. 2005) and bolometric correction factor ($L_{\rm Bol}/L_{2.0-10.0{\rm keV}} = 15$) appropriate for

[1] https://ned.ipac.caltech.edu/

low-luminosity AGN (Lusso et al., 2012).

The high-quality X-ray spectra allow us to analyze how the fitted coronal parameters (photon index Γ and $E_{\rm cut}$) depend on the reflection model, as well as constrain the torus/reflector properties in this low accretion rate regime. This paper is organized as follows: in Sect. 2.2 we present details of the observations and data analysis procedures. The variability and spectral results are reported in Sect. 2.3. The implications of our X-ray spectral analysis are discussed in Sect. 2.4. Finally, a summary of our findings is presented in Sect. 2.5.

2.2 Observations and data reduction

The *XMM–Newton* observations were performed on 2017 October 24 using the medium filter, with Full Frame mode in the EPIC-PN (Turner et al., 2001) and Large Window mode in both EPIC-MOS (Strüder et al., 2001) cameras. The *XMM–Newton* data were processed with SAS version 16.1.0, using the metatasks EPPROC and EMPROC and events were selected with the task EVSELECT. The spectra were constructed from cleaned events files where the flaring times were removed by applying a threshold of 0.7 counts per second on the PN 10.0-12.0 keV count rate integrated over the entire field of view (FOV). Of the original live time of 28.3 ks in the PN CCD 4, only 18.2 ks livetime were used for the spectral analysis. Source events were selected for each detector from circular regions of 40 arcsec in radius, centered on the target. Background events were selected from source-free regions of equal area on the same chip as the source, approximately 100 arcsec away. The same good time intervals were applied to PN, MOS1 and MOS2 data, resulting in source+background counts of 5440 for the PN, 1700 for MOS1 and 2100 for MOS2; the estimated source fractions were 91%, 92.5% and 96%, respectively. Spectral channels were grouped with the SAS task SPECGROUP to contain a minimum of 25 counts per bin. Spectral response (RMF) and ancillary (ARF) files were created using the tasks RMFGEN and ARFGEN.

In case of the *Nuclear Spectroscopic Telescope Array* (*NuSTAR*, Harrison et al. 2013), its two focal plane modules (FPMA and FPMB) operate in the energy range 3–79 keV. The observation was split into four segments spread within 10 days between 2017 October 24 and 2017 November 03, totalling almost 230 ks of exposure time. The *NuSTAR* data were processed using NUSTARDAS v1.6.0, available in the *NuSTAR* Data Analysis Software. The event data files were calibrated with the NUPIPELINE task using the response files from the Calibration Database CALDB v.20180409 and HEASOFT version

Table 2.1: Observational details.

Telescope	Obs ID	Date	Exp. time
NuSTAR	60301031002	2017/10/24	24.52/24.47
	60301031004	2017/10/27	90.39/90.14
	60301031006	2017/10/30	57.37/57.26
	60301031008	2017/11/03	57.01/56.83
XMM-Newton	0795730101	2017/10/24	18.2
Swif/BAT	-	2004/12-2010/08	12.7×10^3

Notes: Instrument (Col. 1), obs ID (Col. 2), date (Col. 3), Net exposure times (Col.4) represents the live time (in ks), of FPMA/FPMB for *NuSTAR* and PN for *XMM-Newton*. *Swift*/BAT data correspond to the 70 month All-sky Hard X-Ray Survey reported in Baumgartner et al. (2013).

6.25. With the NUPRODUCTS script we generated both the source and background spectra, plus the ARF and RMF files. For both focal plane modules, we used a circular extraction region of radius 50 arcsec centered on the position of the source with a source-free. The background selection was made taking a region free of sources of twice the radius of the target. Spectral channels were grouped with the FTOOLS task GRPPHA to have a minimum of 50 counts per spectral bin. The source is significantly detected in the 3–70 keV energy range. Details on the observations can be found in Table 2.1.

We also retrieved a high-energy spectrum for NGC 3718 from the *Swift*/BAT 70 month All-sky Hard X-Ray Survey reported in Baumgartner et al. (2013), together with the corresponding response matrix. The data reduction and analysis for the *Swift*/BAT 70 month All-sky Hard X-Ray Survey are based on the procedures used in the *Swift*/BAT 22 All-Sky Hard X-ray Survey. The complete analysis pipeline is described in the *Swift*/BAT 22 All-sky Hard X-Ray Survey (Tueller et al., 2010).This spectrum contains eight energy channels in the 14–200 keV energy range.

2.3 Analysis and results

The spectral fitting process has two steps: **(1)** variability analysis of each *NuSTAR* exposure to study the possibility of combining them to increase the sensitivity and **(2)** modelling of the resulting spectra.

2.3.1 Variability

We ran the task NUPRODUCTS to construct light curves from the *NuSTAR* data in the energy range 3–70 keV with 500 s bin. We subtracted the background light curves from the corresponding source light curves. The average count rates per segment, i.e., averaging FPMA and FPMB, range from 0.06 ± 0.01 to 0.04 ± 0.01, within 2σ of each other. The data are therefore consistent with no variations on a timescale of 10 days.

We analyzed the light curves to check variability on short timescales, i.e., from hours to days. The light curves are shown in Figure 2.1, where the dashed lines represent 1σ standard deviation. We calculated the χ^2 and the degrees of freedom (d.o.f.) as a first approximation to test the variations. We considered the source to be variable if the count rate differed from the average above 3σ (or 99.7% probability). To check the variability amplitude of the light curves, we calculated the normalized excess variance, σ^2_{NXS}. We followed prescriptions given by Vaughan et al. (2003) to estimate σ^2_{NXS} and its error, err(σ^2_{NXS}). We found that NGC 3718 is not variable at 3σ confidence level. The average count rates of the four segments and both detectors are listed in Table 2.2.

The *XMM–Newton* observation was heavily affected by background flares, causing the loss of nearly half the exposure time. After removal of the flaring intervals, the 0.2–10.0 keV, background-subtracted light curve has an average count rate of 0.26 counts s^{-1}, and no significant variability over the length of the observation, 31 ks. The resulting excess variance is $\sigma^2_{NXS} = 0.002 \pm 0.003$, and therefore consistent with zero.

We also checked for spectral variability between the *NuSTAR* exposures by fitting each individual observation (for FPMA and FPMB) with an absorbed power-law with all parameters free. We found that NGC 3718 showed variations in the normalization smaller than 4% and in Γ smaller than 3%, with values close to $\sim$1.94, on a timescale of ten days, all within the uncertainties in these parameters at 1σ level. The simultaneous fit therefore resulted in a non-variable spectrum on a 10-day timescale.

Variations within the observed timescales were not detected between different spectra studied here. Therefore, the spectra of all the *NuSTAR* epochs were combined to increase the sensitivity, producing a single spectrum for each detector, A and B.

Table 2.2: Statistics for the *NuSTAR* light curves

Obs ID	FPM	σ^2_{NXS}	err(σ^2_{NXS})	counts (counts s^{-1})	error (counts s^{-1})
60301031002	A	0.006	0.014	0.059	0.012
	B	0.084	0.029	0.061	0.013
60301031004	A	0.023	0.012	0.047	0.011
	B	0.015	0.013	0.046	0.012
60301031006	A	0.041	0.015	0.056	0.012
	B	-0.0004	0.009	0.058	0.012
60301031008	A	-0.014	0.014	0.049	0.015
	B	-0.014	0.033	0.035	0.015

Notes: Obs ID (Col. 1), focal plane module (Col. 2), normalized excess variance with errors (Cols. 3 and 4), mean of counts and its errors (Cols. 5 and 6).

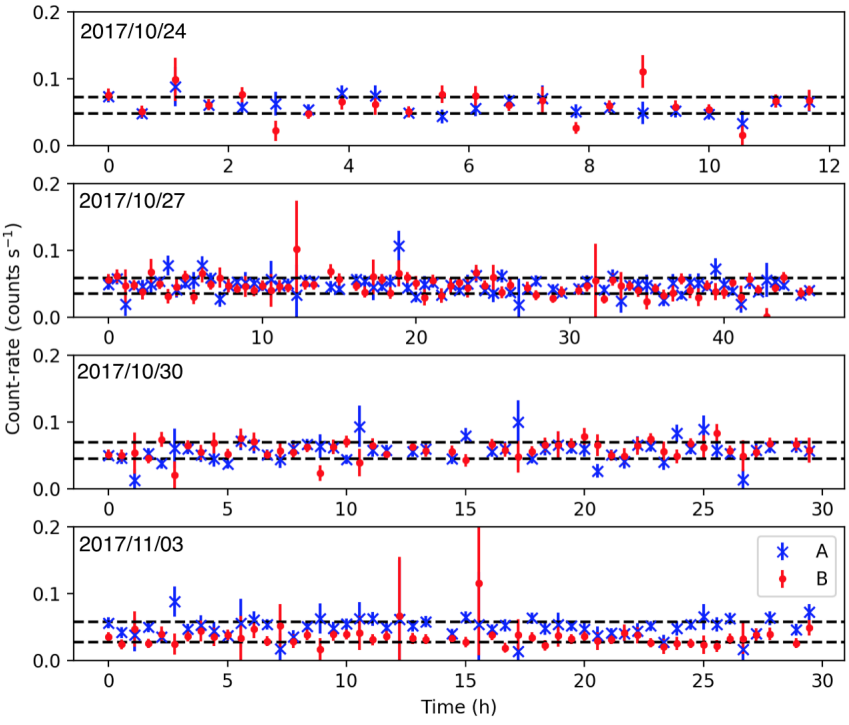

Figure 2.1: Light curve of *NuSTAR* data for NGC 3718 with 500 s bin. Blue stars represent FPMA and red dots FPMB. The black dashed lines represent the 1σ level from the average. The observations are separated by three days.

Since the *XMM–Newton* observation was carried out during one of the *NuSTAR* exposures, the spectra from both observatories can be considered simultaneous. We compared these contemporaneous *XMM–Newton*/*NuSTAR* data sets in the same energy band (3–10 keV) to exclude calibration differences between these instruments. We fitted the data with a power-law and fixed the slope, allowing variations in the normalization. We found values of $N_{XMM} = (5.1 \pm 0.2) \times 10^{-4}$ for *XMM–Newton* and $N_{Nustar} = (5.2 \pm 0.3) \times 10^{-4}$ for *NuSTAR* . Therefore, for this source, the instrument responses are consistent.

2.3.2 Spectral analysis

The spectral analysis of the *NuSTAR*, *XMM–Newton* and *Swift*/BAT data was performed using XSPEC version 12.10.0 (Arnaud, 1996). All the errors reported throughout the paper correspond to 90% confidence, unless otherwise noted. In this chapter we only used *XMM-Newton* observations from the EPIC-PN because of its higher throughput (Strüder et al., 2001) and because inclusion of the EPIC-MOS spectra resulted in too much statistical weight to the low energy range data points compared to the *NuSTAR* and *Swift*/BAT data. For all spectral fits, we included a multiplicative constant normalization between FPMA, FPMB, EPIC-PN and BAT to account for calibration uncertainties between the instruments and possible variations between the *Swift*/BAT and *Nustar* and *XMM-Newton* exposures. We found that these calibration uncertainties are close to unity except in the case of *Swift*/BAT data, where this constant is close to 4. This difference is shown in Table 3 and discussed in Section 4.1.

NGC 3718 shows weak Fe Kα emission. For this reason, we started our spectral analysis with a simple absorbed power-law with a high-energy cut-off (`phabs*zphabs*cutoffpl` in XSPEC. In this model the `phabs` component is associated with absorption from our Galaxy and fixed to 1.07×10^{20} cm^{-2}, obtained using the N_H tool within FTOOLS (Dickey & Lockman, 1990; Kalberla et al., 2005). The `zphabs` component is associated with absorption from the nuclear region. We note that the cut-off power-law model for the continuum emission is a phenomenological model that can represent Comptonized emission from a corona or ADAF or synchrotron emission from a jet, so the source of X-ray emission in the model can correspond to any of these structures.

This fit results in a χ^2= 427.59 for 374 d.o.f. We find a significant intrinsic hydrogen column density of N_H=$(8.9^{+0.7}_{-0.6}) \times 10^{21}$ cm^{-2}, showing that the coronal emission is

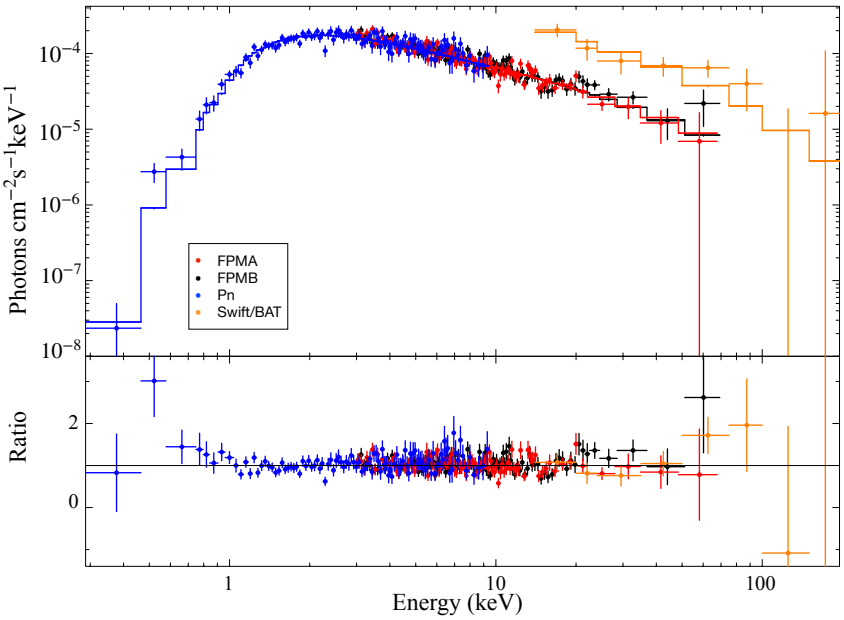

Figure 2.2: Upper panel: Best-fit cut-off power-law model (solid line) to the *NuSTAR* FPMA and FPMB, *XMM-Newton* pn, and *Swift*/BAT spectra of NGC 3718 (filled circles). Lower panel: Residuals in terms of data-to-model ratio.

absorbed, Γ = 1.78±0.08 and $E_{\rm cut}$=73^{+111}_{-30} keV. The data and best-fit cut-off power-law model are shown in Figure 2.2. This model fails to adequately fit the spectral continuum, leaving obvious structured residuals. In order to improve the spectral fit, we studied the residuals in the soft (0.3–2.0 keV) and hard (2.0–110 keV) energy bands.

In order to interpret the parameters of the cut-off powerlaw in a physically meaningful way we replaced this component with the comptonization model `CompTT`, which describes Comptonization of soft photons in a hot plasma (Titarchuk, 1994) to produce the primary continuum. We find the following constraints on the electron temperature (T_e) and optical depth of the corona (τ): $kT_e = 44^{+34}_{-24}$, $\tau = 0.8^{+0.4}_{-0.8}$, where part of the uncertainty in these parameters is due to the degeneracy between them. In order to place tighter constraints on the roll-over energy, below we continue to use a phenomenological model for the continuum, i.e., a cut-off power-law. We note as well that these uncertainties do not incorporate the effect of a possible reflection component, which, as discussed below, can be important.

2.3.3 Soft energy band

In the soft energy band, we added a thermal or scattered power-law component in order to improve the spectral fit. Adding a power-law component under a different host absorber, with a normalization of a few percent of the primary power-law with an identical slope, resulted in a good fit with χ^2= 417.36 for 372 d.o.f., statistically better than the simpler model. An alternative optically thin thermal component, modeled with APEC, performed slightly worse. For this reason, we incorporate the scattered power-law component in the following models. The improvement of the model including the scattered component is clearly seen in Figure 2.3. Note that the intrinsic and scattered power-laws are very similar in shape, in the models they are mainly distinguished by the absorber that they have in front (the scattered component has a lower column density than the intrinsic power-law emission). Leaving the relative normalization free sometimes results in an inversion of the components, which affects the correct identification of the absorbers. To make sure that the spectrum is not dominated by the scattered component at high energies, the relative normalization was restricted to a maximum of 4% of the normalization of the nuclear power-law, where this particular value was obtained from a simple fit.

The column density of the absorber acting on the extended scattered power-law in this fit is $N_{\mathrm{H},S} = (2.1^{+1.0}_{-0.1}) \times 10^{21}$ cm^{-2}, and the absorber acting on the nuclear power-law is $N_{\mathrm{H},H} = (1.0 \pm 0.1) \times 10^{22}$ cm^{-2}, $\Gamma = 1.84^{+0.08}_{-0.06}$ and $\mathrm{E_{cut}} = 99^{+153}_{-50}$ keV. A similar model was shown by González-Martín et al. (2009) to be a good representation of the X-ray spectrum of 82 LINERS in the 0.2–10 keV band with *XMM-Newton* and *Chandra* data.

2.3.4 Hard energy band

The small residuals observed in the hard energy band could be an effect of reflection from an accretion disk or a torus. The effect of this component is thought to affect the curvature of the hard X-ray emission and is responsible for the creation of the iron emission line at 6.4 keV (Pounds et al., 1990; Nandra & Pounds, 1994a). As a first approach to quantify possible reflection features, we investigated the presence of iron emission in the spectrum of NGC 3718. We analyzed data in the energy range 5.0–8.0 keV to constrain the need of a narrow Gaussian component. First, we fit a power-law model in this range and obtain χ^2/d.o.f=20.27/24=0.84. Then we add a Gaussian component to study the improvement of the fit, and found χ^2/d.o.f=16.66/22=0.76. This

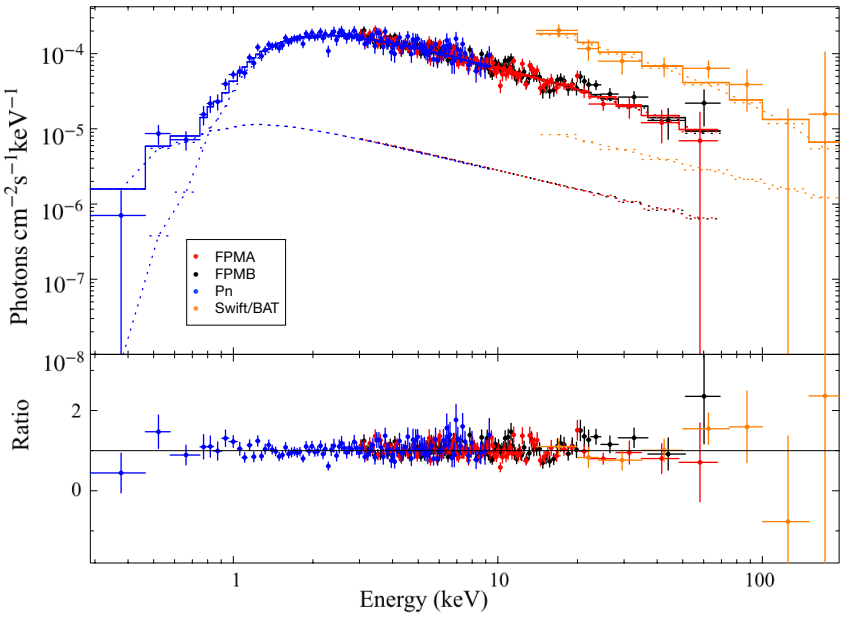

Figure 2.3: Upper panel: Best-fit cut-off power-law + scattered model component (solid line) to the *NuSTAR* FPMA and FPMB, *XMM-Newton* pn, and *Swift*/BAT spectra of NGC 3718 (filled circles). Lower panel: Residuals in terms of data-to-model ratio.

component has a line centered at $6.5^{+0.1}_{-0.2}$ keV, consistent with FeKα (6.4 keV) emission and equivalent width EW = $0.11^{+0.04}_{-0.05}$ keV. Note that we fixed the width of the emission line to 0.01 keV, below the instrumental resolution. Figure 2.4 shows the best-fit model in a zoom-in at 5.0-8.0 keV with a Gaussian fit and its residuals. This figure shows that, although small, an emission line at 6.4 keV is consistent with the spectrum of NGC 3718.

In order to assess the reflection fraction limit that we can derive from our data, we firstly used a simple reflection model. We used the `pexmon` (Nandra et al., 2007) model implemented in XSPEC which uses as continuum an exponentially cut-off power-law. Since the pexmon model represents both the reflected and intrinsic emission, the model employed was pexmon + scattered component, removing the coronal cut-off power-law. In this way, the model parameter R_f corresponds to the reflection fraction and is a free parameter. We found a good fit to the data with this model with χ^2=416.43 for 371 d.o.f, with a best-fitting Γ=1.85$\pm$ 0.08, $E_{\rm cut}$=84^{+93}_{-39} keV and reflection fraction R_f <0.67 (with the best-fitting value of 0.30). The reflection fraction is partially anti-correlated with the cut-off energy as can be seen in the contour plot in Figure 2.5; lower reflection fractions allow higher cut-off energies, although this parameter is still

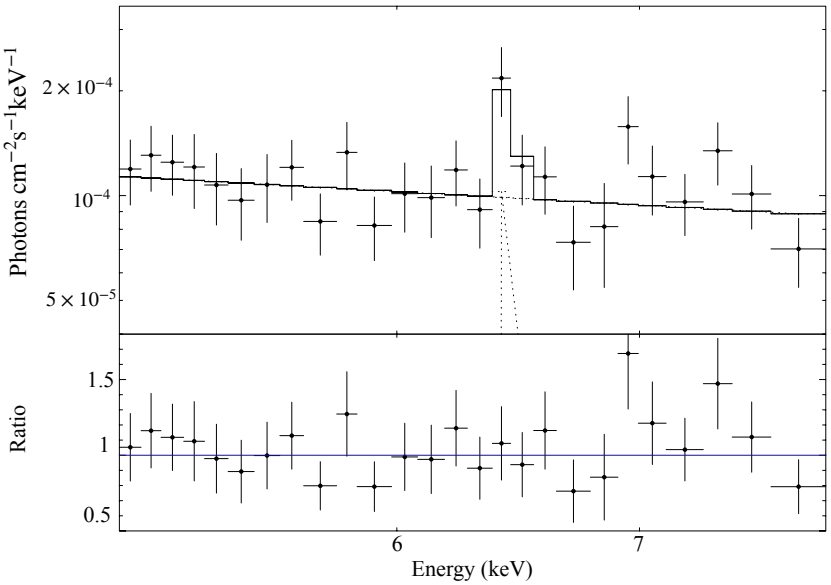

Figure 2.4: Upper panel: Count spectrum of the *XMM-Newton* observation zoomed-in at the Fe complex. Lower panel: Residuals in terms of data-to-model ratio.

constrained at the 1σ level.

The improvement on the fit including `Pexmon` is marginal and an F-test shows that it is not statistically significant. The accreting black hole, however, cannot be completely isolated, there must be material around it, such as the accretion flow itself and a small BLR (Cazzoli et al., 2018). In agreement with this assumption, our previous analysis shows that the spectrum is well described when a reflection component is included, although it is formally also consistent with no reflection, perhaps due to limited signal to noise ratio. Despite the weakness of the possible reflection, it should not be ignored, because if present it will produce curvature in the hard X-ray spectrum that would otherwise be misinterpreted as an intrinsic rollover of the primary continuum. Furthermore, our data (among the deepest available hard X-ray spectrum for a LLAGN) allow us to put physically meaningful limits on the amount and distribution of the material surrounding the AGN. Therefore, in the following discussion we model a reflection component, without a priori restrictions on its strength.

Aiming at fitting the data with the most representative physical model, we studied reflection models which might come from a neutral reflector as modeled by `Borus02` (Baloković et al., 2018) or `MYTorus` (Murphy & Yaqoob, 2009), as well as from an ionized accretion disk (`Relxill`, García et al. 2013). The final model employed in the

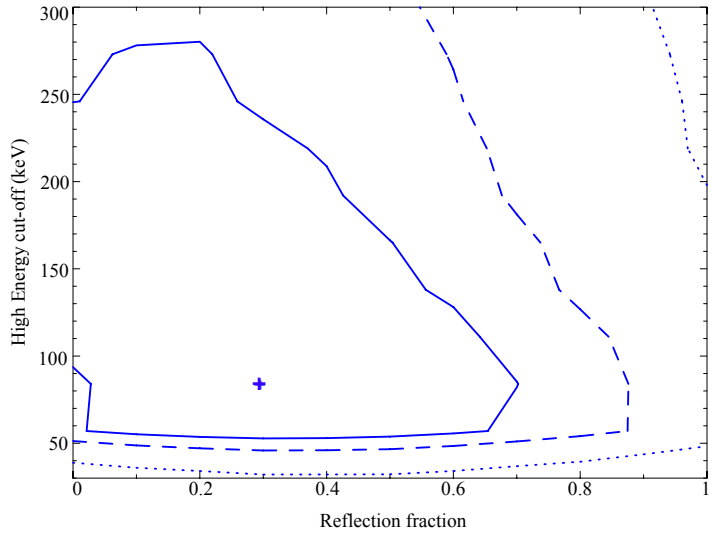

Figure 2.5: Two-dimensional $\Delta\chi^2$ contours for reflection fraction and cut-off energies for NGC 3718 with `pexmon` reflection model. The solid blue line represents the 1σ, the dashed line 2 σ level and the pointed line 3σ contour level. The best-fitting values are marked by a + sign.

analysis is defined as:

$$\boxed{C \times N_{\rm Gal}(N_{{\rm H},S} \times \text{PL} + N_{{\rm H},H} \times \text{cPL} + N_{{\rm H},H} \times table)}$$

where C represents the cross-calibration constant between different instruments and $N_{\rm Gal}$ is the Galactic absorption (`phabs` in XSPEC); $N_{{\rm H},S}$ is the column density of absorbing material acting on the scattered power-law, PL is the power-law of the scattered component; $N_{{\rm H},H}$ is the absorbing material that acts on the nuclear components (power-law and torus or disk reflection)[2]; cPL is a cut-off power-law (`cutoffpl` in XSPEC) representing the primary X-ray emission and "table" represents the different reflection models that will be used. To be consistent, we ignore data below 0.7 keV in the following analysis because the `MYTorus` model only works above that energy. We therefore fixed the parameters of the scattered power-law component to the values that were previously obtained.

In the following, we compare the effect of the different reflectors on the resulting primary continuum parameters (i.e., Γ and $E_{\rm cut}$) and study the properties of the

[2]We made a test with an absorber acting or not in the torus-like reflector and we found that it is indistinguishable. The same result was found for the absorber on the scattered component.

reflector itself. Elemental abundances are assumed to be solar for all models.

Torus reflection model: Borus

Baloković et al. 2018 developed a radiative transfer code that calculates the reprocessed continuum of photons that are propagated through a cold, neutral and static medium. In this chapter, we used the geometry that corresponds to a smooth spherical distribution of neutral gas, with conical cavities along the polar directions (`Borus02`). The opening angle of the cavities, as well as the column density and the inclination of the torus, are free parameters. The reflected spectrum of this torus is calculated for a cut-off power-law illuminating continuum, where $E_{\rm cut}$, Γ and normalization are free parameters. Therefore, combining `Borus02` with a cut-off power-law with parameters tied to those of the `Borus02` illuminating source, a consistent model can be obtained. We tied the opening angle, θ_{tor}, to the inclination angle, θ_{incl}, to ensure a direct view of the central engine, and modeled the direct coronal emission separately with a cut-off power-law under a neutral absorber with `zphabs`. We recall that θ_{tor}=0 corresponds to a pole-on view. The free parameters in this model are the column densities along the line-of-sight, the covering factor and column density of the reflector, Γ of the primary emission, its $E_{\rm cut}$ and normalization, which in turn is tied to the normalization of the reflector.

The best-fit model is shown in Figure 2.6. This fit is statistically acceptable with χ^2= 405.56 for 364 d.o.f. and no clear structure in the residuals. The best-fitting values for the Γ, $E_{\rm cut}$, and absorption can be found in Table 2.3.

We also put constraints on the column density of the reflector and its covering fraction. As can be seen in the contour plot in Figure 2.7, the parameter space allowed by the data is broad. The reflector is only constrained to have a relatively low equatorial column density $N_H < 10^{23.2}$ cm^{-2} for any covering fraction, at the 1σ level, and $N_{\rm H} < 10^{23.5}$ cm^{-2} at the 2σ level. The existing reflection features only require a contribution from the torus in this model at the 1σ level, with a column density $N_{\rm H} > 1.6 \times 10^{22}$ cm^{-2}.

We note that this low column density and high covering fraction solution is consistent with the absorption seen along the line of sight to the corona ($N_{{\rm H},H} \sim 10^{22}$cm^{-2}, see Figure 2.3), so a model where a Compton thin torus covers a high fraction of the sky is consistent with the data both in terms of reflection and absorption.

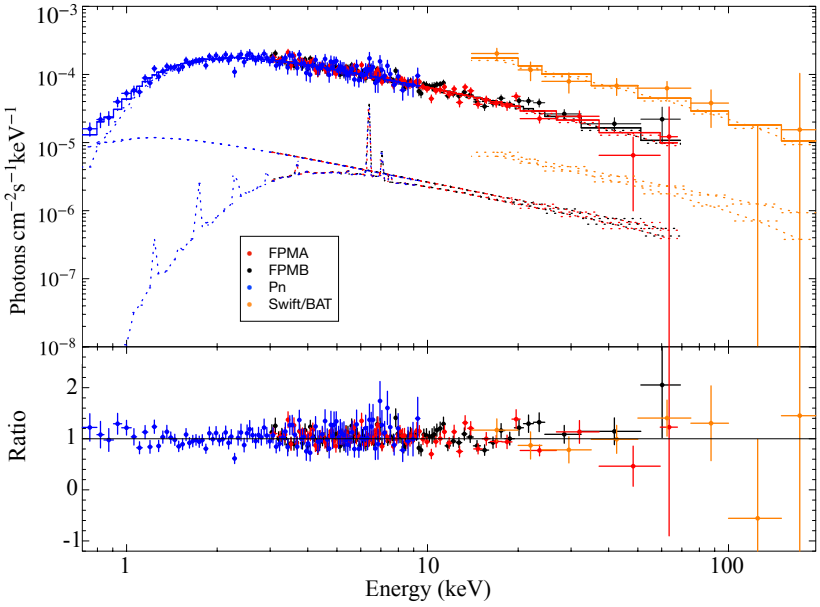

Figure 2.6: Upper panel: Best-fit `Borus+cut-off PL` model (solid line) to the *NuSTAR* FPMA and FPMB, *XMM-Newton* pn, and *Swift*/BAT spectra of NGC 3718 (filled circles). Lower panel: Residuals in terms of data-to-model ratio.

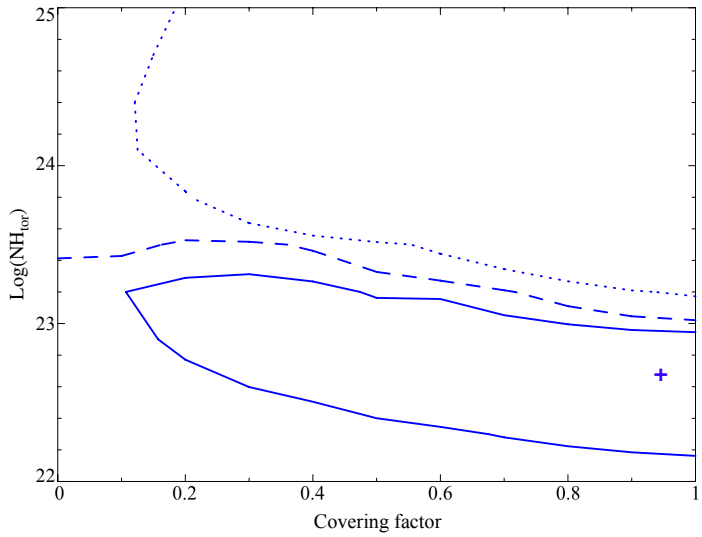

Figure 2.7: Two-dimensional $\Delta\chi^2$ contours for torus column density and covering factor for NGC 3718, modelled with `Borus`. The solid, dashed and dotted contours denote 1σ,2σ and 3σ respectively. The "+" symbol represents the best fit value. The reflector is constrained to have low equatorial column density $N_H < 10^{23.0}$ cm^{-2} with a large best-fitting covering fraction of 0.95 of the sky, although smaller covering fractions down to 0.1 are permitted at the 1σ level.

Torus reflection model: MYtorus

The `MYtorus` (Murphy & Yaqoob, 2009) model proposes a toroidal geometry where the covering fraction is fixed to 0.5, although different values can be mimicked by varying the normalization of the torus relative to the direct coronal emission, as we will do here. The equatorial column density and inclination angle are free parameters. In this model we fix: the metallicity to solar by tying the normalization of the scattered and fluorescent FeKα line components, and the foreground Galactic absorbing column density. We include a cut-off power-law under a neutral absorber as before, to model the direct coronal emission. The model is the same that was used with `Borus`, but replacing the reflector with the `MYTorus` tables. The free parameters in this model are the absorbing column densities along the line of sight, the column density and normalization of the scattered component, the normalization of the power-law, its $E_{\rm cut}$ and its Γ.

The high energy cut-off is not a parameter for the illuminating source in this model, but a few tables exist for different input termination energies. We repeated the spectral fits with the available tables, calculated for illuminating continua with termination energies of 100, 160, 200, 300 and 500 keV to search for a solution where the cut-off energy of the power-law is below the termination energy of the reflection, as otherwise the model would not be consistent.

In this chapter we will use the reflection model with termination energy at 300 keV since this is the lowest value of $E_{\rm cut}$ that satisfies the previous condition. The best-fitting model is plotted in Figure 2.8. This fit is statistically acceptable with χ^2=406.58 for 364 d.o.f. and has an equatorial column density of the reflector of $7.2^{+6.4}_{-5.9}\times$ 10^{22} cm^{-2}. The absorbing column densities can be found in Table 2.3.

The covering fraction can be studied by comparing the normalization of the scattered component with the normalization of the power-law. The column density of the reflector and covering fraction follow the same trend observed with `Borus02`, i.e., a low column density reflector (N_H $\leq 3\times10^{22}$ cm^{-2}) with any covering fraction at 1σ level, although a high covering fraction of the sky is preferred.

The contour plots for the Γ and $E_{\rm cut}$ for the `Borus02` and `MYTorus` reflection models are shown in Figure 2.9. Both models are highly consistent, showing a range of allowed values of Γ (i.e., 1.80-1.90). The main difference between them is the broader range in $E_{\rm cut}$ obtained with `MYTorus`, reaching much lower values at 1σ, but with similar 2σ level contours.

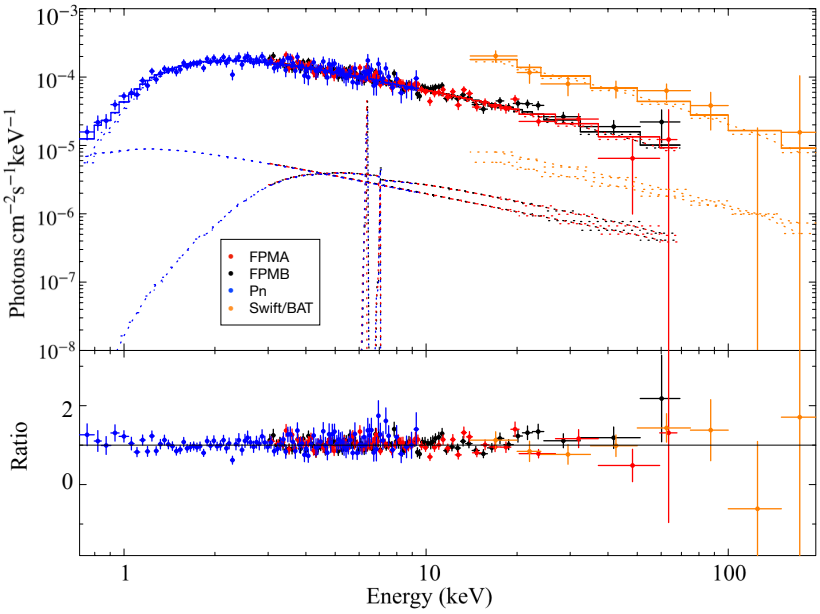

Figure 2.8: Upper panel: Best-fit `MYTorus+cut-off PL` model (solid line) to the *NuSTAR* FPMA and FPMB, *XMM-Newton* pn, and *Swift*/BAT spectra of NGC 3718 (filled circles). Lower panel: Residuals in terms of data-to-model ratio.

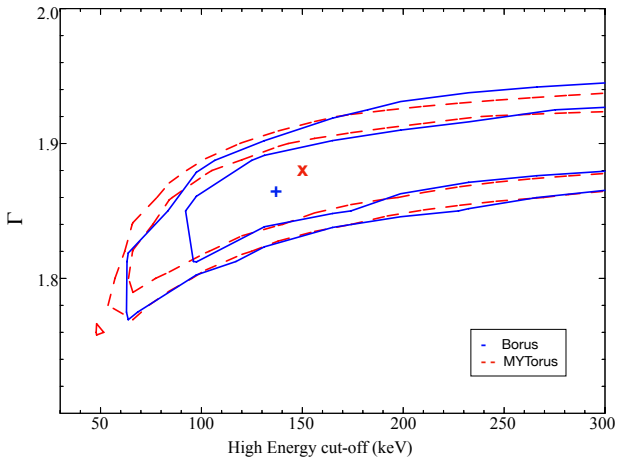

Figure 2.9: Two-dimensional $\Delta\chi^2$ contours for Γ and cut-off energies for NGC 3718 for a neutral material as a reflector. Red dashed lines show the 1σ and 2σ levels for `MYTorus` and the "x" symbol represents the best fit values. Blue solid lines the 1σ and 2σ levels for `Borus02` and the "+" symbol represents the best fit values. Both models are in agreement. `Borus02` model starts in $\sim$100 keV at 1σ level and `MYTorus` covers from $\sim$80 keV.

Disk reflection models

`MYTorus` and `Borus` both model a neutral reflector with toroidal geometry. Another alternative is that reflection arises from an accretion disk. Thus we now put constraints on the properties of a disk-like reflector and estimate the parameters of the primary emission.

We explore ionized accretion disk reflectors using `Relxill` reflection models (García et al., 2013). This model calculates the reflected spectrum from the surface of an X-ray illuminated accretion disk by solving the equations of radiative transfer, energy balance, and ionization equilibrium in a Compton-thick and plane-parallel medium. `Relxill` is composed of many models; in this chapter we consider the case where the coronal spectrum is either a power-law with an exponential cut-off (`Xillver`) or a thermalized Compton spectrum (`XillverCp`). In the former case, the spectrum is described by the photon index (Γ) and the high energy cut-off ($E_{\rm cut}$). In the latter case, the spectrum is described by Γ and the electron temperature of the corona (kT_e). The other common parameter is the ionization, described by the ionization parameter (ξ), defined as the incident flux (F) divided by the density of the disk (n): $\xi = 4\text{ßF/n}$ [erg cm s^{-1}]. A low value implies that the disk is neutral. For increasing ionization parameter, the number and strength of the emission lines observed in the spectra generally decreases, leading to a fully ionized disk, which acts almost as a mirror and therefore the spectrum exhibits no line features (see García et al. 2013, for a more detailed description). In this model, this parameter is described by $\log(\xi)$ ranging from 0 for a neutral disk to 4.7 for a heavily ionized disk.

Other important parameters are the iron abundance A_{Fe} relative to the solar value (assumed to be solar in this chapter[3]), redshift, and inclination. This model contains both the direct spectrum of the corona and the reflection spectrum. We removed the coronal power-law from the model setup and replaced it, together with the reflected component, with either `Xillver` or `XillverCp` with a positive reflection fraction. In this way, the model parameter R_f corresponds to the relative fraction of coronal photons hitting the disk to those escaping to infinity. Our model in these cases is defined as:

$$\boxed{C \times N_{\rm Gal}(N_{\rm H,S} \times \text{PL} + N_{\rm H,H} \times \text{table})}$$

where "table" represents the accretion disk reflection model. We made a test using the

[3]We varied these parameters and found minimal effects on our results.

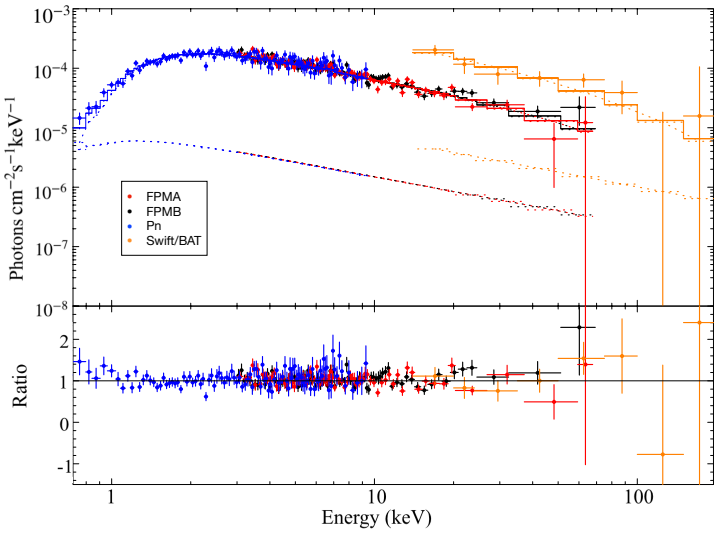

Figure 2.10: Upper panel: Best-fit `Xillver` model (solid line) to the *NuSTAR* FPMA and FPMB, *XMM-Newton* pn, and *Swift*/BAT spectra of NGC 3718 (filled circles). Lower panel: Residuals in terms of data-to-model ratio.

`Xillver` model with a neutral accretion disk ($\log \xi = 0$), leaving the reflection fraction as a free parameter, in order to study consistency with the results previously found with `pexmon`. We found that our result is compatible with `pexmon`, observing that the best fitting values of $E_{\rm cut}$ and Γ are almost identical.

Allowing the `Xillver` ionization parameter to vary, we find a good fit to the data, with $\chi^2 = 409.59$ for 363 d.o.f. The flat residuals suggest that all features in the data are fitted by this solution. Replacing `Xillver` with `XillverCp` results in χ^2= 407.21 for 363 d.o.f. and similar residuals. The best value for Γ, $E_{\rm cut}$ and $N_{{\rm H},H}$ of both models are presented in Table 3. The best-fitting `Xillver` model is shown in Figure 2.10 and `XillverCp` in Fig 2.11.

Figure 2.12 shows contour plots of the disk inclination relative to the line of sight and the ionization degree of the disk for `Xillver`. We found that the inclination is unconstrained for all the model, with the best value reaching ∼80 degrees. The ionization of the disk (logξ) is well restricted to values between 2.8 and 3.5, with the best value $\log(\xi) \sim 3.1$. Replacing `Xillver` with `XillverCp`, the model produces the same result for these parameters.

Figure 2.13 shows the allowed ranges of the coronal parameters, Γ and the high energy cut-off of the corresponding electron temperature. `Xillver` uses as model parameter the high energy cut-off of the incident power-law spectrum, while `XillverCp`

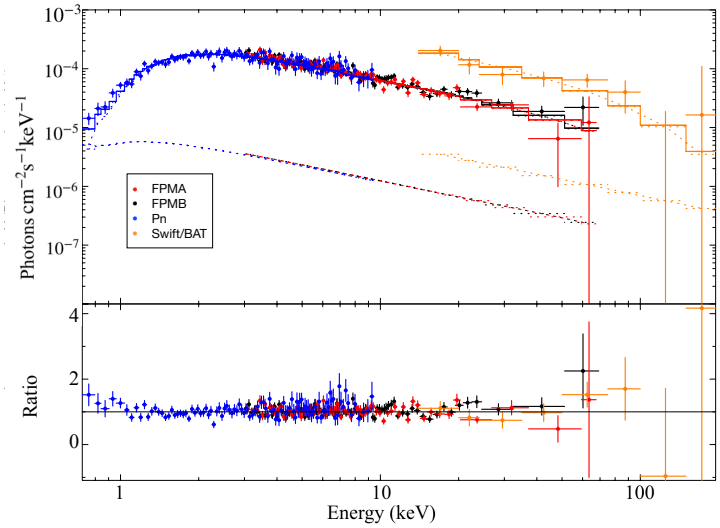

Figure 2.11: Upper panel: Best-fit `XillverCp` model (solid line) to the *NuSTAR* FPMA and FPMB, *XMM-Newton pn, and* Swift/*BAT* spectra of NGC 3718 (filled circles). Lower panel: Residuals in terms of data-to-model ratio.

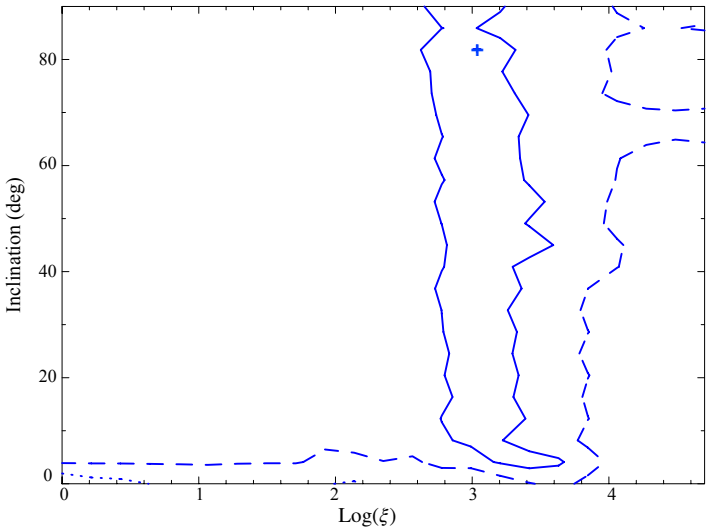

Figure 2.12: Two-dimensional $\Delta\chi^2$ contours for ionization of the disk and inclination of the disk for NGC 3718 for fits with `Xillver`. The blue solid, dashed and dotted contours represent the 1σ, 2σ and 3σ levels, respectively. The best value of $\log \xi$ is restricted to values between 2.8 and 3.4, while the inclination is unconstrained preferring high inclination ($\sim$80 degrees.

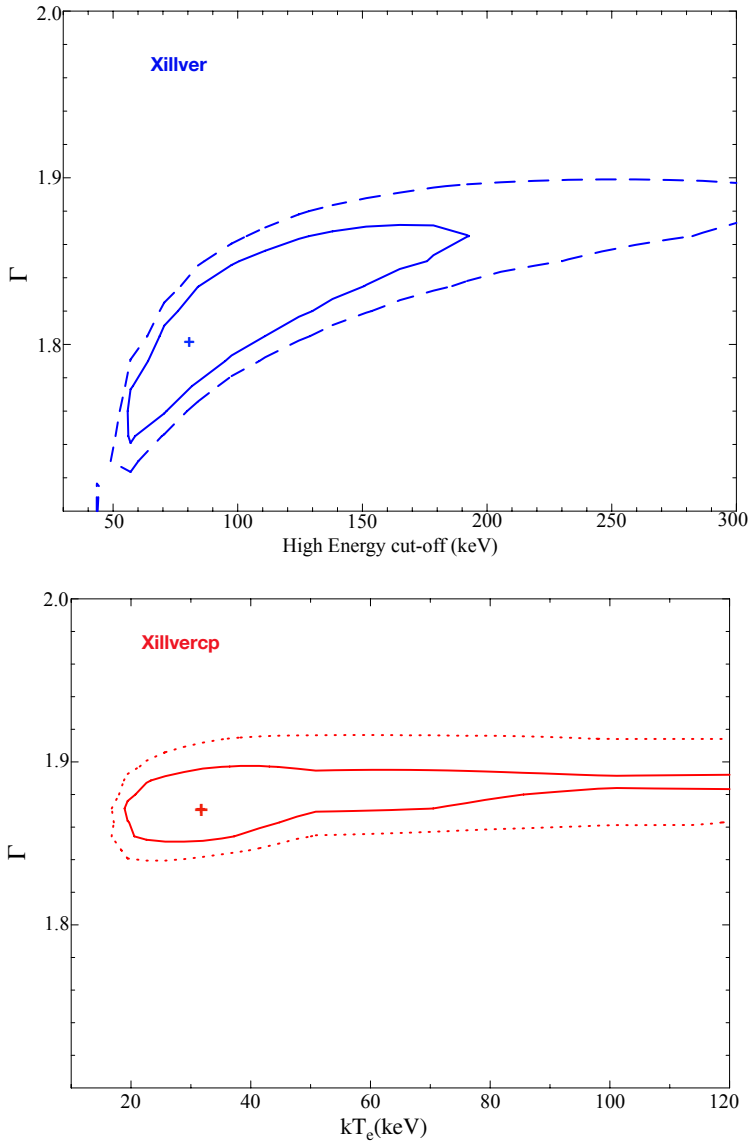

Figure 2.13: Two-dimensional $\Delta\chi^2$ contours for Γ and cut-off energy for NGC 3718. The solid contour is the 1σ level and the dashed contour the 2σ level. In blue, the `Xillver` model and in red, the `XillverCp` model. `XillverCp` shows higher values of Γ (i.e., 1.88-1.92) than `Xillver`.

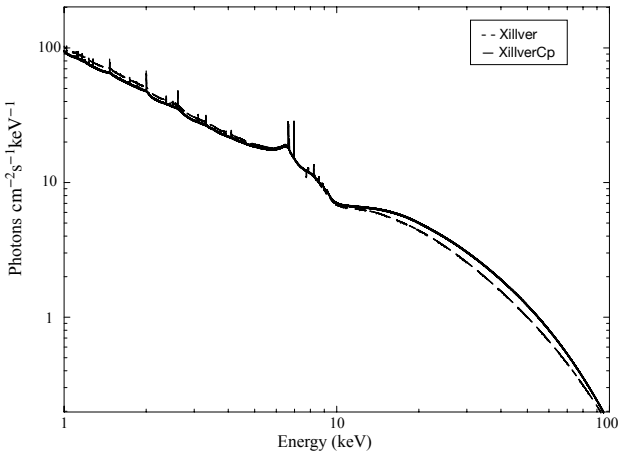

Figure 2.14: Comparison of the reflected spectra as calculated with `Xillver` (dashed line) and `XillverCp` (line), for an illumination with Γ =1.9, energy cut-off 100 keV, inclination 30 degrees and the ionization parameter of the disk $\log(\xi)$=3.5, similar to the best-fitting parameters for our data. Note that the small difference in the high energy slope causes the difference in best-fitting cut-off energy of the power-law, which is constrained to be below 160 keV in the case of `Xillver` and below 250 keV in the case of `XillverCp`.

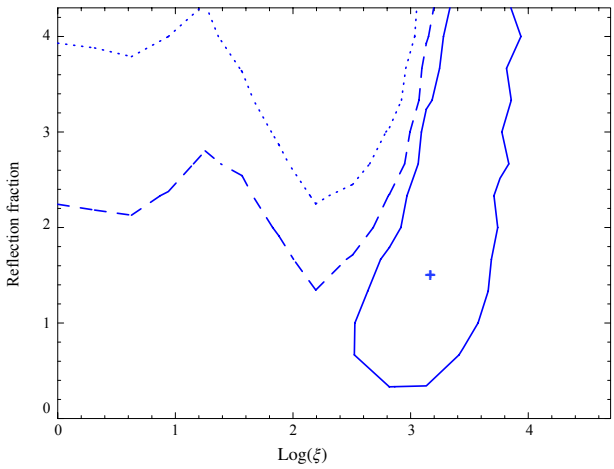

Figure 2.15: Two-dimensional $\Delta\chi^2$ contours for reflection fraction R_f and disk ionization $\log(\xi)$ calculated with `Xillver` model. The reflection fraction has as lower limit of $R_f > 0.3$ and the upper limit is unconstrained. For this high ionization region, the reflected spectrum is very similar to the incident spectrum, so the reflection fraction and overall normalization are degenerate.

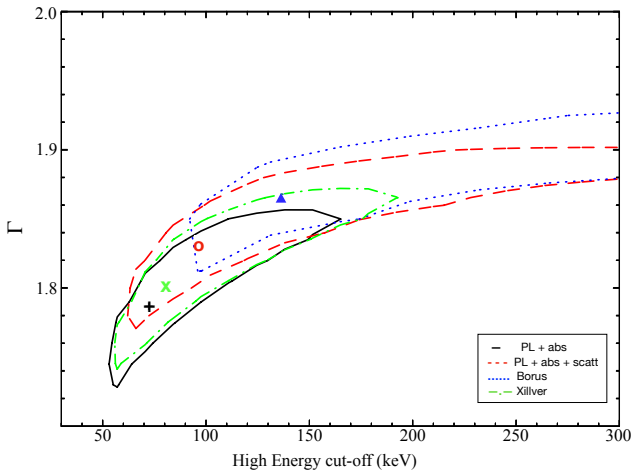

Figure 2.16: Two-dimensional $\Delta\chi^2$ contours for Γ and cut off energies for NGC 3718. The black line represent a power-law absorbed, in red the Power-law absorbed with an scattered component, in green `Xillver` reflection model and in blue `Borus` model. The simplest model shows a Γ (i.e., 1.72–1.85) with a low $E_{\rm cut}$. Adding the scattered component pushes these values slightly higher. Adding the reflection models yields the highest values in the case of torus-like reflector and lower values for a disk reflector.

uses the electron temperature of the Comptonizing plasma (kT_e), which is not directly comparable. The electron temperature produces an effective rollover in the Comptonized spectrum at 2 to 3 times higher energy (see, e.g., Petrucci et al., 2001). Therefore, in the contour plots in Figure 2.13 use different ranges for $E_{\rm cut}$ of `Xillver` (top panel) and the electron temperature of `XillverCp` (bottom panel), considering a conversion factor of 2.5 between them. With this caveat in mind, there is a good overall agreement between the two models in the best-fitting roll-over energies of the incident spectrum. Nevertheless, `Xillver` puts a lower upper-limit for Γ ($\sim$1.87) compared to `XillverCp` ($\sim$1.89) at the 1σ level and a lower lower-limit with $\sim$1.74 for `Xillver` and $\sim$1.85 for `XillverCp`.

To illustrate in more detail the difference in the spectral shape of the ionized reflector to the spectrum, we show in Figure 2.14 reflection-only models ($R_f = -1$) with one particular value of the Γ (1.9), $E_{\rm cut}$= 100 keV for `Xillver` and $kT_e = 40$ keV for `XillverCp` and inclination of 30 degrees. In this case we fix the ionization parameter to 3.5, similar to the best fitting parameter to our data. The spectral shape is very similar between them; the main difference lies in the high energy tails due to the different shapes of the primary continuum. This small difference in the high energy spectrum can account for the different constraints we found for `Xillver` and `XillverCp`, for

$E_{\rm cut}$ and Γ. The other feature highlighted by this plot is the strong contribution from Compton scattering by the disk, which adds a power-law component to the reflected spectrum. This highly-ionized disk, therefore, can be consistent with the low amplitude of the reflection features in our data, even if the reflection fraction is high, i.e., without requiring a truncated disk. We further check whether the degeneracy between ionization parameters and reflection fraction can be constrained. Figure 2.15 shows the best fit and contours of allowed parameter values for the reflection fraction R_f and $\log \xi$. The 1σ contours are restricted to a solution with ionization between 2.5-3.5 with the best value at $\log \xi \sim 3.2$ (the case of a highly ionized accretion disk) and reflection fraction R_f= 1.6, i.e., more than a half of the sky would be covered by the reflector. Therefore, the fit with `Xillver` explains the small reflection features better as an ionized reflector than as a truncated disk. The reflection fraction has a lower limit of $R_{\rm f} = 0.3$ and the upper limit is unconstrained. For this high ionization region, the reflected spectrum is very similar to the incident spectrum, so the reflection fraction and overall normalization are degenerate.

Comparison between models

Our modelling shows two possible configurations to explain the low-amplitude reflection features: a Compton thin reflector covering a high fraction of the sky or a highly ionized accretion disk. From a statistical point of view, these four reflection models, `MYTorus`, `Borus02`, `Xillver` and `XillverCp`, are indistinguishable, with only very small differences in the goodness of the fit. From the ratio plots, it appears that the four models perform equally well in describing the data. Note that there is a general excellent agreement between the values for the column density of the nuclear absorber between the models.

In Table 2.3 we report the best-fit $N_{{\rm H},H}$, Γ and $E_{\rm cut}$ values for our source using the `MYTorus`, `Borus02`, `Xillver` and `XillverCp` models, while in Figure 2.16 we show the 1σ confidence area of the parameter space of the primary emission obtained using the different reflection models. We found a variation of the best-fitting Γ of 0.08 depending on the model. If we use the simple model (an absorbed power-law) we get the lowest value of Γ and $E_{\rm cut}$ (i.e., $\sim$ 76 keV). In case of a power-law with an additional scattered component in the soft band, the values of Γ and $E_{\rm cut}$ increase and show broader extension in the parameter space, indeed, the contour plot at the 1σ level is open for $E_{\rm cut}$. With the inclusion of a disk or torus reflector, we find that the torus reflection model (we plot only the `Borus` model for visualization purposes) shows higher values

in Γ and $E_{\rm cut}$, with only a lower limit for $E_{\rm cut}$. The ionized reflection model (`Xillver`) shows lower values for $E_{\rm cut}$ and Γ. They differ, however, in the best-fitting $E_{\rm cut}$ (81 keV for `Xillver`, 150 keV for torus reflectors and 30 kT_e equivalent to a roll-over energy of $\sim$ 75keV for `XillverCp`) and the allowed range is constrained to be below 200 keV by `Xillver` while it is unconstrained for all the other reflection models.

According to our results, χ^2 decreases (with $\Delta\chi^2$/d.o.f.=0.02) and the coronal parameters (i.e., Γ and $E_{\rm cut}$) decrease when the reflection component is associated to a disk or increase in the case of a torus. From the statistics point of view, the reflection component is not required because it is not statistically significant. However, there must be material around the accreting black hole that will produce the weak reflection observed in this galaxy, such as the accretion flow itself and a small BLR (Cazzoli et al., 2018). We show that if we do not consider it in the model, the values we obtain from the power-law parameters are overly constrained. For this reason, it is crucial to include a reflection component in the X-ray spectral modeling to estimate accurately the parameters of the primary emission.

Comparison with previous results

We calculate the intrinsic luminosity to compare with the luminosity measured 12 years earlier with *XMM-Newton*. We found a luminosity 8% lower compared with that previously found by Hernández-García et al. (2014) fitting two absorbed power-laws and 33% lower compared with Younes et al. (2011) using an absorbed power-law. Also, we compare the values obtained by these authors for the Γ, $N_{{\rm H},S}$ and $N_{{\rm H},H}$. Younes et al. (2011) fitted an absorbed power-law model to the X-ray spectrum below 10 keV. They found a Γ=1.7±0.1, highly consistent with the one obtained in case of a simple power-law (model in black in Figure 2.16), but low compared to the fits including reflection components. Hernández-García et al. (2014) estimated Γ by fitting a two power-law model with different absorbing column densities and found $\Gamma=1.79^{+0.13}_{-0.08}$. Their result is consistent with ours when fitting a simple power-law. Furthermore, they found consistent values of the hydrogen column density for the nuclear component. In either case, the inconsistency between the parameters previously obtained and our results can be attributed to the use of simpler models over a smaller energy range than the analysis presented here. We recall that this is the first time that high quality data at energies above 10 keV are presented for this source, allowing better constraints on the spectral parameters, including reflection.

Likewise, Ricci et al. (2017a) using broad-band X-ray spectroscopy (0.3–150 keV)

Table 2.3: Final compilation of the best-fit models for NGC 3718 with *XMM-Newton-NuSTAR-Swift*/BAT data.

Parameter	`Power-law`	`Power-law+scatt`	`Pexmon`	`Borus`	`MYTorus`	`Xillver`	`XillverCp`
(1)	(2)	(3)	(4)	(5)	(6)	(7)	(8)
Γ	1.79 ± 0.08	$1.83^{+0.08}_{-0.04}$	1.84 ± 0.08	$1.87^{+0.07}_{-0.08}$	$1.88^{+0.06}_{-0.10}$	1.82 ± 0.02	1.87 ± 0.02
$E_{\rm cut}/kT_e$ (keV)	76^{+95}_{-22}	97^{+97}_{-48}	83^{+86}_{-38}	147^{+147}_{-83}	150^{+150}_{-107}	81^{+137}_{-31}	30^{+43}_{-12}
$N_{{\rm H},H}$ (10^{22} cm^{-2})	$0.89^{+0.07}_{-0.06}$	1.02 ± 0.08	1.03 ± 0.08	$1.04^{+0.08}_{-0.09}$	$1.05^{+0.06}_{-0.10}$	0.98 ± 0.04	1.02 ± 0.04
$C_{\rm A/B}$	0.99 ± 0.03	0.99 ± 0.03	0.99 ± 0.03	0.99 ± 0.03	0.99 ± 0.03	1.00 ± 0.03	1.00 ± 0.03
C_{XMM}	0.97 ± 0.05	$0.98^{+0.04}_{-0.05}$	$0.98^{+0.04}_{-0.05}$	$0.98^{+0.04}_{-0.03}$	$0.98^{+0.05}_{-0.04}$	$0.97^{+0.03}_{-0.02}$	$0.98^{+0.03}_{-0.06}$
C_{BAT}	$4.7^{+1.0}_{-0.9}$	4.6 ± 0.9	$4.6^{+0.5}_{-0.9}$	4.5 ± 0.9	4.5 ± 0.9	$4.5^{+1.0}_{-0.9}$	$4.4^{+1.0}_{-0.9}$
$F^{\rm obs}_{2.0-10.0\ {\rm keV}}$ (10^{-12} erg cm^{-2} s^{-1})	$1.39^{+0.03}_{-0.11}$	$1.41^{+0.02}_{-0.14}$	$1.40^{+0.01}_{-0.60}$	$1.41^{+0.01}_{-0.25}$	$1.41^{+0.01}_{-0.16}$	$1.40^{+0.05}_{-0.24}$	$1.39^{+0.09}_{-0.15}$
$F^{\rm int}_{2.0-10.0\ {\rm keV}}$ (10^{-12} erg cm^{-2} s^{-1})	$1.52^{+0.05}_{-0.14}$	$1.54^{+0.30}_{-0.32}$	$1.54^{+0.26}_{-0.45}$	1.55 ± 0.47	$1.54^{+0.62}_{-0.70}$	$1.53^{+0.70}_{-0.13}$	$1.52^{+0.53}_{-0.35}$
$\log(L^{\rm int}_{2.0-10.0\ {\rm keV}})$	$40.57^{+0.01}_{-0.03}$	$40.57^{+0.08}_{-0.10}$	$40.57^{+0.07}_{-0.29}$	$40.57^{+0.17}_{-0.26}$	$40.57^{+0.16}_{-0.26}$	$40.57^{+0.60}_{-0.27}$	$40.57^{+0.81}_{-0.35}$
$F^{\rm obs}_{2.0-70.0\ {\rm keV}}$ (10^{-12} erg cm^{-2} s^{-1})	$3.38^{+0.10}_{-0.07}$	$3.42^{+0.07}_{-0.15}$	$3.40^{+0.03}_{-0.04}$	$3.47^{+0.01}_{-0.14}$	$3.46^{+0.16}_{-0.01}$	$3.46^{+0.08}_{-0.28}$	$3.44^{+0.17}_{-0.22}$
$F^{\rm int}_{2.0-70.0\ {\rm keV}}$ (10^{-12} erg cm^{-2} s^{-1})	3.51 ± 0.05	3.57 ± 0.05	$3.55^{+0.06}_{-0.20}$	3.62 ± 0.80	3.61 ± 0.82	$3.60^{+0.63}_{-0.22}$	$3.68^{+0.35}_{-0.16}$
$\log(L^{\rm int}_{2.0-70.0\ {\rm keV}})$	$40.93^{+0.06}_{-0.07}$	40.93 ± 0.06	$40.93^{+0.17}_{-0.28}$	$40.94^{+0.09}_{-0.11}$	$40.94^{+0.12}_{-0.11}$	$40.94^{+0.58}_{-0.26}$	$40.94^{+0.60}_{-0.25}$
χ^2/d.o.f	418.96/367	409.93/366	408.98/365	405.56/364	406.58/364	409.59/363	407.21/363
χ^2_ν	1.142	1.120	1.121	1.114	1.117	1.128	1.122

combining *XMM-Newton*, *Swift*/XRT, *ASCA*, *Chandra*, and *Suzaku* observations with *Swift*/BAT data and found a value of Γ consistent with our results for the absorbed power-law model. They were not able to constrain $E_{\rm cut}$ from those data.

Finally, Ricci et al. (2018) found from *Swift*/BAT spectra in the 14–195 keV energy range of a large sample of AGN that $E_{\rm cut}$ is inversely proportional to the Eddington ratio: sources with Eddington ratio $\lambda_{\rm Edd} < 0.1$ tend to have $E_{\rm cut}$ of about 370 keV, while ones with $\lambda_{\rm Edd} > 0.1$ possess lower cut-off energies, with $E_{\rm cut}$ ∼160 keV. In the case of NGC 3718 the value of this parameter obtained in all models represents an outlier in this correlation (according to the low Eddington ratio of NGC 3718) but a high value of the cut-off energy is still consistent within 1σ level with all reflection models except `Xillver`.

2.4 Discussion

In this chapter we report for the first time the analysis of the broad-band, 0.5–110 keV, emission from the low-luminosity AGN (LLAGN) NGC 3718, observed simultaneously with *NuSTAR*, *XMM-Newton*, together with archival *Swift*/BAT data. In the following, we discuss the main results of this chapter.

2.4.1 Variability

The *NuSTAR* observations were taken over 10 days for stretches of 25–90 ks, totalling 230 ks. This allowed us to look for variability on day timescales. We do not detect variability, with an upper limit of $\sigma^2_{NXS} < 0.08$. This result conforms to the typical behaviour that most LLAGN do not show variability on day timescales, even in the X-ray range (Binder et al., 2009; Younes et al., 2011; Young et al., 2018). According to McHardy et al. (2006), who used a small sample of AGN for the study, the characteristic variability timescale of AGN is related to the black hole mass and accretion rate. This relation was also explored by González-Martín & Vaughan (2012) using 104 AGN and later updated by González-Martín (2018) taking into account absorption effects. Using the mass of NGC 3718 ($\log(M_{BH})$=7.85 given by Hernández-García et al. 2014 and its accretion rate in terms of the Eddington rate ($\lambda_{Edd} \sim 1.1 \times 10^{-5}$) the largest amplitude variations are expected on timescales of several years using the variability plane reported by these authors. The analysis of other X-ray data sets have shown variations on timescales of years for NGC 3718 (Hernández-García et al., 2014),

in agreement with the expectation from the variability plane in McHardy et al. (2006).

was observed once with *Chandra* in 2003 and twice with *XMM-Newton* in 2004. Younes et al. (2011) and Hernández-García et al. (2014) studied these data and reported a variable flux in the 2–10 keV energy band by 55% and 35%, respectively, on a timescale of one year. They studied also short-term variability from the analysis of the light curves and found no changes on day timescales. This is in agreement with our analysis, where variations on a timescale of ten days were not detected. The variations found by Younes et al. (2011) and Hernández-García et al. (2014), however, can explain the differences in normalization between the *NuSTAR* and *Swift*/BAT data, since the *Swift*/BAT spectrum is the median of data taken over 70 months between December 2004 and September 2010, whereas the *NuSTAR* data were taken outside this period and several years later, in 2017.

2.4.2 Reflection

An important feature in the spectra of AGN is the reflection that imprints its mark at X-ray energies. The shape of this reflection component is usually characterized by the FeKα emission line and the Compton hump peaking at $\sim$ 30 keV (Pounds et al., 1990; Nandra & Pounds, 1994a). As can be seen in Figure 2, the spectrum of NGC 3718 shows a weak FeKα line and Compton hump, suggesting a low reflection fraction, as was confirmed with the `pexmon` reflection model obtaining R_f <0.67, with the best fitting value in $R_f \sim 0.3$ (30%) and a R_f=0 contained within the 1-σ contours for E_{cut} between 100 and 250 keV. This is in agreement with other studies of LINERs where the reflection fraction is small (Younes et al. 2019 and Osorio-Clavijo et al. 2019, with 5% and 10% respectively). Furthermore, the physical structure causing the reflected spectrum is under debate and different possibilities have been proposed to explain its origin. On the one hand, distant absorbing material such as the torus or clouds in the BLR have been proposed as responsible for the observed reflected emission (Brightman & Nandra, 2011a), or even gas in the host galaxy further away from the nucleus and unrelated to the AGN (Arévalo et al., 2014; Bauer et al., 2015), while other authors have argued in favour of the accretion disk as responsible for the reflection (Fabian, 2006). In fact, the most plausible scenario is that reflection originates from a combination of all three structures.

In the case of NGC 3718, we find that the reflection is weak ($R_f < 0.67$ at 1σ, $R_f < 0.88$ at 2σ level) but with a best-fitting value of $R_f = 0.3$, showing that the

inclusion of reflection provides a better description of the data although, possibly due to the limited counts, the improvement is not statistically significant. The presence of a weak iron line and $R_f = 0.3$ is consistent with the fact that the accreting black hole cannot be completely isolated, there must be material around it producing some reflection. Consequently, this component should not be ignored, since leaving it out of the model could lead to overly constrained values in the coronal parameters. In an effort to characterize the properties of the reflector in the LLAGN NGC 3718, we have used different X-ray reflection models. All of the models provide equally good fits to the data, but it is worth noting the differences among the reflection component in order to determine the parameters of the power-law (Γ and $E_{\rm cut}$) as well as their physical implications.

In the case of we detect an absorbing column density of $N_{{\rm H},S} \sim 10^{21}$ cm^{-2} on the soft X-ray emission, which we ascribe to a physically extended component, while the nuclear power-law component is under a column density of $N_{{\rm H},H} \sim 10^{22}$ cm^{-2}. has a prominent dust lane which runs across the entire stellar bulge, and a warped molecular and atomic gas disk, with column density between $\sim 10^{19-20}$ cm^{-2} (Krips et al., 2005; Sparke et al., 2009). The average column density of this gaseous disk, however, is too low to explain the obscuration, accounting for at most 10% of the value measured in the soft X-ray spectrum, and up to 1% of the column density detected on the nuclear component. From this comparison we can conclude that the absorption we detect is likely related to the active nuclear structure, such as the BLR, the torus, or the narrow line region (NLR).

On the assumption that all the reflection is produced by distant clouds like the torus, we found that a reflector modelled with either `MYTorus` or `Borus02` should be Compton thin and potentially cover a large fraction of the sky although smaller covering fractions (down to 0.2) are also possible within 1σ of confidence level. A relation between the covering factor of Compton thin material and the accretion rate was previously reported by Ricci et al. (2017b). They show that accreting black holes with $\lambda_{\rm Edd}$=10^{-5} (the case of NGC 3718) have Compton thin obscurers with covering factors between 0.2-0.6, consistent with our results (see the contour plot in Figure 2.7).

A disk-wind scenario was proposed as an explanation for the torus evolution in LLAGN by Elitzur & Shlosman (2006). This approach establishes that the accretion disk emits vertical winds. For the region inside the dust sublimation radius (R_d), the gas has no dust, is ionized and forms the BLR, while the wind outside R_d has dust and forms the torus. According with this model, in sources with low accretion rates and

low luminosity, the radial column density of the wind is too low ($N_H < 10^{22}$ cm^{-2}) to produce detectable emission lines, so the BLR disappears. As the torus is generated by the same mechanism, it would also have a lower column density for lower luminosity, and accretion rate objects.

Later, Elitzur & Ho (2009) constructed the distribution of Eddington ratio vs black hole masses and vs bolometric luminosity for objects separated by spectral classification. They used a sample of AGN from the Palomar spectroscopic survey (Ho et al., 1997) with measurements of black hole mass and X-ray luminosity (2–10 keV) available in the literature. They show that under a division (corresponding to the theoretical prediction of the disk-wind scenario) in accretion rate and luminosity there are only type 2 objects (Figure 1 in their work) supporting the disappearance of the BLR below the threshold. Also, with these data they estimated the missing constant in their theoretical model to set the limit from where the BLR is observable. According to its accretion rate and luminosity, NGC 3718 falls above the threshold. The BLR and torus, with low column density, are therefore expected, since it is in the region where both AGN types, 1 and 2, are observed. According to the disk wind scenario, should therefore also have a torus, although possibly of low column density. This galaxy is optically classified as a LINER 1.9 (Ho et al., 1997), which means by definition that only the broad Hα is detectable (Osterbrock, 1989). The broad Hα component in general can either arise from the BLR or from an outflow but Cazzoli et al. (2018) showed that in the broad line is from the BLR. Our observation of the gas column density of the reflector in the X-ray spectrum is $N_H \sim 6 \times 10^{22}$ cm^{-2}. This value shows that the total amount of gas around the AGN in , combining the BLR and torus, is close to the threshold column density where the BLR is no longer observable (Netzer, 1990). Therefore the weakness of the optical broad emission lines and of the reflection features together point to a small amount of total gas in the vicinity of the black hole, whether dusty or not.

The disappearance of the dusty torus (e.g., the dusty section of the wind in the disk wind model) at low luminosity is also demonstrated through the evolution of the dust *emission* in the IR. González-Martín et al. (2017), using mid-infrared (MIR) spectra from *Spitzer*/IRS of AGN with bolometric luminosities ranging over more than six orders of magnitude, separated the torus emission from other components in the spectra. They reported a gradual reduction in the contribution of the torus with luminosity, with no presence of the torus below $\log[L_{\rm Bol}\ ({\rm erg\ s^{-1}})] < 41$. For $\log[L_{\rm Bol}\ ({\rm erg\ s^{-1}})] > 43$, they found that the torus contribution to the bolometric luminosity has to be larger

than 40%, while for $\log[L_{\rm Bol}\ ({\rm erg\ s^{-1}})] < 42$ the contribution is less than 20%. This result is also compatible with the Elitzur & Shlosman (2006) model, which indicates less material in the wind for lower luminosities and accretion rates. According to the luminosity of NGC 3718, it should fall in the second category of the González-Martín et al. (2017) work, i.e., showing the presence of absorbing material around the SMBH (the BLR or the torus) with a different configuration compared to more powerful AGN, although a MIR spectrum of this galaxy is not available.

On the other hand, if the reflected spectrum is dominated by emission from the accretion disk, our data shows that it has to be highly ionized. Key features observed in more powerful AGN are the broad FeKα emission line that can be related to reflection from the accretion disk (Fabian et al., 2009; Brenneman et al., 2011; Ricci et al., 2014) or a correlation between the ionization parameter with the Eddington ratio (Ballantyne et al., 2011; Keek & Ballantyne, 2016). However, similar studies have not been possible for LINERs given the weakness of the FeKα emission line, as the case for NGC 3718. Moreover, X-ray reflection models of highly ionized disks have not been performed for other LINERs, preventing us from any comparison with other works. It is worth noting that the geometry of the inner parts of LINERs might differ from more powerful AGN, implying, for instance, that the disk could be truncated (Gu & Cao 2009; Younes et al. 2011; Hernández-García et al. 2013, 2016; She et al. 2018), although our fits with both `Xillver` and `XillverCp` prefer an ionized disk to a truncated one to explain the small amplitude of the reflection features (see Figure2.15).

Therefore, we propose that has a torus/BLR that contributes at least partially to the reflection spectrum, whereas our study prevents us from confirming the presence of reflection off the accretion disk.

2.4.3 Accretion mechanism

The coronal emission of NGC 3718 is fitted by an absorbed power-law with $\Gamma \sim 1.8$ and $N_{{\rm H},H} \sim 10^{22}$ cm^{-2}. This Γ is consistent with typical measurements for AGN, suggesting the same physical origin for the X-ray emission (Brightman & Nandra, 2011a).

Spectral differences between high and low-luminosity AGN may arise from their accretion mechanism. While the standard accretion disk explains well the powering of highly accreting AGN (Shakura & Sunyaev, 1973), it has been suggested that for LLAGN the emission mechanism becomes inefficient and the X-ray emission origi-

nates in ADAFs (Gu & Cao, 2009; Younes et al., 2011; Hernández-García et al., 2013, 2016; She et al., 2018) similar to that in X-ray binaries (XRBs) in their low/hard state (Ma et al., 2007; Ueda et al., 2010; Xu, 2011). AGN are thought to be scaled up versions of Galactic black hole X-ray binaries. The study of the accretion mechanism in XRBs and AGN has been approached by relating Γ to the Eddington ratio ($\lambda_{\rm Edd} = L_{\rm Bol}/L_{\rm Edd}$). This relation shows a positive trend (soft state in XRBs) for high luminosity sources above a threshold value of $\lambda_{\rm Edd}$ and negative trend (low state for XRBs) below this threshold (Gu & Cao, 2009). However, in the case of LLAGN, which fall in the anti-correlation section of this relation, it shows a high dispersion that is still not understood — it could be due to the sensitivity of the measurements or to intrinsic diversity of the nuclei. Estimating Γ using high-quality X-ray data and studying how sensitive Γ is to the reflection model used in the fit is an important step to constrain the origin of the scatter in this relation.

Our best-fitting Γ for NGC 3718, including the reflection component, falls on the mean value of the correlation Γ vs $\lambda_{\rm Edd}$ given by Gu & Cao (2009), Younes et al. (2011), and She et al. (2018). The coincidence between the measured and expected values of Γ suggests that high quality X-ray spectra, together with modelling including the reflection component, can reduce the large scatter seen in this correlation.

Furthermore, we can study the position of in the fundamental dichotomy between the local radio AGN population (see Best & Heckman 2012). This plane proposes that according to the optical spectra, AGN can be classified as quasar mode/HERG (high-excitation) where the material is accreted onto the black hole through a radiatively-efficient, optically-thick, geometrically thin accretion disk (e.g., Shakura & Sunyaev 1973) or radio mode/LERG (low-excitation) dominated by ADAFs. The excitation level of the emission line region is expected to be defined by the hardness of the UV spectrum from the central source, therefore, a thin disk reaching the innermost orbit would produce a hard ionizing UV continuum and more high excitation lines, while a truncated disk, replaced in the innermost regions by an ADAF, would produce a low-excitation spectrum. The excitation index (EI) defined by Buttiglione et al. (2010) is used by Best & Heckman (2012) to separate low from high-excitation sources, with a threshold at EI=0.95. The optical spectrum of characterized by Moustakas & Kennicutt (2006) results in EI=0.89, in the low-excitation region but very close to the high-excitation threshold. The equivalent width of [OIII] is alternatively used as an excitation quantifier and Best & Heckman (2012) propose 5Å as the threshold value. With this criterion also falls in the low-excitation region but at the high excitation end

of LERGs, with an [OIII] EW=2.6Å (Moustakas & Kennicutt, 2006). Based on these criteria, NGC 3718 can be classified as a low excitation galaxy that is in favor of an ADAF instead of accretion via a geometrically thin disk, although it is close to the limit between low and high-excitation sources.

2.4.4 Source of X-ray emission

The source of X-ray emission is generally unresolved in LLAGN and its origin is under debate: it might be the ADAF itself or it might be synchrotron emission from a jet.

The jet origin is supported by the fact that low-luminosity objects tend to be radio loud, as noted by Ho (2002), who shows that radio loudness anti-correlates strongly with $\lambda_{\rm Edd}$. According with this relation, the accretion rate in NGC 3718 should result in a radio loud classification. Moreover, was observed with VLBA (Nagar et al., 2005) and MERLIN (Krips et al., 2007; Markakis et al., 2015) and they reported extended emission at 18 cm with signs of a compact (0.5or 34 pc) radio jet detected at 4σ significance which is weakly present at 6 cm as well. Therefore we need to take into account the possibility that this jet emits X-rays.

Our next step is thus to study the jet dominance in this galaxy. Younes et al. (2012) classified a sample of LINER 1s into radio-loud or radio quiet classes according to the radio loudness parameter (R_x=νL_ν(5 GHz)$/L_{2-10\rm keV}$, Terashima & Wilson 2003) which compares the radio to X-ray fluxes. In agreement with this quantity, a LLAGN can be classified as radio-loud if $\log(R_x)$ >-4.5. For NGC 3718, Younes et al. 2012 found $\log(R_x)$=-3.81, classifying this galaxy as a radio-loud. Using the X-ray luminosity from Younes et al. (2011), Hernández-García et al. (2014) and our results, we calculate slightly different values of R_x, but consistent with a radio loud classification. Panessa et al. (2007), however, challenged this simple criterion to judge radio loudness. These authors studied the Seyferts in the Palomar sample (Ho et al., 1997), which they assumed as radio-quiet, and compared to low-luminosity radio galaxies, i.e., radio-loud, and reported that for low-luminosity AGN the limit for radio-loud should be larger. They showed that a better threshold is $\log(R_x)$ ∼-2.8, placing in the radio-quiet regime. Furthermore, Maoz (2007) compared the radio-to-UV fluxes of a sample of AGN covering a wide range in luminosity and found that $R_{UV} = L_\nu$(5 GHz)$/L_\nu$ (2500Å) increases with decreasing luminosity for both radio loud and radio quiet populations, so a more natural threshold should be a function of UV luminosity. Taking the values of R_{UV} and L_ν(2500 Å) from Li & Xie (2017), falls in the region

between radio-loud and radio-quiet, for its UV luminosity, in the R_{UV} vs L_{UV} plane of Maoz (2007). In agreement with this result, Younes et al. (2012) present the SED of NGC 3718 and compared it with the Elvis et al. (1994) average SEDs from a sample of radio-loud and radio-quiet AGN, finding that the radio emission of falls exactly in the middle of both models. Taking all the information together, the radio loudness for remains unclear. Nevertheless, it is worth remarking that under the criteria that take into account luminosity, and also by the shape of the SED, the radio loudness of is at most borderline, so it is unlikely that the radio jet emission would dominate the X-ray spectrum.

The best way to know if the radio jet dominates in the X-rays would be to confirm or reject the spectral curvature in the nuclear emission, since the ADAF model predicts a curvature while the synchrotron jet emission would be a pure power-law. Our data, however, do not allow us to confirm or rule out this feature; depending on the reflection model used, a cutoff in the nuclear power-law is required or not. A detailed physical modelling of a more complete SED will hopefully reveal the dominance of one of these physical mechanisms in this LLAGN.

2.5 Summary

Through simultaneous *NuSTAR* + *XMM–Newton* plus archival *Swift*/BAT observations, we performed a variability and spectral analysis of the LLAGN NGC 3718. The summary of our main results are reported in the following:

- We do not detect any significant variability in the nucleus of NGC 3718 within the *NuSTAR* observations, on a timescale of 10 days.
- The NGC 3718 obscuration corrected flux in the 2–10 keV energy band is 8% lower than the value previously reported by Hernández-García et al. (2014) and 33% lower than the value reported by Younes et al. (2011) using *XMM–Newton* data from 12 years ago.
- The X-ray spectrum shows a small Fe Kα line, indicative of a reflection component. A simple fit including neutral reflection with `pexmon` indicates $R_f < 0.67$ with the best-fitting reflection fraction R_f=0.3, although a R_f=0 is also allowed within the $1-\sigma$ contours. Even though the reflection is weak it should not be ignored as this could lead to a misinterpretation of the coronal parameters as explained in Sec.2.4.

- The type of reflector affects the measurement of the power-law parameters. Both the Γ and the cut-off energy are marginally lower for a disk reflector than for a torus. While one of the disk reflectors results in a low and bounded cut-off energy, the torus reflectors produce a best fitting cut-off energy above the observed energy range and unconstrained to higher values. Therefore we cannot confirm or rule out curvature in the continuum in this spectral range.

- We cannot differentiate between the four reflection models fitted to the data, but these fits allow us to put constraints on each physical scenario. Reflection dominated by a smooth, neutral torus, as modelled be `MYTorus` or `Borus02` should be Compton thin and preferentially cover a large fraction of the sky, although covering fractions as low as 0.1 are still allowed by the data at 1 σ level. In the case of an ionized disk dominating the reflected spectrum, as modelled by `Relxill`, a highly ionized disk is required.

- The column density obtained for a neutral reflector, compatible with the small features seen in the X-ray spectrum, is $N_{\rm H} \sim 6 \times 10^{22}{\rm cm}^{-2}$. This is similar to the column density observed in absorption $N_{{\rm H},H} \sim 10^{22}{\rm cm}^{-2}$ and of the same order of magnitude of the limiting column density for an observable BLR.

- Our results show the importance of including the reflection when analyzing the accretion mechanism in LLAGN and to understand degeneracies with the intrinsic power-law parameters.

The application of the methodology explained here will be subject of the forthcoming chapter using a sample of AGN covering a large range in $\lambda_{\rm Edd}$ to estimate the intrinsic Γ and $E_{\rm cut}$ with high accuracy in order to study the accretion mechanism in LLAGN, as well as the physical origin of the reflected spectrum.

CHAPTER 3

Application of the methodology to a sample of a LLAGN from the BASS/DR2

The work in this chapter has been submitted for publication in Astronomy and Astrophysics

The subsequent chapter will address several outstanding issues in studies of AGN and the reflection. In the following we will apply the same methodology previously explained in Section 2 t a sample of 17 LLAGN. Our purpose is to constrain the geometry and column density of potential reflectors in a sample of LLAGN covering a broad range of energy combining data from *XMM-Newton+ NuSTAR + Swift* and investigate the accretion mechanism in LLAGN.

3.1 Introduction

Obscuration gives evidence of material in the line of sight, which could be associated with the torus. Gas that is not in the line of sight of the observer can also imprint some features on the X-ray spectrum. Between 10 keV and up to hundreds of keV there

is a reflection hump created by X-rays being reflected at the accretion disk or more distant material, like the torus. Furthermore, the strongest emission line seen in the X-rays, the Fe Kα emission line (e.g., Fabian 2006), can be related with circumnuclear material, being broad and exhibiting relativistic effects due to its creation close to the SBMH, and narrow, presumably originating from more distant material. The reflection features are therefore a useful tool to study the configuration of the accretion disk as well the torus. To better understand the properties of the reflector, many models have been developed, like `BORUS` (Baloković et al., 2018) where the reprocessing medium is assumed to be a sphere with conical cut off at both poles, approximating a torus with variable covering factor, `cTORUS` (Liu & Li, 2014), similat to `BORUS` but clumpy and with no Compton shoulder, `MYTORUS` (Murphy & Yaqoob, 2009) that proposes a toroidal geometry where the covering fraction is fixed to 0.5, or `RELXILL` (García et al., 2013) that calculates the reflected spectrum from the surface of an X-ray illuminated, ionized accretion disk by solving the equations of radiative transfer, energy balance, and ionization equilibrium in a Compton-thick and plane parallel medium.

It is not clear how the reflecting structure is formed but clues can be gathered from the relation between reflection strength and the nuclear accretion rate. From the observational point of view, the torus in the infrared (IR) becomes weaker in the low luminosity regime (i.e., low accretion rates - below 10^{-3}, González-Martín et al. 2017). Furthermore, in the X-rays, it has been seen that the Compton thin absorption (N_H $<$1.5x10^{24} cm^{-2}) is less frequent in objects with low accretion rates: the fraction of Compton-thin obscured sources (10^{22} $<N_H$ $<10^{24}$ cm^{-2}) decreases in the low luminosity regime (Ricci et al., 2017b), while the fraction of Compton thick sources apparently remains constant. Both Compton thick and thin absorbers can produce reflection features, with different shapes and strengths. In this chapter we attempt to measure the global distribution of gas around the nucleus, whether in the line of sight or not, through their contribution to the reflection. In particular, we aim at establishing whether the changes in the gas configuration become flatter or overall optically thinner as the accretion rate goes down.

Additionally, by modelling the X-ray reflection we are able to study the continuum emission, estimating the coronal parameters: Γ and E_{cut}. It has been shown that the slope of the power law depends on the accretion rate with changes at intermediate accretion rates (L_{Bol}/L_{Edd}=λ_{Edd} $\sim10^{-3}$), pointing to a change in the accretion mechanism, for example between a corona on a thin disk to an advection dominated accretion flow (ADAF, Narayan et al., 1994). The relationship toward low accretion

rates is usually seen with a lot of scatter, which can be intrinsic or due to observational uncertainties (Shemmer et al., 2006; Gu & Cao, 2009; Younes et al., 2011; Yang et al., 2015a; She et al., 2018). Our second objective is to re-evaluate this relationship in the low accretion rate range, through a detailed modelling of the reflection and broadband X-ray data, using observations from XMM-Newton-*Newton*+*NuSTAR*+*Swift*).

This paper is organized as follows: in Sect. 3.2 we present details of the observations and sample. The data reduction is reported in Sect. 3.3. The methodology followed during this chapter is shown in Sect. 3.4. All the results are reported in Sect. 3.5. The implications of our X-ray spectral analysis are discussed in Sect. 3.6. Finally, a summary of our findings is presented in Sect. 3.7.

3.2 Sample and data

A hard X-ray (E$\geq$10 keV) selection of AGN is less affected by the obscuring material and allows us to obtain the least biased X-ray sample.

Our work focuses on LLAGN selected through their hard-band X-ray emission as identified in the *Swift*/BAT 70-month catalogue (Baumgartner et al., 2013) on board the Neil Gehrels Swift Observatory (Gehrels et al., 2004). BAT operates in the 14–195 keV energy band. The BAT AGN Spectroscopic Survey (BASS) is a survey which provides high-quality multi-wavelength data for the BAT AGN, including black hole mass measurements (Koss et al., 2017) and X-ray spectroscopy modelling (Ricci et al., 2017a). The first data release (DR1) of the BASS project (Koss et al., 2017) includes 642 of Swift/BAT AGN and a second release of optical spectroscopy (BASS/DR2) will also soon be publicly available (Koss et al., in prep; Oh et al., in prep).

Our sample of galaxies were selected from the BASS/DR2 with accretion rates $\log(\lambda_{Edd}) \leq$-3.0 obtaining in total a sample of 24 AGN. We used the HEASARC[1] archive to search simultaneous and not simultaneous observations with *NuSTAR* and *XMM-Newton* data with publicly available data until August 2020. This analysis provided data with both telescopes for 16 sources. We include the proprietary data of the galaxy NGC 5033 (PI: Diaz Y.; $\log(\lambda_{\rm Edd}) =$-4.0), an AGN also contained in the BASS/DR2.

Our final sample of LLAGNs contains 17 objects, 11 of which are classified as Seyfert 2 (i.e. only narrow lines are visible in the optical spectrum) and six classified as Seyfert 1.9 (a broad component is visible in Hα but not in Hβ) in the BASS/DR2. Table

[1]http://heasarc.gsfc.nasa.gov/

C.17 shows the general properties of our sample. Notes for the individual galaxy are in the Appendix B and Table C.1 shows the log of the observations.

3.3 Data Reduction

Data reduction was performed following the methodology explained in this section. Details on the observations can be found in Table C.1.

3.3.1 XMM-Newton-Newton data

We processed the Observation Data Files (ODFs) from the European Photon Imaging Camera (EPIC) PN detector using the Science Analysis System (SAS version 17.0.0). We followed standard procedures to obtain calibrated and concatenated event lists, filter them for periods of high background flaring activity and extract light curves and spectra. Source events were extracted using a circular region of 49 arcsec centred on the target, and background events were extracted from a circular region of 98 arcsec on the same chip far from the source. We verified the photon pile-up is negligible in the filtered event list with the *XMM-Newton*SAS task EPATPLOT. We generated response matrix files (RMFs) and ancillary response files (ARFs) and rebinned the spectra in order to include a minimum of 25 counts in each background-subtracted spectral channel and to not oversample the intrinsic energy resolution by a factor larger than 3.

3.3.2 NuSTAR data

The *NuSTAR* data were processed using NUSTARDAS V1.6.0, available in the *NuSTAR* Data Analysis Software. The event data files were calibrated with the NUPIPELINE task using the response files from the Calibration Data base CALDB v.20180409 and HEASOFT version 6.25. With the NUPRODUCTS script we generated both the source and background spectra, plus the ARF and RMF files. For both focal plane modules (FPMA, FPMB), we used a circular extraction region of radius 49 arcsec centered on the position of the source. The background selection was made taking a region free of sources of twice the radius of the target and located in the same detector quadrant. Spectral channels were grouped with the FTOOLS task GRPPHA to have a minimum of 20 counts per spectral bin in the 3.0 – 79.0 keV energy range.

Table 3.1: General properties of the sample galaxies

Name	RA	DEC	Type	Redshift	N_{gal}	M_{BH}	L_{Bol}	λ_{Edd}
	(J2000)	(J2000)			(10^{20} cm^{-2})	$M_\odot$	(log)	(log)
(1)	(2)	(3)	(4)	(5)	(6)	(7)	(8)	(9)
NGC 3998	179.484	55.454	Sy1.9	0.003	20.09	8.93^{L}	42.29	-4.74
NGC 3718	173.145	53.068	Sy1.9	0.003	20.03	8.14	41.74	-4.49
NGC 4258*	184.740	47.304	Sy1.9	0.001	20.08	7.56^{L}	41.39	-4.28
NGC 5033	198.364	36.593	Sy1.9	0.002	20.00	7.68	41.78	-4.00
ESO253-G003*	81.325	-46.00	Sy2	0.042	20.62	9.84+	43.89	-3.95
NGC 1052	40.270	-8.256	Sy2	0.005	20.49	8.67	42.83	-3.94
NGC 2655	133.907	78.223	Sy2	0.004	20.32	8.20	42.43	-3.87
NGC 3147*	154.223	73.400	Sy2	0.009	20.54	8.81	43.10	-3.81
NGC 2110*	88.047	-7.456	Sy2	0.007	21.27	9.38	43.81	-3.67
LEDA 96373*	111.610	-35.906	Sy2	0.029	21.47	9.21	43.80	-3.51
NGC 2992	146.425	-14.326	Sy1.9	0.007	20.72	8.33	43.13	-3.30
M51	202.484	47.230	Sy2	0.001	20.19	6.59	41.40	-3.29
NGC 2273*	102.536	60.845	Sy2	0.006	20.84	7.99	42.84	-3.25
HE 1136-2304	174.713	-23.360	Sy1.9	0.027	20.63	9.39	44.28	-3.21
IGRJ11366-6002	174.175	-60.052	Sy1	0.014	21.81	8.56	43.51	-3.15
IC4518A	224.421	-43.132	Sy2	0.016	20.96	8.79	43.83	-3.06
NGC 7674*	351.986	8.779	Sy2	0.028	20.70	9.18	44.28	-3.0

(Col. 1) Name, (Col. 2 and 3) right ascension and declination in Equatorial (J2000.0) from Swift BAT 105-month hard X-ray survey (Oh et al., 2018a), (Col. 4, 5, 7, 8 and 9) optical classification from BASS/DR2, redshift, Black hole mass using the velocity dispersion method, bolometric luminosity and accretion rate λ_{Edd}=L_{Bol}/L_{Edd} from BASS/DR2 survey (^{L} identify masses taken from literature by the BASS/DR2 survey and the symbol + means from MgII). (Col. 6) represents the galactic absorption (Dickey & Lockman, 1990). Objects marked with * are the galaxies with non-simultaneous observations with *XMM-Newton* and *NuSTAR* .

3.3.3 Swift data

We retrieved the binned and calibrated spectra, together with the response matrices for our targets from the *Swift*/BAT 105 month All-sky Hard X-Ray Catalog reported in Oh et al. (2018b). The observations were taken with the Burst Alert Telescope (BAT) on board the *Swift* observatory. This survey has a sensitivity of 8.4×10^{-12} erg s^{-1} cm^{-2} in the 14 – 195 keV band over 90% of the sky with eight-channel spectra averaged over the 105 month duration of the survey. The complete analysis pipeline is described in the *Swift*/BAT 22 All-sky Hard X-Ray Survey (Tueller et al., 2010).

3.4 Methodology

The analysis of the data comprises two steps: (1) Combination of *XMM-Newton* and *NuSTAR* observations; and (2) homogeneous spectral fitting of the sample. All the spectra have been fitted using XSPEC version 12.10.0 (Arnaud, 1996) and all the errors reported throughout the paper correspond to 90% of confidence level.

3.4.1 Combination of the XMM-Newton and NuSTAR observations

In this chapter, we have *NuSTAR* observations, with an energy range from 3 to 79 keV, vital to study the Compton hump which is a key signature of the reflection. Additionally, we have *XMM-Newton* data, which provides the best combination of sensitivity, bandpass, and spectral resolution at energies ranging from 0.5 - 10.0 keV. Objects with simultaneous observations with *XMM-Newton* and *NuSTAR* were fitted with all model parameters tied between the different spectra, except for a free cross normalization factor. Objects with non-simultaneous observations (denoted with the symbol * in our work) were tested for spectral variability between the observation epochs. In order to detect spectral variability, we simultaneously fitted the *XMM-Newton* + *NuSTAR* spectra in the overlapping 3.0 – 10.0 keV range for each object with a power-law model under neutral absorption. In cases where the spectrum was not well fitted with this model we added a Gaussian component centered at 6.4 keV and studied the improvement of the fit.

At first, all parameters were tied between the spectra of the different epochs/instruments. If this model produced a satisfactory fit the source is consid-

ered non variable and treated in the same way as the objects with simultaneous observations. For the remaining objects we allowed the normalization of the power-law to vary between epochs which resulted in a satisfactory fit in most cases. For these objects, in the subsequent fitting the normalization of the power-law was left free between the epochs but the remaining parameters were tied. For one object, (ESO 253-G003) allowing the slope of the power-law to vary freely improved the fit significantly according to the F-test. Given the spectral variability in this source we had to leave most parameters untied between the epochs, and therefore the inclusion of the lower energy spectrum would not constrain the reflection model further. For this reason in this source we used the high energy spectra only. Finally, one object (NGC 7674) could not be fitted well with a free slope and normalization, as this is a known changing look AGN and its spectrum changed significantly in shape between observations (Bianchi et al., 2005), so we retained only the *NuSTAR* spectrum for the following analysis. The best model and the final configuration for each object is summarized in Table C.4.

3.4.2 Spectral analysis

For all spectral fits, we included a multiplicative constant normalization between FPMA, FPMB, EPIC-PN and *Swift*/BAT to account for calibration uncertainties between the instruments. We started with a baseline model and added different components until a satisfactory fit was obtained. We have selected three broad components in order to parametrise three scenarios.

1. **Cut off Power-law model (cPL) obscured by neutral material:** a single power law model, which corresponds to the primary emission of a non-thermal source. The column density, $N_{H,los}$, is added as a free parameter to take the absorption by matter along our line of sight to the target into account. The free parameters in this model are the column density, $N_{H,los}$, the slope of the power law, Γ, the high energy cut-off, E_{cut} and the normalization.

2. **Reflection models (Refl):** When the X-ray continuum is scattered by the surrounding gas, it can produce fluorescent emission lines (most notably Fe Kα 6.4 keV) and a broad hump-like continuum peaking around 10–30 keV. The reflection was modelled with three possible scenarios:

- A neutral reflector with a semi-infinite column density modelled with `PEXMON` (Nandra et al., 2007). This model assumes the existence of optically thick and cold material, distributed in a slab and covering a given fraction of the X-ray source. The `PEXMON` model include fluorescence, adding some spectral features, such the emission lines FeKα and Fekβ, following the Monte Carlo calculations of George & Fabian (1991). This model represents both the reflected and intrinsic emission defined with Γ and the high energy cut-off (E_{cut}) and the reflection fraction, R_f. The free parameters in this model are the reflection fraction, R_f (to account the reflection component and the contribution from the intrinsic power-law continuum), the spectral index, Γ, the high energy cut-off, E_{cut}, the inclination and the normalization.

- A torus modelled with `BORUS` (Baloković et al., 2018) which calculates the reprocessed continuum of photons that are propagated through a cold, neutral and static medium. `BORUS` is similar to the torus model `BNtorus` of Brightman & Nandra (2011a) but it has additional free parameters (E_{cut}, A_{Fe}), additional chemical elements included, calculation extending to higher energies and line-of-sight component separated out. Furthermore, this model has a variable covering factor which is an advantage comparing with other models, as `MYTORUS` (Murphy & Yaqoob, 2009) that proposes a toroidal geometry where the covering fraction is fixed to 0.5. In this chapter, we used the geometry of a smooth spherical distribution of neutral gas, with conical cavities along the polar directions (`BORUS02`). The column density and the inclination of the torus are free parameters in this model. BORUS includes fluorescent emission lines, according to fluorescent yields for Kα and Kβ lines from Krause & Oliver (1979), for all elements up to zinc ($Z < 31$). The reflected spectrum of this torus is calculated for a cut-off power-law illuminating continuum, where E_{cut}, Γ and normalization are free parameters. We modeled the direct coronal emission separately with a cut-off power-law under a neutral absorber as described above. We have set as free parameters the column densities along the line-of-sight, $N_{H,los}$, the inclination, $Cos(\theta_{incl})$, the covering factor, CF, the column density of the reflector, $\log(N_{H,refl})$, the spectral index of the primary emission, Γ, the high energy cut off, E_{cut} and the normalization of the reflector tied to the primary emission.

- The accretion disk reflection modelled with XILLVER (García et al., 2013) where the coronal spectrum is a power-law with an exponential cut-off described by the photon index, Γ and the high energy cut-off, $E_{\rm cut}$. Another important parameter is the ionization parameter, ξ, defined as the incident flux divided by the density of the disk. This parameter is described by $\log(\xi)$ ranging from 0 for a neutral disk to 4.7 for a heavily ionized disk (see García et al. 2013, for a more detailed description). Other parameters in this model are the iron abundance, $A_{\rm Fe}$ relative to the solar value (assumed to be solar in this chapter), redshift, reflection fraction, R_f and the inclination. Also, this model takes takes into account both the reflected continuum and the FeKα. The free parameters in this model are the spectral index, Γ, the high energy cut-off, E_{cut}, the ionization degree, $\log(\xi)$, the inclination, incl, the reflection fraction, R_f (to normalized the reflection component relative to the intrinsic power-law continuum) and the normalization.

3. **Soft X-ray Emission (SE):** When the combination of the above models does not produce a good fit, we explore if the addition of spectral component(s) improves the fit. The following spectral components are considered:

   - An absorbed scattered Power-law: an absorbed power-law PL to model the scattered emission that is deflected by ionized gas. The photon index, Γ, of the scattered component is tied to the primary power-law. We set as free parameters the column density, $N_{H,ext}$ and the normalization of the scattered component but restricted to be less than 5% of the main one.

   - Thermal emission: An optically-thin thermal component, modeled by MEKAL in XSPEC, to model the soft excess observed below 1 keV, and potentially due to either star formation processes and/or thermal emission from a hot interstellar medium. We kept the hydrogen column density, abundance, and switch at their default values (1, 1, and 1 respectively) and we let the temperature, ionization and normalization free to vary.

- An ionized absorber (ab): a warm absorber was modelled with `zxipcf` within XSPEC. This model uses a grid of XSTAR photionised absorption models (calculated assuming a microturbulent velocity of 200 km s^{-1}) for the absorption and assumes an absorbent covering some fraction of the source, cf_W. `zxipcf` has as free parameters the column density, $N_{H,W}$, the ionization state, $\log(\xi_W)$, the covering fraction, cf_W, and redshift. We set the covering fraction to cf_W=1 to mimic an absorber covering all the sky. We let as a free parameter $N_{H,W}$ and $\log(\xi_W)$.

We started our analysis by fitting a baseline model that is defined as `MOD = Refl + cPL` to the data. Then we added one SE emission or absorption component (we tested one by one: `MOD + PL`, `MOD + MEKAL` and `MOD*ab`) and explore if the inclusion of any of these components improves the fit. If any of the improvements was significant, we selected the model that returned the lowest value of χ^2/d.o.f., shows improvements with the F-test and according to the visual inspection of the residuals and select it as the new baseline model and the process of including and testing an additional SE component was repeated. When none of the additional SE components provided a significant improvement, the iteration stopped. Up to 4 iterations were necessary for each object and reflection model.The best-fitting model parameters are used in the analyses below if the corresponding χ^2/d.o.f $\leq$1.4, otherwise we conclude that the particular reflection model used cannot provide a good fit and its parameters are not reported. The method is represented in Fig. 3.1.

The process was repeated separately for each reflection model thus we report up to three best-fitting models for each object.

The models that were selected to fit the data are represented in XSPEC as:

$$\boxed{\mathrm{C} \times \mathrm{N_{Gal}} \times \mathrm{ab} \times (\mathrm{N_{H,ext}} \times \mathrm{SE} + \mathrm{N_{H,los}} \times \mathrm{cPL} + N_{\mathrm{H,los}} \times \mathrm{Refl})}$$

Where C represents the cross-calibration constant between different instruments, $N_{H,Gal}$ is the Galactic absorption (`phabs` in XSpec) predicted using N_H tool within FTOOLS (Dickey & Lockman, 1990; Kalberla et al., 2005). "ab" is the ionized absorption component modelled with `zxipcf`, in cases where this component is used, otherwise is equal to unity. Two absorbing column densities are used, which will be called here $N_{H,ext}$ and $N_{H,los}$ (`zphabs` in XSpec). $N_{H,los}$ is assumed to cover the nuclear

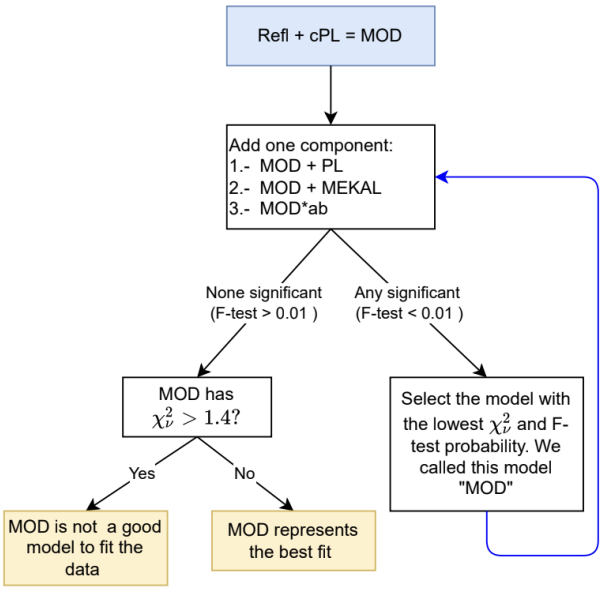

Figure 3.1: Schematic view of the methodology followed to fit the data. Note that the loop in blue iterate maximum four times. For a detailed explanation of the method we refer the reader to the text.

components (power-law and disk reflection)[2] and $N_{H,ext}$ covers the SE component[3]. Moreover, cPL is a cut-off power-law (`cutoffpl` in XSpec) representing the primary X-ray emission and "Refl" represents the different reflection models used.

Note that we imposed the following conditions to the resulting best-fit Γ >0.5, $N_{H,Gal} \leq N_{H,ext}$ and $N_{H,los} > N_{H,ext}$. In the case of NGC 1052, additional Gaussian lines were required at soft energies from a visual inspection, we included S XIV at 2.4 keV and Si XIII at 1.85 keV. They were added as a narrow Gaussian line with fixed centroid energy and a width fixed at 0.01 keV.

3.5 Results

In the following we will show the main results of the analysis for the sample of 17 LLAGNs with accretion rate $\log(\lambda_{Edd}) \leq$-3.0 from the BASS/DR2. We refer the reader to the following sections and tables for details on the analysis. Comparison with previous works and our results on individual objects can be found in Appendix B. The

[2]In case of a torus like reflection, the absorber is not acting in the torus-like reflector
[3]In case MEKAL, the absorber is not acting in this component

coronal parameters (i.e., Γ, E_{cut}, and χ^2) are listed in Table C.6. The reflection parameters, i.e., R_f and inclination for `PEXMON`; $\log(N_{H,refl})$, CF and inclination for `BORUS`; $\log(\xi)$, R_f and inclination for `XILLVER` are listed in Table C.8. In Table C.10 we show all the additional components required for the fit with each of the reflection models, i.e., the column density of the neutral absorbers in the line of sight to the extended and nuclear components and the temperature of the optically thin thermal emission components. Additional parameters, i.e., the column density and ionization parameter of the ionized absorbers in the line of sight and the normalization of the scattered power law can be seen in Table C.12. All cross-calibration constants are listed in Table C.14. The plots of the spectra with the best-fit models and their residuals can be found in Appendix D.

3.5.1 Models

In this chapter we used three reflection models (`PEXMON`, `borus02`, and `XILLVER`) that were used to fit the spectrum of each of the sources in the sample, i.e., each of the sources are fitted by three different models.

The simplest model used in our work (`PEXMON`) is a good representation of the data, however, we will focus on models that can explore different reflector geometries as `borus02` and `XILLVER`. To decide which model provides the best description of the observations, we estimate the "evidence ratio" using the Akaike information criterion (AIC) for both models. This evidence ratio allows us to compare if one model is better than another one, it is defined using as ϵ=W(AIC_{torus})/W(AIC_{disk}) where W(AIC_{torous}) and W(AIC_{disk}) are the "Akaike weight" (see Emmanoulopoulos et al. 2016 for more details). The evidence ratio is a measure of the relative likelihood of the torus versus the disk model. The torus model is 200 times more likely than the disk model when $\epsilon \leq 0.0067$. The disk model is 200 times more likely than the torus model when $\epsilon \geq 150$. The evidence ratio are listed in Table 3.2.

For nine (53%) objects (NGC 4258,NGC 1052, NGC 2110, LEDA 96373, NGC 2992, M 51, HE 1136-2304, IC 451A, and NGC 5033) `borus02` is preferred. Then in the following sections we choose this model as the best representation of the data in these objects. On the other hand, two (12%) objects (NGC 2273 and NGC 7674) are well fited with a disk (`XILLVER`) model and in six (35%) objects (NGC 3998, NGC 3718, ESO 253-G003, NGC 2655, NGC 3147, and IGRJ 11366-6002) both models fit similarly well the data.

Table 3.2: Best model results according with Akaike criterion

Name	ϵ	Model
NGC 3998	8.06E-01	T/D
NGC 3718	1.68E+00	T/D
NGC 4258*	2.57E-16	Torus
NGC 5033	5.67E-04	Torus
ESO 253-G003*	1.20E+00	T/D
NGC 1052	3.86E-59	Torus
NGC 2655	3.86E-02	T/D
NGC 3147*	6.44E-02	T/D
NGC 2110*	1.65E-53	Torus
LEDA 96373*	8.97E-26	Torus
NGC 2992	1.77E-74	Torus
M 51	1.68E-04	Torus
NGC 2273*	4.41E+07	D
HE 1136-2304	5.31E-15	Torus
IGRJ 11366-6002	5.88E+01	T/D
IC 4518A	1.18E-06	Torus
NGC 7674*	2.23E+02	D

Evidence ratio for the Akaike method and resulting model best to each source. T/D represents the cases when either torus or disk models provide an equally good fits. T represents the torus model (`borus02`) and D the disk model (`XILLVER`). Objects marked with * are the galaxies with non-simultaneous observations with and .

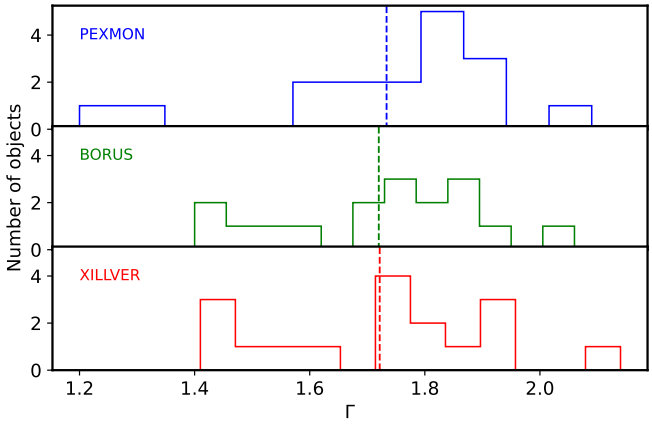

Figure 3.2: Comparison between the spectral index estimation, Γ, between the models. The dotted lines represents the mean values.

Since it is not possible to distinguish between a reflection dominated by a torus or a disk, we will treat them separately in the following sections. When referring to the torus case, we refer to all `borus02` models for the whole sample (15 galaxies: indistinguishable and distinguishable cases). In the disk case, we refer to the `XILLVER` model, considering the indistinguishable cases and the cases where the disk is a good representation of the data (8 galaxies in total), since in the other cases a torus model is not a good representation of the data.

X-Ray Continuum Properties

The X-ray continuum of AGN is described by a power-law with a high-energy cut-off. The free parameters of this component are the spectral index (Γ) and the high energy energy of the cut-off (E_{cut}). In Fig. 3.2 we show the histogram derived from the broadband spectral analysis with each reflection model. Note that the spectral index between both the reflected and intrinsic emission are tied. We find that the mean values (dashed vertical lines) of Γ for the sample using `PEXMON`, `borus02` and `XILLVER` are consistent (1.73±0.21, 1.72±0.17 and 1.72±0.20 respectively). Note that the simplest model used in our analysis is `PEXMON`, which shows values of the photon index consistent with more geometrical models.

Considering the torus model (15 galaxies), we found median values of Γ= 1.76 and σ=0.16, with values ranging between [1.40, 2.06]. Another important parameter that could be estimated with the data is the high energy cut-off (E_{cut}). This parameter can be considered as an indicator of the temperature of the X-ray corona. Consequently, its

knowledge provides information about the dynamics of the corona and the physical processes occurring within it. Nevertheless, this parameter is poorly constrained. A lower (upper) limit of E_{cut} could be determined for eight (two) sources. The five AGN for which E_{cut} could be determined (NGC 3998, ESO 253-G003, NGC 2110, NGC 2992, and NGC 5033) have a mean value of E_{cut}=193.28 keV with a standard deviation of σ=99.19 keV.

Furthermore, taking into account the disk model (8 galaxies), we found median values of Γ=1.71 and σ=0.23, with values ranging between [1.40, 2.06]. Regarding the high energy cut-off, we could find five (one) lower (upper) limits and for six object we obtained a mean value of E_{cut}=371.47.58 keV with a standard deviation of σ=619.99 keV.

Soft band spectral fit

In the soft (0.3 – 10.0 keV) energy band, we added a thermal (MEKAL in `xspec`), scattered power-law, absorption by ionized gas (also referred to as "warm absorption") (modelled with `zxipcf` in `xspec`) or a combination of these components to improve the spectral fit.

When considering the torus model (15 objects), six objects (NGC 3998, ESO 253-G003, NGC 3147, M 51, IGRJ 11366-6002, and NGC 5033) do not require an additional component to improve the fit. Two objects (NGC 3718 and HE 1136-2304) required a `MEKAL` component (with kT=$0.88^{**}_{0.67}$ keV and kT=$0.59^{0.67}_{0.51}$ keV, respectively). Two objects are well fitted with a combination of `MEKAL`, power-law, and warm absorber (NGC 1052 with `MEKAL+PL` and NGC IC 451A with `MEKAL*ab`). Composite models are needed for five galaxies (NGC 4258, NGC 2655, NGC 2110, LEDA 96373, and NGC 2992). In the cases where two `MEKAL` were required, the values of the temperatures are in the range kT_1 = [0.58 - 0.62] keV with a mean value of kT_1=0.60 keV and σ=0.02 keV, and kT_2 = [0.15 - 0.22] keV with a mean value of KT_2=0.19 keV and σ=0.03 keV. The mean value of the ionized absorber is $N_{H,W}$=1.66 $\times 10^{22}$ cm^{-2} and σ=1.41 $\times 10^{22}$ cm^{-2} The degree of ionization is in the range [-1.14, 4.30] with the mean $\log(\xi_W)$=1.31 and σ=1.99.

In relation to the disk model (8 objects), five galaxies do not require any component to improve the spectral fit (NGC 3998, ESO 253-G003, NGC 3147, IGRJ 11366-6002 and NGC 7674). One galaxy (NGC 3718) require a `MEKAL` component to improve the fit. Two galaxies (NGC 2655 and NGC 2273) are well fitted with a composite model `MEKAL*ab`.

Line-of-sight column density

Absorption of X-rays by neutral material is the result of the combined effect of Compton scattering and photoelectric absorption. The Compton scattering and the photoelectric absorption were modelled using `CABS` and `ZPHABS` in `xspec` respectively. In `ZPHABS`, we fixed the redshift at the value of each source. The only free parameter is the column density, which is tied in all fits (i.e., $N_{H-ZPHABS} = N_{H-CABS} = N_{H-los}$).

According with the torus model, we can classify six galaxies as unobscured ($\log(N_{H,los})$ >22) (NGC 3998, NGC 3147, NGC 2992, HE 1136-2304, IGRJ 11366-6002 and NGC 5033) with values between $\log(N_{H,los})$=[20.0, 21.89] and eight galaxies (NGC 3718, NGC 4258, ESO 253-G003, NGC 1052, NGC 2655, NGC 2110, IC 451A, and LEDA 96373) as obscured (22¡log(N_H)¡24.18) with values ranging $\log(N_{H,los})$=[22.01, 24.09]. According with our spectral analysis one galaxy (M 51) in our sample can be classified as Compton thick (CT) (using as a threshold $N_H = 1.5 \times 10^{24} cm^{-2}$, or $\log(N_{H,los})$=24.18). The mean values of spectral index, column density in the line of sight and column density of the torus are reported in Table 3.3. All the parameters are consistent between the groups. Note that the values of the cross-calibration constant between the groups are consistent.

Regarding the disk model, two galaxies (NGC 3998 and IGRJ 11366-6002) can be classified as unobscured. Six galaxies (NGC 3718, ESO 253-G003, NGC 2655, NGC 3147, NGC 2273, and NGC 7674) as obscured with values $\log(N_{H,los})$=[22.03, 23.36]. The mean values of the spectral index, the column density in the line of sight, the ionization degree of the accretion disk and the reflection fraction are reported in Table 3.3 and showed values consistent between the categories. Note that according to a reflection dominated by accretion disk, none of the galaxies in our sample can be classified as CT.

The reflection component

The reflection features observed in the hard X-ray spectra of AGN may be caused by neutral and distant material such as the torus or by the ionized material of the accretion disk.

For the case where the reflection is dominated by the torus, the mean value of our sample for the column density for this structure is $\log(N_{H,refl})$=23.69 and σ=0.76 with values between [22.50, 25.40]. Four objects (NGC 1052, M 51, IGRJ 11366-6002, and IC451A) show a column density of the torus consistent with a Compton thick

Table 3.3: Mean values and standard deviation of the spectral parameters for the subgroups with the torus and the disk models.

Group	$\Gamma \pm \sigma$	$\log(N_{H,los}) \pm \text{œ}$	$\log(N_{H,refl}) \pm \text{œ}$
Unobscured (6)	1.80±0.12	20.85±0.56	23.45±0.68
Obscured (8)	1.74±0.17	22.99±0.65	23.65±0.58

Group	$\Gamma \pm \sigma$	$\log(N_{H,los}) \pm \text{œ}$	$\log(\xi) \pm \sigma$	$R_f \pm \sigma$
Unobscured (2)	1.85±0.05	21.90±1.32	3.61±0.47	3.97±0.12
Obscured (6)	1.74±0.26	22.90±0.44	2.43±0.77	6.59±3.29

Group, The standard deviation(s) and the mean value of the following parameters: For the Torus: Γ, column density in the line of sight in log units and column density of the torus like reflector in units of log. For a disk: Γ, column density in the line of sight in log units, ionization degree and the reflection fraction. The parentheses show the number of AGN in each category.

structure. Another important parameter derived from the torus reflector model is the covering factor. We were only able to determine a lower (upper) limit for three (six) objects (a lower limit for NGC 3998, NGC 2655, and IC451A, and an upper limit for NGC 3718, NGC 4258, ESO 253-G003, NGC 3147, NGC 2992, and M 51). This parameter was determined for six (40%) objects (NGC 1052, NGC 2110, LEDA 96373, HE 1136-2304, IGRJ 11366-6002, and NGC 5033) with a mean value of CF =0.59 and σ=0.25. The half-opening angle of the polar cutouts, $\cos(\theta_{incl})$, is also measured with the torus model. However, we obtain only lower (upper) limits for seven (three) objects and properly constrained it for five sources.

To the disk like reflection, we constrain the value of the ionization degree of the accretion disk in six galaxies (NGC 3718, ESO 253-G003, NGC 3147, NGC 2273, IGRJ 11366-6002 and NGC 7674), we found median values of ionization degree of the disk of $\log(\xi)$=2.44 and σ=0.81. In one(one) objects, we only obtain upper (lower) limit (NGC 3998 a lower limit and NGC 2655 an upper limit). Regarding to the reflection fraction, R_f, we obtain six lower limits, one upper limit (NGC 2655) and it is constrained in one case (NGC 7674). This model also allow us to estimate the inclination, and this parameter is constrained in five sources with mean value Incl=70.10 deg and σ=27.23 deg and four upper limits.

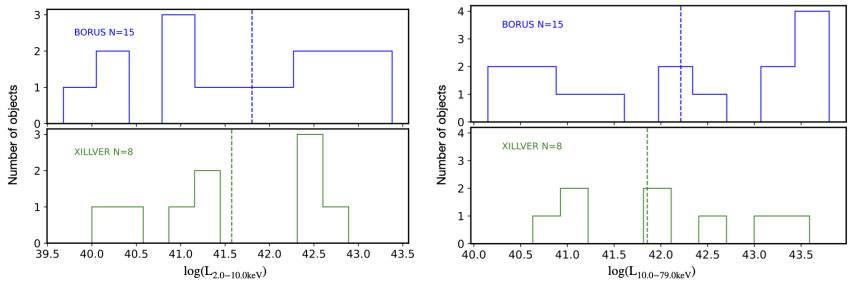

Figure 3.3: Histogram of the intrinsic luminosity in the band 2.0 – 10.0 keV (left) and 10.0 – 79.0 (right) in the and with number of objects in each group.

Flux and Luminosity

We computed the X-ray flux and luminosities in two energy bands: 2.0 – 10.0 keV and 10.0– 79.0 keV using `xspec`. Note that redshift of the sources were taken from NASA/IPAC Extragalactic Database (NED). The values can be seen in Table C.16. Taking into account a torus model, the mean value of the intrinsic luminosities in the case are $\log(L_{2.0-10.0})$=41.73 and σ=1.16 $\log(L_{10.0-79.0})$=42.14 with σ=1.29. In the case, we found $\log(L_{2.0-10.0})$=41.57 with σ=1.06 and $\log(L_{10.0-79.0})$=41.85 with σ=1.24 and they are equivalent. The distribution of the intrinsic luminosity obtained in both cases can be seen in Fig. 3.3.

3.6 Discussion

We have performed the X-ray spectral analysis of an AGN sample with accretion rates, $\log(L_{\rm Bol}/L_{\rm Edd}) \leq$ -3 selected from the BASS/DR2 that have available + + *Swift* data. Models from a neutral reflector (`PEXMON`), reflection from an ionized accretion disk (`XILLVER`) and from the torus (`borus02`) have been used to fit the data. This sample is composed by 17 objects, and our main results are summarized as follows:

1. In our sample, six (35%) objects are equally well fitted with a disk or with a torus-like reflector. For nine (53%) galaxies, the torus reflection model is the best representation of the data. In tow cases (12%) the disk model well fit the data.

2. When modelling the reflection with `borus02`, seven objects are well fitted by a single neutrally-absorbed cut-off power-law plus reflection (i.e., no component are required in the soft band). When modelling the reflection with `XILLVER` instead, five objects can be well modeled in the same way. The remaining objects

require the addition of a MEKAL and/or scattered power-law, an ionized absorber or a combination of two or more of these components.

3. According with the torus model, six sources can be classified as unobscured (log(N_H)¡22), eight galaxies as obscured (22¡log(N_H)¡24.18) and one object have a column density in the line of sight consistent with a Compton thick source (log(N_H)¿24.18). According with the disk reflection, two (six) objects can be classified as unobscured (obscured). These classifications are consistent among the models, except in the case of NGC 3147 (unobscured according withe the torus and obscured with the disk).

The high quality and broad spectral coverage available combining ++*Swift* allowed us to put constraints on spectral parameters related to the accretion mechanism and reflection of LLAGN. Our analysis covers energies above 10.0 keV, where the reflection has an important role in the spectral fit, and considering this feature in the X-ray spectral analysis can affect the estimation of the coronal parameters (see Diaz et al. 2020). In the following we discuss the physical interpretations of the results presented in this work.

3.6.1 Determination of the $L_{\rm Bol}/L_{\rm Edd}$

The selection of the sample presented in this chapter was based on sources with $\log(L_{\rm Bol}/L_{\rm Edd}) \leq$ -3 according to those values reported in BASS/DR2. However, because variability is one of the properties that characterize AGN, we will estimate these accretion rates using the data that have been analyzed here.

To estimate $L_{\rm Bol}/L_{\rm Edd}$, we follow the relation given in Eracleous et al. (2010), which uses the black hole mass and bolometric luminosities. According to Koss et al. (2017), the black hole masses available for the BASS sources were determined using different methods. For 14 of our sources these were estimated using the velocity dispersion method, from the M_{BH}-σ_* relation by Kormendy & Ho (2013). Two galaxies have M_{BH} taken from the literature (NGC 3998 via the M-σ relation and NGC 4258 by a rotating H_2O maser disk) and for one source it was estimated from the MgII emission line (ESO253-G003). The uncertainties on these M_{BH} determinations are of the order $\sim$0.3-0.4 dex (as explained in the BASS/DR1 paper - Koss et al. 2017). We conservatively assume that the typical uncertainty on M_{BH} is $\sim$0.4 dex.

The other key parameter is the bolometric luminosity, for instance, BASS/DR1

(Koss et al., 2017) focused in the bolometric correction derived by Vasudevan & Fabian (2007, 2009), where $L_{bol}/L_{2-10keV}$ = 20 for $L_{Bol}/L_{Edd} \leq 0.4$, and $L_{bol}/L_{2-10keV}$ = 70 for $L_{Bol}/L_{Edd} \geq 0.4$. As the bolometric luminosity is fundamental in the estimation of the accretion rate, we examine an alternative determination of L_{Bol}/L_{Edd} based on the available X-ray luminosities estimated using the data of our sample of AGN.

We use the intrinsic luminosities in the 2–10 keV rest-frame energy range, $L_{2.0-10.0keV}$, derived from the best-fitting spectral models of the X-ray data. Note that in case of indistinguishable cases, we use the values form the `BORUS` model. Using the `XILLVER` model the results are the same. A comparison between our $L_{2.0-10.0keV}$ calculation and the BASS/DR2 is presented in Fig. 3.4, showing differences in the luminosity, possibly related with variability. The difference between the fluxes measured by BASS/DR2 integrated 70 months and the flux measured in the short exposures with NuSTAR that we use here can be quite large for highly variable sources such as NGC2992 (Gilli et al., 2000; Shu et al., 2010; Hernández-García et al., 2017; Marinucci et al., 2018, 2020) and LEDA 96373 (Landi et al., 2009).

To be consistent between the state of each AGN when measuring Γ and other parameters, we recalculate L_{Bol}/L_{Edd} using the fluxes measured here and refine it by changing the bolometric correction as described below.

We use our $L_{2.0-10.0keV}$ calculation in combination with the bolometric correction K(2.0-10.0 keV) from Duras et al. (2020), who used a sample of $\sim$1000 type 1 and type 2 AGN from five different AGN surveys for which they performed a SED -fitting. They reported a bolometric correction as a function of 2.0-10.0 keV X-ray luminosity. The resulting K(2.0-10.0 keV) are slightly smaller than those used previously ($L_{bol}/L_{2-10keV}$ = 20), with a median value of K(2.0-10.0 keV)= 15.60 with a scatter of $\sim$0.37 dex (Duras et al., 2020). The values of bolometric luminosity and Eddington ratio are given in table C.17. The errors in the bolometric luminosity correspond to the error propagation of M_{BH} (0.4 dex), K(2.0-10.0 keV) (0.37 dex), and $L_{2-10keV}$ (estimated with XSPEC). In the following analysis, we will use these L_{Bol}/L_{Edd} values to minimize the effects of source variability.

3.6.2 Accretion mechanism: The Γ vs L_{Bol}/L_{Edd} relation

It has been suggested that the accretion mechanism in LLAGN ($L_{Bol}/L_{Edd} < 10^{-3}$) is different from that in more powerful AGN (e.g., Seyferts) and similar to that of X-ray binaries (XRB) in their low/hard state (Yamaoka et al., 2005b; Gu & Cao, 2009; Younes

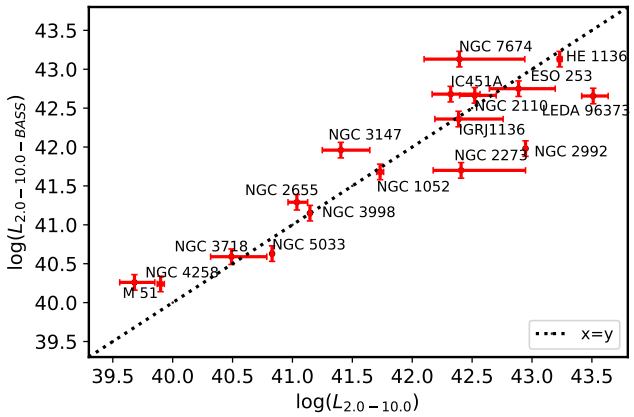

Figure 3.4: Intrinsic luminosities 2.0-10.0 keV from BASS DR2 and our work. Dotted black line represents x=y.

et al., 2011; Xu, 2011; Yuan & Narayan, 2014; Hernández-García et al., 2016).

Some authors, following the relations obtained for XRB, have studied the accretion mechanism using the relation between the spectral index Γ and the accretion rate $\lambda_{\rm Edd}$, finding a positive correlation between these quantities at high accretion rates, suggesting a geometrically thin and optically thick disk, known as the standard model for accretion disks (Shakura & Sunyaev, 1973; Koratkar & Blaes, 1999). A negative correlation has also been found at low accretion rates, indicating radiatively inefficient accretion (e.g., Yuan et al. 2007). In this configuration, the accretion disk becomes truncated near the SMBH, with a geometrically thick and optically thin disk at lower radii and a thin disk at higher radii. However, these correlations show a large scatter (Shemmer et al., 2006; Gu & Cao, 2009; Younes et al., 2011; Yang et al., 2015a; She et al., 2018), with Γ values between [1,3] (Gu & Cao, 2009; Younes et al., 2011) and [0.5, 3.5] (She et al., 2018). The high scatter in the spectral index estimate is still not understood - it could be due to the sensitivity of the measurements or to intrinsic properties of the galaxies.

Thanks to the excellent statistics of *NuSTAR* in combination with *XMM-Newton*, we were able to better constrain the spectral index Γ in our low accretion rate sample. In Fig. 3.5 we show the relation between Γ and $\lambda_{\rm Edd}$ using the best fitting reflection model (*BORUS*). We have added data from Esparza-Arredondo et al. (2021), who studied the torus configuration of 36 AGN using *NuSTAR* and *Spitzer* data and estimated the spectral parameters using the same reflection model used in this chapter (*BORUS*). We applied the same bolometric correction to these data (see Sect. 3.6.1 In Fig. 3.5, the

blue points correspond to this chapter and the light yellow stars represent the data points from Esparza-Arredondo et al. (2021). We also compare our estimates with previous works. For high luminosity AGN ($\log(\lambda_{\rm Edd})$ >-3.0), we compare with Fanali et al. (2013), who studied a sample of 71 type 1 AGN using *XMM-Newton* data (purple dashed line). In the low luminosity branch ($\log(\lambda_{\rm Edd})$ < -3.0), we compare with Gu & Cao (2009), which used a sample of 55 LLAGN using *Chandra* and XMM-Newton-*Newton* data (green dashed line); She et al. (2018) used a sample of 314 AGN with *Chandra* (cyan dashed line); and Younes et al. (2011) used *Chandra* and XMM-Newton-*Newton* data from a sample of 13 LINER with accretion rates below -4.5 (orange dashed line).

In this chapter, we have shown that the inclusion of XMM-Newton-*Newton* + *NuSTAR* data and reflection models in the spectral fit improves the estimation of the spectral index - as also reported in Hinkle & Mushotzky (2021) - which could improve the scatter compared to what was previously found by Gu & Cao (2009); Younes et al. (2011); She et al. (2018). For details on the improvement of the uncertainties in the spectral index estimation, see Appendix A. Indeed, in Fig. 3.5 can be seen that our results, when compared with previous studies, seem to be in agreement with the correlations found by Gu & Cao (2009), She et al. (2018), and Younes et al. (2011), but the effect of the large scatter in previous studies can be appreciated. The same is true for the high-energy branch, where the relation of Fanali et al. (2013) (at $\log(\lambda_{\rm Edd})$ >-3.0) fits well the data of Esparza-Arredondo et al. (2021).

To determine whether a relation between Γ and λ_{Edd}, we use the tool `pymccorrelation` in Python (Isobe et al., 1986; Curran, 2014; Privon et al., 2020) to test the relationship between two variables. We use the Kendall τ correlation test[4] compared to the Spearman correlation test. A Kendall's τ close to zero indicates that there is no trend, and if they are perfectly related, the Kendall's τ becomes 1.0 (or -1.0 for anti-correlation). For the LLAGN, $\log(\lambda_{Edd})$ < -3.0, Kendall's correlation coefficient is τ=-0.09. However, possibly because of the small number of sources, the associated p-value is 0.58, so the correlation is not formally significant and confirmation would require a larger sample. In the high luminosity branch ($\log(\lambda_{Edd})$ > -3.0), we obtain τ=0.32 and a corresponding p-value of 0.03. Thus, it appears that our sample provides evidence of a Γ-λ_{Edd} relation that is consistent with previous studies, although at lower statistical significance. In any case, the change in correlation between these parame-

[4]The Kendall τ shows more robustness to smaller samples and uncertainties in censored data (upper/lower limits)

ters at $\log(\lambda_{Edd})$ $\sim$-3.0 highlights the change in accretion physics between high- and low-luminosity AGNs, consistent with previous studies (Shemmer et al. 2006; Younes et al. 2011 and reference therein).

Despite the small number of sources in our sample, we performed the anti-correlation of the sample presented here using the tool `linregress` in Python. Then, for the low-luminosity branch where $\log(\lambda_{\rm Edd}) <$ -3.0:

$$\Gamma = (-0.034 \pm 0.054) \times \log(\lambda_{\rm Edd}) + (1.642 \pm 0.191)$$

Our work allowed us to identify the change in correlation between the spectral index and the accretion rate at $\log(\lambda_{\rm Edd})$ $\sim$-3.0, which is highly suggestive of a change in accretion physics in AGN. We recall that a larger sample of sources combining XMM-Newton–*Newton* and *NuSTAR* data and fitting physical reflection models would be very useful to confirm this relation.

Reflection

An important feature in the spectra of AGN is the reflection that imprints its mark at X-ray energies. The shape of this reflection component is usually characterized by the FeKα emission line and the Compton hump peaking at $\sim$ 30 keV (Pounds et al., 1990). The gas producing the X-ray reflection in AGN could be related to the accretion disk, a neutral reflector such as the torus or a combination of both emissions. Because we cannot separate these scenarios, in the following we will analyze the scenarios in which each of the structures dominate the X-ray spectra.

We started our analysis studying the column density of the reflector. Ricci et al. (2017b) found that the probability that a source is obscured in the X-rays (covering factor of gas) depends primarily on Eddington ratio instead of on absolute luminosity. They propose that the radiation pressure on dusty gas is responsible for regulating the distribution of obscuring material around the central black hole. At high accretion rates, radiation pressure expels the obscuring material in the form of outflows (Fabian, 2006). However, this chapter was made for the line of sight (LOS) column density which is different to the torus column density ($\rm N_{H-LOS} \neq N_{H-tor}$). In this section we will analyze for the first time, the relation between the column density of the torus like reflector and the Eddington ratio. We plot this relation in Fig. 3.6, where the pink circles and light yellow stars are the data points of the best fit model (`BORUS` in the indistinguishable cases) in this chapter and the ones obtained by Esparza-Arredondo

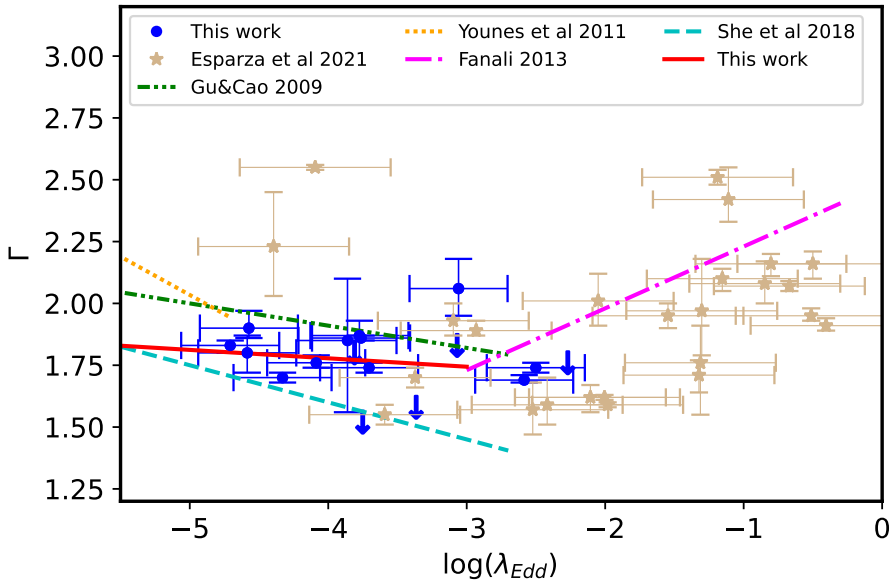

Figure 3.5: Correlation between the spectral index, Γ from individual fits, vs. the Eddington ratio, $\log(\lambda_{\rm Edd}) = \log(L_{\rm Bol}/L_{\rm Edd})$, for our sample of galaxies of the best fit models (BORUS). The dot and dashed green line represents the relation given by Gu & Cao (2009), the orange dotted represents Younes et al. (2011), the magenta dashed line is the relation obtained by She et al. (2018), while the solid black line is the correlation obtained in this chapter. The purple dashed line correspond to the relation found by Fanali et al. (2013). The blue points represented the binned data. The pink points and light yellow stars are the data point of the best fit model in this chapter and the one obtained by Esparza-Arredondo et al. (2021).

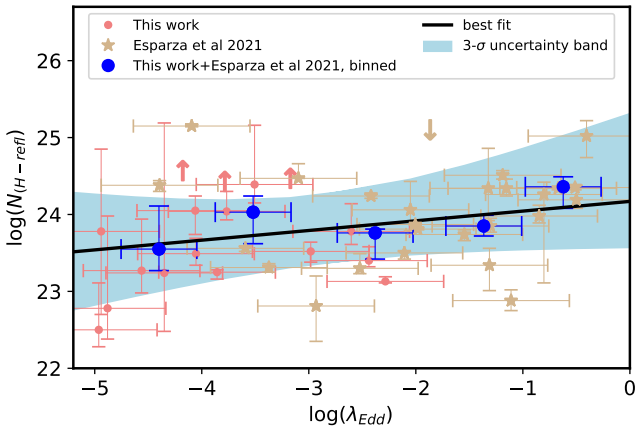

Figure 3.6: Relation between the column density of the torus-like reflector (in log) vs. the Eddington ratio, $\lambda_{\rm Edd} = L_{\rm bol}/L_{\rm Edd}$, for the sample of this chapter. The pink points and light yellow stars are the data point of the best fit model of this chapter (BORUS) and the one obtained by Esparza-Arredondo et al. (2021). The blue points represented the binned data point for a bin size equal to 0.5. The black solid line represents the best fit and the light blue zone the 3σ confidence level.

et al. (2021), respectively. The blue points represent the binned data points for a bin size equal to 0.5 dex in $\lambda_{\rm Edd}$.

Using the Kendall's tau correlation coefficient we found a correlation coefficient of τ=0.22 and p-value of 0.04 for a torus-like reflector $\log(N_{H,refl})$ and $\lambda_{\rm Edd}$, suggestive of a correlation - but confirmation is required using a larger sample. As the parameters are positively correlated, we perform a linear regression of the data using `polyfit` in python and we found the following relation:

$$\log(N_{H,refl}) = (0.126 \pm 0.303) \times \lambda_{\rm Edd} + (24.166 \pm 0.102)$$

Therefore, we find that lower accretion rate objects have, on average, lower column density material in their surroundings. We note that our torus fits allow for a free covering factor, so the lower column densities are not a by-product of a fixed covering factor in the model and a geometrically narrower reflector in lower accretion rate objects. For the LLAGN ($\log(\lambda_{\rm Edd})$ <-3.0) we obtain a mean value of the torus column density $\log(N_{H,refl}$ cm$^{-2})$=23.85 with σ=0.77 and in the high luminosity regime, $\log(N_{H,refl}$ cm$^{-2})$=23.95$\pm$0.62 with a standard deviation σ=0.61. This result can be compared with the molecular gas in the centers of low luminosity AGN. Müller-Sánchez et al. (2013) based on VLT/SINFONI AO-assisted integral-field spectroscopy of H2 1–0 S(1)

emission of four LLAGN (NGC 1052, NGC 2911, NGC 3169 and NGC 1097). On scales of 50–150 pc, the spatial distribution and kinematics of the molecular gas are consistent with a rotating thin disk, where the ratio of rotation (V) to dispersion (σ) exceeds unity. However, in the central 50 pc in their sample, the observations reveal a geometrically and optically thick structure of molecular gas (V/σ <1 and N_H >10^{23} cm^{-2}) this can be associated with the outer extent of any smaller scale obscuring structure. In contrast to Seyfert galaxies, the molecular gas in LLAGNs has V/σ <1 over an area that is ∼9 times smaller and column densities that are on average ∼3 times smaller. They interpret these results as evidence for a gradual disappearance of the nuclear obscuring structure and consistent to what was previously found by González-Martín et al. (2017) using a sample of 109 AGN using *IRS/Spitzer* observations. Consequently, our result is in line with the results previously observed in the infrared by these authors.

Then, we compare the column density of the reflector and the column density in the line of sight (LOS). Zhao et al. (2021), using all AGN in the 100-month Palermo *Swift*/BAT catalog with line-of-sight column density between 10^{23} and 10^{24} cm^{-2} with available *NuSTAR* data shows that the average torus column density is similar for both Compton thin and CT-AGN, independent of the observing angle, with $\log(N_{\rm H-Tor}$ cm$^{-2})$ ∼24.15. In Fig. 3.7 we compare the column density of the torus and the absorption in the line of sight of our work. The black dotted line represents the mean value of $\log(N_{\rm H-Tor}$ cm$^{-2})$ previously found by Zhao et al. (2021), and the green zone the interval of $\log(N_{\rm H-LOS})$ of their work. Note that our data points and their fit are in agreement in the interval of $\log(L_{\rm H-LOS})$ of their work, i.e. for the moderately obscured sources in our sample. The majority of galaxies with $\log(L_{\rm H-LOS})$<23.0 in our sample are clearly below the value previously obtained, with mean value of $\log(N_{\rm H-Tor}$ cm$^{-2})$ ∼23.36 and $\sigma = 0.59$.

In order to explore any correlation between these parameters, we calculate the Kendall τ correlation coefficient, and we found τ=-0.17 and p-value of 0.51 , suggesting a negative correlation between them. However more data points are necessary to establish any correlation between these parameters. The majority of the objects show a larger $\log(N_{\rm H-Tor})$ than $\log(L_{\rm H-LOS})$, suggesting that the torus is observed through an underdense region, consistent with what was reported by Zhao et al. (2021).

Regarding the covering factor of the torus-like reflector, we obtain a mean value of CF=0.64 and σ=0.26. Note that this parameter could be constrained for seven sources. For another seven sources a best fitting value and an upper limit could be placed

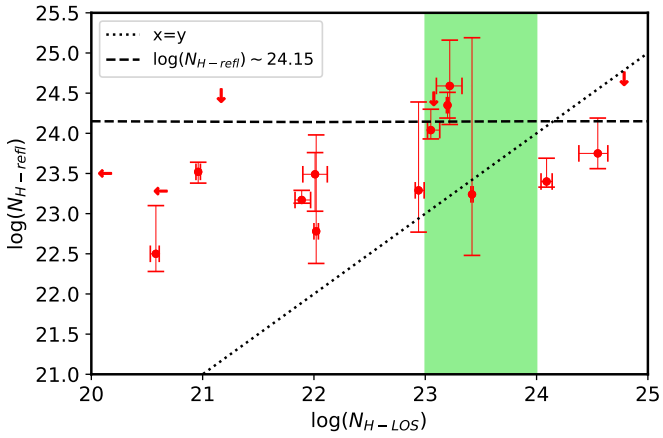

Figure 3.7: Relation between the column density of the torus like reflector (in log) vs. column density in the line of sight (in log). The red points represents the data point of this chapter. The black dashed line correspond to the value obtained by Zhao et al. (2021) and the black dotted represents x=y . The green zone is the interval of the column density in the line of sight analyzed in their work.

and for an additional three a best fitting value and lower limit could be placed. In addition, we analyze the correlation between this parameter and the accretion rate by the Kendall τ correlation test. We find a correlation coefficient τ=-0.06 and p-value of 0.73 suggesting that these parameters are negatively correlated.

Considering a disk like reflector, we could constrain R_f only for one object (NGC 7674), while for the others we only obtain lower limits. Also, this model allows us to study the ionization degree of the disk, however this parameter is also unconstrained with only six galaxies with well constrained values and one upper limit and five lower limits.

The results presented in this paper suggest that the distribution of the gas in the torus in AGN is a dynamic and very complex structure, showing changes in the physical properties of the torus linked to the luminosity of the AGN, in agreement to what was previously found in the literature in the X-rays and the infrared. Certainly combining *XMM-Newton* + *NuSTAR* is key to explore the structure and distribution of the reflector and constrain its physical and geometrical parameters, specially in the low luminosity range.

3.7 Conclusions

In this chapter, we study the reflection of LLAGN by analyzing the broadband X-ray spectra of a BASS/DR2 sample with $\log(\lambda_{Edd}) < -3$ (17 objects) using *XMM-Newton+NuSTAR+Swift* observations and characterizing the reflection features using the `BORUS` model to represent torus reflection and `XILLVER` to model accretion disk emission. The goal was to investigate the accretion mechanism by the relation between the spectral index and the accretion rate as well as constraining the properties of the potential reflector. The main results are summarized below:

1. All objects in our sample are well fitted with a torus-like reflector. Of these, 12 objects are equally well fitted with a torus and a disk (they are indistinguishable from a statistical point of view and visual inspection). These 12 objects have consistent values for the spectral index Γ and luminosities when modeled with a torus or a disk reflector.

2. In our sample we can classify six objects as unobscured ($\log(N_H) < 22$), nine galaxies as obscured galaxies ($22 < \log(N_H) < 24.18$) and two Galaxies can be classified as Compton-thick (using as a threshold $N_H = 1.5 \times 10^{24} cm^{-2}$, or in log 24.18), according with the torus model). According with the disk case, all the galaxies can be classified as Compton thin.

3. Combining *XMM-Newton+ NuSTAR* and considering the reflection component in the spectral fitting, the uncertainties on the spectral index increased and the scatter in the relation between this parameter and the accretion rate is reduced when compared to previous works over similar ranges in accretion rate.

4. Our work is consistent with the negative slope found in previous works at $\log(\lambda_{Edd}) \sim -3$, and a change in the $\Gamma - \log(\lambda_{Edd})$ relation is seen towards high accretion rates, where the slope is known to be positive.

5. The torus has decreasing column density with decreasing accretion rate. AGN at $\log(\lambda_{Edd})$¡-3 has a lower torus column density compared with more luminous AGN. This column density is derived from reflection as opposed to absorption

in the line of sight, so it is representative of the global column density of gas around the X-ray corona.

6. All AGN in our sample with a column density in the line of sight, $\log(N_{H-LOS}) < 23.0$ have a torus with a column density higher than their $\log(N_{H-LOS})$, then the torus could be observed through an underdense region.

CHAPTER 4

Conclusions and future work

AGN are still a mystery and a very hot topic in extragalactic astronomy. In particular, LLAGN are still interesting objects, who clearly shows a different characteristics and properties compared with the luminosity objects. Throughout this thesis, I have presented an spectral study of these objects using data from *XMM-Newton*, *NuSTAR* and *Swift*, which provide a broad band of spectral coverage. The main conclusions obtained from this study are summarized in the following:

- In chapter 2, the case of NGC 3718 is presented, a LLAGN with $L/L_{\rm Edd} \sim 10^{-5}$ and weak reflection.
  - ▷ The importance of including the reflection when analyzing the accretion mechanism in LLAGN and to understand degeneracy with the intrinsic power-law parameters was shown. We see that the type of reflector affects the measurement of the power-law parameters. Both the Γ and the cut-off energy are marginally lower for a disk reflector than for a torus in case of the LLAGN NGC 3718. While one of the disk reflectors results in a low and bounded cut-off energy, the torus reflectors produce a best fitting cut-off energy above the observed energy range and unconstrained to higher values.
  - ▷ This galaxy The X-ray spectrum shows a weak reflection component and consistent with a torus with a low column density covering a large fraction

of the sky and in case of an ionized accretion disk dominating the reflected spectrum, a highly ionized disk is required. Note that even though the reflection is weak it should not be ignored as this could lead to a misinterpretation of the coronal parameters as explained in Chapter 2.

- In chapter 3, observations of a hard X-ray-flux limited sample of LLAGN from BASS/DR2 with accretion rates λ_{Edd}=L_{Bol}/L_{Edd} $<10^{-3}$ using *XMM-Newton*+ *NuSTAR* + *Swift* observations is presented.

  ▷ The uncertainties on the spectral index and the scatter in the relation between this parameter and the accretion rate is reduced when compared to previous works over similar ranges in accretion rate, as a result of combining *XMM-Newton*+ *NuSTAR* and considering the reflection component in the spectral fitting.

  ▷ The relation between $\Gamma - \log(\lambda_{Edd})$ obtained is consistent with the negative slope found in previous works at $\log(\lambda_{Edd})$ $\sim$-3.

  ▷ The relation between the column density of the torus like reflector and the accretion rate is consistent with a torus with a decreasing column density with decreasing accretion rate. This correlation is indicative that AGN at $\log(\lambda_{Edd})$ <-3 has a lower torus column density compared with more luminous AGN.

  ▷ All AGN in the sample presented in this chapter, shows a column density in the line of sight, $\log(N_{H-LOS}) < 23.0$ and a torus with a column density higher than their $\log(N_{H-LOS})$, then the torus could be observed through an underdense region.

All the above results were obtained in order to constrain the reflector parameters and to have an overview of the physics and the structure of the torus and the accretion mechanism of AGN. To increase our knowledge of the AGN further work is clearly needed. This is why we are planning to perform a simultaneous study of the properties of the dust and gas and its relation with the properties of the central engine, in all the AGN in BASS/DR2. This will give us important clues on the torus evolution with the central mechanism.

Appendix A

Effect of the inclusion of the NuSTAR data and reflection models in the spectral index estimation

In this work we use *NuSTAR+XMM-Newton+Swift* observations of a sample of LLAGN from BASS /DR2. We fit all our data with reflection models such as `BORUS` to model a torus-like reflector and `XILLVER` to model a disk-like emission. This may affect the best-fit parameters we obtain compared to results in the literature that use data from other instruments and with other reflection models.

In previous studies, the Γ parameter has large error bars (see, for example, She et al. 2018). To investigate the improvement in the spectral index estimation, we will compare the error bars of the present work using `PEXMON` and *NuSTAR+XMM-Newton+Swift* observations, with those obtained by Ricci et al. (2017a) using `PEXRAV` of the same sample with *Swift/XRT*, *Swift/BAT*, *ASCA*, *Chandra*, and *Suzaku* observations. In Fig. A.1 we compare these error bars, with the blue stars representing the lower limits and the red circles the upper limits of the parameter. The black dotted line represents x=y. We found that the errors in this work are smaller compared to Ricci et al. (2017a). Then, the uncertainties in the photon index improve by including *NuSTAR* data and/or using models such as `BORUS` or `XILLVER`.

Moreover, the Γ-log(λ_{Edd}) relation shows a high scatter (especially in the case of LLAGN), which is still not understood - it could be due to the sensitivity of the measurements or the intrinsic diversity of the nuclei (see Gu & Cao, 2009; Younes et al., 2011; Yang et al., 2015b; She et al., 2018). In this work, we found a significant decrease in the scatter in this correlation. To understand this improvement, the natural question is whether this is related to the inclusion of *NuSTAR* data or could be an effect of using more physical models than BORUS to perform the spectral analysis. In the upper panel in Fig. A.2, the spectral index is plotted against the accretion rate previously determined by Ricci et al. (2017a) using PEXMON. In the middle, we plot the relation between the same sample and the values determined in this work with *PEXMON* including the *NuSTAR* data. Note that we have not indicated the error bars in the accretion rate for illustrative purposes only. There is an improvement in the scatter and error bars, with smaller uncertainties in the photon index than in the results without including the *NuSTAR* data. Thus, the inclusion of the *NuSTAR* data is crucial for the determination of one of the fundamental parameters describing the X-ray emission, like the spectral index Γ. We also investigate the improvement of the estimate of the parameter by including the BORUS model. Comparing the lower panel in Fig. A.2 with the middle panel in the same figure, we see that there is a significant improvement in the scatter of the relation and the uncertainties of the parameter have improved significantly.

We found that we get lower uncertainties with a more physical model like BORUSṪhe process of combining *NuSTAR* data with more physical models like BORUS is key to improve the scatter previously observed in this relationship. With our small error bars and improved constraints on the parameters, we can continue the search for the expected correlations in detail.

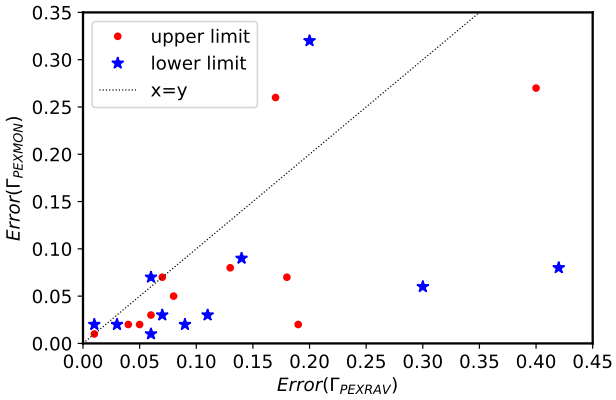

Figure A.1: Relation between the error between our work using *NuSTAR* data and `PEXMON` model and the error values obtained using `PEXRAV` and observation from *Swift/XRT*, *Swift/BAT*, *ASCA*, *Chandra*, and *Suzaku* by Ricci et al. (2017a). The red circles represents the upper limit of the error bar and the blue stars the lower limit. The dotted black line is x=y.

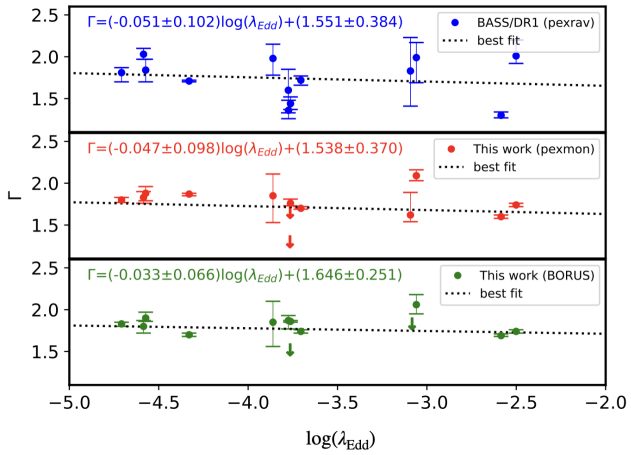

Figure A.2: Relation between the spectral index, Γ, and the accretion rate, $\log(\lambda_{Edd})$. The blue points (top panel) represents the values obtained by (Ricci et al., 2017a) using `PEXRAV` model from the DR1. The middle panel (red points) represents the data points obtained in this work using `PEXMON` reflection model. In the lower panel (green points) are the values obtained in this work using `BORUS` reflection model. In all the panels, the dotted black lines is the best fit model.

APPENDIX B

Notes and comparisons with previous results for individual objects

B.0.1 NGC 3998

This object is spectroscopically classified as a LINER (Heckman, 1980; Ho et al., 1997), and no significant broad-line polarization (Barth et al., 1999). *HST*/WFPC2 optical images revealed an unobscured nucleus and the presence of a bright circumnuclear ionized gas disk (Pogge et al., 2000; Cazzoli et al., 2018).

In radio, it contains a nucleus (Hummel et al., 1984) displaying a weak jet-like northern structure (Filho et al., 2002) and according with Frank et al. (2016), the radio source in NGC 3998 shows two S-shaped lobes.

Pian et al. (2010) found that the spectra of NGC 3998 is better fitted with a simple absorbed power-law model, allowing the overall normalization of the model fit to each detector to be independent. Later, Kawamuro et al. (2016) found the same result using *Suzaku* and *Swift*/BAT and fitting the reflection with `PEXRAV` reflection model. They found that the reflection strength is very weak with an upper-limit of $R_f < 0.10$ and no significant iron Kα line emission is detected, either. They suggest that there is little surrounding matter around the nucleus.

Later, Younes et al. (2019), using *XMM-newton* and *NuSTAR* data found that it is a unabsorbed AGN and its spectrum in the energy range 0.5–60 keV using *NuSTAR* data is best fit with a power-law and cutoff energy. They also studied the reflection hump and found only an upper limit for the reflection fraction, with value R_f <0.3 at 3σ.

In the present work, the data was fitted with PEXMON and the result is consistent with a reflection fraction R_f <0.15. Using BORUS we found that the data is consistent with a Compton thin torus (with $\log(N_{H,refl})$=$22.50^{23.11}_{22.28}$) covering more than 20% of the sky. The inclination in this model is unconstrained. In case of XILLVER we found a model consistent with a disk with $\log \xi$ >3.99 and R_f >0.26. From a statistical point of view, BORUS and XILLVER models show the same χ^2_ν, then they are indistinguishable. All the models are consistent with a column density in the line of sight to classify this galaxy as a Compton-thin source with $\log(N_{H,los}) \sim 20.5$.

B.0.2 NGC 3718

NGC3718 was optically classified as a type 1.9 LINER (Ho et al., 1997). Cazzoli et al. (2018) showed that its broad Hα line is produced in the BLR rather than an outflow. The X-ray spectrum shows a small Fe Kα line, indicative of a reflection component (Younes et al., 2011; Hernández-García et al., 2014; Diaz et al., 2020).

Modelling the reflection with PEXMON we found $R_f < 0.24$. This low reflection signature can be produced by a torus like neutral reflector (BORUS), if it is Compton thin ($\log(N_{H,refl}) = 22.78^{23.98}_{22.38}$), with an unconstrained covering factor (CF <$0.99^{1.00}_{0.05}$). Fitting a disk like reflector instead, using XILLVER requires high levels of ionization with $\log \xi = 3.12^{3.61}_{1.35}$ and a $R_f > 0.86$. A (MEKAL) component was necessary to improve the fit at low energies in all the models. The XILLVER model shows the lowest χ^2_ν (1.097) although all models show similar quality fits (χ^2_ν =1.1 for both PEXMON and BORUS). All the models are consistent with a Compton-thin absorber in the line of sight to the primary coronal emission with $\log(N_{H,los}) \sim 22$.

B.0.3 NGC 4258*

NGC 4258* is a SABbc spiral galaxy, spectroscopically classified as a 1.9 Seyfert (Ho et al., 1997) and as LINER (Balmaverde & Capetti, 2014). This source has a highly obscured central X-ray source and is well known for its anomalous arms, discovered on the basis of Hα imaging (Wilson et al., 2001) and for its nuclear H_2O megamaser, which

traces a dense, edge-on disk on sub-parcsec scales (Watson & Wallin, 1994; Greenhill et al., 1995). The nucleus of NGC 4258* also contains a relativistic radio jet (Doi et al., 2013).

Reynolds et al. (2009) combined *Suzaku*, *XMM-Newton* and *Swift*, and detected robust flux variability of the 6.4 keV iron line and suggested a model in which the line originates from the surface of a warped accretion disk. Also, during their *Suzaku* observation, they detected high amplitude intraday variability, with fluctuations on timescales as short as 5 ksec. Herrnstein et al. (2005) found that the absorption may well arise in the outer layers of the warped geometrically thin accretion disk, further reducing the need for any cold structure other than the accretion disk itself.

NuSTAR and *XMM–Newton* observations of this object are not simultaneous, so we explored possible spectral variability. We found variations in the normalization of the power-law, so we let the normalizations of the power-law free. We then fitted the models. Using `PEXMON` we found $R_f=0.78^{3.744}_{0.20}$. Using `BORUS` we found $\log(N_{H,refl})=23.29^{24.39}_{22.77}$, so borderline Compton-thin/thick torus. The torus covers less than 81% of the sky. Fitting with `XILLVER` we found a disk with $\log\xi$ <1.77 and R_f >3.80. In order to improve the fit in the soft energy band, it was necessary to add three components, modelled with two MEKAL plus a scattered power-law in all the models. The `BORUS` model shows the lowest χ^2_v. All the models are consistent with a Compton-thin absorber in the line of sight to the primary coronal emission with $\log(N_{H,los}) \sim 22.94$.

B.0.4 ESO 253-G003

This source is spectroscopically catalogued as a Seyfert 2 in Véron-Cetty & Véron (2006). The *XMM-Newton* and *NuSTAR* observations of this object are separated by 3 days, so we fit the overlapping 3.0–10.0 keV range of both instruments with a simple absorbed power-law model and checked whether they where consistent. This test showed there was spectral variability between both epochs, with a significant change in the slope Γ. Due to its complexity, the *XMM-Newton* data was excluded for our analysis. We performed a simultaneous fit of the *NuSTAR* and *Swift*/BAT data with `PEXMON` and significant reflection was detected with R_f >1.59. Modelling this reflection with `BORUS` instead of `PEXMON` results in a marginally Compton thin torus reflector ($\log(N_{H,refl})=24.04^{24.30}_{23.93}$) covering more than 73% of the sky. Fitting the reflector using `XILLVER` instead of `BORUS` results in a highly ionized disk with $\log\xi = 2.68^{2.84}_{1.34}$ and

$R_f > 0.85$. The PEXMON model shows the lowest $\chi^2_\nu = 0.89$ although all models show similar quality fits (χ^2_ν=0.905 for BORUS and χ^2_ν=0.903 for XILLVER).

All the models are consistent with a Compton-thin absorber in the line of sight to the primary coronal emission with $\log(N_{H,los}) \sim 23$.

B.0.5 NGC 1052

NGC 1052 is the brightest elliptical galaxy in the Cetus I group. It was optically classified as a LINER by Heckman (1980), then it was classified as LINER type 1.9 (Ho et al., 1997). Cazzoli et al. (2018) proposed that this object presents signs of outflowing winds by using optical 2D spectra.

This source is a radio loud galaxy (Maoz, 2007). At 1.4 GHz *Very Large Array (VLA)* image of NGC 1052 shows a core-dominated radio structure, with only about 15% of the flux density in extended emission: there are two lobes spanning 3 kpc, possibly with hot spots (Wrobel, 1984).

At X-rays, Osorio-Clavijo et al. (2020) presented an extensive study of NGC 1052 using observations from *Chandra*, *XMM-Newton*, *NuSTAR*, and *Suzaku*. They reported variability in the nucleus and found variations both in the intrinsic continuum flux, photon index, and on the obscuration along the line of sight. The reflection component is a steady emission both in flux and shape, fully consistent with reflection in a distant structure, perhaps the torus. They argue that NGC 1052 is in the regime of Compton-thin sources, consistent with the fact that the flux of the reflection component is not dominant in the hard band. In addition, Baloković et al. (2021) using *NuSTAR*, *XMM-Newton*, *Suzaku* and *BeppoSAX* observations and fitting the BORUS model, found covering factor of ∼80-100% and a column density in the range (1-2)$\times 10^{23}$ cm^{-2} and matching with line-of-sight column density.

In this work we fit the data with PEXMON and it is consistent with R_f=$1.26^{3.05}_{0.79}$. Using BORUS model it has ($\log(N_{H,refl})$=$24.35^{24.57}_{24.19}$) so a borderline Compton-thin/thick torus, and CF=$0.50^{0.54}_{0.27}$. Using XILLVER we found $\log\xi$=$1.88^{2.00}_{1.78}$ and R_f >9.18. In case of BORUS it was necessary to add a MEKAL and an scattered power-law to improve the fit. In case of XILLVER, it was necessary to add two components to improve the fit (an absorber and a MEKAL) and in case of PEXMON three components were necessary (MEKAL, power-law and an absorber). From a visual inspection we had to add two Gaussian emission lines centered at: S XIV at 2.4 keV and Si XIII at 1.85 keV. The BORUS model shows the lowest χ^2_ν. All the models are consistent with a Compton-thin

absorber in the line of sight to the primary coronal emission with $\log(N_{H,los}) \sim 23.2$.

B.0.6 NGC 2655

NGC 2655 is the brightest member of a group NBGG 12-10 in the Nearby Galaxy Groups catalog of Tully (1988). It is classified as Seyfert 2 in *Swift*/BAT 70 month catalog (Baumgartner et al., 2013) and as a Type-2 LINER according to the optical classification done by Ho et al. (1997); Véron-Cetty & Véron (2010).

In the X-rays, (González-Martín et al., 2009) found that the 0.2–10 keV *XMM-Newton* spectrum is well modelled by a MEKAL plus 2 power-law components. Kawamuro et al. (2016) fit 2 APEC models to the *Suzaku* spectrum of this galaxy and obtained a line of sight $\log(N_H) = 2.61^{+0.27}_{-0.17} \times 10^{23}$ cm^2 and $\Gamma = 1.77^{+0.19}_{-0.07}$, which are consistent with earlier fits to *ASCA* data (Terashima & Wilson, 2002). Kawamuro et al. (2016) also detected an Fe Kα line at 6.4 keV, which was not detected in the previous *ASCA* and *XMM-Newton* observations Terashima & Wilson (2002); González-Martín et al. (2009).

We fitted the data with `PEXMON` placing an upper limit on R_f <0.52. Modeling the reflector with a torus instead, using `BORUS`, we found a column density of the reflector of $\log(N_{H,refl})$=$23.24^{25.19}_{22.48}$ and CF>0.11. Modeling the reflection with an ionized disk instead of a torus, using `XILLVER` results in a highly ionized disk with a large reflection fraction $\log \xi < 3.55$ and R_f=9.84^{10}_{**}. In the case of `BORUS` was necessary to add two MEKAL and and scattered power-law to improve the fit. In case of `XILLVER` it was necessary to add a MEKAL and an absorber (modelled with zxipcf) components to improve the fit at low energies. In the case of PEXMON an additional MEKAL component was required. The three reflection models showed similar quality fits with $\chi^2_\nu = 0.97$ for `PEXMON`, $\chi^2_\nu = 1.01$ for both `BORUS` and `XILLVER`.

All the models are consistent with a heavy but Compton-thin absorber in the line of sight to the primary coronal emission with $\log(N_{H,los}) \sim 23.4$. We note that if a torus is producing the reflection then its average column density is *lower* than the absorber column density in the line of sight.

B.0.7 NGC 3147*

NGC 3147* is an isolated Seyfert 2 galaxy (Ho et al., 1997) of Hubble morphological type SA(rs)bc. It was suggested as a true type 2 Seyfert candidate (Bianchi et al., 2012),

but later confirmed as an AGN accreting at low rate (Bianchi et al., 2019). In the radio it shows a point-like structure (Ulvestad & Ho, 2001; Krips et al., 2006).

At X-rays, Bianchi et al. (2017) using *NuSTAR* data shows that spectrum of NGC 3147* can be simply modelled by a power-law with a standard $\Gamma \sim 1.7$ and an iron emission line. These spectral properties, together with significant variability on time-scales as short as weeks, strongly support a line-of-sight free of absorption for this source. They suggested that *NuSTAR* data adds further evidence in favour of an X-ray spectrum completely unaffected by absorption, confirming NGC 3147 as one of the best cases of true Type 2 Seyfert galaxies, intrinsically characterised by the absence of a BLR.

NuSTAR and *XMM-Newton* observations of this objects are not simultaneous, then we explored possible spectral variability. We found variations in the normalization if the power-law, so this parameter was left free. We perform a simultaneous fit with this configuration of the data with `PEXMON` and found R_f=$3.99^{6.41}_{0.97}$. We also fitted the data using `BORUS` model and found that the data is consistent with a Compton thin torus with density $\log(N_{H,refl})$=$23.27^{23.94}_{22.98}$ covering less than 89% of the sky. Using the `XILLVER` model the fit was consistent with $\log \xi$=$0.79^{1.15}_{0.06}$ and a $R_f > 0.91$. In case of `PEXMON`, it was necessary to add one component to improve the fit (an warm absorber modelled with zxipcf). `BORUS` model shows the lowest χ^2_ν. All the models are consistent with a Compton-thin absorber in the line of sight to the primary coronal emission with $\log(N_{H,los}) < 20.9$.

B.0.8 NGC 2110*

NGC 2110* is a nearby S0 galaxy (de Vaucouleurs, 1991) Seyfert 2 AGN. NGC 2110* shows a prominent Fe Kα line accompanied by variable intrinsic emission (Hayashi et al., 1996).

Marinucci et al. (2014) report the X-ray spectral analysis of NGC 2110* observed by *NuSTAR* in 2012, when the source was at the highest flux level ever observed, and in 2013, when the source had more typical flux levels. They found an upper limit on $R_f < 0.14$, confirming results from past high-energy *BeppoSAX* and *Suzaku* observations (Malaguti et al., 1999; Reeves et al., 2006; Rivers et al., 2014). Using MyTorus (Murphy & Yaqoob, 2009) to model the reflection, they found a CF of 0.5 with equatorial $N_H = 2.0 \pm 1.1 \times 10^{23}$ cm^{-2}.

We re-examine the 2013 *NuSTAR* observations together with the 2003 *XMM-*

Newton observation in the overlapping 3–10 keV band finding a consistent slope and variable normalization. We therefore fit jointly the broad band spectra with untied normalization for the cutoff power-law component between instruments. Modelling the reflection with PEXMON gives R_f=$1.01^{1.12}_{0.91}$. Modeling the reflection with a torus instead, using BORUS we found a Compton thin reflector with $\log(N_{H,refl})$=$23.49^{23.76}_{23.03}$ covering 13% of the sky. Modeling the reflection with a disk instead of the torus, with XILLVER, we obtain $\log \xi$=$1.99^{2.01}_{1.82}$ and R_f >7.80. In the case of XILLVER it was necessary to add two components to improve the fit at low energies: a MEKAL and zxicpf. In case of BORUS three components were necessary to improve the fit: a scattered power-law, MEKAL and a zxipcf, and in the other case, four components were necessary: 2 zxipcf + 2*MEKAL. The torus reflector produces the best fit with $\chi^2_\nu = 1.03$ while modeling the reflection with either PEXMON or XILLVER gives $\chi^2_\nu \sim 1.3$.

All the models are consistent with a Compton-thin absorber in the line of sight to the primary coronal emission with $\log(N_{H,los}) \sim 22.01$.

B.0.9 LEDA 96373*

LEDA 96373 (also 2MASX J07262635–3554214 or IGR J07264–3553) was first observed at high energies during the all-sky hard X-ray IBIS survey (Krivonos et al., 2007) and reported in the Palermo *Swift*/BAT survey. This galaxy is classified in NED as a Seyfert 2 and as a Compton thick galaxy (Koss et al., 2016).

Landi et al. (2009) observed this galaxy with *Swift* XRT data and reports an excess emission below 2 keV and found that a double power law model is a good fit. They found an intrinsic column density of $\sim 7 \times 10^{22}$ cm^2 and a photon index $\Gamma \sim 2.5$. The source seems to vary by a factor of 2 within a time-scale of few days, with an average 2–10 keV flux of $\sim 4.2 \times 10^{13}$ erg cm^2 s^{-1}.

Simultaneous *NuSTAR* and *XMM-Newton* data are not available for this source, so we explored possible variability. We found variations in the normalization of the power-law, so this parameter was left free. Using PEXMON we found R_f >9.38. Using BORUS we found that the data is consistent with a Compton thin torus ($\log(N_{H,refl})$=$23.40^{23.69}_{23.33}$) covering 59% of the sky. Then we fitted XILLVER and found $\log \xi$=$2.08^{2.17}_{2.03}$ and R_f >9.37. In case of PEXMON and BORUS, it was necessary to add three components to improve the fit (two MEKAL*zxipcf), and in case of XILLVER, (MEKAL + an scatter power-law)*zxipcf components were necessary. The BORUS model shows the lowest χ^2_ν. Note that in case of PEXMON and XILLVER we obtained χ^2_ν >1.4. We clas-

sify this source as a Compton-thick galaxy, consistent with the previous results in the literature. The fit with BORUS requires Compton thick absorption in the line of sight to the coronal emission with $\log(N_{H,los})= 24.09^{24.17}_{24.06}$.

B.0.10 NGC 2992

NGC 2992 is a spiral galaxy classified as a Seyfert 1.9 in the optical. This Seyfert galaxy is a changing-look AGN that varies from type 2 to intermediate type sometimes accompanied by extreme X-ray activity and back, over the span of a few years (Shu et al., 2010) which is attributed to intrinsic variations of the powerlaw flux and to changes in the absorption in the line of sight (Parker et al., 2015; Hernández-García et al., 2017).

At higher X-ray energies, a combined study with *INTEGRAL*, *Swift* and *BeppoSAX* data published by Beckmann et al. (2007) showed that variations in the normalization of the power law were needed when using an absorbed broken power law model to fit the data simultaneously. They found a constant Γ and flux variations by a factor of 11 in timescales of months to years.

We used only the *XMM-Newton* data that overlaps in time with the *NuSTAR* exposure and perform a simultaneous fit. Modelling the reflection with PEXMON results in R_f=$0.37^{0.39}_{0.33}$. Using BORUS model for the reflection instead of PEXMON we found a Compton thin torus reflector with $\log(N_{H,refl})$=$23.17^{23.29}_{23.13}$ covering more than 75% of the sky. Then we fit XILLVER instead of BORUS and the fit was consistent with a disk with $\log\xi$ <0.08 producing R_f >8.80. In the case of PEXMON and BORUS it was necessary to add a MEKAL, an scattered power-law and zxicpf components; in case of XILLVER, two MEKAL components were required. The BORUS model shows the lowest $\chi^2_\nu = 1.08$ and does not show structured residuals above 10 keV. On the other hand, PEXMON and XILLVER show an acceptable $\chi^2_\nu \sim 1.3 - 1.5$ but showing clear residuals at high energies.

All the models are consistent with a Compton-thin absorber in the line of sight to the primary coronal emission with $\log(N_{H,los}) \sim 21.9$.

B.0.11 M51

M51 (also known as Messier 51a, M51a, and NGC 5194) is a very nearby (7.1 Mpc; Takáts & Vinkó 2006) Compton-thick AGN. It hosts a Seyfert 2 nucleus (Ho et al., 1997; Dumas et al., 2011) and shows two radio lobes that are filled with hot X-ray gas

(Terashima et al., 2000) and an outflow of ionised gas (Bradley et al., 2004). This is an interacting spiral galaxy and lies in the constellation Canes Venatici.

Brightman et al. (2018) reported an ULX located close enough to the nucleus of M51 that *NuSTAR* cannot resolve it. They modelled this emission with a cut off power-law model where $\Gamma = 2.21^{-2.16}_{-2.26}$ and $E_{cut} = 1.2^{1.4}_{1.1}$ keV. We included the emission from the ULX using the same model setting Γ and E_{cut} frozen to the parameters already obtained by them. Here we perform a simultaneous fit of the *XMM-Newton*, *NuSTAR* and *Swift*/BAT data. Using `PEXMON` reflection model we find $R_f > 7.86$. Using `BORUS` we found a Compton thick torus reflector ($\log(N_{H,refl}) > 24.68$) covering less than 57% of the sky. Then we fit `XILLVER` and the fit was consistent with an accretion disk with $\log \xi < 1.26$ and with $R_f > 8.96$. In case of `PEXMON` and `XILLVER` one additional component was needed (modelled with zxipcf). All the models give a $\chi^2_\nu \sim 1.4$.. *The fit with* `BORUS` *requires Compton thick absorption in the line of sight to the coronal emission with* $\log(N_{H,l}$ 24.45 otherwise with the other models, a Compton thin column density is a good representation of the data.

B.0.12 NGC 2273*

NGC 2273* is a Seyfert 2 galaxy (Risaliti et al., 1999) considered a Compton-thick due to the detection of a strong Fe Kα line with an equivalent width > 1 keV and a low ratio of L_X/L[OIII] Guainazzi et al. (2005b). Observations with *Suzaku* suggested that the nucleus of NGC 2273 is obscured by a Compton thick column of 1.5×10^{24} cm^2 (Awaki et al., 2009). A hidden nucleus is also suggested by the detection of polarized broad lines (Moran et al., 2000).

We explore the spectral variability in this galaxy between the 2003 *XMM-Newton* observation and the 2014 *NuSTAR* observation by fitting an absorbed power-law plus 6.4 keV Gaussian model to the overlapping 3–10 keV spectra. we find that allowing only the power-law normalization to vary between instruments/epochs produced an acceptable fit with $\chi^2_\nu = 1.08$ and with consistent values of the normalization, so we will fit these spectra with all the parameters tied. We perform a simultaneous fit of the *XMM-Newton*, *NuSTAR* and *Swift*/BAT data with `PEXMON` reflection model and the result is consistent with $R_f > 9.02$. We modeled the reflection using `BORUS` instead of `PEXMON` finding a Compton thin torus ($\log(N_{H,refl}) = 23.75^{24.19}_{23.56}$) with a covering factor lower than 59% of the sky. Modeling the reflection with`XILLVER` instead produced moderately ionized disk with $\log \xi = 2.15^{2.31}_{1.74}$ and $R_f > 8.80$. In all the models was

necessary to add two components (MEKAL and absorber). The torus like reflector modelled with BORUS shows the lowest $\chi^2_\nu = 0.87$, compared to $\chi^2_\nu = 1.1$ for PEXMON and $\chi^2_\nu = 1.27$ for XILLVER. The fit with BORUS requires Compton thick absorption in the line of sight to the coronal emission with $\log(N_{H,los}) > 24.55$.

B.0.13 HE 1136-2304

HE 1136-2304 changed its optical spectral classification from 1994 (Seyfert 2) to 2014 (Seyfert 1.5) and can be considered an optical changing look AGN (Zetzl et al., 2018). HE 1136-2304 has been detected as a variable X-ray source by the *XMM-Newton* slew survey in 2014 (Parker et al., 2016). The 0.2—2 keV flux increased by a factor of about 30 in comparison to the 1990 *ROSAT* All-Sky Survey flux (RASS; Voges et al. (2000)). However, no clear evidence of X-ray absorption variability has been seen.

(Parker et al., 2016) found an absorbing column density on the X-ray spectrum around 10^{21} cm^2 in addition to Galactic absorption. This spectrum shows a moderate soft excess and a narrow Fe line at 6.4 keV and a high energy cut-off at $\sim$ 100 keV.

Although the X-ray flux is highly variable in this source, a joint spectral fitting with *XMM-Newton* and *NuSTAR*could be made since the observations were simultaneous. Using PEXMON reflection model we found $R_f = 3.99^{5.10}_{2.85}$. We also fit the data using BORUS model instead of PEXMON and we found that reflection features can be produced by a Compton thin torus with $\log(N_{H,refl}) = 23.52^{23.64}_{23.38}$ covering 59% of the sky. Modelling the reflection with a disk instead, using XILLVER results in a highly ionized disk with $\log \xi = 3.78^{3.79}_{3.77}$ and $R_f > 1.45$. To improve the fit in the low energy range it was necessary to add one MEKAL component in all the models. The BORUS model shows the lowest $\chi^2_\nu = 1.07$, marginally better than the fit using PEXMON ($\chi^2_\nu = 1.08$) and XILLVER ($\chi^2_\nu = 1.14$).

All models required a Compton-thin absorber on the line of sight to the primary coronal emission, with $\log(N_{H,los}) \sim 20.97$.

B.0.14 IGRJ11366 6002:

We did not find previous information about this galaxy in the literature.

Here we perform the fit of the *NuSTAR* and *Swift*/BAT data. When using PEXMON reflection model we find $R_f = 0.72^{1.57}_{0.49}$. We also fit the data using BORUS model and we found that the data is consistent with a Compton thick reflector torus

($\log(N_{H,refl})$ >24.47) covering $\sim$ 93% of the sky. Using XILLVER, the fit was consistent with $\log\xi$=$3.14^{3.32}_{3.03}$ and R_f >1.12. The XILLVER model shows the lowest χ^2_ν. All the models are consistent with a Compton-thin absorber in the line of sight to the primary coronal emission with $\log(N_{H,los}) < 21.2$.

B.0.15 IC4518A

This galaxy was optically classified as a type 2 Seyfert galaxy (Zaw et al., 2009) and it is classified as a Compton-thin source (Bassani et al., 1999; de Rosa et al., 2008; Hernández-García et al., 2015).

de Rosa et al. (2008) presented a 0.2–200 keV broad-band study of this galaxy with *INTEGRAL*, *XMM-Newton*, *Chandra* and *ASCA* to investigate the continuum shape and the absorbing/reflecting medium properties. They fitted PEXRAV reflection model and found that in this object the presence of the reflection component above 10 keV is statistically required by the data. However, they found a best fit value larger than 1 that they suggested that could be related with the geometry of the reflector, which should be more complex than that used in their work.

Hernández-García et al. (2015) studied *XMM–Newton* data of this galaxy and found variations in an eight-day period, that correspond to a flux variation of 40% (41%) in the soft (0.5 - 2 keV) (hard - 5 - 10.0 keV) energy band.

for this work, *NuSTAR* and *XMM-Newton* data were not simultaneous, thus we explored possible spectral variability. The best fit resulted when the normalization of the power-law is a free parameter. Using PEXMON we found R_f=$3.41^{6.17}_{1.10}$. Using BORUS we find a Compton-thick reflector torus with $\log(N_{H,refl})$=$24.59^{25.16}_{24.11}$, covering more than 39% of the sky. Using XILLVER we found a model consistent with $\log\xi$ <1.73 and R_f >2.94. To improve the fit, three additional components are necessary (MEKAL + scatter power-law)*zxipcf for PEXMON, MEKAL + zxipcf for BORUS) and XILLVER). The BORUS model shows the lowest χ^2_ν. In all the models the absorption in the line of sight is consistent with being Compton-thin ($\log(N_{H,los}) \sim 23.22$).

B.0.16 NGC 7674*

NGC 7674* (Mrk 533) is a nearby luminous infrared galaxy (LIRG). This galaxy is the brightest member of the Hickson 96 interacting galaxy group and it is a known as a Seyfert 2 galaxy with broad Hα and Hβ components in polarized light (Young et al., 1996). Later, Bianchi et al. (2005) classified it as a changing look AGN in the X-ray

range, switching between Compton-thin and Compton thick absorption in the line of sight.

In the X rays, NGC 7674* was first reported to be a reflection-dominated AGN by Malaguti et al. (1998) from *BeppoSAX* X-ray observations carried out in 1996, with the direct (intrinsic) continuum being fully absorbed by a Compton-thick gas column. Bianchi et al. (2005) studied the *XMM-Newton* spectra of this galaxy finding a reflection fraction R_f $\sim$1.5 and argue that the changes on the CT regimes in this galaxy is associated with material in the line of sight. Later, Gandhi et al. (2017) present *NuSTAR*, *Suzaku* and *Swift* reporting a flat X-ray spectrum, suggesting that it is obscured by Compton-thick gas. Based upon long-term flux dimming, previous work suggested the alternate possibility that the source is a recently switched-off AGN with the observed X-rays being the lagged echo from the torus. Their data show the source to be reflection-dominated in hard X-rays, but with a relatively weak neutral Fe Kα emission line and a strong Fe XXVI ionised line. Also, they construct an updated long term X-ray light curve of NGC 7674* and find that the observed 2—10 keV flux has remained constant for the past 20 years.

As this galaxy is a changing look galaxy and the *XMM-Newton* and *NuSTAR* observations are separated by several years, we do not attempt a joint fit and exclude the *XMM-Newton* observation for our analysis. Using `PEXMON` we found that the data is consistent with R_f >2.21. Using `BORUS` to model the reflection instead of `PEXMON` we found a torus with $\log(N_{H,refl})$ >24.43 covering 70% of the sky. Modelling the reflection with a disk instead of a torus, using `XILLVER` the fit was consistent with $\log \xi$=$2.82^{3.02}_{2.77}$ and R_f=$3.25^{6.07}_{2.26}$. The `XILLVER` model shows the lowest $\chi^2_\nu = 1.07$ compared to $\chi^2_\nu = 1.12$ for `PEXMON` and $\chi^2_\nu = 1.14$ for `BORUS`.

We find heavy but Compton thin absorption in the line of sight to the primary coronal emission with $\log(N_{H,los}) \sim 23$ for all the models used .

B.0.17 NGC 5033

NGC 5033 is a nearby spiral galaxy with a low-luminosity Seyfert 1.8 type nucleus (Véron-Cetty & Véron, 2010) with a point-like central X-ray source (Terashima et al., 1999). This galaxy has been alternatively classified as a Seyfert of type 1.5 (Ho et al., 1997). This object has a giant neighbor within a short distance: NGC 5005, a Seyfert SAB(rs) galaxy.

In the radio, it is predominated by a compact core (Ho & Ulvestad, 2001), and

showing extended jet-like features to the East-West (Pérez-Torres & Alberdi, 2007).

In the X-rays, Terashima et al. (1999) using ASCA observations found a point-like X-ray source in the 2–10 a keV band. Their X-ray light curve showed variability on a timescale of $\sim 10^4$ s with an amplitude of $\sim$20%.

In this work, we combine the *NuSTAR* observations and perform a simultaneous fit of the *XMM-Newton*, *NuSTAR* and *Swift*/BAT data. Using `PEXMON` reflection model results in $R_f > 1.0$. Using `BORUS` we found that the data is consistent with a Compton thin torus ($\log(N_{H,refl})$=$23.49^{23.69}_{23.34}$) covering 77% of the sky. Then we fit `XILLVER` instead of `BORUS` and the fit was consistent with $\log \xi < 1.0$ and $R_f > 4.88$. To improve the fit, it was necessary to two MEKAL to `XILLVER`. The `BORUS` and `XILLVER` have the same χ^2_ν, then they are indistinguishable. In all the models the required line of sight absorption is compatible with being Compton-thin ($\log(N_{H,los}) < 21.0$).

APPENDIX C

Tables

Table C.1: Observational Details.

Name	Instrument	ObsID	Date	R	Exp. Time
				(″)	(ks)
(1)	(2)	(3)	(4)	(5)	(6)
NGC 3998	*XMM-Newton*	0790840101	2016-10-26	49	25
	NuSTAR	60201050002	2016-10-25	49	103
NGC 3718	*XMM-Newton*	0795730101	2017-10-24	49	38
	NuSTAR	60301031002	2017-10-24	49	24
NGC 4258*	*XMM-Newton*	0400560301	2006-11-17	49	64
	NuSTAR	60101046004	2016-01-10	49	103
ESO 253-G003*	*XMM-Newton*	0762920501	2015-08-19	49	27
	NuSTAR	60101014002	2015-08-21	49	22
NGC 1052	*XMM-Newton*	0790980101	2017-01-17	49	70
	NuSTAR	60201056002	2017-01-17	49	59
NGC 2655	*XMM-Newton*	0301650301	2016-11-10	49	11
	NuSTAR	60160341004	2016-11-10	49	15
NGC 3147*	*XMM-Newton*	0405020601	2006-10-06	49	17
	NuSTAR	60101032002	2015-12-27	49	49
NGC 2110*	*XMM-Newton*	0145670101	2003-03-05	49	59
	NuSTAR	60061061002	2012-10-05	49	15
		60061061004	2013-02-14	49	12
LEDA 96373*	*XMM-Newton*	0674940101	2012-04-09	49	56
	NuSTAR	60061073002	2014-07-31	49	22
NGC 2992	*XMM-Newton*	0840920201	2019-05-07	49	134
		0840920301	2019-05-09	49	134
	NuSTAR	90501623002	2019-05-10	49	57
M 51	*XMM-Newton*	0852030101	2019-07-11	49	77
	NuSTAR	60501023002	2019-07-10	49	169

Table C.2: Cont: Observational Details

Name	Instrument	ObsID	Date	R (″)	Exptime (ks)
(1)	(2)	(3)	(4)	(5)	(6)
NGC 2273*	*XMM-Newton*	0140951001	2003-09-05	49	13
	NuSTAR	60001064002	2014-03-23	49	23
HE 1136-2304	*XMM-Newton*	0741260101	2014-07-02	49	110
	NuSTAR	80002031003	2014-07-02	49	63
		80002031002	2014-07-02	49	23
IC 4518A	*XMM-Newton*	0401790901	2006-08-07	11	134
		0406410101	2006-08-15	49	25
	NuSTAR	60061260002	2013-08-02	49	7
NGC 7674*	*XMM-Newton*	0200660101	2004-06-02	49	10
	NuSTAR	60001151002	2014-09-30	49	51
IGRJ11366-6002	*NuSTAR*	60061213002	2014-10-29	49	21
NGC 5033	*XMM-Newton*	0871020101	2020-12-10	49	21
	NuSTAR	60601023002	2020-12-08	49	104
		60601023004	2020-12-12	49	53

Notes: (Col. 1) Name, (Col. 2) instrument, (Col. 3) obsID, (Col. 4) date, (Col. 5) radii of the extraction region and (Col. 5) exposure time (ks). Objects with * symbols are the galaxies with not simultaneous observations.

Table C.3: Spectral variability not simultaneous data between 3.0-10.0 keV.

Name	Instrument	ObsID	Model	Γ	N_H	**Norm PL**	Norm G	Flux	χ^2/d.o.f	χ^2_ν	Notes
(1)	(2)	(3)	(4)	(5)	(6)	**(7)**	(8)	(9)	(10)	(11)	(12)
NGC 4258*	*XMM-Newton*	0400560301	PL	#	#	$\mathbf{1.48}^{1.92}_{1.42}$	-	$3.84^{5.35}_{1.14}$	-	-	We select
	NuSTAR	60101046004A		$1.61^{1.77}_{1.18}$	$7.67^{8.66}_{6.90}$	$\mathbf{0.84}^{1.11}_{0.81}$	-	$2.18^{3.06}_{0.65}$	443.2/387	1.145	PL norm
		60101046004B		#	#	#	-	-	-	-	variable
ESO253-G003*	*XMM-Newton*	0762920501	PL	$\mathbf{1.76}^{1.92}_{1.11}$	#	#	-	$0.45^{0.51}_{**}$	-	-	We select
	NuSTAR	60101014002A		$\mathbf{1.23}^{1.33}_{**}$	$2.29^{5.13}_{**}$	$0.19^{0.30}_{0.11}$	-	$1.07^{1.24}_{**}$	119.4/86	1.389	Γ
		60101014002B		#	#	#	-	-	-	-	variable
NGC 3147*	*XMM-Newton*	0405020601	PL	#	#	$\mathbf{0.53}^{0.78}_{0.38}$	-	$1.14^{1.19}_{1.05}$	-	-	We select
	NuSTAR	60101032002A		$1.79^{2.02}_{1.69}$	$2.98^{4.80}_{1.47}$	$\mathbf{1.05}^{1.56}_{0.98}$	-	$2.19^{2.25}_{2.03}$	243.5/217	1.122	PL norm
		60101032002B		#	#	#	-	-	-	-	variable
NGC 2110*	*XMM-Newton*	0145670101	PL+G	#	#	$\mathbf{6.78}^{7.46}_{6.34}$	#	$25.00^{30.10}_{21.28}$	-	-	We select
	NuSTAR	60061061004A		$1.53^{1.61}_{1.50}$	$3.84^{4.14}_{3.57}$	$\mathbf{37.08}^{40.83}_{34.72}$	$0.049^{0.53}_{0.045}$	$134.85^{163.9}_{112.7}$	527.3/453	1.164	PL norm
		60061061004B		#	#	#	#	-	-	-	variable
LEDA 96373*	*XMM-Newton*	0674940101	PL+G	#	#	$0.13^{0.23}_{0.09}$	#	$1.14^{1.67}_{0.16}$	-	-	We select PL norm tied, they
	NuSTAR	60061073002A		$0.93^{1.13}_{0.70}$	$13.59^{17.14}_{10.32}$	$0.17^{0.31}_{0.11}$	$0.022^{0.24}_{0.20}$	$1.40^{2.19}_{0.16}$	245.2/141	1.739	are consistent. The model
		60061073002B		#	#	#	#	-	-	-	is not enough to fit the data
NGC 2273*	*XMM-Newton*	0140951001	PL+G	#	#	$0.49^{1.40}_{0.04}$	#	$0.93^{1.48}_{0.19}$	-	-	We select
	NuSTAR	60001064002A		$1.56^{1.74}_{0.79}$	$30.04^{44.99}_{21.21}$	$0.53^{1.75}_{0.31}$	$0.037^{0.047}_{0.031}$	$0.98^{1.47}_{0.19}$	109.7/102	1.075	PL norm tied, they
		60001064002B		#	#	#	#	-	-	-	are consistent

(Col. 1) name, (Col. 2) instrument, (Col. 3) obsID, (Col. 4) model, where "PL" represents the power-law and "G" a Gaussian component at 6.4 keV and σ=0.01 keV. (Col. 5) photon index, (Col. 6) column density (10^{22} cm^{-2}), (Col. 7) Power-law normalization (10^{-3}), (Col. 8) Normalization of the Gaussian component (10^{-3}), (Col. 9) Flux (10^{-12} erg cm^{-2} s^{-1}), (Col. 10 and 11) χ^2/d.o.f., and χ^2_ν, (Col. 12) Notes about selection of the model. The case where the Normalization of the power-law (Norm PL) is a free parameter between the *XMM-Newton* and *NuSTAR* data is marked in bold face. The parameter in this table marked with means that is tied to FPMA/*NuSTAR*. - denotes that these were not require to improve the fit.

Table C.4: Spectral variability not simultaneous data between 3.0-10.0 keV.

Name	Instrument	ObsID	Model	Γ	N_H	**Norm PL**	Norm G	Flux	χ^2/d.o.f	χ^2_ν	Notes
(1)	(2)	(3)	(4)	(5)	(6)	**(7)**	(8)	(9)	(10)	(11)	(12)
NGC 7674*	*XMM-Newton*	0200660101	PL+G	#	#	$0.20^{0.50}_{**}$	#	$0.052^{1.243}_{0.029}$	-	-	Is a changing look, we
	NuSTAR	60001151002A		$1.71^{2.17}_{1.34}$	$18.28^{26.89}_{13.05}$	$0.49^{1.33}_{0.24}$	$0.0059^{0.0079}_{0.0037}$	$0.79^{1.43}_{0.03}$	12.4/76	1.479	did not combine the data.
		60001151002B		#	#	#	#	-	-		
IC 451A*	*XMM-Newton*	0406410101	PL+G	#	#	$\mathbf{0.97}^{1.06}_{0.56}$	#	$1.64^{3.46}_{0.09}$	-	-	We select
	NuSTAR	60061260002A		$1.70^{1.83}_{1.36}$	$21.57^{24.35}_{18.30}$	$\mathbf{2.64}^{2.89}_{1.44}$	$0.015^{0.017}_{0.012}$	$4.29^{9.22}_{0.09}$	143.4/123	1.166	PL norm
		60061260002B		#	#	#	#	-	-	-	variable

Table C.5: Final compilation of the coronal parameters of the best-fit models for the sample. Photon index (Γ), the high energy cut-off (E_cut) in keV, χ^2/d.o.f and χ^2_ν for PEXMON, BORUS (B) and XILLVER (X). BM shows the model with the lowest χ^2_ν. The symbol ? represents that according with their χ^2_ν values, the models are indistinguishable. Objects with * symbols are the galaxies with not simultaneous observations. The quantities in this table marked with ** are unconstrained errors.

	PEXMON			
Name	Γ	$E_{\rm cut}$ (keV)	χ^2/d.o.f	χ^2_ν
NGC 3998	$1.80^{1.83}_{1.77}$	$81.78^{123.99}_{61.07}$	840.7/896	0.938
NGC 3718	$1.88^{1.96}_{1.79}$	$111.57^{994.30}_{55.39}$	408.2/371	1.100
NGC 4258*	$1.83^{1.90}_{1.76}$	$142.15^{396.60}_{93.54}$	740.0/666	1.111
ESO 253-G003*	$1.30^{1.65}_{**}$	$79.45^{2000.0}_{**}$	107.1/121	0.885
NGC 1052	$1.76^{1.81}_{1.73}$	$134.55^{223.48}_{95.96}$	956.7/872	1.097
NGC 2655	$1.85^{2.11}_{1.53}$	$209.70^{**}_{59.54}$	171.8/168	1.022
NGC 3147*	$1.71^{1.75}_{1.66}$	$65.65^{138.94}_{**}$	394.3/378	1.043
NGC 2110*	$1.87^{1.88}_{1.85}$	$3000.0^{**}_{1419.73}$	1600.4/1261	1.269
LEDA 96373*	$1.20^{1.30}_{**}$	$38.02^{44.08}_{33.40}$	403.1/276	1.460
NGC 2992	$1.60^{1.62}_{1.58}$	$55.28^{58.83}_{51.78}$	2092.1/1619	1.2922
M 51	$1.90^{2.06}_{1.76}$	$3000^{**}_{381.74}$	482.9/341	1.416
NGC 2273*	$1.80^{2.10}_{1.51}$	$57.86^{313.43}_{**}$	226.8/197	1.151
HE 1136-2304	$1.74^{1.76}_{1.72}$	$97.20^{136.22}_{77.12}$	1066.0/987	1.080
IGRJ11366 6002	$2.09^{2.16}_{2.03}$	$2999.36^{**}_{2999.19}$	254.1/240	1.059
IC 4518A*	$1.62^{1.89}_{1.54}$	$50.0^{85.95}_{**}$	245.7/215	1.143
NGC 7674*	$1.82^{2.02}_{1.45}$	$180.88^{**}_{107.29}$	189.0/169	1.118
NGC 5033	$1.70^{1.72}_{1.69}$	$50^{55.13}_{**}$	1215.4/1059	1.148

Table C.6: Cont.: Final compilation of the coronal parameters of the best-fit models for the sample.

	BORUS				XILLVER				
Name	Γ	$E_{\rm cut}$ (keV)	χ^2/d.o.f	χ^2_ν	Γ	$E_{\rm cut}$ (keV)	χ^2/d.o.f	χ^2_ν	BM
NGC 3998	$1.83^{1.85}_{1.80}$	$119.02^{173.06}_{92.00}$	837.6/895	0.936	$1.79^{1.83}_{1.76}$	$568.75^{**}_{108.96}$	838.0/895	0.936	?
NGC 3718	$1.90^{1.97}_{1.86}$	$252.99^{**}_{80.04}$	405.9/369	1.100	$1.86^{1.95}_{1.77}$	$142.89^{1140.6}_{64.63}$	404.8/369	1.097	X
NGC 4258*	$1.80^{1.87}_{1.72}$	$371.07^{**}_{120.95}$	731.5/665	1.100	$1.48^{1.53}_{1.43}$	$30.59^{46.59}_{**}$	812.7/666	1.220	B
ESO 253-G003*	$1.40^{1.52}_{**}$	$90.08^{187.57}_{38.99}$	108.6/120	0.905	$1.41^{1.62}_{**}$	$228.04^{**}_{89.35}$	108.37/120	0.903	X
NGC 1052	$1.86^{1.87}_{1.85}$	$2000.0^{**}_{374.77}$	949.9/872	1.089	$1.45^{1.57}_{1.40}$	$40.39^{42.05}_{38.09}$	1286.0/872	1.4747	B
NGC 2655	$1.85^{2.10}_{1.56}$	$221.28^{2000.0}_{**}$	171.2/167	1.025	$1.90^{2.23}_{1.78}$	$230.86^{1183.5}_{79.97}$	178.1/169	1.054	B
NGC 3147*	$1.76^{1.79}_{1.74}$	$2000^{**}_{177.53}$	379.3/377	1.006	$1.72^{1.80}_{1.64}$	$71.68^{191.61}_{44.69}$	384.7/377	1.020	B
NGC 2110*	$1.70^{1.72}_{1.68}$	$354.86^{465.42}_{303.67}$	1293.2/1260	1.026	$1.82^{1.83}_{1.81}$	$1870.56^{**}_{764.82}$	1564.3/1263	1.239	B
LEDA 96373*	$1.87^{1.93}_{1.77}$	$2000.0^{**}_{596.45}$	309.9/275	1.127	$1.77^{1.84}_{1.69}$	$114.47^{184.62}_{53.53}$	461.0/276	1.670	B
NGC 2992	$1.69^{1.71}_{1.68}$	$259.51^{376.14}_{183.62}$	1738.7/1618	1.075	$1.61^{1.62}_{1.60}$	$64.80^{69.13}_{61.66}$	2140.5/1620	1.3213	B
M 51	$1.56^{1.76}_{**}$	$2000^{**}_{70.89}$	470.5/343	1.372	$1.90^{2.24}_{1.72}$	$3000^{**}_{395.18}$	493.8/341	1.448	B
NGC 2273*	$1.44^{1.80}_{**}$	$60.41^{**}_{36.33}$	173.0/196	0.882	$2.14^{2.27}_{1.99}$	$575.64^{**}_{298.54}$	246.3/196	1.257	B
HE 1136-2304	$1.74^{1.76}_{1.72}$	$394.08^{**}_{172.4}$	1054.5/986	1.069	$1.567^{1.598}_{1.553}$	$1014.66^{**}_{554.79}$	1126.3/986	1.142	B
IGRJ11366 6002	$2.06^{2.18}_{1.95}$	$198.01^{**}_{103.71}$	249.4/239	1.043	$1.90^{1.97}_{1.84}$	$2000^{**}_{249.04}$	241.34/239	1.010	X
IC 4518A*	$1.57^{1.83}_{**}$	$34.19^{75.18}_{**}$	222.6/217	1.026	$1.76^{1.92}_{1.66}$	$73.03^{173.61}_{44.59}$	250.4/217	1.154	B
NGC 7674*	$1.47^{1.58}_{**}$	$30^{40.22}_{**}$	190.7/168	1.135	$1.42^{1.84}_{**}$	$95.68^{116.13}_{67.58}$	179.4/168	1.068	X
NGC 5033	$1.74^{1.76}_{1.72}$	$142.95^{200.67}_{102.90}$	1177.4/1058	1.113	$1.77^{1.81}_{1.72}$	$61.35^{74.93}_{48.78}$	1193.8/1054	1.133	?

Table C.7: Final compilation of the reflector parameters of the best-fit models for the sample. Reflection fraction (R_f), the inclination (Incl) and the ionization degree (in log) of PEXMON and XILLVER (X) models. The column density of the torus like reflector ($\log(N_{H,refl})$), the covering factor (CF) and the inclination ($\mathrm{Cos}(\theta_{incl})$) for BORUS (B). BM shows the model with the lowest χ^2_ν. The symbol ? represents that according with their χ^2_ν values, the models are indistinguishable. Objects with * symbols are the galaxies with not simultaneous observations. The quantities in this table marked with ** are unconstrained errors except in the case of the CF, where we report the cases the error is limited by the model.

	PEXMON			
Name	R_f	Incl	χ^2/d.o.f.	χ^2_ν
NGC 3998	$0.07^{0.15}_{**}$	$0.01^{90.0}_{**}$	840.7/896	0.938
NGC 3718	$0.01^{0.24}_{**}$	0.02^{90}_{**}	408.2/371	1.100
NGC 4258*	$0.78^{3.44}_{0.20}$	$80.14^{87.67}_{**}$	740.0/666	1.111
ESO 253-G003	$10.00^{**}_{1.59}$	$86.60^{89.03}_{69.93}$	107.1/121	0.885
NGC 1052	$1.26^{3.05}_{0.79}$	$74.71^{84.16}_{61.54}$	956.7/872	1.097
NGC 2655	$0.07^{0.51}_{**}$	$0.01^{80.10}_{**}$	171.8/168	1.022
NGC 3147*	$3.99^{6.41}_{0.97}$	$87.11^{88.19}_{**}$	394.3/378	1.043
NGC 2110*	$1.01^{1.12}_{0.91}$	$79.58^{80.68}_{79.27}$	1600.4/1261	1.2691
LEDA 96373*	$10.00^{**}_{9.38}$	$65.49^{69.11}_{50.08}$	403.1/276	1.460
NGC 2992	$0.37^{0.39}_{0.33}$	$0^{11.76}_{**}$	2092.1/1619	1.292
M 51	$10.00^{**}_{7.86}$	$0.06^{52.70}_{**}$	482.9/341	1.416
NGC 2273*	$10.00^{**}_{9.02}$	$0.09^{52.65}_{**}$	226.8/197	1.151
HE 1136-2304	$3.99^{5.10}_{2.85}$	$87.77^{88.41}_{86.75}$	1066.0/987	1.080
IGRJ 11366-6002	$0.72^{1.57}_{0.49}$	$22.92^{75.39}_{**}$	254.1/240	1.059
IC 4518A*	$3.41^{6.17}_{1.10}$	$75.58^{83.72}_{**}$	245.7/215	1.143
NGC 7674*	$3.22^{**}_{2.21}$	$18.17^{80.86}_{**}$	189.0/169	1.118 NGC 5033
$1.35^{**}_{1.00}$	$78.47^{87.66}_{56.20}$	1232.9/1058	1.165	

Table C.8: Cont.: Final compilation of the reflector parameters of the best-fit models for the sample.

	BORUS					XILLVER					
Name	$\log(N_{H,refl})$	CF	$\cos(\theta_{incl})$	χ^2/d.o.f.	χ^2_ν	$\log \xi$	R_f	Incl (deg)	χ^2/d.o.f.	χ^2_ν	BM
NGC 3998	$22.50^{23.11}_{22.28}$	$1.00^{1.00}_{0.20}$	$0.18^{**}_{0.05}$	837.6/895	0.936	$4.07^{**}_{3.99}$	$4.1^{**}_{0.26}$	$18.33^{58.68}_{0.94}$	837.95/895	0.936	?
NGC 3718	$22.78^{23.98}_{22.38}$	$0.99^{1.0}_{0.05}$	$0.30^{0.95}_{**}$	405.9/369	1.100	$3.12^{3.61}_{1.35}$	$4.91^{**}_{0.86}$	$88.74^{89.93}_{81.30}$	404.8/369	1.097	X
NGC 4258*	$23.29^{24.39}_{22.77}$	$0.38^{0.81}_{0.05}$	$0.95^{**}_{0.27}$	731.5/665	1.100	$1.66^{1.77}_{**}$	$9.33^{**}_{3.80}$	$89.02^{89.44}_{54.57}$	812.7/666	1.220	B
ESO 253-G003	$24.04^{24.30}_{23.93}$	$0.73^{1.00}_{0.05}$	$0.76^{0.94}_{**}$	108.6/120	0.905	$2.68^{2.84}_{1.34}$	$2.08^{**}_{0.85}$	$65.99^{83.64}_{**}$	108.3/120	0.903	X
NGC 1052	$24.35^{24.51}_{24.19}$	$0.50^{0.54}_{0.27}$	$0.55^{0.73}_{0.45}$	949.9/872	1.089	$1.88^{2.00}_{1.78}$	$10.00^{**}_{9.18}$	$88.12^{88.29}_{86.06}$	1286.0/872	1.4747	B
NGC 2655	$23.24^{25.19}_{22.48}$	$0.83^{1.00}_{0.11}$	$0.85^{**}_{0.05}$	159.4/167	0.954	$1.85^{3.55}_{**}$	9.84^{10}_{**}	$89.09^{89.51}_{24.98}$	178.1/169	1.054	B
NGC 3147*	$23.27^{23.94}_{22.98}$	$0.89^{1.00}_{0.26}$	$0.90^{0.05}_{**}$	379.3/377	1.006	$0.79^{1.15}_{0.06}$	$9.48^{**}_{0.91}$	$87.61^{88.14}_{62.87}$	384.7/377	1.020	B
NGC 2110*	$23.49^{23.76}_{23.03}$	$0.13^{0.30}_{0.11}$	$0.45^{0.73}_{0.23}$	1293.2/1260	1.026	$1.99^{2.01}_{1.82}$	$10.00^{**}_{7.80}$	$88.94^{89.05}_{88.47}$	1564.3/1263	1.236	B
LEDA 96373*	$23.40^{23.69}_{23.33}$	$0.59^{0.76}_{0.41}$	$0.95^{**}_{0.59}$	309.9/275	1.127	$2.08^{2.17}_{2.03}$	$10.00^{**}_{9.37}$	$19.10^{43.32}_{1.51}$	461.0/276	1.670	B
NGC 2992	$23.17^{23.29}_{23.13}$	$0.75^{1.00}_{0.05}$	$0.85^{**}_{0.63}$	1738.7/1618	1.075	$0.006^{0.08}_{**}$	$10.00^{**}_{8.80}$	$88.41^{88.55}_{88.11}$	2140.5/1620	1.3213	B
M 51	$25.40^{**}_{24.68}$	$0.34^{0.57}_{0.05}$	$0.95^{**}_{0.80}$	470.5/343	1.372	$0.05^{1.26}_{**}$	$10.00^{**}_{8.96}$	$18.00^{47.80}_{**}$	493.8/341	1.448	B
NGC 2273*	$23.75^{24.19}_{23.56}$	$0.15^{0.59}_{0.05}$	$0.94^{**}_{0.72}$	173.5/196	0.882	$2.14^{2.31}_{2.02}$	$9.99^{**}_{8.80}$	$8.90^{45.34}_{**}$	246.3/196	1.257	B
HE 1136-2304	$23.52^{23.64}_{23.38}$	$0.59^{0.68}_{0.50}$	$0.05^{0.39}_{**}$	1054.5/986	1.069	$3.78^{3.79}_{3.77}$	$9.93^{**}_{1.45}$	$0.05^{26.84}_{**}$	1126.3/986	1.142	B
IGRJ 11366-6002	$24.76^{**}_{24.47}$	$0.93^{0.99}_{0.78}$	$0.94^{0.95}_{0.87}$	249.4/239	1.043	$3.14^{3.32}_{3.03}$	$3.85^{**}_{1.12}$	$66.72^{82.74}_{10.12}$	141.34/239	1.010	X
IC 4518A*	$24.59^{25.16}_{24.11}$	$0.56^{1.00}_{0.39}$	$0.55^{0.72}_{0.30}$	222.6/217	1.026	$1.35^{1.73}_{**}$	$9.99^{**}_{2.94}$	$82.47^{84.84}_{59.56}$	250.4/217	1.154	B
NGC 7674*	$25.40^{**}_{24.43}$	$0.70^{0.90}_{0.52}$	$0.95^{**}_{0.84}$	190.7/168	1.135	$2.82^{3.02}_{2.77}$	$3.25^{6.07}_{2.26}$	$0.0001^{71.42}_{**}$	179.4/168	1.068	X
NGC 5033	$23.49^{23.69}_{23.34}$	$0.77^{0.92}_{0.53}$	$0.95^{**}_{0.76}$	1177.4/1058	1.113	$0.45^{1.00}_{**}$	$10.00^{**}_{4.88}$	$87.41^{87.83}_{84.68}$	1193.8/1054	1.133	?

Table C.9: Summary of other parameters of the best fit model. Name, column density in the hard energy band ($\log(N_{\mathrm{H},los})$), column density in the soft energy band ($\log(N_{\mathrm{H},ext})$), temperature of the thermal components (kT_1 and kT_2). BM means the best model added to the reflection and the central emission to improve the fit. ME means MEKAL, PL power-law in the scattered component and ab the warm absorption modelled with zxipcf in Xspec. - denotes that these were not require to improve the fit. Objects with * symbols are the galaxies with not simultaneous observations.

	PEXMON				
Name	$\log(N_{\mathrm{H},los})$	$\log(N_{\mathrm{H},ext})$	kT_1	kT_2	BM
NGC 3998	$20.54^{20.62}_{20.46}$	-	-	-	-
NGC 3718	$22.03^{22.07}_{21.98}$	-	$0.89^{**}_{0.69}$	-	ME
NGC 4258*	$22.94^{22.95}_{22.92}$	$20.08^{20.52}_{**}$	$0.58^{0.59}_{0.57}$	$0.20^{0.21}_{0.19}$	2ME+PL
ESO 253-G003*	$22.78^{23.09}_{22.15}$	-	-	-	-
NGC 1052	$23.16^{23.18}_{23.15}$	$20.53^{20.70}_{**}$	$0.65^{0.68}_{0.61}$	-	ab*(ME+PL)
NGC 2655	$23.31^{23.36}_{23.19}$	-	$0.65^{0.69}_{0.61}$	$0.09^{0.43}_{**}$	ab*2ME
NGC 3147*	$20.54^{20.61}_{**}$	-	-	-	ab
NGC 2110*	$21.76^{21.85}_{21.72}$	-	$0.65^{0.67}_{0.64}$	$0.09^{0.39}_{**}$	2ME*2ab
LEDA 96373*	$22.67^{22.76}_{22.57}$	-	$0.63^{0.76}_{0.55}$	$0.22^{0.23}_{0.20}$	2ME*ab
NGC 2992	$21.89^{21.91}_{21.88}$	$21.20^{21.26}_{21.11}$	$0.81^{0.84}_{0.78}$	-	(PL+ME)*ab
M 51	$22.36^{22.88}_{**}$	-	-	-	ab
NGC 2273*	$23.15^{23.31}_{22.75}$	-	$0.71^{0.79}_{0.52}$	-	ME*ab
HE 1136-2304	$20.96^{20.98}_{20.94}$	-	$0.59^{0.67}_{0.51}$	-	ME
IGRJ11366 6002	$21.15^{22.24}_{**}$	-	-	-	-
IC 4518A*	$23.22^{23.30}_{23.16}$	-	$0.71^{0.75}_{0.59}$	-	ME*ab
NGC 7674*	$23.06^{23.21}_{22.98}$	-	-	-	-
NGC 5033	$20.0^{20.12}_{**}$	-	-	-	-

Table C.10: Cont.:Summary of other parameters of the best fit model.

	BORUS					XILLVER				
Name	$\log(N_{\mathrm{H},los})$	$\log(N_{\mathrm{H},ext})$	kT_1	kT_2	BM	$\log(N_{\mathrm{H},los})$	$\log(N_{\mathrm{H},ext})$	kT_1	kT_2	BM
NGC 3998	$20.58^{20.61}_{20.53}$	-	-	-	-	$20.51^{20.62}_{20.40}$	-	-	-	-
NGC 3718	$22.02^{22.07}_{21.99}$	-	$0.88^{**}_{0.67}$	-	ME	$22.03^{22.08}_{21.98}$	-	$0.89^{**}_{0.69}$	-	ME
NGC 4258*	$22.94^{22.96}_{22.92}$	$20.08^{2}_{**}0.63$	$0.58^{0.59}_{0.57}$	$0.20^{0.21}_{0.19}$	2ME+PL	$22.85^{22.86}_{22.83}$	$20.08^{20.36}_{**}$	$0.595^{0.604}_{0.586}$	$0.197^{0.208}_{0.185}$	2ME+PL
ESO 253-G003*	$23.05^{23.16}_{22.94}$	-	-	-	-	$22.94^{23.12}_{22.74}$	-	-	-	-
NGC 1052	$23.20^{23.21}_{23.19}$	$20.71^{20.82}_{20.60}$	$0.63^{0.67}_{0.59}$	-	ME+PL	$23.83^{23.87}_{23.76}$	-	$0.86^{0.87}_{0.85}$	-	ab*ME
NGC 2655	$23.42^{23.51}_{23.25}$	$20.32^{21.79}_{**}$	$0.62^{0.70}_{0.58}$	$0.15^{0.30}_{**}$	2ME+PL	$23.29^{23.37}_{23.22}$	-	$0.66^{0.69}_{0.62}$	-	ME*ab
NGC 3147*	$20.54^{20.62}_{**}$	-	-	-	-	$22.78^{20.98}_{**}$	-	-	-	-
NGC 2110*	$22.01^{22.06}_{21.96}$	$21.27^{21.82}_{**}$	$0.71^{0.72}_{0.69}$	-	(ME+PL)*ab	$21.88^{21.93}_{21.83}$	-	$0.70^{0.71}_{0.69}$	-	ME*ab
LEDA 96373*	$24.09^{24.17}_{24.06}$	-	$0.59^{0.76}_{0.41}$	$0.22^{0.23}_{0.19}$	2ME*ab	$23.56^{23.62}_{23.49}$	$23.11^{23.18}_{23.03}$	$0.79^{0.80}_{0.76}$	-	(ME+PL)*ab
NGC 2992	$21.89^{21.90}_{21.88}$	$20.00^{21.25}_{**}$	$0.79^{0.82}_{0.76}$	-	(PL+ME)*ab	$21.90^{21.89}_{21.88}$	-	$0.63^{0.65}_{0.62}$	$0.19^{0.21}_{0.18}$	2ME
M 51	$24.77^{**}_{24.45}$	-	-	-	-	$21.93^{22.69}_{**}$	-	-	-	ab
NGC 2273*	$24.55^{24.66}_{24.43}$	-	$0.26^{0.34}_{0.22}$	-	ME*ab	$23.36^{23.44}_{23.27}$	-	$0.71^{0.80}_{0.50}$	-	ME*ab
HE 1136-2304	$20.96^{20.98}_{20.94}$	-	$0.59^{0.67}_{0.51}$	-	ME	$20.96^{20.99}_{20.94}$	-	$0.65^{0.77}_{0.54}$	-	ME
IGRJ11366 6002	$21.15^{22.24}_{**}$	-	-	-	-	$21.81^{**}_{20.09}$	-	-	-	-
IC 4518A*	$23.22^{23.30}_{23.16}$	-	$0.71^{0.75}_{0.59}$	-	ME*ab	$23.21^{23.28}_{23.15}$	-	$0.70^{0.74}_{0.68}$	-	ME*ab
NGC 7674*	$23.06^{23.21}_{22.98}$	-	-	-	-	$22.99^{23.08}_{22.75}$	-	-	-	-
NGC 5033	$20.0^{20.12}_{**}$	-	-	-	-	$20.99^{21.13}_{20.75}$	-	$0.82^{**}_{0.59}$	$0.23^{0.54}_{0.18}$	2ME

Table C.11: Summary of other parameters of the best fit models. Name, Column density and ionization degree of the warm absorber ($N_{H,W}$ and $\log(\xi_W)$) and the normalization of the power law emission of *XMM-Newton* and *NuSTAR* observations (Norm PL_{XMM} and Norm PL_{Nu}). The parameter in this table marked with (power-law normalization of *XMM-Newton*) is tied to *NuSTAR*. - denotes that these were not require to improve the fit. Objects with * symbols are the galaxies with not simultaneous observations. NGC 2110 (denoted as NGC 2110^{w}) need two warm absorbers to improve the PEXMON fit. In addition to the absorber presented in this table, the other correspond to: $N_{H,W}=5.38^{5.52}_{5.23}$ and $\log(\xi_W)=1.31^{1.35}_{1.27}$.

	PEXMON			
Name	$N_{H,W}$ (10^{22} cm^{-2})	$\log(\xi_W)$	Norm PL_{XMM} (10^{-3})	Norm PL_{Nu} (10^{-3})
NGC 3998	-	-	#	$2.33^{2.43}_{2.23}$
NGC 3718	-	-	#	$0.53^{0.59}_{0.47}$
NGC 4258*	-	-	$1.70^{1.83}_{1.50}$	$1.13^{1.24}_{0.99}$
ESO 253-G003*	-	-	-	$0.17^{0.36}_{0.11}$
NGC 1052	$0.05^{45.54}_{**}$	$6^{**}_{2.37}$	#	$2.79^{3.03}_{2.66}$
NGC 2655	$2.11^{2.81}_{1.23}$	$1.32^{1.55}_{1.15}$	#	$0.91^{1.22}_{0.42}$
NGC 3147*	-	-	$1.89^{6.21}_{0.92}$	$0.68^{0.72}_{0.64}$
NGC 2110*^{w}	$0.17^{0.24}_{0.13}$	$-0.55^{-0.43}_{-0.83}$	$10.80^{13.10}_{9.70}$	$59.40^{60.50}_{58.50}$
LEDA 96373*	$0.79^{0.87}_{0.67}$	$-0.93^{-0.65}_{-1.07}$	#	$0.12^{0.14}_{0.11}$
NGC 2992	$0.49^{0.63}_{0.43}$	$2.53^{2.69}_{2.39}$	#	$18.58^{19.06}_{18.16}$
M 51	$499.96^{**}_{224.16}$	$4.25^{4.53}_{3.36}$	#	$0.056^{0.099}_{0.036}$
NGC 2273*	$2.95^{5.33}_{1.78}$	$1.24^{1.49}_{0.26}$	#	$0.29^{0.57}_{0.08}$
HE 1136-2304	-	-	#	$2.53^{2.59}_{2.47}$
IGRJ11366 6002	-	-	-	$2.36^{2.71}_{2.10}$
IC 4518A*	$3.79^{6.03}_{1.91}$	$1.37^{1.50}_{1.09}$	$0.77^{1.46}_{0.60}$	$1.65^{1.98}_{1.41}$
NGC 7674*	-	-	-	$0.36^{0.47}_{0.14}$
NGC 5033	-	-	#	$1.93^{1.98}_{1.90}$

Table C.12: Cont:Summary of other parameters of the best fit models.

	BORUS				XILLVER			
Name	$N_{H,W}$ (10^{22} cm^{-2})	$\log(\xi_W)$	Norm PL_{XMM} (10^{-3})	Norm PL_{Nu} (10^{-3})	$N_{H,W}$ (10^{22} cm^{-2})	$\log(\xi_W)$	Norm PL_{XMM} (10^{-3})	Norm PL_{Nu} (10^{-3})
NGC 3998	-	-	#	$2.35^{2.44}_{2.26}$	-	-	#	$2.05^{3.41}_{**}$
NGC 3718	-	-	#	$0.52^{0.58}_{0.47}$	-	-	#	$0.08^{0.09}_{0.05}$
NGC 4258*	-	-	$1.60^{1.74}_{1.42}$	$1.04^{1.25}_{0.92}$	-	-	$0.019^{0.022}_{0.015}$	$0.011^{0.013}_{0.010}$
ESO 253-G003*	-	-	-	$0.30^{0.46}_{0.26}$	-	-	-	$0.02^{0.03}_{0.01}$
NGC 1052	-	-	#	$3.46^{3.51}_{**}$	$19.25^{19.51}_{19.00}$	$2.032^{2.043}_{2.029}$	#	$0.043^{0.044}_{0.042}$
NGC 2655	-	-	#	$0.80^{1.39}_{0.54}$	$2.57^{3.77}_{1.71}$	$1.36^{1.64}_{1.23}$	#	$0.02^{0.03}_{0.01}$
NGC 3147*	-	-	$0.34^{0.38}_{0.30}$	$0.71^{0.75}_{0.66}$	-	-	$0.0066^{0.0071}_{0.0056}$	$0.012^{0.016}_{0.010}$
NGC 2110*[w]	$1.53^{1.66}_{1.39}$	$4.30^{4.51}_{4.03}$	$8.38^{8.79}_{7.51}$	$4.44^{4.61}_{4.22}$	$5.23^{5.37}_{5.07}$	$1.36^{1.43}_{1.29}$	$0.30^{0.59}_{0.28}$	$1.54^{1.57}_{1.37}$
LEDA 96373*	$0.80^{0.83}_{0.68}$	$-0.55^{-0.33}_{-1.50}$	#	$5.93^{9.06}_{4.52}$	$7.94^{8.85}_{7.28}$	$2.01^{2.04}_{1.97}$	#	$0.005^{0.006}_{0.004}$
NGC 2992	$0.64^{0.79}_{0.52}$	$2.48^{2.59}_{2.36}$	#	$20.80^{21.40}_{20.30}$	-	-	#	$0.40^{0.41}_{0.39}$
M 51	-	-	#	$0.36^{1.18}_{0.22}$	$488.99^{**}_{278.02}$	$4.18^{4.38}_{3.88}$	#	$0.0012^{0.0016}_{0.0011}$
NGC 2273*	$0.94^{1.24}_{0.24}$	$-1.14^{0.35}_{-1.31}$	#	$5.14^{10.52}_{1.60}$	$2.97^{5.72}_{2.43}$	$1.23^{1.39}_{0.45}$	#	$0.006^{0.010}_{0.005}$
HE 1136-2304	-	-	#	$2.53^{2.59}_{2.48}$	-	-	#	$0.0042^{0.069}_{0.0041}$
IGRJ11366 6002	-	-	-	$2.26^{2.53}_{2.00}$	-	-	-	$1.41^{2.5}_{**}$
IC 4518A*	$4.41^{5.77}_{1.95}$	$1.44^{1.64}_{1.22}$	$0.65^{0.95}_{0.45}$	$2.13^{3.00}_{1.59}$	$3.97^{5.79}_{2.23}$	$1.39^{1.57}_{1.31}$	$0.015^{0.199}_{0.010}$	$0.032^{0.041}_{0.026}$
NGC 7674*	-	-	-	$0.24^{0.32}_{0.19}$	-	-	-	$0.003^{0.005}_{0.002}$
NGC 5033	-	-	#	$1.90^{1.95}_{1.86}$	-	-	#	$0.032^{0.033}_{0.029}$

Table C.13: Summary of the Cross normalization constants between the instruments. Name, cross normalization constant between the detector FPMA and FPMB of *NuSTAR* ($C_{A/B}$, *NuSTAR* and *XMM-Newton* (C_{XMM}) and *NuSTAR* and *Swift* (C_{BAT}). In case of the not simultaneous data *XMM-Newton+NuSTAR* observations, where the normalization of the power-law is a free parameter (objects denoted in bold face), we put the restriction of C_{XMM}=[0.9,1.10]. The error of this parameters is in the normalization of the power-law then we reported here only the best fit value. The quantities in this table marked with ** are unconstrained errors.

	PEXMON		
Name	$C_{A/B}$	C_{XMM}	C_{BAT}
NGC 3998	$1.04^{1.06}_{1.02}$	$0.91^{0.94}_{0.88}$	$0.98^{1.17}_{0.80}$
NGC 3718	$0.99^{1.03}_{0.96}$	$0.98^{1.03}_{0.94}$	$4.53^{5.53}_{3.60}$
NGC 4258*	$0.99^{1.02}_{0.96}$	$\mathbf{1.09}^{**}_{1.03}$	$2.64^{2.98}_{2.31}$
ESO 253-G003*	$1.14^{1.23}_{1.06}$	-	$0.89^{1.14}_{0.66}$
NGC 1052	$1.00^{1.03}_{0.98}$	$0.89^{0.91}_{0.87}$	$0.86^{0.96}_{0.76}$
NGC 2655	$1.16^{1.05}_{1.05}$	$1.09^{1.27}_{0.93}$	$2.21^{2.90}_{1.63}$
NGC 3147*	$1.04^{1.09}_{0.99}$	$\mathbf{0.95}^{0.97}_{**}$	$1.08^{1.47}_{0.71}$
NGC 2110*	$1.03^{1.05}_{1.02}$	$\mathbf{1.03}^{1.10}_{**}$	$0.58^{0.59}_{0.57}$
LEDA 96373*	$1.12^{1.20}_{1.05}$	$0.84^{0.90}_{0.79}$	$0.87^{1.06}_{0.71}$
NGC 2992	$1.027^{1.033}_{1.019}$	$0.91^{0.92}_{0.90}$	$0.127^{0.133}_{0.119}$
M 51	$0.99^{1.06}_{0.93}$	$1.06^{1.16}_{0.97}$	$2.67^{3.46}_{1.95}$
NGC 2273*	$1.09^{1.18}_{0.99}$	$1.15^{1.33}_{0.99}$	$0.84^{1.17}_{0.54}$
HE 1136-2304	$1.07^{1.08}_{1.05}$	$1.03^{1.04}_{1.01}$	$0.63^{0.77}_{0.50}$
IGRJ11366 6002	$1.15^{1.22}_{1.09}$	-	$1.45^{1.80}_{1.18}$
IC 4518A*	$1.12^{1.20}_{1.04}$	$\mathbf{0.97}^{0.99}_{**}$	$1.11^{1.25}_{0.95}$
NGC 7674*	$1.02^{1.09}_{0.95}$	-	$1.58^{2.03}_{1.15}$
NGC 5033	$1.05^{1.07}_{1.03}$	$0.75^{0.76}_{0.73}$	$0.28^{0.42}_{0.13}$

Table C.14: Cont.: Summary of the Cross normalization constants between the instruments.

	BORUS			XILLVER		
Name	$C_{A/B}$	C_{XMM}	C_{BAT}	$C_{A/B}$	C_{XMM}	C_{BAT}
NGC 3998	$1.04^{1.06}_{1.02}$	$0.91^{0.94}_{0.90}$	$0.96^{1.13}_{0.79}$	$1.04^{1.06}_{1.02}$	$0.92^{0.94}_{0.89}$	$0.96^{1.14}_{0.79}$
NGC 3718	$1.00^{1.02}_{0.96}$	$0.99^{1.03}_{0.94}$	$4.42^{5.26}_{3.52}$	$0.99^{1.03}_{0.96}$	$0.98^{1.03}_{0.94}$	$4.46^{5.41}_{3.57}$
NGC 4258*	$0.99^{1.02}_{0.96}$	$\mathbf{1.07}^{**}_{0.96}$	$2.56^{2.93}_{2.24}$	$0.99^{1.02}_{0.96}$	**1.10**	$2.94^{3.29}_{2.58}$
ESO 253-G003*	$1.14^{1.23}_{1.06}$	-	$0.88^{1.13}_{0.67}$	$1.14^{1.23}_{1.06}$	-	$0.85^{1.08}_{0.65}$
NGC 1052	$1.00^{1.02}_{0.97}$	$0.87^{0.89}_{0.85}$	$0.83^{0.93}_{0.74}$	$1.00^{1.02}_{0.99}$	$0.89^{0.90}_{0.87}$	$0.90^{1.00}_{0.79}$
NGC 2655	$1.07^{1.25}_{0.91}$	$2.22^{2.89}_{1.63}$	$1.15^{1.28}_{1.04}$	$1.07^{1.16}_{0.92}$	$2.18^{2.78}_{1.62}$	
NGC 3147*	$1.04^{1.09}_{0.99}$	$\mathbf{0.99}^{**}_{0.90}$	$1.00^{1.34}_{0.64}$	$1.04^{1.09}_{0.90}$	$\mathbf{0.92}^{0.99}_{**}$	$1.08^{1.47}_{0.70}$
NGC 2110*	$1.04^{1.05}_{1.02}$	$\mathbf{0.90}^{0.97}_{**}$	$0.60^{0.61}_{0.59}$	$1.03^{1.05}_{1.02}$	$\mathbf{0.97}^{1.08}_{**}$	$0.58^{0.59}_{0.57}$
LEDA 96373*	$1.13^{1.21}_{1.05}$	$0.87^{0.94}_{0.81}$	$0.85^{1.03}_{0.70}$	$1.12^{1.20}_{1.05}$	$0.86^{0.92}_{0.80}$	$0.88^{1.06}_{0.71}$
NGC 2992	$1.026^{1.033}_{1.020}$	$0.909^{0.915}_{0.903}$	$0.122^{0.136}_{0.110}$	$1.026^{1.033}_{1.019}$	$0.915^{0.920}_{0.909}$	$0.13^{0.15}_{0.12}$
M 51	$1.00^{1.07}_{0.94}$	$1.06^{1.16}_{0.98}$	$2.08^{2.77}_{1.54}$	$0.99^{1.06}_{0.92}$	$1.07^{1.17}_{0.98}$	$2.67^{3.52}_{1.91}$
NGC 2273*	$1.08^{1.17}_{0.99}$	$1.04^{1.19}_{0.90}$	$0.65^{0.91}_{0.43}$	$1.09^{1.18}_{1.00}$	$1.09^{1.97}_{0.94}$	$0.84^{1.14}_{0.55}$
HE 1136-2304	$1.064^{1.082}_{1.046}$	$1.03^{1.04}_{1.01}$	$0.58^{0.71}_{0.45}$	$1.065^{1.081}_{1.047}$	$1.023^{1.039}_{1.015}$	$0.62^{0.75}_{0.49}$
IGRJ11366 6002	$1.15^{1.22}_{1.09}$	-	$1.42^{1.71}_{1.10}$	$1.15^{1.22}_{1.09}$	-	$1.44^{1.76}_{1.14}$
IC 4518A*	$1.11^{1.19}_{1.03}$	$\mathbf{1.10}^{**}_{0.90}$	$1.09^{1.28}_{0.93}$	$1.11^{1.19}_{1.04}$	$\mathbf{0.90}^{1.00}_{**}$	$1.09^{1.27}_{0.94}$
NGC 7674*	$1.02^{1.09}_{0.96}$	-	$1.60^{2.07}_{1.17}$	$1.02^{1.09}_{0.95}$	-	$1.57^{2.00}_{1.16}$
NGC 5033	$1.05^{1.07}_{1.04}$	$0.76^{0.78}_{0.74}$	$0.27^{0.41}_{0.14}$	$1.05^{1.07}_{1.04}$	$0.76^{0.78}_{0.74}$	$0.28^{0.42}_{0.13}$

Table C.15: Soft (2-10 keV) and hard (10–79 keV) intrinsic and observed luminosities for all the sample.

	Observed		Intrinsic		
Name	$\log(L_{2.0-10.0})$	$\log(L_{10.0-79.0})$	$\log(L_{2.0-10.0})$	$\log(L_{10.0-79.0})$	Model
NGC 3998	$41.14^{41.15}_{41.12}$	$41.33^{41.34}_{41.27}$	$41.15^{41.16}_{41.14}$	$40.67^{40.71}_{40.62}$	BORUS
	$41.28^{41.40}_{41.12}$	$41.46^{41.62}_{41.16}$	$41.28^{41.40}_{41.12}$	$41.16^{41.33}_{40.88}$	XILLVER
NGC 3718	$40.45^{40.46}_{40.39}$	$40.64^{40.65}_{40.45}$	$40.49^{40.52}_{40.46}$	$40.64^{40.72}_{40.55}$	BORUS
	$40.45^{40.61}_{40.10}$	$40.63^{40.71}_{40.03}$	$40.49^{40.67}_{40.20}$	$40.63^{40.79}_{40.36}$	XILLVER
NGC 4258*	$39.93^{37.90}_{40.65}$	$40.14^{40.22}_{40.07}$	$40.15^{40.05}_{40.70}$	$40.15^{40.22}_{40.07}$	BORUS
	$39.93^{40.10}_{39.25}$	$40.07^{40.08}_{39.98}$	$40.11^{40.32}_{39.67}$	$40.07^{40.11}_{40.02}$	XILLVER
ESO 253-G003$^{*}_{nu}$	$42.69^{42.99}_{42.37}$	$42.80^{43.67}_{42.61}$	$42.89^{43.13}_{42.57}$	$43.59^{43.75}_{43.35}$	BORUS
	$42.69^{43.03}_{42.47}$	$43.61^{43.64}_{42.34}$	$42.89^{43.14}_{42.21}$	$43.62^{44.34}_{44.13}$	XILLVER
NGC 1052	$41.44^{41.48}_{41.36}$	$42.13^{42.18}_{41.83}$	$41.76^{41.70}_{41.81}$	$42.15^{42.23}_{42.04}$	BORUS
NGC 2655	$40.61^{40.67}_{39.90}$	$41.18^{41.21}_{40.76}$	$41.03^{41.11}_{40.95}$	$41.19^{41.26}_{41.08}$	BORUS
	$40.60^{40.74}_{40.19}$	$40.19^{40.32}_{40.09}$	$40.96^{41.14}_{40.66}$	$41.20^{41.51}_{39.85}$	XILLVER
NGC 3147*	$41.40^{41.60}_{40.08}$	$42.01^{42.04}_{41.69}$	$41.40^{41.56}_{41.16}$	$42.01^{42.12}_{41.87}$	BORUS
	$40.39^{41.77}_{40.18}$	$41.95^{42.07}_{41.93}$	$41.39^{41.73}_{40.62}$	$41.95^{42.02}_{41.86}$	XILLVER
NGC 2110*	$42.44^{42.58}_{42.25}$	$43.61^{43.62}_{43.60}$	$42.52^{42.65}_{42.34}$	$43.61^{43.62}_{43.60}$	BORUS
LEDA 96373*	$42.34^{42.34}_{42.10}$	$43.41^{43.42}_{42.98}$	$43.48^{43.56}_{43.38}$	$43.80^{43.92}_{43.63}$	BORUS
NGC 2992	$42.911^{42.914}_{42.907}$	$43.318^{43.322}_{43.290}$	$42.95^{42.95}_{42.94}$	$43.32^{43.34}_{43.30}$	BORUS
M 51	$38.94^{40.11}_{38.72}$	$39.81^{40.41}_{37.38}$	$39.68^{39.80}_{39.51}$	$40.25^{40.75}_{40.32}$	BORUS
	$38.95^{39.83}_{37.47}$	$39.69^{39.86}_{37.69}$	$39.69^{40.37}_{39.13}$	$40.00^{41.24}_{39.42}$	XILLVER
NGC 2273*	$40.90^{41.24}_{37.49}$	$41.90^{41.93}_{39.30}$	$42.36^{42.68}_{41.33}$	$42.58^{42.77}_{42.25}$	BORUS
HE 1136-2304	$43.23^{43.24}_{43.19}$	$43.54^{43.55}_{43.36}$	$43.23^{43.25}_{43.21}$	$43.54^{43.61}_{43.46}$	BORUS
	$43.22^{43.36}_{42.36}$	$43.52^{43.75}_{42.88}$	$43.23^{42.44}_{41.81}$	$43.52^{43.76}_{42.94}$	XILLVER
IGRJ11366-6002$_{nu}$	$42.35^{42.34}_{42.14}$	$42.58^{42.59}_{40.95}$	$42.39^{42.59}_{42.02}$	$42.58^{42.76}_{42.27}$	BORUS
	$42.24^{42.43}_{42.14}$	$42.58^{42.69}_{41.10}$	$42.39^{42.53}_{42.18}$	$42.58^{42.79}_{42.15}$	XILLVER
IC 4518A*	$41.97^{42.10}_{41.37}$	$43.08^{43.13}_{42.88}$	$42.21^{42.40}_{41.86}$	$43.10^{43.16}_{43.02}$	BORUS
	$41.97^{42.39}_{41.00}$	$43.08^{43.07}_{42.48}$	$42.25^{42.50}_{41.59}$	$43.09^{43.23}_{42.89}$	XILLVER

Name, soft and hard luminosities (observed and intrinsic) and the best fit model. Objects with * symbols are the galaxies with not simultaneous observations. The quantities in this table marked with ** are unconstrained errors. $_{nu}$ mark objects with only *NuSTAR* data, then the luminosity in the soft bad (2.0–10.0 keV), was calculated in the band (3.0 – 10.0 keV).

Table C.16: Cont.: Soft (2-10 keV) and hard (10–79 keV) intrinsic and observed luminosities for all the sample.

	Observed		Intrinsic		
Name	$\log(L_{2.0-10.0})$	$\log(L_{10.0-79.0})$	$\log(L_{2.0-10.0})$	$\log(L_{10.0-79.0})$	Model
NGC 7674$^{*}_{nu}$	$42.17^{42.19}_{41.24}$	$43.00^{42.88}_{42.14}$	$42.42^{42.59}_{42.15}$	$43.02^{43.14}_{42.86}$	BORUS
	$42.15^{42.49}_{41.41}$	$42.99^{43.12}_{42.00}$	$42.39^{42.689}_{40.85}$	$43.03^{43.23}_{42.63}$	XILLVER
NGC 5033	$41.04^{40.05}_{40.01}$	$41.43^{41.44}_{41.34}$	$41.04^{41.06}_{41.02}$	$41.43^{41.47}_{41.38}$	BORUS
	$41.04^{41.14}_{40.97}$	$41.38^{41.33}_{41.16}$	$41.04^{41.12}_{40.94}$	$41.38^{41.44}_{41.31}$	XILLVER

Name, soft and hard luminosities (observed and intrinsic) and the best fit model. Objects with * symbols are the galaxies with not simultaneous observations. The quantities in this table marked with ** are unconstrained errors. $_{nu}$ mark objects with only *NuSTAR* data, then the luminosity in the soft bad (2.0–10.0 keV), was calculated in the band (3.0 – 10.0 keV).

Table C.17: Bolometric correction, bolometric luminosity and accretion rate for the sample of galaxies.

Name	$k_{2.0-10.0}$	L_{Bol}	$\log(\lambda_{Edd})$
(1)	(2)	(3)	(4)
NGC3998	$15.35^{15.41}_{15.29}$	$42.33^{42.34}_{42.32}$	$-4.71^{-5.40}_{-4.02}$
NGC3718	$15.33^{15.40}_{15.27}$	$41.68^{41.85}_{41.38}$	$-4.57^{-5.10}_{-4.17}$
NGC4258*	$15.33^{15.39}_{15.27}$	$41.08^{41.11}_{41.05}$	$-4.59^{-5.26}_{-3.92}$
NGC5033	$15.34^{15.40}_{15.28}$	$42.02^{42.03}_{42.00}$	$-3.77^{-4.46}_{-3.09}$
ESO253-G003*	$15.82^{16.11}_{15.57}$	$44.09^{44.34}_{43.77}$	$-3.76^{-4.21}_{-3.38}$
NGC1052	$15.39^{15.45}_{15.33}$	$42.92^{42.95}_{42.89}$	$-3.86^{-4.53}_{-3.19}$
NGC2655	$15.34^{15.40}_{15.28}$	$42.22^{42.30}_{42.13}$	$-4.09^{-4.71}_{-3.48}$
NGC3147*	$15.36^{15.43}_{15.29}$	$42.59^{42.75}_{42.35}$	$-4.33^{-4.87}_{-3.87}$
NGC2110*	$15.59^{15.70}_{15.47}$	$43.71^{43.84}_{43.53}$	$-3.78^{-4.35}_{-3.26}$
LEDA96373*	$16.74^{16.99}_{16.46}$	$44.73^{44.84}_{44.60}$	$-2.59^{-3.18}_{-2.02}$
NGC2992	$15.88^{15.92}_{15.83}$	$44.15^{44.15}_{44.14}$	$-2.29^{-2.99}_{-1.60}$
M51	$15.33^{15.39}_{15.27}$	$40.87^{40.99}_{40.69}$	$-3.83^{-4.41}_{-3.31}$
NGC2273*	$15.54^{15.69}_{15.35}$	$43.60^{43.84}_{43.06}$	$-2.50^{-2.96}_{-2.34}$
HE1136	$16.22^{16.27}_{16.16}$	$44.44^{44.46}_{44.42}$	$-3.06^{-3.74}_{-2.38}$
IGRJ11366	$15.53^{15.66}_{15.38}$	$43.58^{43.78}_{43.20}$	$-3.09^{-3.59}_{-2.77}$
IC4518A	$15.51^{15.61}_{15.39}$	$43.51^{43.67}_{43.26}$	$-3.39^{-3.93}_{-2.94}$
NGC7674*	$15.53^{15.72}_{15.35}$	$43.59^{43.89}_{43.03}$	$-3.70^{-4.10}_{-3.56}$

(Col. 1) name, (Col. 2) bolometric correction, (Col. 3) bolometric luminosity and (Col. 4) accretion rate. All these values were estimated using Duras et al. (2020).

Appendix D

Spectral models

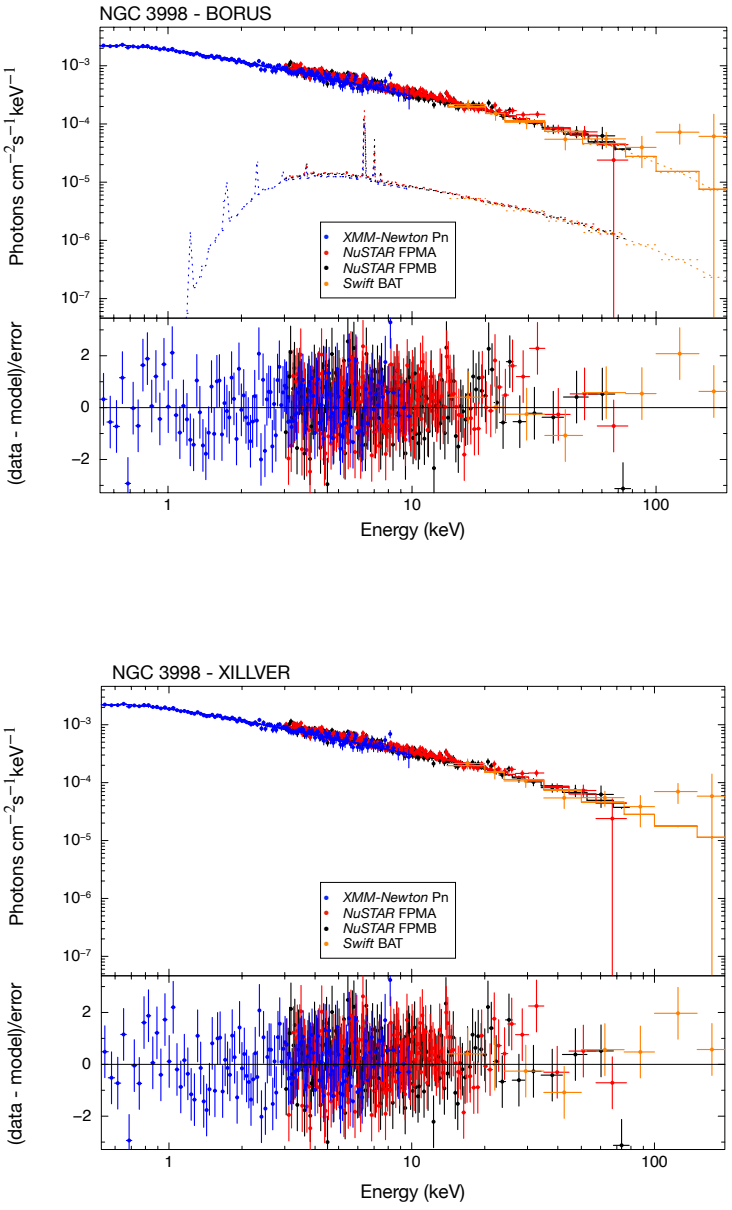

Figure D.1: Spectral modelling of NGC 3998. The plots correspond to BORUS (left) and XILLVER (right)

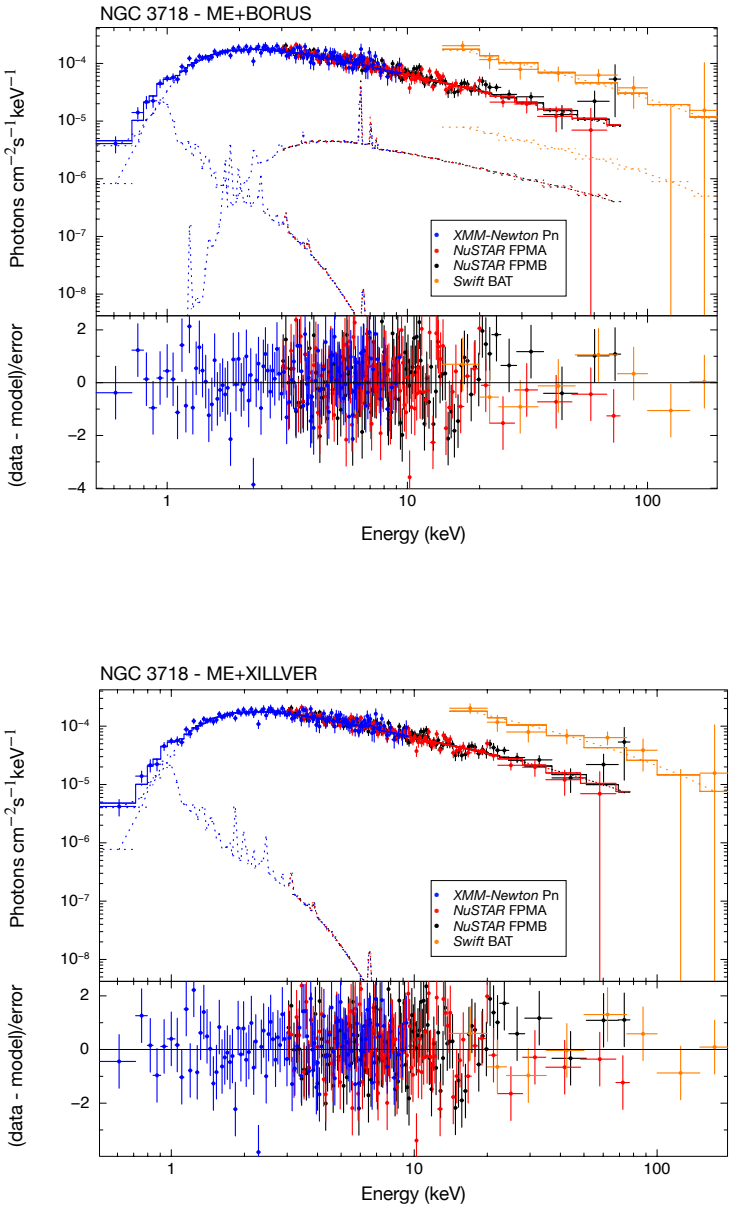

Figure D.2: Spectral modelling of NGC 3718. The plots correspond to BORUS (left) and XILLVER (right)

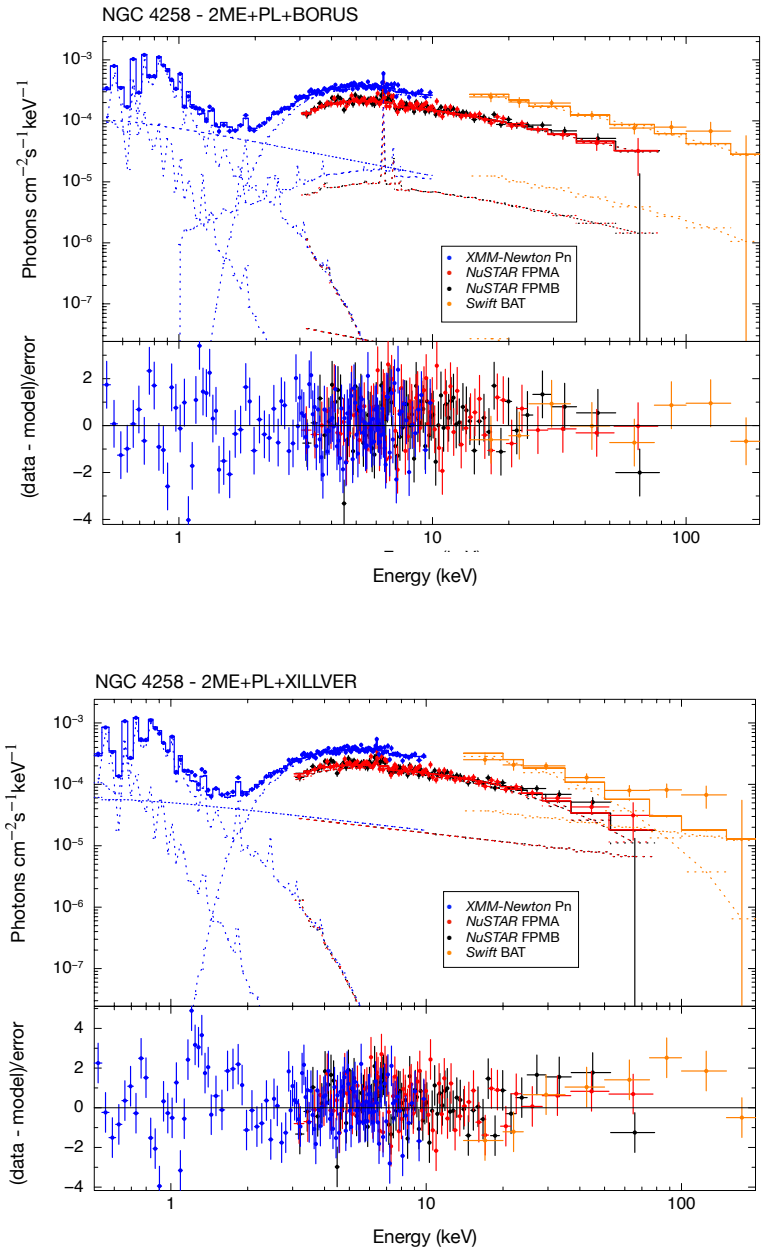

Figure D.3: Spectral modelling of NGC 4258*. The plots correspond to BORUS (left) and XILLVER (right)

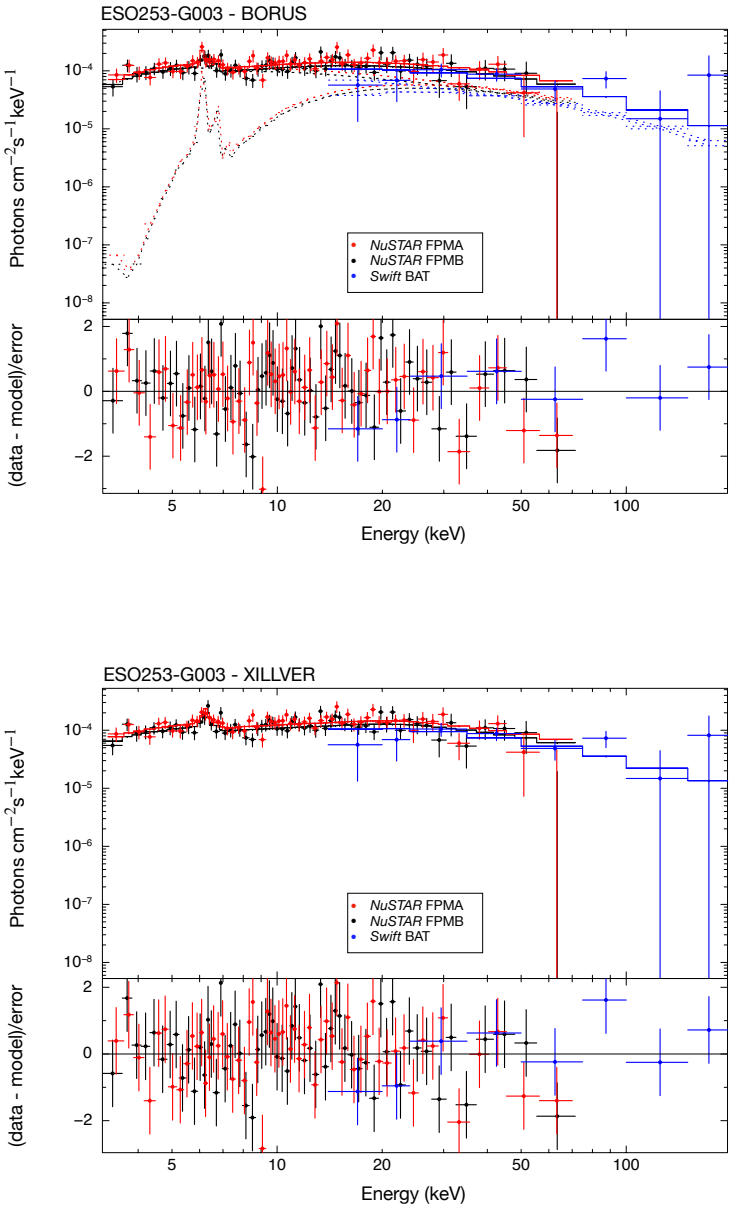

Figure D.4: Spectral modelling of ESO253-G003*. The plots correspond to BORUS (left) and XILLVER (right)

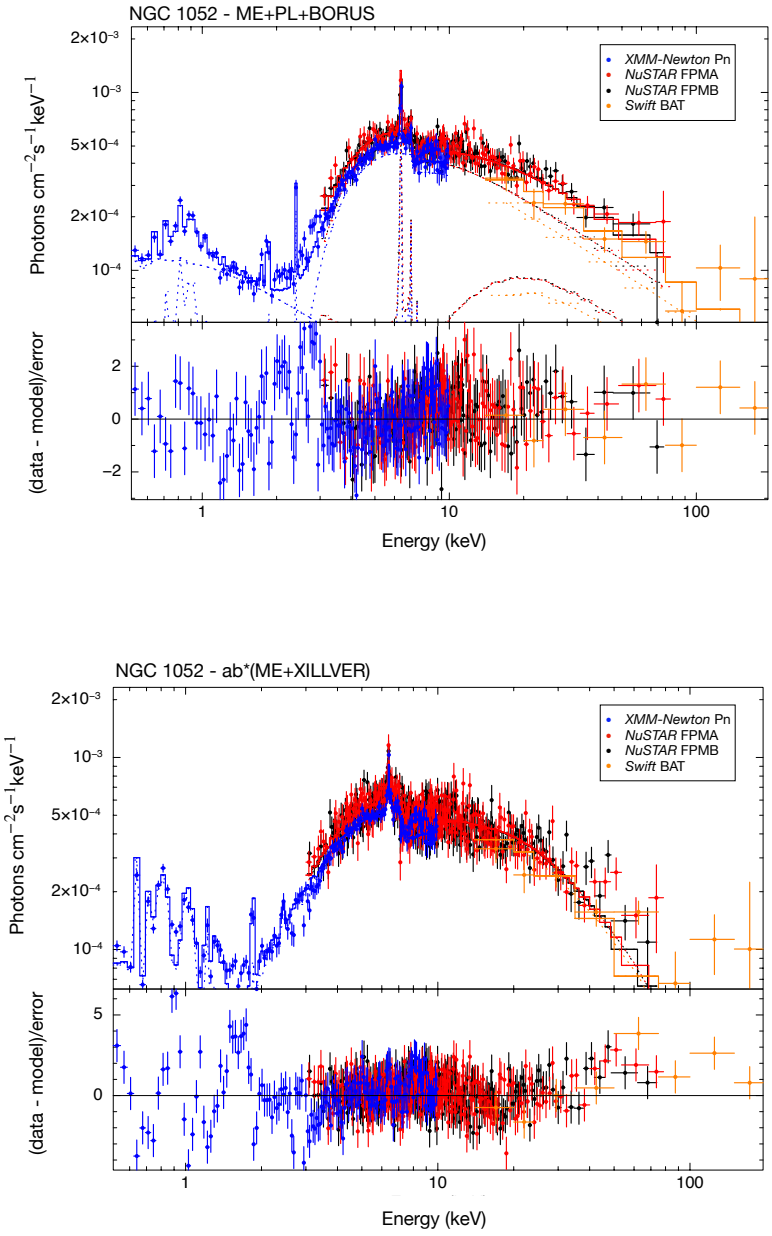

Figure D.5: Spectral modelling of NGC 1052. The plots correspond to BORUS (left) and XILLVER (right)

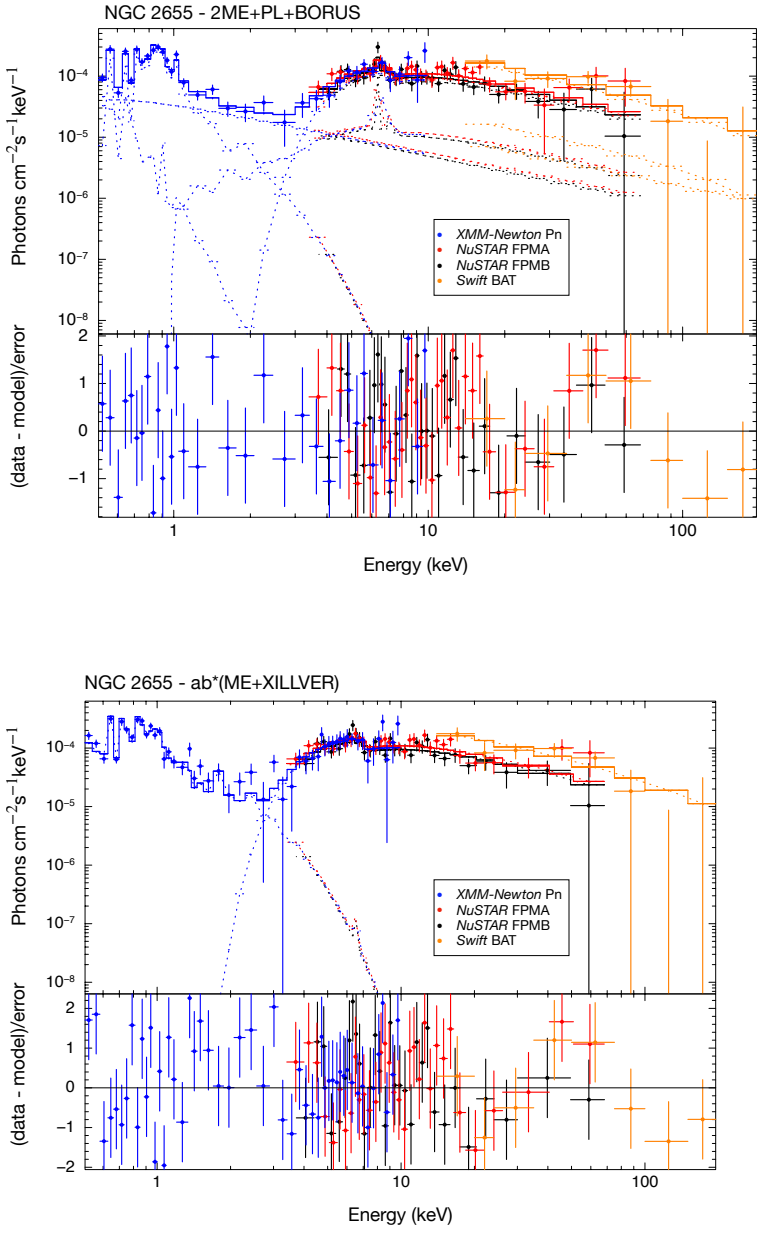

Figure D.6: Spectral modelling of NGC 2655. The plots correspond to BORUS (left) and XILLVER (right)

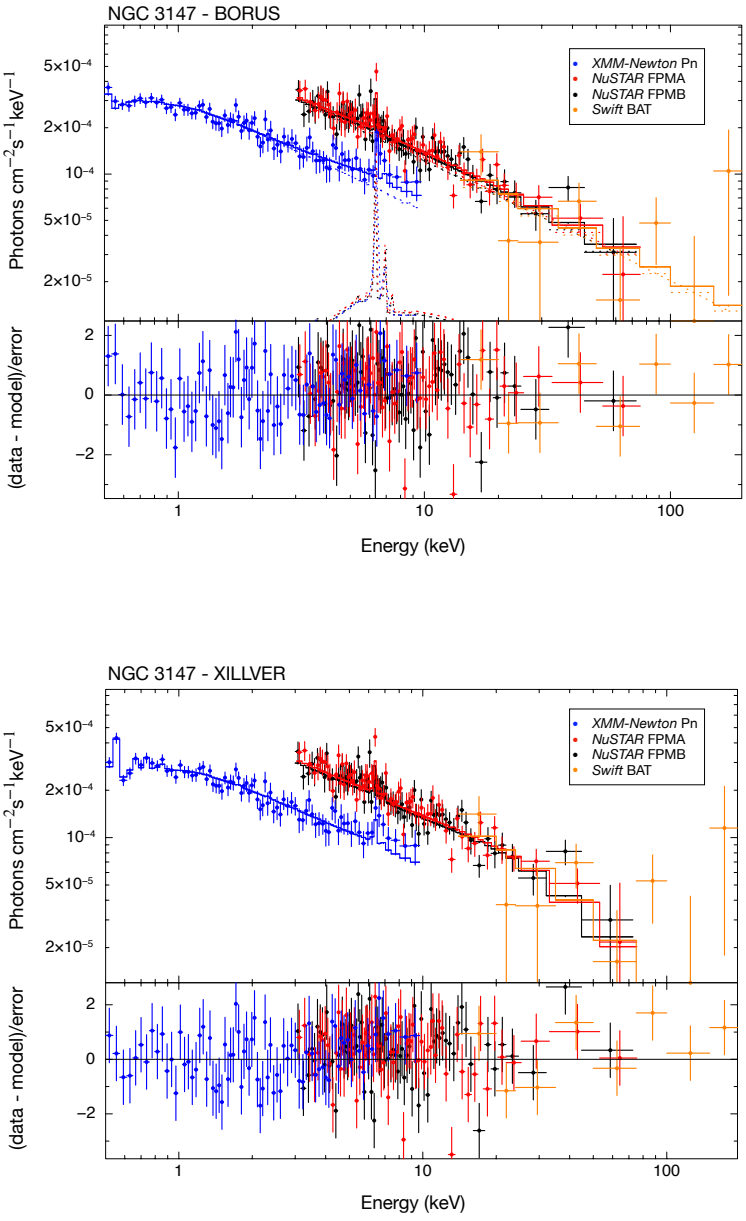

Figure D.7: Spectral modelling of NGC 3147. The plots correspond to BORUS (left) and XILLVER (right)

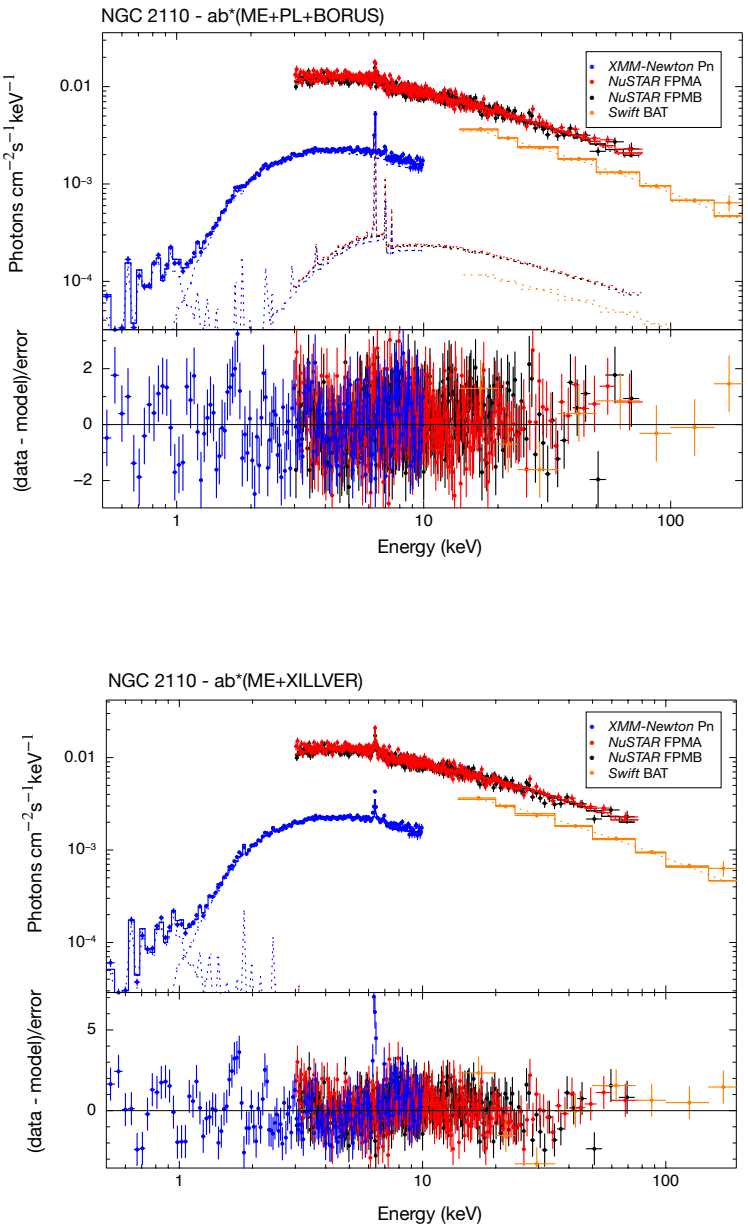

Figure D.8: Spectral modelling of NGC 2110. The plots correspond to BORUS (left) and XILLVER (right)

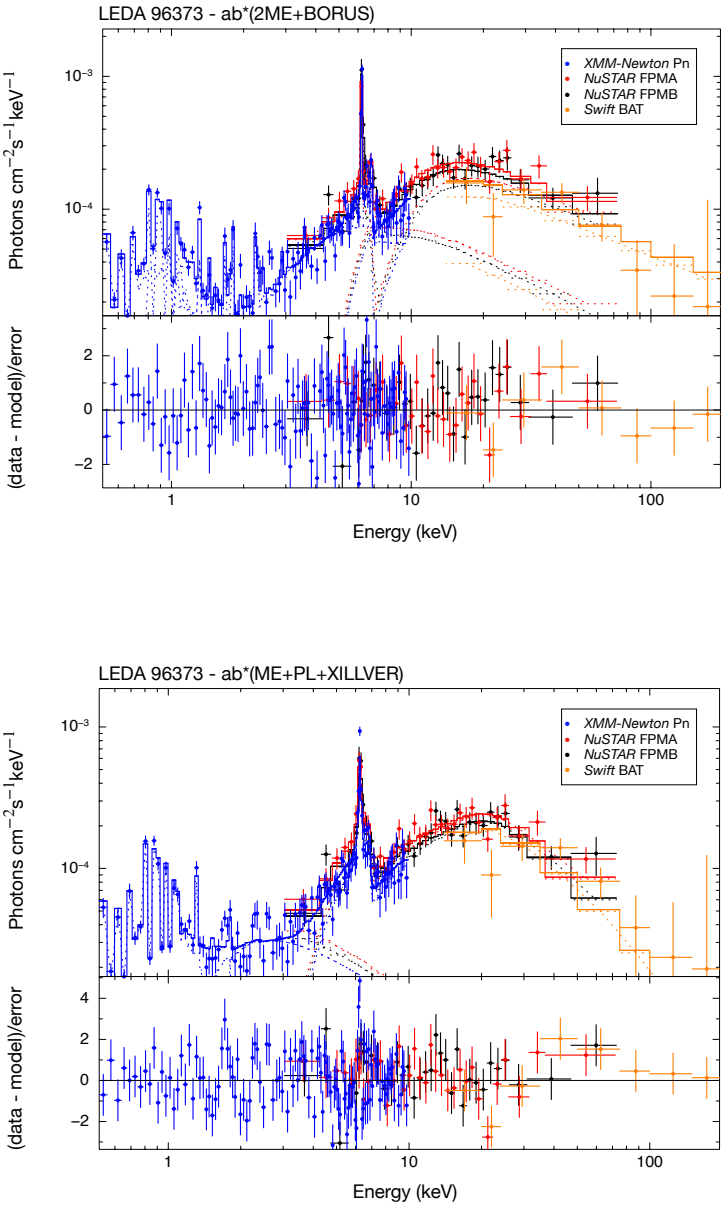

Figure D.9: Spectral modelling of LEDA 96373. The plots correspond to BORUS (left) and XILLVER (right)

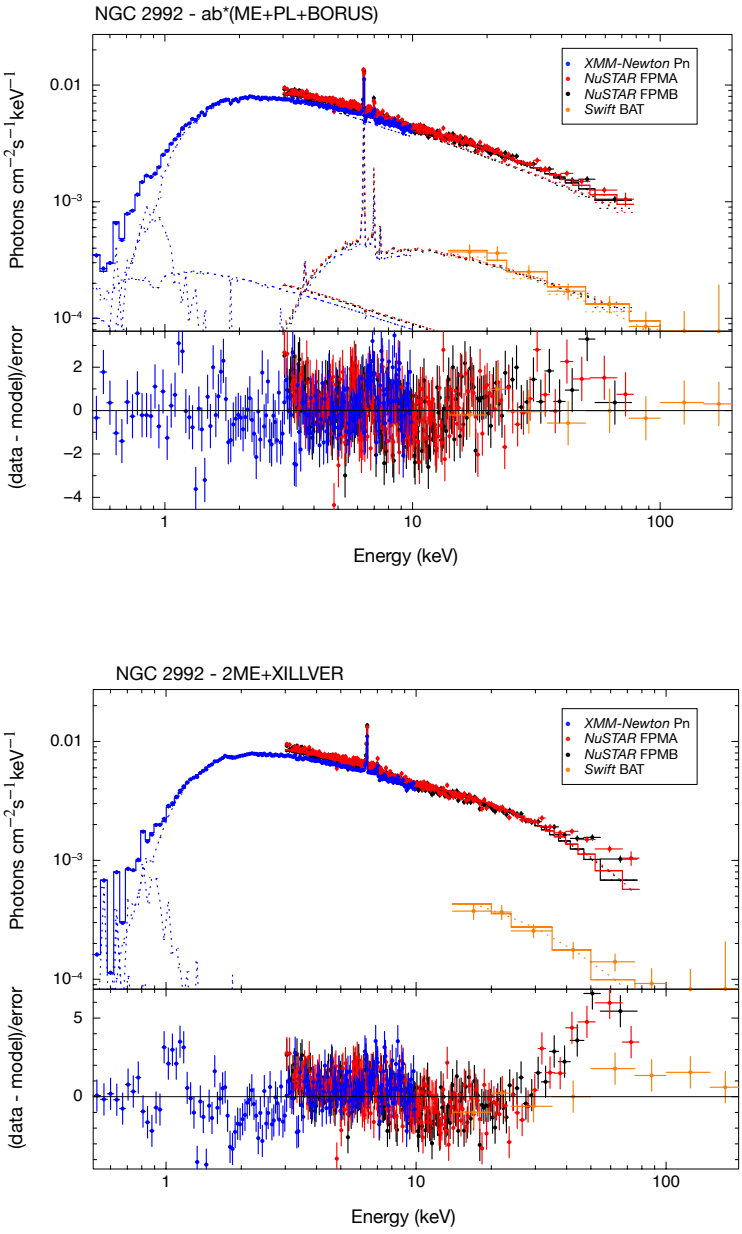

Figure D.10: Spectral modelling of NGC 2992. The plots correspond to BORUS (left) and XILLVER

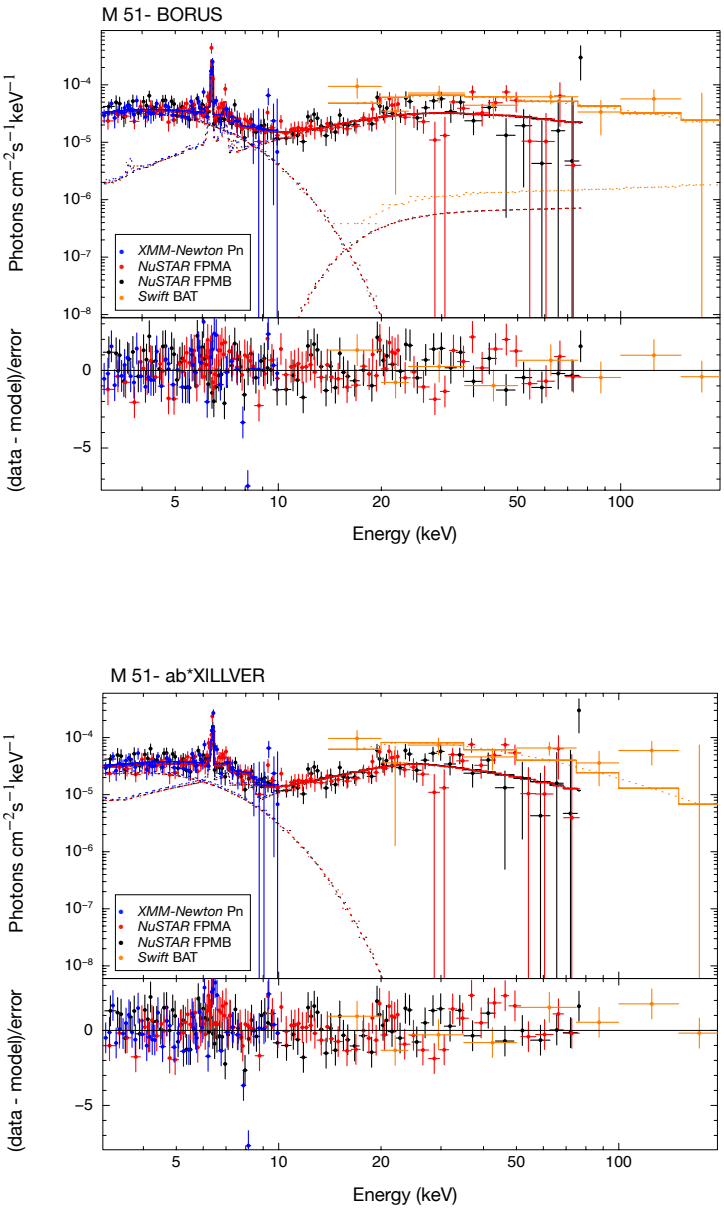

Figure D.11: Spectral modelling of M 51. The plots correspond to BORUS (left) and XILLVER

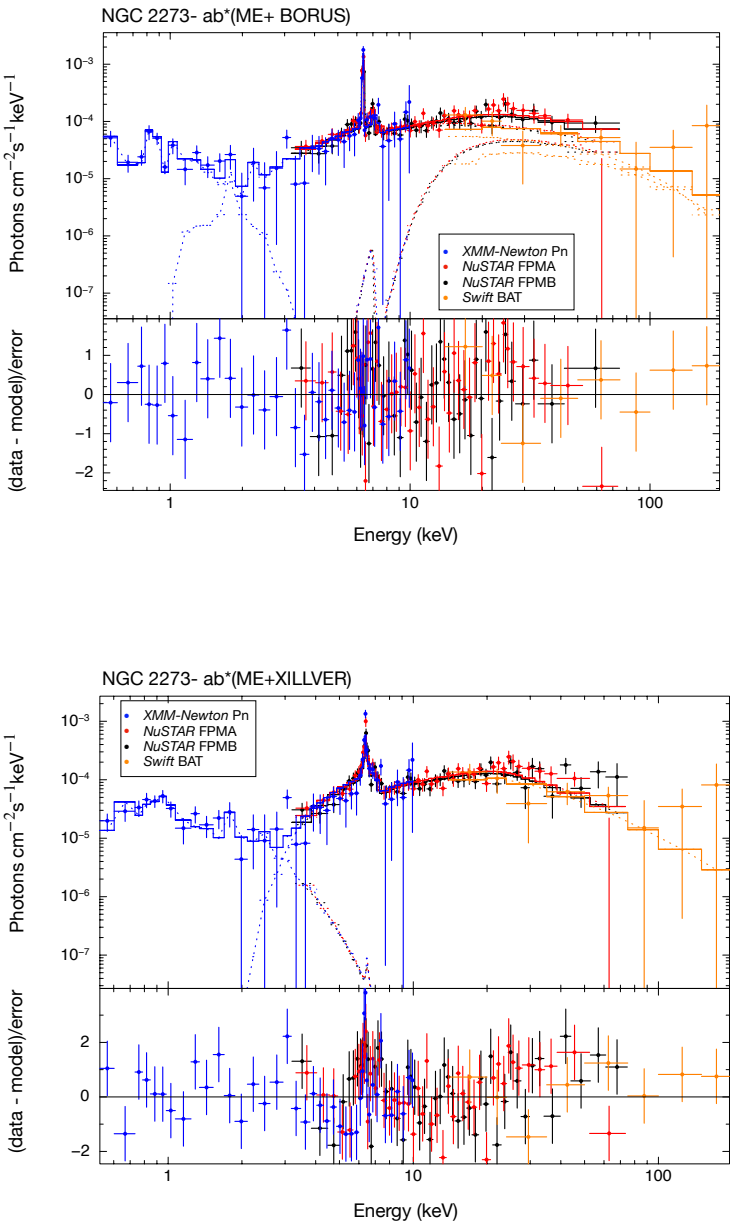

Figure D.12: Spectral modelling of NGC 2273. The plots correspond to BORUS (left) and XILLVER (right)

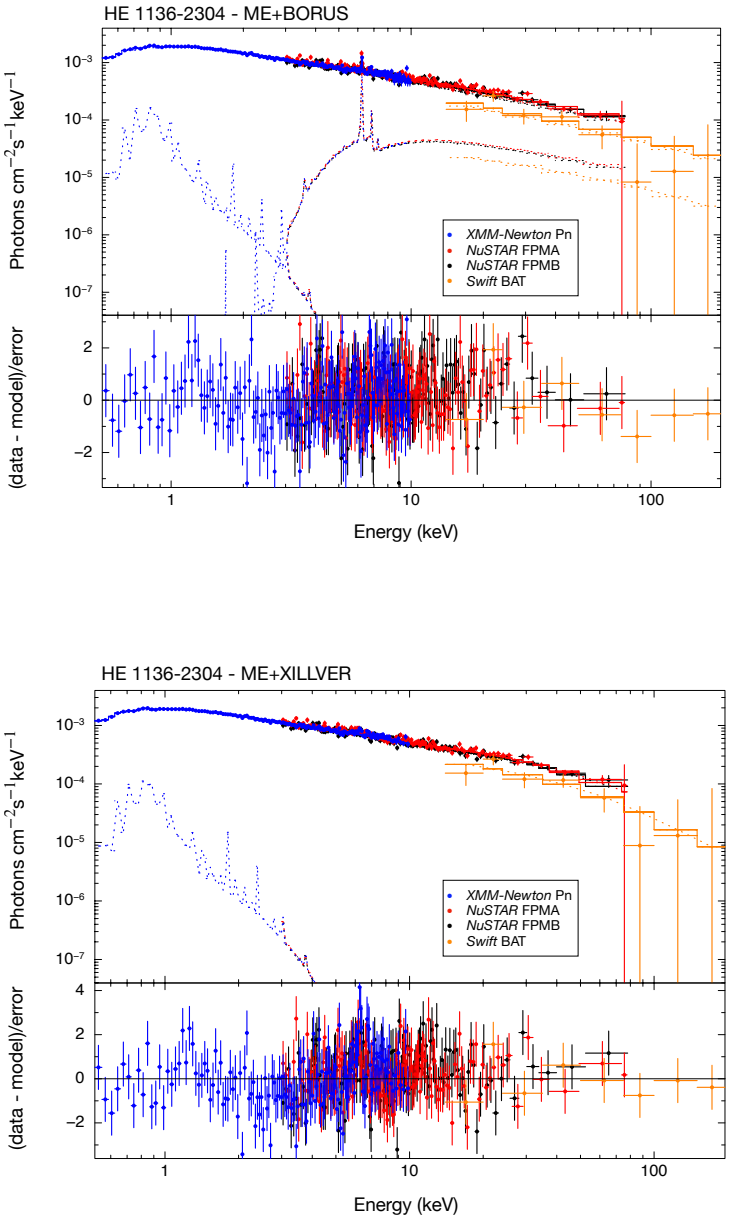

Figure D.13: Spectral modelling of HE 1136-2304. The plots correspond to BORUS (left) and XILLVER (right)

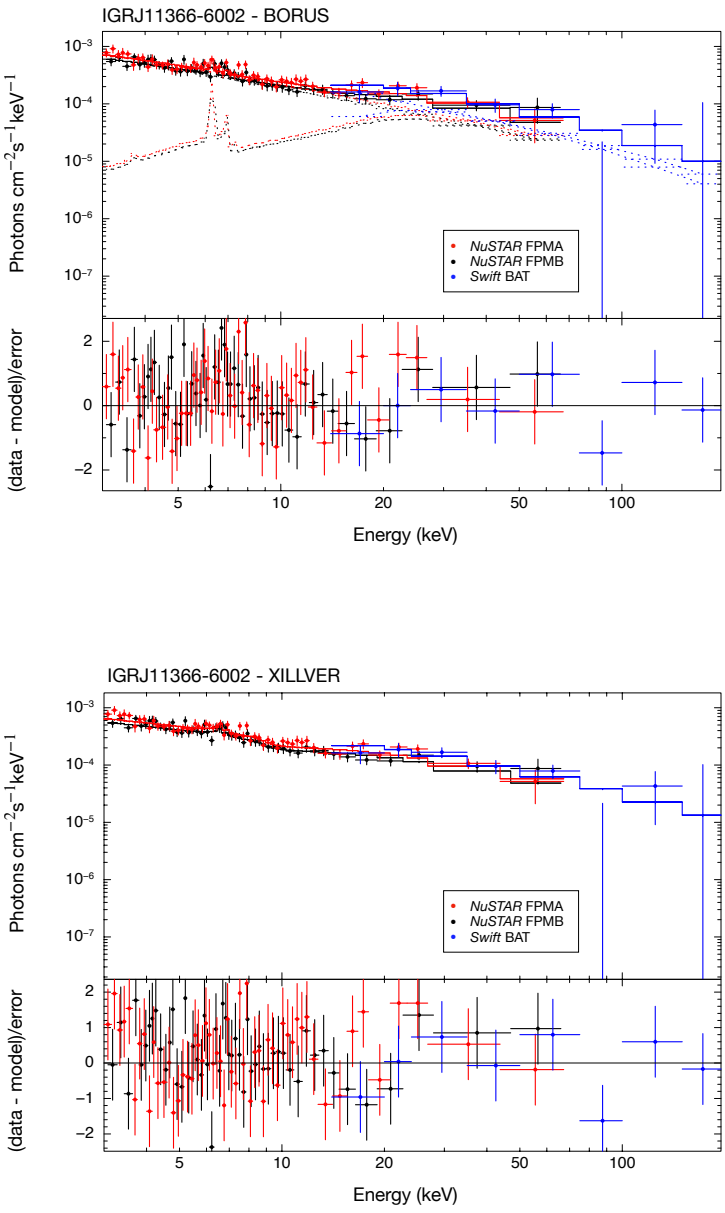

Figure D.14: Spectral modelling of IGRJ11366-6002. The plots correspond to BORUS (left) and XILLVER (right)

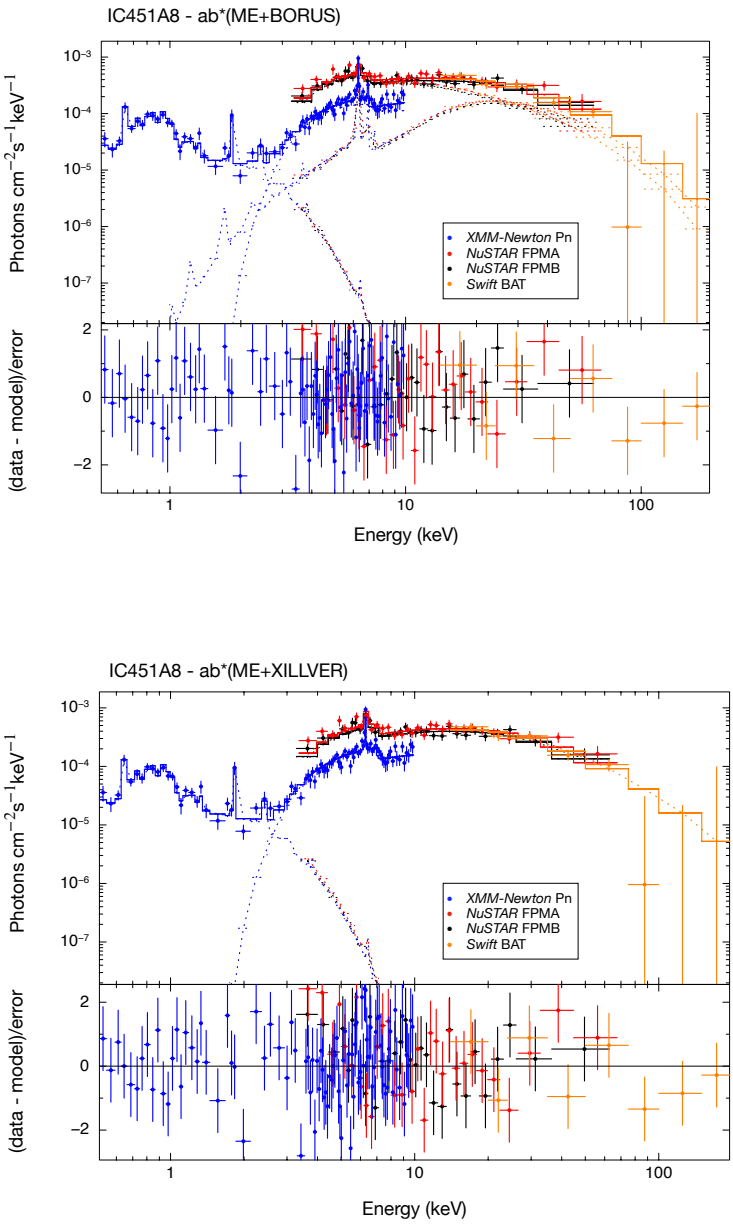

Figure D.15: Spectral modelling of IC4518. The plots correspond to BORUS (left) and XILLVER (right)

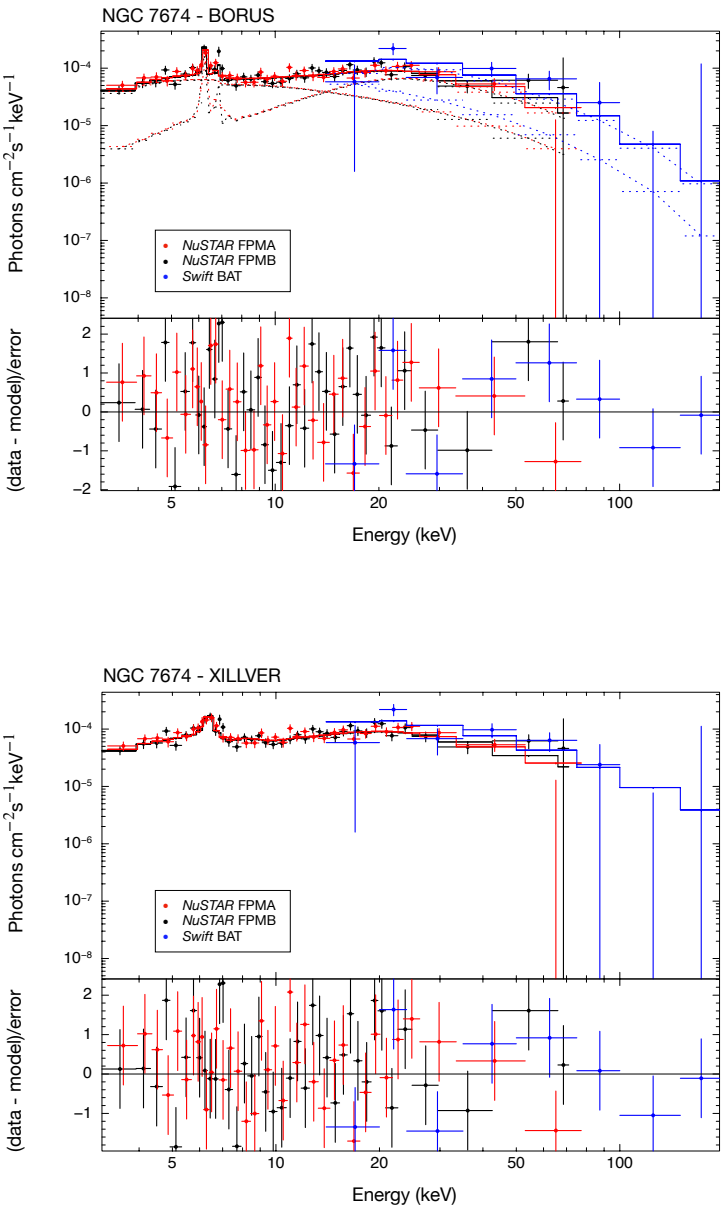

Figure D.16: Spectral modelling of NGC 7674. The plots correspond to BORUS (left) and XILLVER (right)

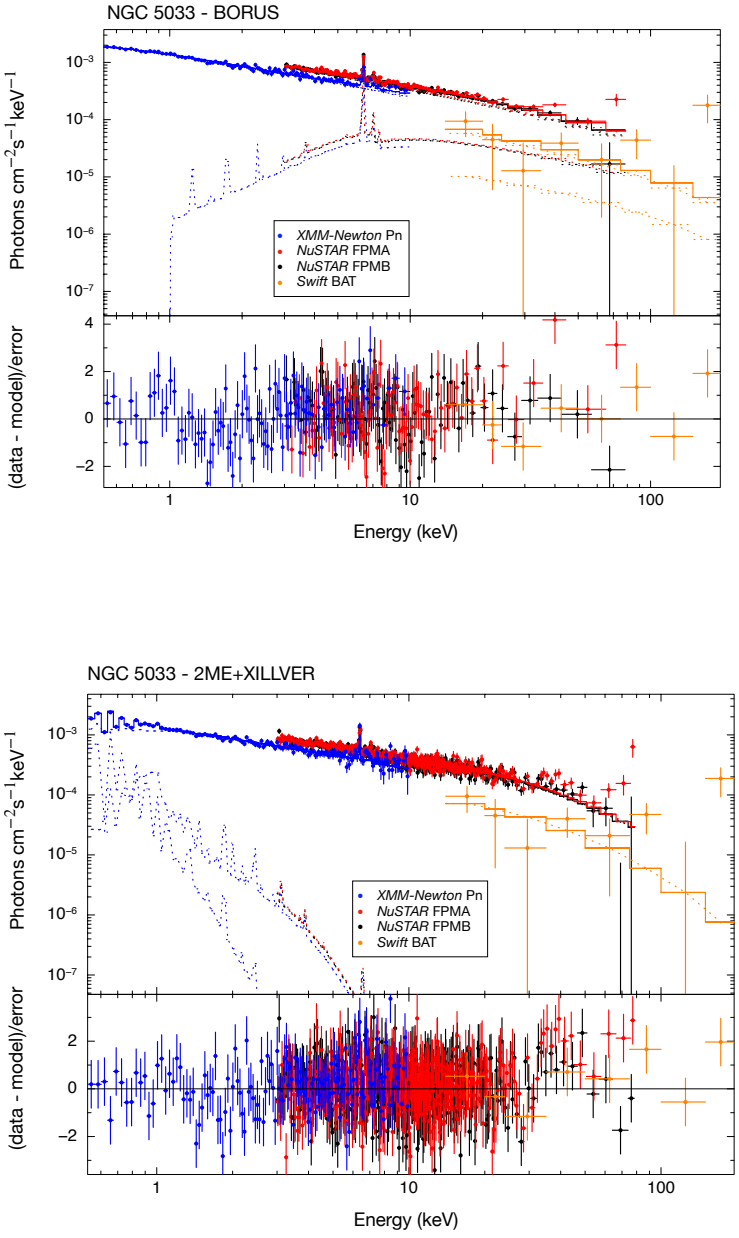

Figure D.17: Spectral modelling of NGC 5033. The plots correspond to BORUS (left) and XILLVER (right)

Appendix E

Other Scientific Contributions

Finally, in this Chapter, I will summarize other scientific works in which I have participated during the development of my PhD but do not constitute the core of my main research. I was invited to collaborate in these studies because they are related to my PhD work.

A closer look at NGC 7314 nuclear region: a multiwavelength analysis of the Seyfert nucleus and its surroundings

Patrícia da Silva,[1]★ R. B. Menezes[2]† Y. Díaz[5]‡ A. Rodríguez-Ardila[3,4]§ E. López-Navas[5], P. Arévalo[5] and L. Hernández-García[5,6]
[1]*Instituto de Astronomia, Geofísica e Ciências Atmosféricas, Departamento de Astronomia, Universidade de São Paulo, 05508-090, SP, Brazil*
[2]*Instituto Mauá de Tecnologia, Praça Mauá 1, 09580-900, São Caetano do Sul, SP, Brazil*
[3]*Laboratório Nacional de Astrofísica, Rua dos Estados Unidos, 154, CEP 37504-364, Itajubá, MG, Brazil*
[4]*Divisão de Astrofísica, Instituto Nacional de Pesquisas Espaciais, Avenida dos Astronautas 1758, São José dos Campos, 12227-010, SP, Brazil*
[5]*Instituto de Física y Astronomía, Facultad de Ciencias, Universidad de Valparaíso, Gran Bretaña No. 1111, Playa Ancha, Valparaíso, Chile*
[6]*Millennium Institute of Astrophysics (MAS), Nuncio Monseñor Sótero Sanz 100, Providencia, Santiago, Chile*

Accepted XXX. Received YYY; in original form ZZZ

ABSTRACT
The central regions of galaxies harboring Active Galactic Nuclei can be quite complex, especially at high activity, presenting, besides variability, a variety of phenomena related, for example, to ionization/excitation mechanisms. A detailed study is necessary in order to understand better those objects. For that reason, we performed a multiwavelength analysis of the nuclear region of the nearby Seyfert galaxy NGC 7314, using an optical data cube obtained with the Integral Field Unit from the Gemini Multi-Object Spectrograph, together with Hubble Space Telescope images, X-ray data from the *XMM–Newton* and the *Nuclear Spectroscopic Telescope Array* and radio data from Atacama Large Millimeter/Submillimeter Array. The goals were to study the nuclear and circumnuclear emission, the emission of the AGN and the gas kinematics. The optical nuclear spectrum shows emission of Seyfert nucleus, with broad components in the Hα and Hβ emission lines, characterizing a type 1 AGN, with a spectrum rich in coronal line emission. We also found a "very broad" component in Hα emission line profile. The spatial morphology of the [O III]λ5007 suggests the presence of an ionization cone, west of the nucleus, meanwhile the east cone seems to be obscured by dust. The modeling of the X-ray and optical data indicates that our line-of-sight passes through the border of the dusty torus. An extended [Fe VII]λ6087 emission was also detected, which could possibly be explained by a scenario involving photoionization+shocks mechanisms. Evidences of feeding process occurring from the bar to the nucleus were also detected.

Key words: galaxies:nuclei – galaxies:active – galaxies:individual: NGC 7314 – galaxies: kinematics and dynamics

Reference: Patricia Da Silva et al. (2022), submitted to MNRAS.

My contribution to this work was to extract and analyse the X-ray spectra used to compare with optical and infrared data. In addition, I perform the variability analysis and develop a method to fit a complex model in the spectra fitting. Furthermore, I actively participated in the discussion of the paper.

Observational hints on the torus obscuring gas behaviour through X-rays with *NuSTAR* data

N. Osorio-Clavijo,[1] ⋆ O. González-Martín,[1] S.F. Sánchez,[2] D. Esparza-Arredondo,[1] J. Masegosa,[3] C. Victoria-Ceballos,[1] L. Hernández-García[4,5] Y. Díaz,[5]
[1]*Instituto de Radioastronomía and Astrofisica (IRyA-UNAM), 3-72 (Xangari), 8701, Morelia, Mexico*
[2]*Instituto de Astronomía, Universidad Nacional Autónoma de México, A. P. 70-264, C.P. 04510, México, D.F., Mexico*
[3]*IAA – Instituto de Astrofísica de Andalucía (CSIC), Glorieta de la Astonomía, 18008 Granada, Spain*
[4]*Millennium Institute of Astrophysics (MAS), Nuncio Monseñor Sótero Sanz 100, Providencia, Santiago, Chile*
[5]*Instituto de Física y Astronomía, Facultad de Ciencias, Universidad de Valparaíso, Gran Bretaña 1111, Playa Ancha, Valparaíso, Chile*

Accepted 2021 December 19. Received 2021 December 16; in original form 2021 March 25.

ABSTRACT

According to theory, the torus of active galactic nuclei (AGN) is sustained from a wind coming off the accretion disk, and for low efficient AGN, it has been proposed that such structure disappears. However, the exact conditions for its disappearance remain unclear. This can be studied throughout the reflection component at X-rays, which is associated with distant and neutral material at the inner walls of the torus in obscured AGN. We select a sample of 81 AGNs observed with NuSTAR with a distance limit of D< 200 Mpc and Eddington rate $\lambda_{\rm Edd} \equiv L_{\rm bol}/L_{\rm Edd} < 10^{-3}$. We fit the 3-70 keV spectra using a model accounting for a partial-covering absorber plus a reflection component from neutral material. We find that the existence of the reflection component spans in a wide range of black-hole mass and bolometric luminosities, with only ∼13% of our sample (11 sources) lacking of any reflection signatures. These sources fall in the region in which the torus may be lacking in the L-MBH diagram. For the sources with a detected reflection component, we find that the vast majority of them are highly obscured (log $N_{\rm H} > 23$), with ∼ 20% being Compton-thick. We also find an increase on the number of unobscured sources and a tentative increase on the ratio between FeKα emission line and Compton-hump luminosities toward $\lambda_{\rm Edd} = 10^{-5}$, suggesting that the contribution of the FeKα line changes with Eddington ratio.

Key words: galaxies: active - X-rays: galaxies - galaxies: Seyfert.

Reference: Osorio-Clavijo et al. (2022), Monthly Notices of the Royal Astronomical Society (MNRAS), Volume 510, pp.5102-5118.

My contribution to this work was the participation in the analysis of the X-ray spectra in the discussion of the paper.

The nuclear environment of NGC 2442: a Compton-thick low-luminosity AGN

Patrícia da Silva,[1]★ R. B. Menezes[2]† Y. Díaz[3]‡ Elena López–Navas,[3] J. E. Steiner[1]
[1]*Instituto de Astronomia, Geofísica e Ciências Atmosféricas, Departamento de Astronomia, Universidade de São Paulo, 05508-090, SP, Brazil*
[2]*Instituto Mauá de Tecnologia, Praça Mauá 1, 09580-900, São Caetano do Sul, SP, Brazil*
[3]*Instituto de Física y Astronomía, Facultad de Ciencias, Universidad de Valparaíso, Gran Bretaña No. 1111, Playa Ancha, Valparaíso, Chile*

Accepted: 2021 April 27. Received: 2020 December 29

ABSTRACT

The detailed study of nuclear regions of galaxies is important because it can help understanding the active galactic nucleus (AGN) feedback mechanisms, the connections between the nuclei and their host galaxies, and ultimately the galaxy formation processes. We present the analysis of an optical data cube of the central region of the galaxy NGC 2442, obtained with the integral field unit (IFU) of the Gemini Multi-Object Spectrograph (GMOS). We also performed a multiwavelength analysis, with *Chandra* data, *XMM–Newton* and *NuSTAR* spectra, and *Hubble Space Telescope* (*HST*) images. The analysis revealed that the nuclear emission is consistent with a Low Ionization Nuclear Emission-line Region (LINER) associated with a highly obscured compact hard X-ray source, indicating a Compton-thick AGN. The *HST* image in the F658N filter (Hα) reveals an arched structure corresponding to the walls of the ionization cone of the AGN. The gas kinematic pattern and the high gas velocity dispersion values in the same region of the ionization cone suggest an outflow emission. The stellar archaeology results indicate the presence of only old stellar populations ($\sim$ 10 Gyr), with high metallicity (z = 0.02 and 0.05), and the absence of recent star formation in the central region of NGC 2442, which is possibly a consequence of the AGN feedback, associated with the detected outflow, shutting off star formation. NGC 2442 is a late-type galaxy similar to the Milky Way, and comparisons show that the main difference between them is the presence of a low-luminosity AGN.

Key words: galaxies: active – galaxies: individual: NGC 2442 – galaxies: kinematics and dynamics – galaxies: nuclei

Reference: Patricia Da Silva et al. (2021), Monthly Notices of the Royal Astronomical Society, Volume 505, pp.223-235

My contribution to this work was to extract and analyse the X-ray spectra used to compare with optical and infrared data. Furthermore, I actively participated in the discussion of the paper.

Resolving accretion flows in nearby active galactic nuclei with the Event Horizon Telescope

Bidisha Bandyopadhyay,[1]★ Fu-Guo Xie,[2] Neil M. Nagar,[1] Dominik R. G. Schleicher,[1] Venkatessh Ramakrishnan,[1] Patricia Arévalo,[3] Elena López,[3] and Yaherlyn Diaz[3]
[1] *Departamento de Astronomía, Facultad Ciencias Físicas y Matemáticas, Universidad de Concepción, Av. Esteban Iturra s/n Barrio Universitario, Casilla 160-C, Concepción, Chile*
[2] *Key Laboratory for Research in Galaxies and Cosmology, Shanghai Astronomical Observatory, Chinese Academy of Sciences, 80 Nandan Road, Shanghai 200030, China*
[3] *Instituto de Física y Astronomía, Facultad de Ciencias, Universidad de Valparaíso, Gran Bretana No. 1111, Playa Ancha, Valparaíso, Chile*

Accepted XXX. Received YYY; in original form ZZZ

ABSTRACT
The Event Horizon Telescope (EHT), now with its first ever image of the photon ring around the supermassive black hole of M87, provides a unique opportunity to probe the physics of supermassive black holes through Very Long Baseline Interferometry (VLBI), such as the existence of the event horizon, the accretion processes as well as jet formation in Low Luminosity AGN (LLAGN). We build a theoretical model which includes an Advection Dominated Accretion Flow (ADAF) with emission from thermal and non-thermal electrons in the flow and a simple radio jet outflow. The predicted spectral energy distribution (SED) of this model is compared to sub-arcsec resolution observations to get the best estimates of the model parameters. The model-predicted radial emission profiles at different frequency bands are used to predict whether the inflow can be resolved by the EHT or with telescopes such as the Global 3-mm VLBI array (GMVA). In this work the model is initially tested with high resolution SED data of M87 and then applied to our sample of 5 galaxies (Cen A, M84, NGC 4594, NGC 3998 and NGC 4278). The model then allows us to predict if one can detect and resolve the inflow for any of these galaxies using the EHT or GMVA within an 8 hour integration time.

Key words: galaxies: nuclei – accretion, accretion discs – (galaxies:) quasars: supermassive black holes

Reference: Bandyopadhya, Bidisha et al. (2019), Monthly Notices of the Royal Astronomical Society, Volume 490, Issue 4, p.4606-4621.

My contribution to this work was the estimation of the fluxes (in the soft, 0.5–10.0 keV and hard 10.0–79.0 keV energy band) used to perform the SED as well as to participate in the discussion section.

A young and obscured AGN embedded in the giant radio galaxy Mrk 1498

L. Hernández-García[1⋆], F. Panessa[2], L. Bassani[3], G. Bruni[2], F. Ursini[3], V. Chavushyan[4], O. González-Martín[5], S. Cazzoli[6], E. F. Jiménez-Andrade[7,8], P. Arévalo[1], Y. Díaz[1], A. Bazzano[2], and P. Ubertini[2]

[1]*Instituto de Física y Astronomía, Facultad de Ciencias, Universidad de Valparaíso, Gran Bretaña 1111, Playa Ancha, Valparaíso, Chile*
[2]*INAF - Istituto di Astrofisica e Planetologia Spaziali (IAPS-INAF), Via del Fosso del Cavaliere 100, 00133 Roma, Italy*
[3]*INAF-Osservatorio di astrofisica e scienza dello spazio di Bologna, Via Piero Gobetti 93/3, 40129 Bologna, Italy*
[4]*Instituto Nacional de Astrofísica, Optica y Electrónica, Apartado Postal 51-216, 72000 Puebla, Mexico*
[5]*Instituto de Radioastronomía y Astrofísica (IRyA-UNAM), 3-72 (Xangari), 8701, Morelia, Mexico*
[6]*Instituto de Astrofísica de Andalucía, CSIC, Glorieta de la Astronomía, s/n, 18008 Granada, Spain*
[7]*Argelander Institute for Astronomy, University of Bonn, Auf dem Hügel 71, D-53121 Bonn, Germany*
[8]*International Max Planck Research School of Astronomy and Astrophysics at the Universities of Bonn and Cologne*

Draft:5 August 2021

ABSTRACT

Mrk 1498 is part of a sample of galaxies with extended emission line regions (extended outwards up to a distance of ∼7 kpc) suggested to be photo-ionized by an AGN that has faded away or that is still active but heavily absorbed. Interestingly, the nucleus of Mrk 1498 is at the center of two giant radio lobes with a projected linear size of 1.1 Mpc. Our multi-wavelength analysis reveals a complex nuclear structure, with a young radio source (Giga-hertz Peaked Spectrum) surrounded by a strong X-ray nuclear absorption, a mid-infrared spectrum that is dominated by the torus emission, plus a circum-nuclear extended emission in the [OIII] image (with radius of ∼ 1 kpc), most likely related to the ionization of the AGN, aligned with the small and large scale radio jet and extended also at X-rays. In addition a large-scale extended emission (up to ∼ 10 kpc) is only visible in [OIII]. These data show conclusive evidence of a heavily absorbed nucleus and has recently restarted its nuclear activity. To explain its complexity, we propose that Mrk 1498 is the result of a merging event or secular processes, such as a minor interaction, that has triggered the nuclear activity and produced tidal streams. The large-scale extended emission that gives place to the actual morphology could either be explained by star formation or outflowing material from the AGN.

Key words: galaxies: active – galaxies: jets – galaxies: individual: Mrk 1498

Reference: Hernández-García, L et al. (2019), Monthly Notices of the Royal Astronomical Society, Volume 489, Issue 3, p.4049-4062.

In this work, I develop models in CLOUDY to study the existence (or not) of an AGN in this galaxy. In addition, I participate actively in the discussion.

Bibliography

Abramowicz M. A., Czerny B., Lasota J. P., Szuszkiewicz E., 1988, ApJ, 332, 646

Antonucci R., 1993, ARA&A, 31, 473

Antonucci R., 2012, Astronomical and Astrophysical Transactions, 27, 557

Antonucci R. R. J., Miller J. S., 1985, ApJ, 297, 621

Arévalo P. et al., 2014, ApJ, 791, 81

Arévalo P., Uttley P., Lira P., Breedt E., McHardy I. M., Churazov E., 2009, MNRAS, 397, 2004

Arnaud K. A., 1996, in Astronomical Society of the Pacific Conference Series, Vol. 101, Jacoby G. H., Barnes J., eds, Astronomical Data Analysis Software and Systems V, p. 17

Arnaud K. A. et al., 1985, MNRAS, 217, 105

Awaki H., Terashima Y., Higaki Y., Fukazawa Y., 2009, PASJ, 61, S317

Baldwin J. A., Phillips M. M., Terlevich R., 1981, PASP, 93, 5

Ballantyne D. R., McDuffie J. R., Rusin J. S., 2011, ApJ, 734, 112

Ballantyne D. R., Ross R. R., Fabian A. C., 2001, MNRAS, 327, 10

Balmaverde B., Capetti A., 2014, A&A, 563, A119

Baloković M. et al., 2018, ApJ, 854, 42

Baloković M., Cabral S. E., Brenneman L., Urry C. M., 2021, ApJ, 916, 90

Bambi C. et al., 2021, Space Sci. Rev., 217, 65

Bambi C., Cárdenas-Avendaño A., Dauser T., García J. A., Nampalliwar S., 2017, ApJ, 842, 76

Barth A. J., Filippenko A. V., Moran E. C., 1999, ApJ, 525, 673

Barthelmy S. D. et al., 2005, Space Sci. Rev., 120, 143

Bassani L., Dadina M., Maiolino R., Salvati M., Risaliti G., Della Ceca R., Matt G., Zamorani G., 1999, ApJS, 121, 473

Bauer F. E. et al., 2015, ApJ, 812, 116

Baumgartner W. H., Tueller J., Markwardt C. B., Skinner G. K., Barthelmy S., Mushotzky R. F., Evans P. A., Gehrels N., 2013, The Astrophysical Journal Supplement Series, 207, 19

Beckmann V., Gehrels N., Tueller J., 2007, ApJ, 666, 122

Best P. N., Heckman T. M., 2012, MNRAS, 421, 1569

Bian W.-H., Zhao Y.-H., 2003, PASJ, 55, 599

Bianchi S. et al., 2019, MNRAS, 488, L1

Bianchi S., Guainazzi M., Matt G., Chiaberge M., Iwasawa K., Fiore F., Maiolino R., 2005, A&A, 442, 185

Bianchi S. et al., 2017, MNRAS, 468, 2740

Bianchi S., Matt G., Balestra I., Guainazzi M., Perola G. C., 2004, A&A, 422, 65

Bianchi S. et al., 2012, MNRAS, 426, 3225

Bianchi S., Piconcelli E., Chiaberge M., Bailón E. J., Matt G., Fiore F., 2009, ApJ, 695, 781

Binder B., Markowitz A., Rothschild R. E., 2009, ApJ, 691, 431

Blandford R. D., McKee C. F., 1982, ApJ, 255, 419

Blandford R. D., Rees M. J., 1974, MNRAS, 169, 395

Bradley L. D., Kaiser M. E., Baan W. A., 2004, ApJ, 603, 463

Brenneman L. et al., 2011, The Astrophysical Journal, 736, 103

Brightman M. et al., 2018, ApJ, 867, 110

Brightman M., Nandra K., 2011a, MNRAS, 413, 1206

Brightman M., Nandra K., 2011b, MNRAS, 414, 3084

Burrows D. N. et al., 2005, Space Sci. Rev., 120, 165

Buttiglione S., Capetti A., Celotti A., Axon D. J., Chiaberge M., Macchetto F. D., Sparks W. B., 2010, A&A, 509, A6

Cappi M. et al., 2006, A&A, 446, 459

Cazzoli S. et al., 2018, MNRAS, 480, 1106

Chang C. S., Ros E., Kovalev Y. Y., Lister M. L., 2010, A&A, 515, A38

Clavel J., Wamsteker W., Glass I. S., 1989, ApJ, 337, 236

Crummy J., Fabian A. C., Gallo L., Ross R. R., 2006, MNRAS, 365, 1067

Curran P. A., 2014, arXiv e-prints, arXiv:1411.3816

Davidson K., Netzer H., 1979, Reviews of Modern Physics, 51, 715

de Rosa A., Bassani L., Ubertini P., Panessa F., Malizia A., Dean A. J., Walter R., 2008, A&A, 483, 749

de Vaucouleurs G., 1991, MNRAS, 249, 28P

den Herder J. W. et al., 2001, A&A, 365, L7

Dewangan G. C., Griffiths R. E., Dasgupta S., Rao A. R., 2007, ApJ, 671, 1284

Diaz Y. et al., 2020, MNRAS, 496, 5399

Dickey J. M., Lockman F. J., 1990, ARA&A, 28, 215

Doi A., Asada K., Fujisawa K., Nagai H., Hagiwara Y., Wajima K., Inoue M., 2013, ApJ, 765, 69

Done C., Gierliński M., Kubota A., 2007, A&A Rev., 15, 1

Draine B. T., Li A., 2001, ApJ, 551, 807

Dumas G., Schinnerer E., Tabatabaei F. S., Beck R., Velusamy T., Murphy E., 2011, AJ, 141, 41

Duras F. et al., 2020, A&A, 636, A73

Elitzur M., 2008, , 52, 274

Elitzur M., Ho L. C., 2009, ApJ, 701, L91

Elitzur M., Shlosman I., 2006, ApJ, 648, L101

Elvis M., 2017, ApJ, 847, 56

Elvis M., Maccacaro T., Wilson A. S., Ward M. J., Penston M. V., Fosbury R. A. E., Perola G. C., 1978, MNRAS, 183, 129

Elvis M. et al., 1994, ApJS, 95, 1

Emmanoulopoulos D., Papadakis I. E., Epitropakis A., Pecháček T., Dovčiak M., McHardy I. M., 2016, MNRAS, 461, 1642

Eracleous M., Hwang J. A., Flohic H. M. L. G., 2010, ApJS, 187, 135

Eracleous M., Lewis K. T., Flohic H. M. L. G., 2009, , 53, 133

Esparza-Arredondo D., Gonzalez-Martín O., Dultzin D., Masegosa J., Ramos-Almeida C., García-Bernete I., Fritz J., Osorio-Clavijo N., 2021, A&A, 651, A91

Event Horizon Telescope Collaboration et al., 2022, ApJ, 930, L17

Fabian A. C., 2006, in ESA Special Publication, Vol. 604, Wilson A., ed, The X-ray Universe 2005, p. 463

Fabian A. C., Canizares C. R., Barcons X., 1989, MNRAS, 239, 15P

Fabian A. C., Lohfink A., Belmont R., Malzac J., Coppi P., 2017, MNRAS, 467, 2566

Fabian A. C., Lohfink A., Kara E., Parker M. L., Vasudevan R., Reynolds C. S., 2015, MNRAS, 451, 4375

Fabian A. C. et al., 2009, Nature, 459, 540

Fanali R., Caccianiga A., Severgnini P., Della Ceca R., Marchese E., Carrera F. J., Corral A., Mateos S., 2013, MNRAS, 433, 648

Ferrarese L., Ford H., 2005, Space Sci. Rev., 116, 523

Filho M. E., Barthel P. D., Ho L. C., 2002, A&A, 385, 425

Frank B. S., Morganti R., Oosterloo T., Nyland K., Serra P., 2016, A&A, 592, A94

Gandhi P. et al., 2017, MNRAS, 467, 4606

García J., Dauser T., Reynolds C. S., Kallman T. R., McClintock J. E., Wilms J., Eikmann W., 2013, ApJ, 768, 146

Gehrels N. et al., 2004, ApJ, 611, 1005

George I. M., Fabian A. C., 1991, MNRAS, 249, 352

Gilli R., Comastri A., Hasinger G., 2007, A&A, 463, 79

Gilli R., Maiolino R., Marconi A., Risaliti G., Dadina M., Weaver K. A., Colbert E. J. M., 2000, A&A, 355, 485

Goddi C. et al., 2019, The Messenger, 177, 25

González-Martín O., 2018, ApJ, 858, 2

González-Martín O. et al., 2017, ApJ, 841, 37

González-Martín O., Masegosa J., Márquez I., Guainazzi M., Jiménez-Bailón E., 2009, A&A, 506, 1107

González-Martín O., Masegosa J., Márquez I., Guainazzi M., Jiménez-Bailón E., 2009, A&A, 506, 1107

González-Martín O., Vaughan S., 2012, A&A, 544, A80

Greenhill L. J., Henkel C., Becker R., Wilson T. L., Wouterloot J. G. A., 1995, A&A, 304, 21

Gu M., Cao X., 2009, MNRAS, 399, 349

Guainazzi M., Bianchi S., Dovčiak M., 2006, Astronomische Nachrichten, 327, 1032

Guainazzi M., Matt G., Perola G. C., 2005a, A&A, 444, 119

Guainazzi M., Matt G., Perola G. C., 2005b, A&A, 444, 119

Haardt F., Maraschi L., 1993, ApJ, 413, 507

Harrison F. A. et al., 2013, ApJ, 770, 103

Hayashi I., Koyama K., Awaki H., Yamauchi S. U. S., 1996, PASJ, 48, 219

Heckman T. M., 1980, A&A, 87, 152

Hernández-García L., González-Martín O., Márquez I., Masegosa J., 2013, A&A, 556, A47

Hernández-García L., González-Martín O., Masegosa J., Márquez I., 2014, A&A, 569, A26

Hernández-García L., Masegosa J., González-Martín O., Márquez I., 2015, A&A, 579, A90

Hernández-García L., Masegosa J., González-Martín O., Márquez I., Guainazzi M., Panessa F., 2017, A&A, 602, A65

Hernández-García L., Masegosa J., González-Martín O., Márquez I., Perea J., 2016, ApJ, 824, 7

Herrnstein J. R., Moran J. M., Greenhill L. J., Trotter A. S., 2005, ApJ, 629, 719

Hinkle J. T., Mushotzky R., 2021, MNRAS, 506, 4960

Ho L. C., 2002, ApJ, 564, 120

Ho L. C., 2008a, ARA&A, 46, 475

Ho L. C., 2008b, ARA&A, 46, 475

Ho L. C., Filippenko A. V., Sargent W. L. W., Peng C. Y., 1997, in Bulletin of the American Astronomical Society, Vol. 29, American Astronomical Society Meeting Abstracts #189, p. 735

Ho L. C., Greene J. E., Filippenko A. V., Sargent W. L. W., 2009, ApJS, 183, 1

Ho L. C., Ulvestad J. S., 2001, ApJS, 133, 77

Hönig S. F., Kishimoto M., 2010, A&A, 523, A27

Hopkins P. F., Richards G. T., Hernquist L., 2007, ApJ, 654, 731

Hummel E., van der Hulst J. M., Dickey J. M., 1984, A&A, 134, 207

Isobe T., Feigelson E. D., Nelson P. I., 1986, ApJ, 306, 490

Jennison R. C., Das Gupta M. K., 1953, Nature, 172, 996

Kalberla P. M. W., Burton W. B., Hartmann D., Arnal E. M., Bajaja E., Morras R., Poeppel W. G. L., 2005, VizieR Online Data Catalog, 8076

Kaspi S., Smith P. S., Netzer H., Maoz D., Jannuzi B. T., Giveon U., 2000, ApJ, 533, 631

Kawamuro T., Ueda Y., Tazaki F., Terashima Y., Mushotzky R., 2016, ApJ, 831, 37

Keek L., Ballantyne D. R., 2016, MNRAS, 456, 2722

Kellermann K. I., Sramek R., Schmidt M., Shaffer D. B., Green R., 1989, AJ, 98, 1195

Khachikian E. Y., Weedman D. W., 1974, ApJ, 192, 581

Kollatschny W., 2003, A&A, 407, 461

Koratkar A., Blaes O., 1999, PASP, 111, 1

Kormendy J., Ho L. C., 2013, ARA&A, 51, 511

Kormendy J., Richstone D., 1995, ARA&A, 33, 581

Koss M. et al., 2017, ApJ, 850, 74

Koss M. J. et al., 2016, ApJ, 825, 85

Krause M. O., Oliver J. H., 1979, Journal of Physical and Chemical Reference Data, 8, 329

Krips M. et al., 2007, A&A, 464, 553

Krips M. et al., 2005, A&A, 442, 479

Krips M., Eckart A., Neri R., Schödel R., Leon S., Downes D., García-Burillo S., Combes F., 2006, A&A, 446, 113

Krivonos R., Revnivtsev M., Lutovinov A., Sazonov S., Churazov E., Sunyaev R., 2007, A&A, 475, 775

Landi R. et al., 2009, A&A, 493, 893

Li S.-L., Xie F.-G., 2017, MNRAS, 471, 2848

Lira P., Arévalo P., Uttley P., McHardy I. M. M., Videla L., 2015, MNRAS, 454, 368

Liu B. F., Mineshige S., Ohsuga K., 2003, ApJ, 587, 571

Liu Y., Li X., 2014, ApJ, 787, 52

Lobban A. P., Reeves J. N., Porquet D., Braito V., Markowitz A., Miller L., Turner T. J., 2010, MNRAS, 408, 551

Lubiński P., Zdziarski A. A., Walter R., Paltani S., Beckmann V., Soldi S., Ferrigno C., Courvoisier T. J. L., 2010, MNRAS, 408, 1851

Lusso E. et al., 2012, Monthly Notices of the Royal Astronomical Society, 425, 623–640

Ma R.-Y., Yuan F., Wang D.-X., 2007, ApJ, 671, 1981

Maiolino R., Ruiz M., Rieke G. H., Keller L. D., 1995, ApJ, 446, 561

Maiolino R., Salvati M., Bassani L., Dadina M., della Ceca R., Matt G., Risaliti G., Zamorani G., 1998, A&A, 338, 781

Malaguti G. et al., 1999, A&A, 342, L41

Malaguti G. et al., 1998, A&A, 331, 519

Malizia A., Molina M., Bassani L., Stephen J. B., Bazzano A., Ubertini P., Bird A. J., 2014, ApJ, 782, L25

Malkan M. A., Gorjian V., Tam R., 1998, ApJS, 117, 25

Malkan M. A., Sargent W. L. W., 1982, ApJ, 254, 22

Manmoto T., Kato S., Nakamura K. E., Narayan R., 2000, ApJ, 529, 127

Maoz D., 2007, MNRAS, 377, 1696

Marconi A., Risaliti G., Gilli R., Hunt L. K., Maiolino R., Salvati M., 2004, MNRAS, 351, 169

Marinucci A., Bianchi S., Braito V., De Marco B., Matt G., Middei R., Nardini E., Reeves J. N., 2020, MNRAS, 496, 3412

Marinucci A., Bianchi S., Braito V., Matt G., Nardini E., Reeves J., 2018, MNRAS, 478, 5638

Marinucci A. et al., 2014, MNRAS, 440, 2347

Marinucci A., Tortosa A., NuSTAR AGN Physics Working Group , 2016, Astronomische Nachrichten, 337, 490

Markakis K. et al., 2015, A&A, 580, A11

Matt G., Fabian A. C., Ross R. R., 1996, MNRAS, 278, 1111

Matt G., Guainazzi M., 2005, Chinese Journal of Astronomy and Astrophysics Supplement, 5, 99

Matt G., Guainazzi M., Maiolino R., 2003, MNRAS, 342, 422

Matt G., Perola G. C., Piro L., 1991, A&A, 247, 25

McHardy I. M. et al., 2014, MNRAS, 444, 1469

McHardy I. M., Koerding E., Knigge C., Uttley P., Fender R. P., 2006, Nature, 444, 730

Miller J. S., Goodrich R. W., 1990, ApJ, 355, 456

Moran E. C., Barth A. J., Kay L. E., Filippenko A. V., 2000, ApJ, 540, L73

Mortlock D. J. et al., 2011, Nature, 474, 616

Moustakas J., Kennicutt J., Robert C., 2006, ApJS, 164, 81

Müller-Sánchez F., Prieto M. A., Mezcua M., Davies R. I., Malkan M. A., Elitzur M., 2013, ApJ, 763, L1

Murphy K. D., Yaqoob T., 2009, MNRAS, 397, 1549

Murray N., Chiang J., Grossman S. A., Voit G. M., 1995, ApJ, 451, 498

Nagar N. M., Falcke H., Wilson A. S., 2005, A&A, 435, 521

Nandra K., 2006, MNRAS, 368, L62

Nandra K., George I. M., Mushotzky R. F., Turner T. J., Yaqoob T., 1997, ApJ, 488, L91

Nandra K., O'Neill P. M., George I. M., Reeves J. N., 2007, MNRAS, 382, 194

Nandra K., Pounds K. A., 1994a, MNRAS, 268, 405

Nandra K., Pounds K. A., 1994b, MNRAS, 268, 405

Narayan R., McClintock J. E., 2008, , 51, 733

Narayan R., Yi I., Mahadevan R., 1994, arXiv Astrophysics e-prints

Nemmen R., Storchi-Bergmann T., Eracleous M., 2013, Monthly Notices of the Royal Astronomical Society, 438

Nemmen R. S., Storchi-Bergmann T., Yuan F., Eracleous M., Terashima Y., Wilson A. S., 2006, ApJ, 643, 652

Nenkova M., Sirocky M. M., Ivezić Ž., Elitzur M., 2008, ApJ, 685, 147

Netzer H., 1990, in Blandford R. D., Netzer H., Woltjer L., Courvoisier T. J. L., Mayor M., eds, Active Galactic Nuclei, p. 57

Netzer H., 2013, The Physics and Evolution of Active Galactic Nuclei

Netzer H., 2015, ARA&A, 53, 365

Netzer H., 2019, MNRAS, 488, 5185

Netzer H., Laor A., 1993, ApJ, 404, L51

Netzer H., Lira P., Trakhtenbrot B., Shemmer O., Cury I., 2007, ApJ, 671, 1256

Niedźwiecki A., Zdziarski A. A., Szanecki M., 2016, ApJ, 821, L1

Oh K. et al., 2018a, ApJS, 235, 4

Oh K. et al., 2018b, ApJS, 235, 4

Osorio-Clavijo N., González-Martín O., Papadakis I., Masegosa J., Hernández-García L., 2019, arXiv e-prints, arXiv:1910.01660

Osorio-Clavijo N., González-Martín O., Papadakis I. E., Masegosa J., Hernández-García L., 2020, MNRAS, 491, 29

Osterbrock D. E., 1981, ApJ, 249, 462

Osterbrock D. E., 1989, Astrophysics of gaseous nebulae and active galactic nuclei

Osterbrock D. E., Koski A. T., 1976, MNRAS, 176, 61P

Padovani P., Miller N., Kellermann K. I., Mainieri V., Rosati P., Tozzi P., 2011, ApJ, 740, 20

Panessa F., Barcons X., Bassani L., Cappi M., Carrera F. J., Ho L. C., Pellegrini S., 2007, A&A, 467, 519

Parker M. L. et al., 2015, MNRAS, 447, 72

Parker M. L. et al., 2016, MNRAS, 461, 1927

Perez Garcia A. M., Rodriguez Espinosa J. M., Santolaya Rey A. E., 1998, ApJ, 500, 685

Pérez-Torres M. A., Alberdi A., 2007, MNRAS, 379, 275

Perola G. C., Matt G., Cappi M., Fiore F., Guainazzi M., Maraschi L., Petrucci P. O., Piro L., 2002, A&A, 389, 802

Peterson B. M., 1997, An Introduction to Active Galactic Nuclei

Peterson B. M., Horne K., 2004, Astronomische Nachrichten, 325, 248

Petrucci P. O. et al., 2002, A&A, 388, L5

Petrucci P. O., Merloni A., Fabian A., Haardt F., Gallo E., 2001, MNRAS, 328, 501

Pian E., Romano P., Maoz D., Cucchiara A., Pagani C., La Parola V., 2010, MNRAS, 401, 677

Piconcelli E. et al., 2006, A&A, 453, 839

Piro L., Yamauchi M., Matsuoka M., 1990, ApJ, 360, L35

Pogge R. W., 1988, ApJ, 328, 519

Pogge R. W., Maoz D., Ho L. C., Eracleous M., 2000, ApJ, 532, 323

Pounds K. A., Nandra K., Stewart G. C., George I. M., Fabian A. C., 1990, Nature, 344, 132

Pringle J. E., 1981, ARA&A, 19, 137

Privon G. C. et al., 2020, ApJ, 893, 149

Proga D., Stone J. M., Kallman T. R., 2000, ApJ, 543, 686

Rees M. J., 1984, ARA&A, 22, 471

Rees M. J., Sciama D. W., 1966, Nature, 211, 805

Reeves J. N. et al., 2007, PASJ, 59, 301

Reeves J. N. et al., 2006, Astronomische Nachrichten, 327, 1079

Reynolds C. S., Nowak M. A., Markoff S., Tueller J., Wilms J., Young A. J., 2009, ApJ, 691, 1159

Ricci C., 2011, Ph.D. thesis, University of Geneva, Switzerland

Ricci C. et al., 2018, MNRAS, 480, 1819

Ricci C., Tazaki F., Ueda Y., Paltani S., Boissay R., Terashima Y., 2014, The Astrophysical Journal, 795, 147

Ricci C. et al., 2017a, ApJS, 233, 17

Ricci C. et al., 2017b, Nature, 549, 488

Risaliti G., 2002, A&A, 386, 379

Risaliti G., Elvis M., Nicastro F., 2002, ApJ, 571, 234

Risaliti G., Maiolino R., Salvati M., 1999, ApJ, 522, 157

Rivers E. et al., 2014, ApJ, 786, 126

Roming P. W. A. et al., 2005, Space Sci. Rev., 120, 95

Ross R. R., Fabian A. C., 1993, MNRAS, 261, 74

Ross R. R., Fabian A. C., Young A. J., 1999, MNRAS, 306, 461

Satyapal S., Dudik R. P., O'Halloran B., Gliozzi M., 2005, ApJ, 633, 86

Schmidt M., 1963, Nature, 197, 1040

Seyfert C. K., 1943, PASP, 55, 32

Shakura N. I., Sunyaev R. A., 1973, in IAU Symposium, Vol. 55, Bradt H., Giacconi R., eds, X- and Gamma-Ray Astronomy, p. 155

Shankar F., 2009, , 53, 57

Shankar F., Salucci P., Granato G. L., De Zotti G., Danese L., 2004, MNRAS, 354, 1020

She R., Ho L. C., Feng H., Cui C., 2018, ApJ, 859, 152

Shemmer O., Brandt W. N., Netzer H., Maiolino R., Kaspi S., 2006, ApJ, 646, L29

Shields G. A., 1978, Nature, 272, 706

Shu X. W., Yaqoob T., Murphy K. D., Braito V., Wang J. X., Zheng W., 2010, ApJ, 713, 1256

Shuder J. M., Osterbrock D. E., 1981, ApJ, 250, 55

Sparke L. S., van Moorsel G., Schwarz U. J., Vogelaar M., 2009, AJ, 137, 3976

Storchi-Bergmann T. et al., 2003, ApJ, 598, 956

Strüder L. et al., 2001, A&A, 365, L18

Takáts K., Vinkó J., 2006, MNRAS, 372, 1735

Terashima Y., Ho L. C., Ptak A. F., 2000, ApJ, 539, 161

Terashima Y., Kunieda H., Misaki K., 1999, PASJ, 51, 277

Terashima Y., Wilson A. S., 2002, in Boller T., Komossa S., Kahn S., Kunieda H., Gallo L., eds, X-ray Spectroscopy of AGN with Chandra and XMM-Newton, p. 279

Terashima Y., Wilson A. S., 2003, ApJ, 583, 145

Titarchuk L., 1994, ApJ, 434, 570

Tran H. D., 2003, ApJ, 583, 632

Tremaine S. et al., 2002, ApJ, 574, 740

Tueller J. et al., 2010, ApJS, 186, 378

Tully R. B., 1988, AJ, 96, 73

Turner M. J. L. et al., 2001, A&A, 365, L27

Turner T. J., Miller L., Kraemer S. B., Reeves J. N., Pounds K. A., 2009, ApJ, 698, 99

Ueda Y. et al., 2010, ApJ, 713, 257

Ulvestad J. S., Ho L. C., 2001, ApJ, 558, 561

Urry C. M., Padovani P., 1995, PASP, 107, 803

van den Bergh S., 1999, A&A Rev., 9, 273

Vasudevan R. V., Fabian A. C., 2007, MNRAS, 381, 1235

Vasudevan R. V., Fabian A. C., 2009, MNRAS, 392, 1124

Vaughan S., Edelson R., Warwick R. S., Uttley P., 2003, MNRAS, 345, 1271

Véron-Cetty M. P., Véron P., 2006, A&A, 455, 773

Véron-Cetty M. P., Véron P., 2010, A&A, 518, A10

Vincent F. H., Różańska A., Zdziarski A. A., Madej J., 2016, A&A, 590, A132

Voges W. et al., 2000, IAU Circ., 7432, 3

Watson W. D., Wallin B. K., 1994, ApJ, 432, L35

Weaver K. A., Heckman T. M., Strickland D. K., Dahlem M., 2002, ApJ, 576, L19

Weedman D. W. et al., 2005, ApJ, 633, 706

Wilson A. S., Yang Y., Cecil G., 2001, ApJ, 560, 689

Wrobel J. M., 1984, ApJ, 284, 531

Xu Y.-D., 2011, ApJ, 729, 10

Yamaoka K., Uzawa M., Arai M., Yamazaki T., Yoshida A., 2005a, Chinese Journal of Astronomy and Astrophysics Supplement, 5, 273

Yamaoka K., Uzawa M., Arai M., Yamazaki T., Yoshida A., 2005b, Chinese Journal of Astronomy and Astrophysics Supplement, 5, 273

Yang Q.-X., Xie F.-G., Yuan F., Zdziarski A. A., Gierliński M., Ho L. C., Yu Z., 2015a, MNRAS, 447, 1692

Yang Q.-X., Xie F.-G., Yuan F., Zdziarski A. A., Gierliński M., Ho L. C., Yu Z., 2015b, MNRAS, 447, 1692

Yaqoob T., George I. M., Kallman T. R., Padmanabhan U., Weaver K. A., Turner T. J., 2003, ApJ, 596, 85

Younes G., Porquet D., Sabra B., Reeves J. N., 2011, A&A, 530, A149

Younes G., Porquet D., Sabra B., Reeves J. N., Grosso N., 2012, A&A, 539, A104

Younes G., Ptak A., Ho L. C., Xie F.-G., Terasima Y., Yuan F., Huppenkothen D., Yukita M., 2019, ApJ, 870, 73

Young A. J., McHardy I., Emmanoulopoulos D., Connolly S., 2018, MNRAS, 476, 5698

Young S., Hough J. H., Efstathiou A., Wills B. J., Bailey J. A., Ward M. J., Axon D. J., 1996, MNRAS, 281, 1206

Yuan F., Narayan R., 2014, Annual Review of Astronomy and Astrophysics, 52, 529

Yuan F., Taam R. E., Misra R., Wu X.-B., Xue Y., 2007, ApJ, 658, 282

Yuan F., Zdziarski A. A., 2004, MNRAS, 354, 953

Zackrisson E., 2005, MNRAS, 359, 1193

Zaw I., Farrar G. R., Greene J. E., 2009, ApJ, 696, 1218

Zetzl M. et al., 2018, A&A, 618, A83

Zhang L., Cheng K. S., 1997, ApJ, 487, 370

Zhao X., Marchesi S., Ajello M., Cole D., Hu Z., Silver R., Torres-Albà N., 2021, A&A, 650, A57

Zycki P. T., Czerny B., 1994, MNRAS, 266, 653